Gravitational Microlensing toward the Andromeda Galaxy: A search for Dark Matter in M31

Arno Riffeser

GRAVITATIONAL MICROLENSING TOWARD THE ANDROMEDA GALAXY: A SEARCH FOR DARK MATTER IN M31

Dissertation

an der
Ludwig–Maximilians–Universität (LMU) München

Ph.D. Thesis

at the
Ludwig–Maximilians University (LMU) Munich

submitted by

Arno Riffeser

born on 24th April 1973 in Bozen

Munich, 4th January 2006

1st Evaluator: Prof. Dr. Ralf Bender
2nd Evaluator: Prof. Dr. Andreas Burkert

Date of the oral exam: 24th February 2006

Contents

List of Figures

List of Tables

Zusammenfassung

Aktuelle Forschungsergebnisse deuten darauf hin, dass das Universum insgesamt aus 72% Dunkler Energie, 23% nichtbaryonischer Materie und 4.5% baryonischer Materie besteht. Von dieser baryonischen Materie kann bisher nur ein neuntel sicher zugeordnet werden. Ferner läßt sich aus der Rotation von Spiralgalaxien ableiten, dass diese große Mengen an Dunkler Materie enthalten, die sich rein durch ihren gravitativen Einfluß auf sichtbare Objekte im Bulge und in der Scheibe der Galaxie zeigt. Dabei wird angenommen dass Bulge und Scheibe in den sog. dunklen Halo eingebettet sind, der diese unsichtbare Materie beinhaltet. Eine grundlegende Frage ist daher aus welcher Art die dunkle Materie im Halo von Spiralgalaxien besteht. Mögliche Kandidaten für solche Dunkle Materie sind neben schwach wechselwirkenden massiven Teilchen (WIMPs - Weakly Interacting Massive Particles) auch kompakte dunkle Objekte im Halo von Galaxien (Machos - MAssive Compact Halo Objects). Die vorliegende Doktorarbeit beschreibt die Suche nach solchen Machos im Halo unserer Nachbargalaxie Andromeda (M31). Im Falle von kompakten Objekten mit Massen im Bereich von einem milliardstel bis zum zehntausendfachen einer Sonnenmasse ermöglicht der sogenannte Gravitationslinseneffekt deren direkten Nachweis. Dabei beeinflußt die gravitative Wirkung eines kompakten Objekts die Lichtstrahlen von im Hintergrund liegenden Sternen derart, dass das Licht durch die Relativbewegung kurzzeitig fokussiert und verstärkt wird. Jedoch ist die Wahrscheinlichkeit, dass ein Stern eine meßbare Verstärkung aufweist, weniger als $1 : 1\,000\,000$. Durch Messungen von Millionen von Sternen konnten derartige charakteristische Lichtkurven im letzten Jahrzehnt sehr zahlreich in Richtung zum Zentrum unserer Milchstraße nachgewiesen werden. Eine noch größere Herausforderung stellt der Nachweis von Machos in der hundertmal weiter entfernten Andromeda-Galaxie (M31) dar. Zwar erreicht uns von einzelnen Sternen von dort im Vergleich zum Milchstraßenzentrum nur ein zehntausendstel an Strahlung, jedoch lassen sich mit einer einzigen Aufnahme Millionen von Sternen gleichzeitig auf Helligkeitsänderungen überprüfen. Da die Sichtlinie zum Zentrum von M31 die Halos der Milchstraße und von M31 durchdringt, gestattet dies Rückschlüsse auf den Anteil der Machos in beiden Galaxien. Wegen der deutlich größeren Entfernung und der damit verbundenen geringeren scheinbaren Helligkeit der Hintergrundobjekte sind die Anforderungen an die Datenanalyse ungleich höher. In der vorliegenden Doktorarbeit wurden daher neue Methoden entwickelt und aufgezeigt, um systematische Fehler bei der Aufnahme von Bildern zu kontrollieren und das Rauschen bei der Bildbearbeitung zu minimieren. Da die Zeitdauer eines Gravitationslinsenereignisses sehr kurz ist, mußten am Wendelstein-0.8-m-Teleskop, und während einer 3-jährigen Phase am Calar-Alto-1.23-m-Teleskop, zehntausende Aufnahmen während des Zeitraums von 1997 - 2005 gewonnen und ausgewertet werden. In dieser bezüglich der Zeitüberdeckung einmaligen Datenbasis konnten in 4 Mio. Lichtkurven insgesamt 13 Ereignisse nachgewiesen werden, die die typischen Helligkeitsänderungen des Gravitationslinseneffekts aufweisen. Die Analyse der Lichtkurven zeigt mit den in dieser Arbeit gewonnenen theoretischen Erkenntnissen bezüglich der endlichen Größe der Hintergrundsterne,

dass alle Gravitationslinsenkandidaten mit einem Halo aus dunklen Objekten von 0.2 Sonnenmassen vereinbar sind. Während die Anzahl der Detektionen im Vergleich zu früheren theoretischen Vorhersagen deutlich geringer ausfiel, zeigten die im Rahmen dieser Doktorarbeit entwickelten theoretischen Vorhersagen eine sehr gute Übereinstimmung. Ob sich die beobachteten Gravitationslinsenereignisse wirklich durch Machos im Halo oder eventuell durch Sterne in Bulge oder Scheibe hervorgerufen wurden, soll durch weiterführende Arbeiten mittels Monte-Carlo-Simulationen bezüglich der Detektionseffizienz geklärt werden. Daraus lassen sich dann quantitative Aussagen über die Art der dunklen Materie und den Anteil von Machos im Halo der M31 Galaxie gewinnen.

Chapter 1

Introduction

1.1 Dark Matter - Machos - Microlensing

In the exploration of the universe the only direct accesses to its physical behavior are through measurements of the electromagnetic emission from its consisting matter. Since the spectrum includes many features, astronomers are able to test very complex models and to extract masses, velocities, and densities for all kinds of luminous matter in the universe. Having derived these properties the gravitational interaction between these objects can be tested to check if the main part of the matter is luminous, or if some matter cannot be detected through electromagnetic radiation. The first idea is proven in our solar system: 99.9% of the matter is concentrated in the sun, the rest is present in planets, and asteroids. The second hypothesis also has some direct hints: Stars do not have an infinite energy reservoir and, therefore, can change to a non-luminous state. This non-luminous matter has been named "dark matter", since it cannot be observed directly by collecting photons. The difficulties for exploring the dark matter are clear: As no direct electromagnetic radiation reaches the neighborhood of the earth (where satellites have access to) we are limited to indirect methods, where luminous objects reveal the surrounding dark matter. Therefore the exact determination of mass and mass loss rates of stars have the same importance for our understanding of the dark matter, as astrometry, precise distance indicators, research of galaxies, clusters, high redshift objects, cosmology and particle physics. For this reason the question, of what kind of matter the universe consists, has evolved into the main puzzles of modern astronomy. In the following paragraphs we would like to convince the reader that mass determinations with different methods leads to the same result: Most of the matter in the universe is not detectable by electromagnetic radiation[1]!

Rotation curves

In the 1970's the first hints arose that spiral galaxies rotate faster than their cumulative luminous matter would suggest. Measuring the velocities of stars and gas in spiral galaxies outside a few kilo-parsecs shows flat rotation curves[2]. Summing up the masses of stars and assuming reasonable mass-to-light

---

[1] Note that large scales the density values depend on the Hubble constant, but in this introduction we use the actually most plausible value $H_0 = 70 \, \mathrm{km\,s^{-1}\,Mpc^1}$ and $h = 0.7$ (Freedman *et al.*, 2001; Bennett *et al.*, 2003) for simplicity.

[2] Stars and hydrogen clouds (21 cm radiation) show constant orbital velocities independent from their radial distance from the galactic center (Roberts & Rots, 1973; Rubin *et al.*, 1978)

ratios the visible matter in stars and gas cannot exceed 50% of the total matter[3]. Therefore at least 50% of the matter is invisible. This matter is expected to stay in the so-called halo of the galaxy, commonly assumed to be radially symmetric and decreasing nearly with a r^{-2} law.

Galaxy clusters

Also for galaxy clusters a large difference between luminous and dark matter is observed. Experiments measuring the velocity of galaxies[4] and the temperature of the intra-cluster X-ray-gas[5] confirmed this. Galaxy clusters offer many other independent methods to determine the matter densities, which lead to consistent results. The measurement of the cluster temperature function[6], the mass function[7], or the evolution of the "X-ray luminosity - temperature" relation[8] are promising methods to measure the evolution of the cluster number density and therefore constrain the total amount of matter in clusters. Assuming primordial conditions, the measured baryon fractions in clusters (the ratio between baryonic matter and total matter[9]) was determined[10] to be around $1:9$. Measurements of the mass-to-light ratio in galaxy clusters[11] (assumed to be similar to that of the whole universe) and cluster correlation functions[12] allowed other estimate for the matter densities.

The cosmic microwave background

Recently, the fluctuation features in the primordial background radiation (Cosmic Microwave Background - CMB) (Silk, 1968), which originated from a decoupling of matter and radiation a few hundred thousand after the Big Bang (redshift $z \approx 1000$), allowed for the construction of a relative clear picture how the universe evolved between that early point in time and today. Since theoretically it is clear that this radiation changed over time only mainly due to gravitational influence, it offers a perfect test for all kind of models calculating the perturbations that eventually led to galaxies and their evolution over time. Comparison between different models shows that only a small set of models with a matter density of 28% and a baryon density of 4.5% results in a situation consistent with the measured fluctuations in the cosmic microwave background[13].

---

[3] The ratio between dynamical and luminous mass $M_{\mathrm{dyn}}/M_{\mathrm{lum}}$ is ~ 2 interior the $(25\,\mathrm{mag\,arcsec}^{-2})$ isophotal radius R_{25} (Rubin et al., 1985)

[4] Swiss astronomer Zwicky (1933) measured the peculiar velocities of galaxies in the Coma Cluster and proposed an invisible "dark matter" to describe the large-scale potential. Modern methods use linear perturbation theory for the analysis of the peculiar velocities and lead directly to the gravity potential and to the matter densities, e.g. Willick & Strauss (1998); Susperregi (2001) derived a $\Omega_m \approx 0.3$.

[5] e.g. Böhringer (2002) for an overview

[6] e.g. Eke et al. (1998); Henry (2000); Viana & Liddle (1999); Blanchard et al. (2000)

[7] e.g. Carlberg et al. (1997a): CNOC sample

[8] e.g. Mushotzky & Scharf (1997); Donahue et al. (1998); Della Ceca et al. (2000); Schindler (1999); Fabian et al. (2001), Rosati et al. (1995): ROSAT Deep Cluster Survey, Borgani et al. (1999): EMSS Sample

[9] The gas density in clusters can be derived from the Sunyaev-Zel'dovich effect. Inverse-Compton scattering of the Cosmic Microwave Background Radiation (CMBR) photons by the hot intra-cluster gas shifts the CMBR spectrum to slightly higher energies.

[10] e.g. Grego et al. (2001): $0.081h^{-1}$

[11] e.g. Carlberg et al. (1997b): $19\pm6\%$, Bahcall et al. (2000): $16\pm5\%$

[12] e.g. Croft et al. (1997); Moscardini et al. (2000); Collins et al. (2000); Schuecker et al. (2001)

[13] e.g. BOOMERANG (de Bernardis et al., 2000, 2002; Netterfield et al., 2002), MAXIMA (Lee et al., 2001), DASI (Halverson et al., 2002), WMAP: $\Omega_m h^2 = 0.13 - 0.14$, $\Omega_b h^2 = 0.0224 \pm 0.0009$ (Bennett et al., 2003; Spergel et al., 2003), SDSS and WMAP: $\Omega_m h^2 = 0.145$ (Tegmark et al., 2004)

Supernovae

To measure the curvature of the universe, and to check for an acceleration or deceleration in the expansion, distant Type Ia supernovae were used as standard candles for a good distance measurement. The experiments by the Supernova Cosmology Project (Perlmutter *et al.*, 1999) and the High-z Supernova Search Team (Riess *et al.*, 1998) are consistent with a flat universe[14] and a total matter content of $28^{+9}_{-8}\%$ and $32 \pm 10\%$ respectively[15].

Big Bang nucleosynthesis

The amount of baryonic matter is predicted by calculations using the so-called "element nucleosynthesis", the formation of light elements. During the Big Bang (Big Bang nucleosynthesis - BBN) light elements (D,^{3}He,^{4}He,^{7}Li) are produced with well defined mass fractions depending on the total baryon density, on the expansion rate of the universe and the photon density at the time of BBN[16]. Measured abundances[17] indicate that the present mass density in baryons is around 4.5%$\pm$0.3 compared to the critical density[18].

The energy budget of the universe

Connecting all previous results shows that the total energy density is very close to the critical density ($\rho_c = 3H_0^2/(8\pi G) \approx 10^{-26}\,\text{kg/m}^3$) equivalent to a flat universe. The energy budget of the universe splits into

- 28% attracting matter

  - 23%$\pm$3% dark non-baryonic matter
  - 4.5%$\pm$0.3% baryonic matter

- 72%$\pm$3% dark energy: cosmological constant, vacuum energy[19] or quintessence[20]

Therefore most of the matter in the universe seems to be dark with five times more non-baryonic than baryonic matter.

---

[14] $\Omega_{\text{tot}} = \Omega_{\text{m}} + \Omega_\Lambda = 1$

[15] Future space-based experiments like The SuperNova / Acceleration Probe (SNAP) will study the dark energy and the dark matter with high accuracy measuring light-curves and spectra for over 2000 Type Ia supernovae at redshifts between z = 0.1 and 1.7 (Aldering *et al.*, 2002)

[16] e.g. Burles *et al.* (2001)

[17] e.g. Geiss & Gloeckler (1998)

[18] e.g. Kirkman *et al.* (2003) for deuterium absorption $\Omega h^2 = 0.012^{+0.003}_{-0.002}$ equal to $4.4 \pm 0.4\%$, and Izotov & Thuan (2004) for helium abundance $\Omega h^2 = 0.0214 \pm 0.0020$ equal to $2.4 \pm 0.5\%$

[19] Inserting a cosmological constant unequal to zero, $\Lambda \neq 0$, in the Friedmann equations directly leads to a vacuum energy density, acting like a negative pressure and supporting expansion. Vacuum energy is also strongly connected to inflation theory.

[20] Wetterich (1988) created the idea of quintessence in an attempt to understand the small value of the dark energy in terms of the large age of the universe.

Dark Matter candidates

During the last years a lot of suggestions were made to solve this discrepancy introducing different candidates for dark matter:

i) Hot Dark Matter

- neutrinos[21]

ii) Cold Dark Matter

- Weakly Interacting Massive Particles (WIMPs)[22]
- axions[23]

iii) Machos - MAssive Compact Halo Objects

- primordial black holes, "dark clusters"
- faint baryonic matter: brown dwarfs[24], white dwarfs[25]
- stellar remnants: neutron stars + black holes
- "very small" objects[26]
- "very massive" objects[27]
- dark quark stars[28]

---

[21] Experiments measuring two flavor atmospheric neutrino oscillation (e.g. $\nu_\mu \leftrightarrow \nu_\tau$) led to mass differences $1.6\,10^{-3} < \Delta m_{23}^2 < 4 \cdot 10^{-3}\,\mathrm{eV}^2$ (90% C.L.) (Super-Kamiokande). Assuming this to be the heaviest neutrino mass and transforming this into the contribution to the mass of the universe, means that the neutrino mass is much smaller than the masses required for a viable dark matter candidate (see Kajita (2002)).

[22] The theory of supersymmetry (SUSY), an extension of the Standard Model of particle physics, predicts supersymmetric gauginos: winos, higgsinos and neutralinos with masses expected between 95 GeV and 600 GeV. If these particles exist they will be accessible to the Large Hadron Collider (LHC) under construction at CERN.

[23] A possible solution for the CP problem of quantum chromodynamics (QCD) predicts the existence of a pseudoscalar particle in the mass range of μeV to meV. See e.g. Raffelt (2002) for an introduction.

[24] Brown dwarfs are expected to fill the range between 10^{-2} and $10^{-1} M_\odot$.

[25] The detection of 32 white dwarfs in the halo by Oppenheimer *et al.* (2001) may imply that 3% to 40% of the halo consists of these star remnants. The question is how an Initial Mass Function should be shaped to generate this amount of white dwarfs.

[26] For objects smaller than $10^{-7} M_\odot$ to be stable (Jeans mass) require heavy elements such as oxygen and silicon to have been produced by Pop III stars (an early stellar population). de Rujula *et al.* (1992) underline that lighter objects consisting of H and He would have been evaporated since the formation of the galaxy. Note that measurements of the luminosity of distant Lyα clouds, of the far infrared cosmic background and the Planckian shape of the CMB exclude an early nucleosynthesis phase (Reeves, 2002).

[27] For primordial compact halo objects above $10^4 M_\odot$ Arras & Wasserman (1999) stated that a halo of heavy object could not coexist with globular clusters.

[28] Dark quark stars theoretically consist of a core of quarks, a shell of hadrons, and a shell of hydrogen in the superfluid phase and can have masses between 1.8 and $375 M_\odot$ with radii from 9 to 1200 km (see Kabana & Minkowski (2002))

Baryonic matter

Since the behavior of baryonic matter is well understood by particle physics, baryonic matter seems to be a promising part to investigate.

In the following paragraphs we concentrate on the important question: Is the fraction of baryonic matter the same in the local universe at small scales, as it is on the scales sampled by BBN and CMB experiments.

Fukugita & Peebles (2004)[29] constrained the amount of stars, stellar remnants, substellar objects, atomic gas (HI, HeI), molecular gas (H$_2$), and intra-cluster plasma (hot X-ray gas), to 0.53% of the total density. The measurement of each single component originates from different experiments:

main sequence stars in all classes of galaxies[30]	0.205%	±0.054%
brown dwarfs[31], white dwarfs[32], neutron stars[33], and black holes[34]	0.062%	±0.019%
Lyα clouds (HI + HeI)[35]	0.062%	±0.01%
molecular gas H_2[36]	0.016%	±0.006%
intra-cluster plasma[37]	0.18%	±0.07%
total	0.53%	

This indicates that only a ninth of baryons are clearly identified in our present day local universe (BBN and CMB predict 4.5%). Fukugita & Peebles (2004) stated that a warm-hot intergalactic medium[38] (WHIM) could fill the missing gap contributing with 4.0%. But this value is observationally not well constrained, because the detection of the baryons in stars and diffuse gas requires observations over many wavelengths, something rather difficult in intergalactic gas at redshifts below $z = 3$.

Particularly interesting is the question of how the halos of spiral galaxies are structured. Since the halo is obviously not luminous, baryons may be hidden in small 'invisible' objects like dwarfs, planets, asteroids, stones or gravel. Fukugita & Peebles (2004) conceded that up to 20% of the mass of the halo of the Milky Way could be made of baryonic or non-baryonic Machos (Alcock *et al.*, 2000a; Afonso *et al.*, 2003b) and could contribute significantly to the baryonic or non-baryonic mass budget.

---

[29] For a previous result see Fukugita *et al.* (1998)

[30] Cole *et al.* (2001) derived $\Omega h = 0.0016 \pm 0.00024$ for a Kennicutt IMF $0.23 \pm 0.03\%$

[31] mass range between $0.01 M_\odot$ and $0.08 M_\odot$

[32] stars with an initial mass range between $1 M_\odot$ and $8 M_\odot$

[33] initial mass range between $8 M_\odot$ and $25 M_\odot$, see Heger *et al.* (2003)

[34] initial mass $> 8 M_\odot$

[35] These clouds can be explored by observations of the Lyα-forest, an absorption dominated part of the spectrum from Lyα line down to shorter wavelengths. At redshift $z = 1.5$ the baryon density in the Lyα forest is still comparable to what is seen at higher redshifts: Kim *et al.* (2001) found $\Omega_b h^2 > 0.01$ at $z = 1.6$. According to Penton *et al.* (2000) the local Lyα forest may contain $\sim 0.8\%$ of the local matter. These results are quite uncertain since they depend on the mean intensity of the ionizing UV background which in the local universe is largely unknown.

[36] Far infrared observations by the ISO satellite detected H$_2$ clouds at 50 to 200 K, in the halo of our galaxy, contributes less than a few percent of the dark matter (Jetzer, 2002). More massive and colder H$_2$ clouds would interact with galactic cosmic rays and emit high energy (100 MeV) gamma rays. Although it cannot be ruled out by experiments (Egret), a mechanism which keeps the gas in the halo is still unknown.

[37] A large part of the baryons would be present today in the form of hot X-ray emitting gas (Böhringer, 2002).

[38] The warm-hot intergalactic medium (WHIM) between 10^5 and 10^7 K (too warm to absorb light, but too cold to emit abundant X-rays) is a low-density, shock-heated component, detectable by O VI absorption in low redshift quasar spectra (HST-STIS Echelle spectra). It may represent a large fraction (which is increasing with decreasing redshift) of all baryons. At $\bar{z} = 0.22$ the density was measured to be $\Omega_{WHIM} \geq 0.003 h^{-1}$ (see Savage *et al.* (1998); Tripp *et al.* (2000); Tripp & Savage (2000)). Extrapolating to the local universe 1/3 of all baryons may be hidden in the WHIM. Theoretical results predict $\leq 5\%$ at $z = 3$ to 30-40% at $z = 0$. For a theoretical motivation see Cen & Ostriker (1999) and Davé *et al.* (2001).

Regarding this, the two main questions are: i) Is there a considerable fraction of the compact dark matter hidden in galactic halos? ii) Do we have the possibility to prove or disprove a certain kind of dark matter by methods not relying on the direct emission of electromagnetic radiation?

Gravitational lensing

A very elegant method to directly detect dark matter is the property of clumped matter to change the curvature of the local space-time, which in turn influences light passing through this region. These effects are the subject of a relative new[39] astrophysical field dealing with so-called "gravitational lenses". The name hints at similarities with optical lenses, where light is focused by changes of the dispersion[40].
Galaxy clusters can act as lenses for light rays emitted from background galaxies. This can lead to impressive distortions in the shape of the background galaxies. The analysis of these resulting giant "arcs" are the subject of a field called "strong lensing"[41].
The small distortions of galaxy-shapes by foreground matter allows to constrain the dark matter distribution in these foreground objects: The statistical deviations from an isotropic shape distribution, allow the reconstruction of the mass concentrations[42]. This field is called "weak lensing"[43].

Microlensing

Since foreground mass concentrations act as lenses, they are not only able to change the shape but also to focus the background light. In the case of lenses consisting of single point-like objects and moving with a certain velocity with respect to the source, this amplification changes over time and can be measured as so-called "micro-lensing"-light curves (see Fig. 1.1). The term "micro" is used because the image splitting is below a micro arcsec, which is a factor 50 below the resolution achieved by todays instruments.
In the last decade microlensing studies[44] have proven to be a powerful tool to search for compact dark matter in the Galactic halo, since the mass range for possible Machos is very broad, between $10^{-7} M_\odot$ and $10^4 M_\odot$, corresponding to event durations between hours and decades (Milsztajn, 2002).
Paczyński (1986) obtained that the probability that a star in the Large Magellanic Clouds (LMC) is lensed and has a magnification larger than 1.34 is $1 : 10^6$. Since there are many more stars in the LMC than 10^6 he suggested that a change of magnification, i.e. a microlensing event, should be observable

---

[39] but already proposed by Zwicky (1937)

[40] The gravitational field is responsible for the deflection of background light. In a Friedman-Robertson-Walker curved universe the deflection angle (only for a stationary weak gravitational field) can be written as $\hat{a} = \frac{2}{c^2} \int \nabla_\perp \Phi \, dl$, with c as the light velocity, l the light path, and Φ the gravitational potential in 3 dimensions. This reflects the analogy to the dispersion relation in optics. For thin gravitational systems the "lens equation" combines the source position θ_S with the image position θ_I depending on the angular diameter distances $\theta_I = \theta_S + \frac{D_{ls}}{D_{os}} \hat{a}(\theta_I)$. Using angles and angular distances the equation is also usable for an expanding universe.

[41] e.g. Paczyński (1987)

[42] Kaiser & Squires (1993)

[43] Using statistical methods for weak lensing, the amount and distribution of dark matter can be extracted. Using galaxy-galaxy gravitational lensing Fischer et al. (2000); Van Waerbeke et al. (2000) measured that dark halos exceed the visible diameter by more than an order of magnitude. This means that the dimensions of galaxies are close to the mean distance between galaxies in clusters. Moreover the power spectrum of the matter in the universe can be explored: for weak lensing of large-scale structure (cosmic shear) see Bacon et al. (2000) for weak lensing of faint galaxies (gravitational shear) see Wilson et al. (2001)

[44] For reviews see Roulet & Mollerach (1997), Gould (2001a), Gould (2001b)
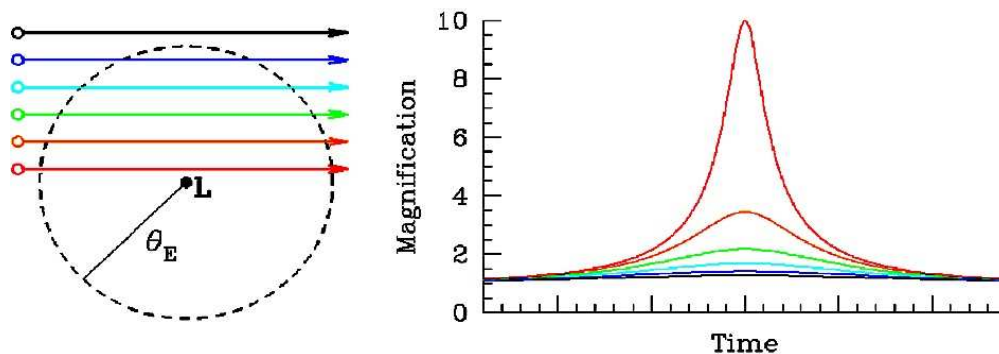
Figure 1.1: Microlensing light curves

if only enough stars are monitored. Following his suggestion several groups in 1992 started surveys of millions of stars (serving as background sources) in the Large and Small Magellanic Clouds (LMC, SMC) and in the Galactic bulge for variability induced by gravitational microlensing. In 1993 the MACHO (Alcock *et al.*, 1993) and EROS (Aubourg *et al.*, 1993) collaborations reported the first microlensing candidates toward the LMC. In the same year the OGLE collaboration (Udalski *et al.*, 1993) found the first candidates in the direction of the Galactic center (see also DUO (Alard *et al.*, 1995)). Three groups are observing microlensing events when alerted by the survey groups: GMAN (Pratt *et al.*, 1995), MPS (Rhie *et al.*, 2000), and PLANET (Albrow *et al.*, 2000). MOA (Bond *et al.*, 2001) is focused to detect planets using microlensing. In the future astrometric microlensing experiments measuring the change of the center of light of the unresolvable image pair are planned using astrometric satellites like FAME, GAIA, and SIM[45].

The search for compact dark matter toward the Galactic bulge identified more than 500 microlensing events in the past decade (MACHO (Alcock *et al.*, 1997), OGLE (Udalski *et al.*, 2000), DUO (Alard & Guibert, 1997)).

The results of gravitational micro-lensing observations on the LMC and SMC by the EROS, MACHO and OGLE collaborations showed around 20 candidates (Paczyński *et al.*, 1994; Ansari *et al.*, 1996; Alcock *et al.*, 1997; Palanque-Delabrouille *et al.*, 1998; Alard, 1999; Afonso *et al.*, 1999; Alcock *et al.*, 2000a,b).

Although all discovered events are compatible with gravitational lensing by Machos, the measurements were not able to derive unambiguous constraints on the amount of compact dark matter and its distribution in the Galactic halo (e.g. Lasserre *et al.*, 2000; Evans & Kerins, 2000, and references therein). Until now only an upper limit for the halo Macho fraction is plausible with a maximum of 20% (Alcock *et al.*, 2000a) to 25% (Afonso *et al.*, 2003b). The possibility has also been discussed that many LMC microlensing candidates derive from an additional stellar population in the direction toward the LMC, that does not contribute to the dark Galactic halo (Zaritsky & Lin, 1997).

---

[45] For an overview see Gould (2003)

Microlensing toward M31

Crotts (1992) and Baillon *et al.* (1993) suggested to include M31 in lensing surveys and pointed out that it should be an ideal target for these kind of experiments. In contrast to microlensing studies toward the LMC and the SMC, which are restricted to similar lines of sight through the Galactic halo, one can study many different lines of sight to M31.
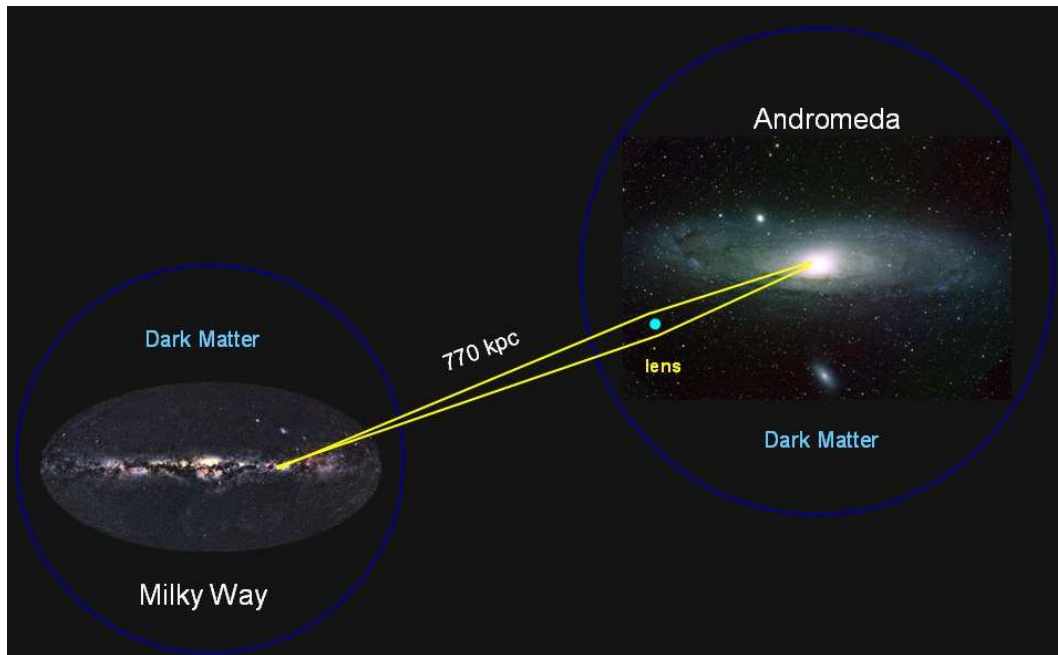
Figure 1.2: Microlensing toward M31

Since the optical depth (the probability that a star is lensed with a magnification larger than 1.34) for Galactic Machos is up to a magnitude greater toward M31 than toward the LMC, SMC or the Galactic bulge, one expects event rates greater than in previous lensing studies. Furthermore, M31 contributes an additional Macho population as it possesses a dark halo of its own. Thus, three populations may contribute to the optical depth along the line of sight: Machos in the Galactic halo, Machos in the halo of M31 and finally stars in the bulge and the disk of M31 itself, a contribution dubbed "self-lensing". The high inclination of M31 ($77°$) (Walterbos & Kennicutt, 1987) produces a near-far asymmetry of the event rates. The near side of the M31 disk will show less events than the more distant one (Crotts, 1992). Since Galactic halo-lensing, as well as self-lensing events are nearly symmetrically distributed, a detected asymmetry will be a hint to the existence of M31 Machos. Moreover, self-lensing predictions can serve as a sanity check for observations and models. An excess of lensing relative to self-lensing can then be attributed to halo-lensing, from which finally the Macho-parameters are inferred.

As most of the sources for possible lensing events are not resolved at M31's distance of 770 kpc (Freedman & Madore, 1990) the name 'pixellensing' (Gould, 1996b) was adopted for microlensing studies of unresolved sources. This definition encompasses surveys at the crowding limit[46], as well as

---

[46]Blending has proven to be a severe limitation in the analysis of microlensing events. It can be partly overcome by using

extragalactic microlensing experiments (e.g. toward M31 or M87) where hundreds of stars contribute to the flux within one pixel. Gould (and also Ansari *et al.* (1997)) showed that the comparison of pixel fluxes at different epochs can extend the search for microlensing events up to distances of a few megaparsecs. Therefore whereas in the microlensing regime (resolved sources), the observables are the maximum magnification of the source and the Einstein time scale of the event, in the pixel-lensing regime only the maximum excess flux of the source above a background and the full-width-half-maximum time of the event can be measured.

In 1994 two projects, AGAPE (Ansari *et al.*, 1997) and Columbia/VATT (Tomaney & Crotts, 1996; Crotts & Tomaney, 1996), started pixellensing surveys toward M31. Using an advanced technique called difference imaging analysis, which is insensitive to crowding and allows the measurement of pixel flux differences at the Poisson noise level, lensing searches could be extended to more distant targets like M31. During these first steps important progress for image subtraction and PSF-matching techniques were established. The first candidate events were reported by Crotts & Tomaney (1996) but could not be confirmed as gravitational lenses (Uglesich *et al.*, 1997, 1998, 1999). This was partly due to an insufficient time coverage, which could not really rule out variable stars as possible sources. Considering the large amount of variable sources detected in M31 later on (Fliri *et al.*, 2006), the possibility that these first candidates are variable sources is high. Therefore, we assume AGAPE Z1 to be the first convincing microlensing event in M31 (Ansari *et al.* (1999)), since the baseline is quite long with respect to the variation signal.

This first short duration, high brightness, microlensing event in M31 pushed microlensing projects to concentrate on observations with good time sampling: POINT-AGAPE (Kerins, 2001) and MEGA (Crotts *et al.*, 1999a,b), the successors of AGAPE and Columbia/VATT. They used service observations at the INT 2.5 m telescope, with its large field of view (34 x 34 arcmin), and concentrated on lensing induced by sources in the disk of M31. Another project, SLOTT-AGAPE, joined this collaboration in 2000 (Bozza *et al.*, 2000). NMS (Joshi *et al.*, 2001) is a independent pixel lensing search.

In Munich the "Wendelstein Pixellensing Project" (described in this thesis) started with a test and preparation phase on the Wendelstein 0.8 m telescope. WePP began its two campaigns in the autumn of 1997 before graduating to WeCAPP (Wendelstein Calar Alto Pixellensing Project) in summer of 1999 through the additional use of the Calar Alto 1.23 m telescope in Spain (Riffeser *et al.*, 2001).

Recently, the micro-lensing searches could also be extended using space-based observations to the more distant galaxy M87 (Baltz *et al.*, 2004).

Theory of microlensing

In parallel to the time consuming observations, a lot of effort has been made to predict the number, spatial distribution, amplitude and duration of lensing events toward these targets. The underlying models require knowledge of density and velocity-distribution, as well as of the luminosity and mass function of lensing and lensed stars. The halo Macho-mass fraction and Macho masses are of course not known and thus free parameters. From that, the contributions of self-lensing and halo-lensing is obtained.

Paczyński (1986) was the first to present such a lensing model for the Galaxy halo and to estimate the optical depth. Based on that work, Griest (1991) evaluated the optical depth with more realistic assumptions on halo density and velocity structure. He also obtained the event rate and distributions

---

low noise, high spatial resolution HST-images for the measurements of the unlensed source fluxes (see Alcock *et al.* (2001a)). For extragalactic objects, however, this can provide a precise source flux only for a fraction of lensed stars.

for lensing time scales and amplifications. Alcock *et al.* (1995) evaluated these distributions for several axisymmetric disk-halo models in the framework of the MACHO project. Gould (1996b), Han (1996) and Han & Gould (1996a) obtained the optical depth and distributions of time scales and event rates for a pixel-lensing survey toward M31.

If one does not know the flux of the unlensed source accurately (i.e. if one is not in the classical microlensing regime), the information that can be extracted from light curves is reduced. Wozniak & Paczyński (1997) were the first to note that the light curve maximum does not provide the maximum magnification of the source and, second, one can not obtain the Einstein time[47] from the time full-width-half-maximum (fwhm) of an event (since the latter is a product of the Einstein time and a function of the magnification at maximum).

This initiated efforts to deal with the missing information of the Einstein time scales in the pixel-lensing regime (see Gondolo (1999); Alard (2001)), and the suggestion to extract the Einstein time using the width of the 'tails' of the lensing light curves (Baltz & Silk, 2000; Gould, 1996b).

However, it is more straightforward to compare quantities that one can easily measure in an experiment with model predictions for the same quantity. The two independent and most precisely measurable observables are the flux excess of the light curve at its maximum, and its fwhm time scale. Baltz & Silk (2000) followed that strategy and derived the event rate as a function of the fwhm time scale of the events.

In this thesis we proceed in this direction and present a comprehensive treatment of the pixel-lensing theory and apply it to lensing experiments and their results toward M31. Using distribution functions for the distances, velocities, masses, and luminosities of stars and (potential) Machos, we derive lensing event rates as a function of the event observables. We calculate the contributions to the event rate as a function of the event's full-width-half-maximum time and maximum excess flux, because both the excess flux and time scale determine the event's detectability. We discuss lensing rates for stars of different type (color and luminosity class) and show for which cases finite source effects[48] become relevant; occurring where the impact parameter of a source-lens system becomes comparable to the source radius projected on the lens plane.

To calculate lensing event distribution functions for the specific case of M31, we use data from the literature to construct a model of M31, that consistently reproduces the photometry, kinematics and stellar populations. Using this model we predict the halo- and self-lensing event rates for bulge and disk stars in M31, and treat events with and without finite source signatures separately. We use the M31-photon-noise profile (related to the surface-brightness-profile) and obtain the event rates as a function of position, field-of-view, and S/N threshold at maximum magnification.

Most interesting are, of course, the object masses responsible for the measured lensing light curves[49]. For the pixel-lensing regime, we derive the probability distribution for the lens masses in M31 as a function of the fwhm-time scale, flux excess, and color. We also include the errors of these observables in the calculations.

We investigate the luminosity function of lensed stars for a typical position in the M31 WeCAPP field and for noise characteristics of WeCAPP and ACS. We predict the expected rates for the WeCAPP

---

[47] The Einstein time is the time required to cross the Einstein radius, which is the limit of a magnification of 1.34. The Einstein time directly depends on the lens mass and is therefore the preferred observable.

[48] The finite size of the source can drastically change the shape of the light curve, if source and lens are very close.

[49] e.g. Jetzer & Massó (1994) have derived the lens mass probability function for an event with given Einstein time and amplification. Han & Gould (1996b) have determined the Macho mass spectrum from 51 Macho candidates using their observed Einstein times.

experiment, and for a potential HST ACS-lensing-campaign.

The Wendelstein Calar Alto Pixellensing Project

WeCAPP is a long-term monitoring project searching for microlensing events toward M31. Since 1997 the bulge of M31 was monitored in two different wavebands with the Wendelstein 0.8 m telescope. In 1999 we extended our observations to the Calar Alto 1.23 m telescope. Observing simultaneously at these two sites, we obtained a time coverage of over 60% during the observability of M31.

To check thousands of frames for variability of unresolved sources we developed a reduction pipeline to search for variable sources in highly crowded fields like the M 31 bulge, and to handle extensive databases due to large time series. We show all steps of the standard reduction with emphasis on the realization of a per pixel error propagation: bias correction, treatment of bad pixels, flatfielding, and filtering of cosmic ray events. We demonstrate a PSF (point spread function) *and* flux conserving alignment procedure and a signal-to-noise maximizing stacking method. We build difference images via image convolution with a technique called optimal image subtraction (OIS, Alard & Lupton (1998)), proceed with PSF-fitting, relative photometry on all pixels, and finally apply an automatic detection of variable sources. The complete error propagation per pixel allows us to give accurate errors for each measurement.

In the past years up to 25 microlensing events toward M31 were published[50], but not all having the same quality. In 2001 POINT-AGAPE reported their first candidate microlensing event (Auriere *et al.*, 2001), that was extended to 7 event candidates (Paulin-Henriksson *et al.*, 2002, 2003; Calchi Novati *et al.*, 2005) with 4 more detected in the same data set (Belokurov *et al.*, 2005). 14 events were presented by the MEGA collaboration (de Jong *et al.*, 2004, 2006). For the first results of SLOTT/AGAPE see Calchi Novati *et al.* (2003) and for NMS see Joshi *et al.* (2005). Our lensing event GL1 (Riffeser *et al.*, 2003) is currently the best-sampled microlensing event in M31, because it was also detected by the POINT-AGAPE group. In total WeCAPP found 13 lensing event candidates in M31, 11 presented in this thesis for the first time. Combining the observed micro lensing events with the theory, allows us constrain the masses causing the lensing events. For all M31 microlensing events we present their probability mass distributions.

The detection of two events, in the WeCAPP 2000/2001 data with a signal-to-noise ratio larger than 10 at peak flux and a time scale larger than 1 day is in good agreement with our theoretical calculations (Riffeser *et al.*, 2003).

For future steps we will use the distribution of lensing events to constrain the disk, bulge, and halo models (mass and luminosity) for M31. This requires detailed efficiency studies which can performed using Monte-Carlo-Simulations.

The use of larger telescopes (Wendelstein 2 m) together with our developed "Optimal image reduction" will offer an access to larger amounts of microlensing events. Analyzing such a large set of microlensing candidates with our theoretical improvements, will make it possible to understand how dark (and even bright) matter is composed and distributed in our neighbor spiral galaxy M31.

---

[50] Some events were detected from more than one group

1.2   Outline of the thesis

This thesis is organized as follows.

In Chap. 2 we present the theory of microlensing published in Riffeser *et al.* (2006). We introduce our notation for the microlensing and pixel-lensing regime in Sec. 2.3. We also describe the treatment of finite source effects and how to extract the observables from the light curves. In Sec. 2.4.3 we motivate an alternative event definition. In Sec. 2.4 we combine the probability distributions for location, mass, source-lens velocity and impact parameter distribution to obtain the lensing event rate distribution as a function of these parameters. Section 2.5 summarizes the statistical properties of the source populations, i.e., luminosity function, number density, color-magnitude and luminosity-radius relation. In Sec. 2.6 we calculate the optical depth and the observables in the microlensing regime: single-star event rate, amplification distribution of the events, Einstein timescale distribution, and FWHM distribution of the events. Section 2.7 deals with the pixel-lensing regime. We calculate the event rate as a function of the maximum excess flux and FWHM time (and color) of the event in the point-source approximation. We also show how the event rate changes, if source sizes (shifting events to larger timescales and smaller flux excesses) are taken into account. In Sec. 2.8 we obtain the event rate for pixel-lensing surveys with spatially varying photon noise (related to the surface brightness contours of M31) but fixed signal-to-noise threshold for the excess flux at maximum magnification. We predict the number of halo- and self-lensing events in the WeCAPP survey (without taking into account the sampling efficiency of the survey) for the M31 model presented in Chap. 3. We demonstrate that accounting for the minimum FWHM of the events is extremely important to correctly predict the number of events and the luminosity distribution of the lensed sources. We also compare the characteristics of self-lensing events with halo-lensing events. Finally Sec. 2.9 derives the lens mass probability distribution from the observables and errors as obtained from light curve fits.

In Chap. 3 we describe and construct ingredients of the M31 lens model, which we use throughout the thesis to calculate examples and applications.

In Chap. 4 we present The Wendelstein Calar Alto Pixellensing Project (WeCAPP) published in (Riffeser *et al.*, 2001). In this chapter we will give an introduction to the project including information about the data obtained. In Sect. 2 we briefly discuss the basic principles of pixellensing. In Sect. 3 we will give an overview of the project including information about the sites used and the data obtained during WeCAPP. Section 4 refers to our data reduction pipeline and describes how light curves are extracted. In Sect. 5 we show first light curves and Sect. 6 summarizes this chapter.

In Chap. 5 we present an image reduction pipeline for variable objects detection in highly crowded fields (Gössl & Riffeser, 2002). We motivate the effort to implement per pixel error propagation. We give a detailed description of our standard reduction for CCD frames. We present our image alignment procedure. We describe the image convolution with OIS, the detection procedure for variable sources and the relative photometry of those sources. In the last section we give the results of performance tests on simulated images.

In Chap. 6 we first summarize those M31 lensing event candidates toward M31 that will be analyzed including the first microlensing candidates of WeCAPP (Riffeser *et al.*, 2003). Then we derive the mass probability functions for all four selflensing scenarios (bulge and disk stars as sources and lenses), and do the same for all MACHO-lensing scenarios (where MW and M31 MACHOS lens M31 bulge and disk stars).

We summarize the thesis in Chap. 7.

Chapter 2

Theory of microlensing toward crowded fields

2.1 Abstract

In Riffeser *et al.* (2006) we present a comprehensive treatment of the pixel-lensing theory and apply it to lensing experiments and their results toward M31. Using distribution functions for the distances, velocities, masses, and luminosities of stars, we derive lensing event rates as a function of the event observables. In contrast to the microlensing regime, in the pixel-lensing regime (crowded or unresolved sources) the observables are the maximum excess flux of the source above a background and the full width at half-maximum (FWHM) time of the event. To calculate lensing event distribution functions depending on these observables for the specific case of M31, we use data from the literature to construct a model of M31, reproducing consistently photometry, kinematics and stellar population. We predict the halo- and self-lensing event rates for bulge and disk stars in M31 and treat events with and without finite source signatures separately. We use the M31 photon noise profile and obtain the event rates as a function of position, field of view, and S/N threshold at maximum magnification. We calculate the expected rates for WeCAPP and for a potential Advanced Camera for Surveys (ACS) lensing campaign. The detection of two events with a peak signal-to-noise ratio larger than 10 and a timescale larger than 1 day in the WeCAPP 2000/2001 data is in good agreement with our theoretical calculations. We investigate the luminosity function of lensed stars for noise characteristics of WeCAPP and ACS. For self-lensing, a S/N-threshold of 10 for the peak amplitude, and an event time scale of $t_{\mathrm{FWHM}} > 1\,\mathrm{d}$ essentially only post main sequence stars are lensed; the probability that a lensing event leads to an observable magnification of a main sequence star is of the order $\approx 10^{-6}$. The observation of a lensed main sequence star with a time scale of $t_{\mathrm{FWHM}} > 1\,\mathrm{d}$ would be a strong indication for the existence of MACHOs. Only at very short time scales of $t_{\mathrm{FWHM}} \ll 1\,\mathrm{d}$, main sequence star self-lensing is becoming relatively more likely. For the pixel-lensing regime, we derive the probability distribution for the lens masses in M31 as a function of the FWHM timescale, flux excess and color. We also include the errors of these observables in the calculations.

2.2   Introduction

Searches for compact dark matter toward the Large and Small Magellanic Clouds (LMC and SMC) and the Galactic bulge identified numerous microlensing events in the past decade (MACHO, Alcock *et al.* 1997; EROS, Aubourg *et al.* 1993; OGLE, Udalski *et al.* 2000; DUO, Alard & Guibert 1997). In parallel to these observations, a lot of effort has been spent on the prediction of the number, the spatial distribution, the amplitude, and the duration of lensing events toward these targets. The underlying models require knowledge of density and velocity distribution, as well as of the luminosity and mass function of lensing and lensed stars. The halo MACHO mass fraction and lens mass are free parameters. From that, the contributions of self-lensing and halo-lensing is obtained. The self-lensing predictions (minimum lensing that has to occur due to star-star lensing) serve as a sanity check for observations and models. An excess of lensing relative to self-lensing can then be attributed to halo lensing, from which the MACHO parameters are finally inferred.

Paczyński (1986) was the first to present such a lensing model for the Galaxy halo and to estimate the probability of lensing (i.e., a magnification larger than 1.34) taking place at any time. This probability is also called the microlensing optical depth. On the basis of this work Griest (1991) evaluated the optical depth with more realistic assumptions on halo density and velocity structure. He also obtained the event rate and distributions for lensing timescales and amplifications. Alcock *et al.* (1995) related the Einstein timescale distribution of the events to the microlensing rate and optical depth. They evaluated these distributions for several axisymmetric disk-halo models in the framework of the MACHO project.

Any microlensing light curve can be characterized by the maximum magnification, the time to cross the Einstein radius (Einstein time) and the time of the event. The first two observables depend on the line-of-sight distance of the source and lens, the minimum projected transverse lens-source distance (impact parameter), transverse lens-source velocity, and lens mass. These quantities therefore cannot be extracted separately from an individual lensing event; instead, one can only derive probability distributions for them (see de Rujula *et al.* 1991 and Dominik 1998). Most interesting are of course the object masses responsible for the measured lensing light curves: Jetzer & Massó (1994) have derived the lens mass probability function for an event with given Einstein time and amplification. Han & Gould (1996b) have determined the MACHO mass spectrum from 51 MACHO candidates using their observed Einstein times.

Blending has proven to be a severe limitation in the analysis of microlensing events. It can be overcome partly by using low-noise, high spatial resolution *Hubble Space Telescope* (*HST*) images for measurements of the unlensed source fluxes (see Alcock *et al.* 2001a). For extragalactic objects, however, this can provide a precise source flux for a fraction of lensed stars only.

One can also use an advanced technique called difference imaging analysis, which is insensitive to crowding and allows to measure pixel flux differences in highly crowded fields at the Poisson noise level. Therefore, lensing searches could be extended to more distant targets like M31 (AGAPE, Ansari *et al.* 1999; Columbia-VATT, Crotts & Tomaney 1996; WeCAPP, Riffeser *et al.* 2001; 2003; POINT-AGAPE, Paulin-Henriksson *et al.* 2003, Calchi Novati *et al.* 2005; MEGA, de Jong *et al.* 2004; SLOTT-AGAPE, Bozza *et al.* 2000, Calchi Novati *et al.* 2003; NMS, Joshi *et al.* 2001), or M87 (Baltz *et al.*, 2004).

Gould (1996b) called microlensing of unresolved sources "pixel-lensing". This definition encompasses surveys at the crowding limit as well as extragalactic microlensing experiments (e.g., toward M31 or M87) where hundreds of stars contribute to the flux within 1 pixel. Gould (and also Ansari

et al. (1997)) showed that the comparison of pixel fluxes at different epochs can extend the search for microlensing events up to distances of a few megaparsecs. Applying his equations Gould (1996b), Han (1996) and Han & Gould (1996a) obtained the optical depth and distributions of timescales and event rates for a pixel-lensing survey toward M31. If one does not know the flux of the unlensed source accurately (i.e., if one is not in the classical microlensing regime anymore), the information that can be extracted from light curves is reduced.

Wozniak & Paczyński (1997) were the first to note that the light curve maximum does not provide the maximum magnification of the source anymore, and, second, one cannot obtain the Einstein time from the FWHM time of an event (since the latter is a product of the Einstein time and a function of the magnification at maximum). This initiated efforts to deal with the lacking knowledge of the Einstein timescales in the pixel-lensing regime (see Gondolo (1999); Alard (2001)) and the suggestion to extract the Einstein time using the width of the "tails" of the lensing light curves by Baltz & Silk (2000) and Gould (1996b).

However, it is more straightforward to compare quantities that one can easily measure in an experiment with model predictions for the same quantity. The two independent and most precisely measurable observables are the flux excess of the light curve at its maximum and its FWHM timescale. Baltz & Silk (2000) followed that strategy and derived the event rate as a function of the FWHM timescale of the events. We proceed in that direction and calculate the contributions to the event rate as a function of the event's FWHM time and maximum excess flux, because both the excess flux and timescale determine the event's detectability.

The definition of Gould for pixel-lensing may imply that a pixel-lensing event should be called a microlensing event, if its source has been resolved (e.g., with *HST* images) after the event has been identified from ground. Analogously, one could feel forced to call a microlensing event a pixel-lensing event, once it has turned out that "the source star" is a blend of several stars, and therefore the source flux is not known. Therefore, the classification of an event as a pixel-lensing event or a microlensing event is not unique.

One can take the following viewpoint: the physical processes are the same, and therefore classical microlensing is a special case of pixel-lensing, in which the source flux probability distribution is much more narrow than the stellar luminosity function, i.e., the distribution function used in the pixel-lensing regime. The two methods only differ in how to analyze a light curve and how to derive the probability distribution for the source flux: One can make use of a noisy and potentially biased baseline value of the light curve (hence, stay in the classical microlensing regime), or ignore the baseline value and obtain a source flux estimate from the wings of the light curve (analyze the difference light curve). Other possibilities are to obtain the source flux from an additional, direct measurement or to constrain its distribution by theory. After having determined the source flux probability distribution by one of these methods, one can use the formalism described in this chapter to derive, e.g., the lens mass probability function.

2.3   Basics of Lensing by a Point Mass

In this section we summarize the basics of microlensing theory and introduce our notation. The change in flux $\Delta_F(t)$ caused by a microlensing event depends on the unlensed flux F_0 and the magnification $A(t)$:

$$\Delta_F(t) := F_0 \left[A(t) - 1 \right]. \tag{2.1}$$

For a pointlike deflector and a pointlike source moving with constant relative transversal velocity v_t, the amplification is symmetric around its time of maximum t_0 and is connected to the Einstein radius R_E and the impact parameter b as follows (Paczyński, 1986):

$$A(u(t)) = \frac{u^2 + 2}{u \sqrt{u^2 + 4}} \overset{u \ll 1}{\approx} \frac{1}{u}, \tag{2.2}$$

$$u(r(t)) := \frac{r(t)}{R_E} := \sqrt{\frac{v_t^2(t - t_0)^2 + b^2}{R_E^2}}, \tag{2.3}$$

$$R_E := \frac{\sqrt{4GM}}{c} \sqrt{\frac{D_{ol}(D_{os} - D_{ol})}{D_{os}}}, \tag{2.4}$$

where M is the mass of the lens, D_{ol} and D_{os} are the distances to the lens, and $r(t)$ is the distance between source and lens in the lens plane.

With the Einstein timescale[1] $t_E := \frac{R_E}{v_t}$ and the normalized impact parameter $u_0 := \frac{b}{R_E}$ we obtain

$$u(t) = \sqrt{\frac{(t - t_0)^2}{t_E^2} + u_0^2}. \tag{2.5}$$

The maximum amplification (at $t = t_0$) becomes

$$A_0 := \frac{u_0^2 + 2}{u_0 \sqrt{u_0^2 + 4}} \overset{u_0 \ll 1}{\approx} \frac{1}{u_0}. \tag{2.6}$$

Equation (2.2) can be inverted to

$$u(A) = \left[2A(A^2 - 1)^{-1/2} - 2 \right]^{1/2} \overset{A \gg 1}{\approx} \frac{1}{A}. \tag{2.7}$$

Inserting A_0 in equation (2.7) its derivative can be written as

$$\frac{du_0}{dA_0} = -\frac{2\left[(A_0^2 - 1)^{-1/2} - 1/2 A_0 (A_0^2 - 1)^{-3/2} 2 A_0 \right]}{2\left[2A_0(A_0^2 - 1)^{-1/2} - 2 \right]^{1/2}} = -\left\{ 2\left[\frac{A_0}{(A_0^2 - 1)^{1/2}} - 1 \right] (A_0^2 - 1)^3 \right\}^{-1/2}$$
$$= \frac{-\sqrt{2}}{2} \frac{\left[A_0 + (A_0^2 - 1)^{1/2} \right]^{1/2}}{(A_0^2 - 1)^{5/4}}. \tag{2.8}$$

---

[1] Griest (1991) defines the event duration t_e as the time span where the lens is closer than a relative impact parameter u_T to the source. This can be converted to the Einstein timescale using $t_e \equiv 2t_E \sqrt{u_T^2 - u_0^2}$, $\cos\theta \equiv \sqrt{1 - u_0^2/u_T^2}$. Baltz & Silk (2000) use a different definition for the Einstein timescale t_E; for comparison use $t_E \equiv 2t_E$ in their formulas.

The FWHM timescale t_{FWHM} of a light curve is defined by $A\left(\frac{t_{\text{FWHM}}}{2}\right) - 1 := \frac{A_0 - 1}{2}$. It is related to the Einstein timescale t_{E} by

$$t_{\text{FWHM}} = t_{\text{E}} \, w(u_0) = t_{\text{E}} \Upsilon(A_0), \tag{2.9}$$

where $w(u_0)$ was first obtained by Gondolo (1999)[2]:

$$w(u_0) := 2\sqrt{u\left(\frac{A(u_0)+1}{2}\right)^2 - u_0{}^2} = 2\sqrt{\frac{2[A(u_0)+1]}{\sqrt{[A(u_0)-1][A(u_0)+3]}} - 2 - u_0{}^2} \overset{u_0 \ll 1}{\approx} \sqrt{12}\, u_0, \tag{2.10}$$

and $\Upsilon(A_0) := w(u(A_0))$ is

$$\Upsilon(A_0) = 2\sqrt{u\left(\frac{A_0+1}{2}\right)^2 - u(A_0)^2} = \sqrt{8} \frac{\left[(A_0+1)^{3/2} - A_0(A_0+3)^{1/2}\right]^{1/2}}{[(A_0-1)(A_0+1)(A_0+3)]^{1/4}} \overset{A_0 \gg 1}{\approx} \frac{\sqrt{12}}{A_0}. \tag{2.11}$$

Hence, the easy measurable timescale t_{FWHM} is a product of the quantity t_{E}, which contains the physical information about the lens, and the magnification of the source at maximum light A_0.

2.3.1   Finite Source Effects

If the impact parameter of a source-lens system becomes comparable to the source radius projected on the lens plane $R_* \frac{D_{\text{ol}}}{D_{\text{os}}}$, the point-source approximation is not valid anymore. The amplification then saturates at a level below the maximum magnification in equation (2.6).
The finite source light curve for extended sources can be derived for a disk-like homogeneously radiating source,

$$
\begin{aligned}
A^*(u) &= \int_0^{\frac{R_* D_{\text{ol}}}{D_{\text{os}}}} \int_0^{2\pi} A\left(\left(u^2 + \frac{\tilde{r}^2}{R_{\text{E}}{}^2} - 2u\frac{\tilde{r}}{R_{\text{E}}}\cos\theta\right)^{1/2}\right) \frac{\tilde{r}\,d\theta\,d\tilde{r}}{\pi\left(R_* \frac{D_{\text{ol}}}{D_{\text{os}}}\right)^2} \\
&= \frac{1}{\pi}\left(\frac{R_{\text{E}} D_{\text{os}}}{R_* D_{\text{ol}}}\right)^2 \int_0^{2\pi} \int_0^{\frac{R_* D_{\text{ol}}}{R_{\text{E}} D_{\text{os}}}} A\left(\left(u^2 + \tilde{u}^2 - 2\tilde{u}\cos\theta\right)^{1/2}\right) \tilde{u}\,d\tilde{u}\,d\theta \\
&=: \frac{z^2}{\pi} \int_0^{2\pi} \int_0^{1/z} A\left(u\left(1 + q^2 - 2q\cos\theta\right)^{1/2}\right) q\,dq\,d\theta \\
&= \frac{z^2}{\pi} \int_0^{2\pi} \int_0^{1/z} \frac{\left(1 + q^2 - 2q\cos\theta\right) + 2/u^2}{\sqrt{\left(1+q^2-2q\cos\theta\right)^2 + 4/u^2\left(1+q^2-2q\cos\theta\right)}} q\,dq\,d\theta
\end{aligned}
\tag{2.12}
$$

source-lens separation $r(t)$ and where the definitions

$$z(t) := u(t)\frac{R_{\text{E}} D_{\text{os}}}{R_* D_{\text{ol}}} = \frac{r(t)}{R_*}\frac{D_{\text{os}}}{D_{\text{ol}}}$$

and $q := \frac{\tilde{u}}{u}$ have been inserted. For high magnifications, where $A(u) \approx u^{-1}$ is a valid approximation, equation (2.12) becomes equivalent to Gould (1994b, eq. (2.5)).
The maximum amplification in the finite source regime then becomes

$$A_0^* = \int_0^{R_* \frac{D_{\text{ol}}}{D_{\text{os}}}} A(r/R_{\text{E}}) \frac{2\pi r\,dr}{\pi\left(R_* \frac{D_{\text{ol}}}{D_{\text{os}}}\right)^2} = 2\left(\frac{R_{\text{E}} D_{\text{os}}}{R_* D_{\text{ol}}}\right)^2 \int_0^{\frac{R_* D_{\text{ol}}}{R_{\text{E}} D_{\text{os}}}} \frac{\tilde{u}^2 + 2}{\sqrt{\tilde{u}^2+4}}\,d\tilde{u} = \sqrt{1 + \left(\frac{2R_{\text{E}} D_{\text{os}}}{R_* D_{\text{ol}}}\right)^2} \overset{A_0^* \gg 1}{\approx} \frac{2R_{\text{E}} D_{\text{os}}}{R_* D_{\text{ol}}}, \tag{2.13}$$
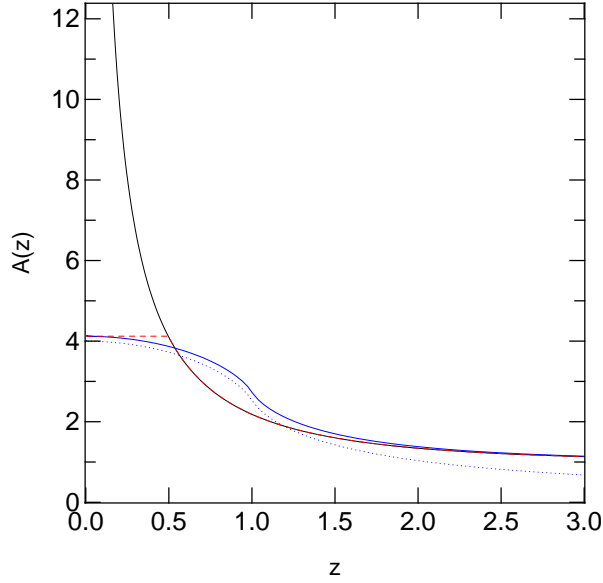
Figure 2.1: Amplification $A(z)$ versus $z(t) := \frac{r(t)}{R_*} \frac{D_{\mathrm{os}}}{D_{\mathrm{ol}}}$ plotted for $\frac{R_*}{D_{\mathrm{os}}} = 0.5 \frac{R_{\mathrm{E}}}{D_{\mathrm{ol}}}$. *Black curve:* point-source approximation, see equation (2.2). *Blue curve:* finite source magnification $A^*(z)$ for a homogeneously radiating disk of size R_*, exact solution, see equation (2.12). *Red dashed curve:* simple approximation $A^*(z)$ for finite source effects according to equation (2.15). *Blue dots:* finite source size approximation in the high-magnification regime, introduced by (Gould, 1994b, eq. (2.5)).

which equals the approximation of Baltz & Silk (2000, eq. (19)) for high amplifications.
For small source-lens distances with $D_{\mathrm{ol}} \approx D_{\mathrm{os}}$ (e.g., for bulge-bulge self-lensing) the above relation becomes $A_0^* \approx \sqrt{1 + 1.5 \times 10^6 \frac{M}{M_\odot} \left(\frac{R_*}{R_\odot} \right)^{-2} \frac{D_{\mathrm{os}} - D_{\mathrm{ol}}}{1\,\mathrm{kpc}}}$. For a source radius of supergiants of $R_* \approx 200 R_\odot$ a source-lens distance of $1\,\mathrm{kpc}$, and a lens with $M = 1 M_\odot$ finite source effects already arise above a magnification of $A_0^* \approx 6.2$. For smaller masses $M = 0.1 M_\odot$ finite source effects become important even at a low magnification $A_0^* \approx 2$. Although typical source radii are smaller, this example shows that finite-source effects cannot be neglected. We will show in § 2.7.3 and Table 2.2 that indeed a large fraction of the M31 bulge-bulge lensing events will show finite source effects.
Figure 2.1 shows that for $u < u_0^*$ (or $z \lesssim \frac{1}{2}$) with

$$u_0^* := u(A_0^*) = \left\{ 2 \left[1 + \left(\frac{R_* D_{\mathrm{ol}}}{2 R_{\mathrm{E}} D_{\mathrm{os}}} \right)^2 \right]^{1/2} - 2 \right\}^{1/2} \overset{A_0^* \gg 1}{\approx} \frac{R_* D_{\mathrm{ol}}}{2 R_{\mathrm{E}} D_{\mathrm{os}}}, \tag{2.14}$$

the amplification is no longer directly connected to the source-lens separation (Gould, 1995), but all $u < u_0^*$ have nearly the same amplification equal to the point-source approximation $A(u)$ at u_0^*. Therefore we generalize equation (2.2) to approximately account for finite-source effects

$$A^*(u) \approx \begin{cases} \sqrt{1 + \left(\frac{2 R_{\mathrm{E}} D_{\mathrm{os}}}{R_* D_{\mathrm{ol}}} \right)^2}, & u < u_0^* \\ \frac{u^2 + 2}{u \sqrt{u^2 + 4}}, & u \geq u_0^*. \end{cases} \tag{2.15}$$

---

[2] With $\beta \equiv u_0$ and $\delta(\beta) \equiv A_0 - 1$.

For light curves with finite source signatures ($u_0 < u_0^*$) at an impact parameter

$$u(1 + (A_0^* - 1)/2) \overset{A_0^* \gg 1}{\approx} (R_* \, D_{ol})/(R_E \, D_{os})$$

(or $z \approx 1$) the amplification of our approximation is half of the maximum and can be used to define the t_{FWHM}^*:

$$t_{FWHM}^* := t_E \Upsilon^* := \frac{2R_E}{v_t} \sqrt{u\left(\frac{A_0^* + 1}{2}\right)^2 - u_0^2} \overset{A_0^* \gg 1}{\approx} 2t_E \sqrt{\left(\frac{2}{A_0^*}\right)^2 - u_0^2}$$

$$\approx 2t_E \sqrt{\left(\frac{R_* \, D_{ol}}{R_E \, D_{os}}\right)^2 - u_0^2} \approx t_{FWHM} \frac{1}{\sqrt{3}} \sqrt{\left(\frac{R_* \, D_{ol}}{b \, D_{os}}\right)^2 - 1} \geq t_{FWHM} \quad u_0 < u_0^*. \tag{2.16}$$

with

$$\Upsilon^*(u_0, R_*, D_{ol}, D_{os}, M) := 2\sqrt{u\left(\frac{A_0^* + 1}{2}\right)^2 - u_0^2} = 2\sqrt{\frac{2(A_0^* + 1)}{\sqrt{(A_0^* - 1)(A_0^* + 3)}} - 2 - u_0^2}.$$

In equation (2.16) the FWHM timescales for light curves that show finite source signatures are related to the values t_{FWHM} for the point-source approximation using equations (2.9) and (2.10). This demonstrates that the source does affect the timescale of an event severely: a source with an impact parameter of one-tenth the projected source radius will have an event timescale almost 6 times as long as that in the point-source approximation.

The shortest and longest FWHM timescales for an event with finite source signature ($u_0 \leq u_0^*$) are equal (insert $u_0 = u_0^*$ and $u_0 = 0$ into eq. [2.16]),

$$t_{FWHM,min}^* = t_E \Upsilon(A_0^*) \overset{A_0^* \gg 1}{\approx} \sqrt{3} \, \frac{R_* \, D_{ol}}{v_t \, D_{os}},$$

$$t_{FWHM,max}^* = 2t_E u\left(\frac{A_0^* + 1}{2}\right) \overset{A_0^* \gg 1}{\approx} 2 \, \frac{R_* \, D_{ol}}{v_t \, D_{os}}. \tag{2.17}$$

For a given transversal velocity the minimum timescale becomes the larger, the larger the source sizes are.

The largest flux excess of a lensed, extended star becomes

$$\Delta_{F,max} = F_0(A_0^* - 1) = F_0 \left[\sqrt{1 + \frac{16GM D_{os}(D_{os} - D_{ol})}{c^2 R_*^2 D_{ol}}} - 1\right]$$

$$\overset{A_0^* \gg 1}{\approx} \frac{4\sqrt{G}}{c} \sqrt{\frac{D_{os}(D_{os} - D_{ol})}{D_{ol}}} \sqrt{M} \, \frac{F_0}{R_*}, \tag{2.18}$$

irrespective of whether the light curve shows finite source signatures.

2.3.2 Extracting Observables from Light Curves

Measuring Δ_F and t_{FWHM}

In this section we present three methods for measuring the excess flux Δ_F at maximum and the FWHM time t_{FWHM}. One can see in equations (2.9) and (2.16) that t_E and u_0 (or A_0) enter the value of t_{FWHM} as a product, giving rise to the "Einstein time magnification" degeneracy, which may lead to poor error estimates for t_E (and u_0) even for well-determined values of t_{FWHM} and Δ_F.

Accounting for this degeneracy, Gould (1996b)[3] approximated the Paczynski light curve with one

---

[3] Gould's (1996b) eq. (2.4) with $\beta \equiv u_0$, $\omega \equiv t_E^{-1}$.

fewer parameter for the special case of high amplification:

$$\Delta_F^{\text{Gould}}(t) \approx F_{\text{eff}} \left[\frac{(t-t_0)^2}{t_{\text{eff}}^2} + 1 \right]^{-1/2}. \tag{2.19}$$

The three free parameters are $F_{\text{eff}} := \frac{F_0}{u_0}$, $t_{\text{eff}} := u_0 t_{\text{E}}$, and t_0. This approximation has turned out to be a very useful filter for detecting lensing events; however, it fails to describe light curves when the magnification is not very large. We suggest using

$$\Delta_F(t) \approx \Delta_F \left[\frac{12(t-t_0)^2}{t_{\text{FWHM}}^2} + 1 \right]^{-1/2} \tag{2.20}$$

instead. This approximation provides a good description also for lower magnifications. The three free parameters of this approximation are the time of maximum t_0, the excess flux Δ_F, and the FWHM timescale t_{FWHM}.

Figure 2.2 shows that equation (2.20) better approximates the Paczynski light curve than the Gould approximation in the core and in the inner part of the wings, and also provides the correct value for t_{FWHM} and Δ_F.

There are two situations that can require a fourth, additive, free parameter in the light curve fit. The first one is the transition regime from pixel-lensing to microlensing (i.e., where the errors are small enough to sample the wings of the light curve). We suggest using

$$\Delta_F(t) \approx F_{\text{eff}} \left[\frac{(t-t_0)^2}{t_{\text{eff}}^2} + 1 \right]^{-1/2} - F_0, \tag{2.21}$$

which provides an excellent fit to the Paczynski light curve (see Fig. 2.2, *green curve*).

The second situation is the following: imagine that the photon noise of the background becoming larger and finally exceeding the unlensed flux of the star F_0. Then the star cannot be resolved anymore and the rms error of the baseline of the light curve becomes proportional $N_{\text{data points}}^{-1/2} \sigma$. The (minimum) systematic error is given by the fact that the subtracted reference image (with error σ_{ref}) is a sum of (high-quality) images, potentially including some of the amplified phases of the sources.[4] This implies that there are fundamental limits to the accuracy of the baseline, and we thus require an additive parameter to account for that. The approximation of any pixel-lensing light curve then becomes

$$\Delta_F(t) \approx F_{\text{eff}} \left[\frac{(t-t_0)^2}{t_{\text{eff}}^2} + 1 \right]^{-1/2} + C. \tag{2.22}$$

In fact, numerical simulations showed that much more accurate values are derived for F_{eff} and t_{eff} if this additional constant C is allowed for.

---

[4] The measured light curve varies around the theoretical light curve $L(t)$ due to noise of amplitude σ. We can therefore write the light curve measured at times t as

$$L(t) + \sigma := [\Delta_F(t) + B + \sigma] - [\Delta_F(t_{\text{ref}}) + B + \sigma_{\text{ref}}] = \Delta_F(t) - \Delta_F(t_{\text{ref}}) - \sigma_{\text{ref}} + \sigma = \Delta_F(t) + \sigma + C',$$

with the background B, the epoch for the reference measurement t_{ref}, and a constant $C' := -\Delta_F(t_{\text{ref}}) - \sigma_{\text{ref}}$.
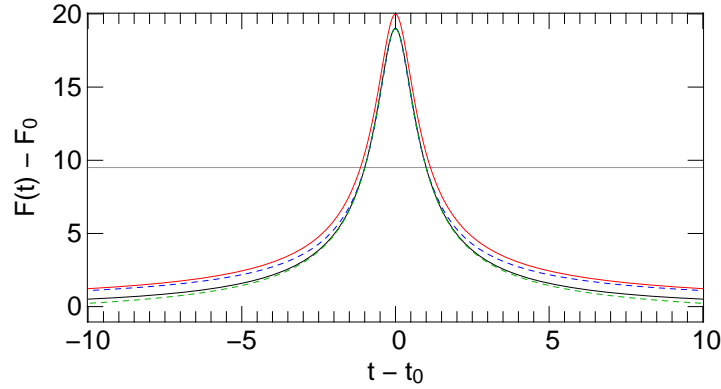
Figure 2.2: Different light curve approximations using the following parameters: $t_{\mathrm{FWHM}} = 2$, $A_0 = 20$, $F_0 = 1$, $u_0 = 0.05005$, and $t_{\mathrm{E}} = 12.28$. *Black curve:* Paczynski (eqs. [2.1] and [2.2]). *Red curve:* Gould (eq. [2.19]). *Blue dashed curve:* Eq. [2.20]. *Green dashed curve:* Gould fit with additional free constant (eq. [2.21]). *Gray line:* $\Delta_F/2$ marks the flux level where t_{FWHM} is defined for the Paczynski curve.

Constraining F_0

In this section we address the important question, how to extract the source flux F_0 from a lensing light curve. There are four potential ways to constrain the flux of the lensed star:

i) The lensed star is resolved and isolated, and therefore a bias in the flux measurement (by crowding) can be excluded (assuming no systematic effects in the baseline). One would of course call such an event a classical microlensing event. A microlensing fit (using χ^2 analysis methods) to the light curve then directly provides F_0 and its probability distribution, ideally given by an Gaussian error σ_{F_0}. In this case the flux measurement error is directly correlated to Q, the signal-to-noise ratio at maximum magnification.[5]

ii) The flux F_0 is obtained through the information that is in the shape of the wings of the difference light curve $F_0(A(t)-1)+C \equiv F_0 A(t)+B$. The χ^2 analysis leads to a probability distribution for F_0. This flux estimate method is used if no alternative unbiased flux measurement is available, i.e., cases in which the source star is resolved but blended (see (Alard, 1999) for applications in the microlensing regime), and cases in which the source star is not resolved (usually called a pixel-lensing event). Note that other methods using the shape of the wings (Baltz & Silk, 2000) provide similar results.

iii) The flux F_0 is obtained from an additional, direct measurement, e.g., low-noise, high spatial resolution photometry from space.

iv) The flux F_0 is constrained by theory through plausible distribution functions, e.g., the luminosity function Φ, the color-magnitude relation of stars, and the distance distribution of stars, which together yield the source flux distribution function (see § 2.9.3). Another constraining example

---

[5] If the noise is dominated by background sky, one can write $\sigma_{F_0} = \Delta_F Q^{-1} N_{\mathrm{data\ points}}^{-1/2}$, where $N_{\mathrm{data\ points}}$ is the number of the light curve data points.

is an upper source flux limit that can be obtained from the fact that the source star is not resolved in the absence of lensing.

Since the physical processes are the same in pixel-lensing and microlensing, microlensing is a special case of pixel-lensing, where the source flux probability distribution is much more narrow than the stellar luminosity function, i.e., the distribution function used in the pixel-lensing regime. The methods only differ in how to analyze a light curve and how to derive the probability distribution for the source flux.

Evaluating t_E

In this section we use the distribution of F_0 (from measurement or theory; see previous section) to estimate the probability distribution for a value of t_E. Note that transforming the distribution of F_0 to a distribution of t_E can lead to a different value compared to a t_E obtained directly from the best estimate for F_0.

As the fitting process in the light curve analysis yields the non degenerate observables t_{FWHM} and Δ_F, we can combine their (Gaussian) measurement errors with the probability distribution for the source flux F_0 and obtain the probablity distribution for t_E:

$$
\begin{aligned}
p_{t_E}(t_E) &= \int \int \int p_{t_{FWHM}}(t_{FWHM}) \, p_{\Delta_F}(\Delta_F) \, p_{F_0}(F_0)) \, \delta\left(t_E - \tfrac{t_{FWHM}}{\Upsilon}\right) dt_{FWHM} \, d\Delta_F \, dF_0 \\
&= \int \int \int p_{t_{FWHM}}(t_{FWHM}) \, p_{\Delta_F}(\Delta_F) \, p_{F_0}(F_0) \, \tfrac{\delta(t_{FWHM} - t_E \Upsilon)}{|\Upsilon^{-1}|} \, dt_{FWHM} \, d\Delta_F \, dF_0 \\
&= \int \int p_{t_{FWHM}}(t_E \Upsilon) \, p_{\Delta_F}(\Delta_F) \, p_{F_0}(F_0) \Upsilon\left(\tfrac{\Delta_F}{F_0} + 1\right) d\Delta_F \, dF_0.
\end{aligned}
\tag{2.23}
$$

This also allows to include non-Gaussian distributions for the source flux.

By transforming the measurements of Δ_F and t_{FWHM} together with a probability distribution of F_0, we derive a general formalism that is applicable to all microlensing and pixel-lensing problems. In § 2.9 we further develop this idea using plausible distribution functions as physical constraints, which narrows the width of the distribution of the lens mass M (connected to t_E).

2.4   Distribution Function for Lens Parameters

For a source of fixed intrinsic flux F_0, position $\vec{r}_s = (x, y, D_{\mathrm{os}})$ and velocity vector $\vec{v}_s = (v_{s,x}, v_{s,y}, v_{s,z})$, the number and characteristics of lensing events are determined by the probability function $p(\vec{r}_l, \vec{v}_l, M)$ for a lens with mass M and velocity $\vec{v}_l$ being at position $\vec{r}_l$. For the change of magnification of the background source, only the transversal velocity components of source and lens are relevant (we assume velocities to be constant). For parallax microlensing events (Gould, 1994a,b) the nonuniform velocity of the observer changes the observed light curves, since the observer's reference frame is not fixed. However, this effect is unimportant for extragalactic microlensing events.

Therefore, in addition to M and D_{ol} only the projected relative transversal positions $r := r_{\mathrm{t},l} - \frac{D_{\mathrm{ol}}}{D_{\mathrm{os}}} r_{\mathrm{t},s}$ and velocities $v_{\mathrm{t}} := v_{\mathrm{t},l} - \frac{D_{\mathrm{ol}}}{D_{\mathrm{os}}} v_{\mathrm{t},s}$ and the angle ϕ enclosed by relative position and velocity vector enter the lensing properties. The distributions in r and ϕ can be reduced to the distribution of one parameter, the impact parameter b of the lens-source trajectory. This is obvious, since in a symmetric potential the trajectory of a particle is fully described by its minimum distance.

So, the relevant lens parameters are D_{ol}, v_{t}, M, and b. We introduce the lens density and the distributions of D_{ol}, v_{t}, and M in the next two subsections and then come up with a new lensing event definition in § 3.3. For those lenses that satisfy the event definition, i.e., those which cause events, we will then derive the distribution of the impact parameters dN/db. We will show that our event definition gives the familiar relation for the event rate but is more easy to implement in numerical simulations.

2.4.1   Distance and Mass Distribution

The probability distributions for a lens with mass M being at distance D_{ol} are given by

$$p_{D_{\mathrm{ol}}} = \rho(D_{\mathrm{ol}}) \left[\int_0^{D_{\mathrm{os}}} \rho(D_{\mathrm{ol}}) \, dD_{\mathrm{ol}} \right]^{-1}, \tag{2.24}$$

$$p_M = \xi(M) \left[\int_0^{\infty} \xi(M) \, dM \right]^{-1}, \tag{2.25}$$

where $\rho(D_{\mathrm{ol}})$ is the lens mass density and $\xi(M)$ is the lens mass function (which itself is normalized to $\int \xi(M) M \, dM = 1$; see Binney & Tremaine (1987, p. 747)). The number density per lens mass interval finally is defined by

$$n(D_{\mathrm{ol}}, M) := \rho(D_{\mathrm{ol}}) \xi(M), \tag{2.26}$$

where $n(D_{\mathrm{ol}}, M)$ has units of length^{-3} mass^{-1}.

2.4.2   Velocity Distribution for Lenses

We assume that the velocity distribution of the lenses around their mean streaming velocity is Gaussian:

$$p(v_{l,i}) = C_l \, e^{-\frac{v_{l_i}^2}{2\sigma_l^2}}, \quad i = x, y, z, \quad C_l = \frac{1}{\sqrt{2\pi} \, \sigma_l}.$$

where σ_l is the dispersion and depends on the position (x, y, z). We furthermore assume that the combined transverse motion of observer and source relative to the mean transverse streaming velocity of the lenses is known and occurs in the x-direction with amplitude $v_0(x, y, z)$ as projected onto the lens plane. This means that the velocity v_s of the source turns into a projected velocity $v_p = D_{ol}/D_{os} v_s$ (lensing timescales are determined by relative proper motions not absolute motions of lens and source).

We now define the relative projected velocity $v_{ls,x} := v_{l,x} + v_0$ (analogously $v_{ls,y} := v_{l,y} + 0$) and obtain the transverse lens-source velocity distribution as[6]

$$
\begin{aligned}
p_{v_t}(v_t, v_0) &= \frac{1}{2\pi\sigma_l^2} \int_{-\infty}^{+\infty}\int_{-\infty}^{+\infty} \delta\left(v_t - \sqrt{v_{ls,x}^2 + v_{ls,y}^2}\right) \exp\left(-\frac{(v_{ls,x}-v_0)^2}{2\sigma_l^2}\right) \exp\left(-\frac{v_{ls,y}^2}{2\sigma_l^2}\right) dv_{ls,y}\, dv_{ls,x} \\
&= \frac{1}{2\pi\sigma_l^2} \int_{-v_t}^{v_t}\int_{-\infty}^{+\infty} \frac{\delta\left(v_{ls,y} - \sqrt{v_t^2 - v_{ls,x}^2}\right) + \delta\left(v_{ls,y} + \sqrt{v_t^2 - v_{ls,x}^2}\right)}{\left|v_{ls,y}/\sqrt{v_{ls,x}^2 + v_{ls,y}^2}\right|} \exp\left(-\frac{(v_{ls,x}-v_0)^2}{2\sigma_l^2}\right) \exp\left(-\frac{v_{ls,y}^2}{2\sigma_l^2}\right) dv_{ls,y}\, dv_{ls,x} \\
&= \int_{-v_t}^{v_t} \frac{1}{\pi\sigma_l^2} v_t \exp\left(-\frac{v_t^2 + v_0^2}{2\sigma_l^2}\right) \frac{\exp\left(-\frac{-2v_0 v_{ls,x}}{2\sigma_l^2}\right)}{\sqrt{v_t^2 - v_{ls,x}^2}} dv_{ls,x} \\
&= \frac{1}{\sigma_l^2} v_t \exp\left(-\frac{v_t^2 + v_0^2}{2\sigma_l^2}\right) I_0\left(\frac{v_0 v_t}{\sigma_l^2}\right).
\end{aligned}
$$

$$(2.27)$$

Here the Bessel function I_0 stretches the distribution depending on v_0.

2.4.3 Maximum Light Curve Event Definition

In Paczyński (1986) definition for lensing events (hereafter called standard definition) lens-source configurations become lensing events if the magnification of a source rises above a given threshold within the survey time interval Δt. This means that for each lens mass one can define a "microlensing-tube" along the line-of-sight to the source, which separates the high-magnification region from the low-magnification region, and a lens causes an event if it enters the tube.

We use (for the motivation, see § 2.4.3) an alternative event definition: a lens-source configuration becomes an event, if the lensing light curve reaches the maximum within the survey time Δt. This definition does not specify any specific magnification threshold at the time of maximum magnification because this magnification threshold will in reality depend on the observational setup and the brightness of the source. We show that the impact parameter distribution for the maximum light curve event definition agrees with the standard definition, if the same magnification threshold is used.

Standard Event Definition and Maximum Light Curve Event Definition

We motivate our alternative event definition in that section and illustrate the differences from the standard definition.

---

[6] We extract the desired distribution functions using

$$
p(s) = \int_{y_0}^{y_1}\int_{x_0}^{x_1} p(x, y)\, \delta(s - s(x, y))\, dx\, dy = \int_{\tilde{y}_0}^{\tilde{y}_1}\int_{x_0}^{x_1} p(x, y) \frac{\delta(x - x(s, y))}{\left|\frac{ds(x,y)}{dx}\right|} dx\, dy = \int_{\tilde{y}_0}^{\tilde{y}_1} p(x(s, y), y) \left|\frac{ds(x, y)}{dx}\right|_{x=x(s,y)}^{-1} dy.
$$

Note that if $ds(x, y)/dx|_{x=x(s,y)}$ has a different domain for y than $f(x, y)$, the limits for y have to change to $\tilde{y}_0$ and $\tilde{y}_1$.
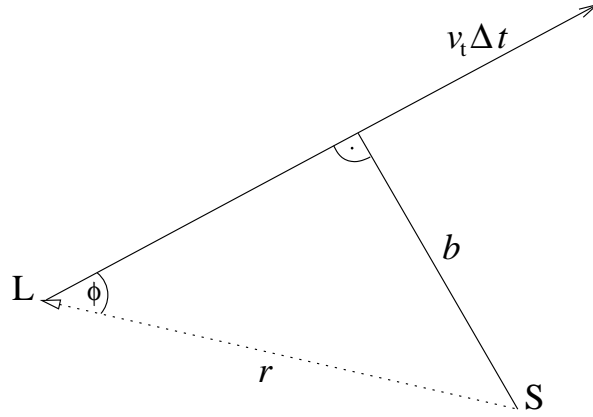
Figure 2.3: For a projected lens-source separation r and an angle ϕ between the projected distance vector and the projected relative velocity vector the impact parameter of the source-lens configuration is $b = r\sin(\phi)$. The lens approaches the source only for angles between $-\pi/2$ and $\pi/2$.

The standard definition, in which a lens becomes an event if it exceeds a threshold in magnification A_T (equivalent to entering the microlensing tube with the corresponding radius b_T for a given lens mass) has two consequences:

i) Since only lenses that enter are counted, only the formal event times (when the magnification threshold is exceeded) but not the event maxima are homogeneously distributed within the survey time interval, if their event timescales are not much shorter than that. (see Figure 2.4, *red and green curves*; for the events with red light curves, the maximum will arise after the survey has ended)

ii) The microlensing tube changes with the magnification threshold, and so does the spatial distribution of lenses that cause events within Δt (see Figure 2.6, *red curves*, for a special example with $v_t \Delta t = 1$). Lenses that cause events with a higher magnification threshold within the survey time are not all a subset of those with a lower magnification threshold. Taking this event definition literally would make Monte-Carlo simulations time-ineffective, since high-magnification threshold subsamples could not be picked out from a more general sample.

For event searches in data one usually requires to measure the light curve around maximum (to check the light curve form, in particular its symmetry), and of course, in practice, one would not exclude a light curve from an event list, if it was above the magnification threshold at the beginning of the survey.

This motivates the use of the maximum light curve definition, which only accepts events that obtain their maximum within the survey time interval Δt. A threshold of the magnification A_T at light curve maximum, then, is equivalent to a maximum impact parameter b_T of the lens (for a given mass).

We now consider events with a threshold b_T for both event definitions. We calculate the location of those lenses at survey begin that become events within the survey time interval. We assume the lenses to be distributed in a plane and to have velocities $v_t \Delta t = 1$. Length scales are given in arbitrary units and the density of lenses is assumed to equal $n = 1$ in these units. The number of lenses per radius interval is $\frac{dN}{dr} = 2\pi r$. This curve is shown in black in Figure 2.6.
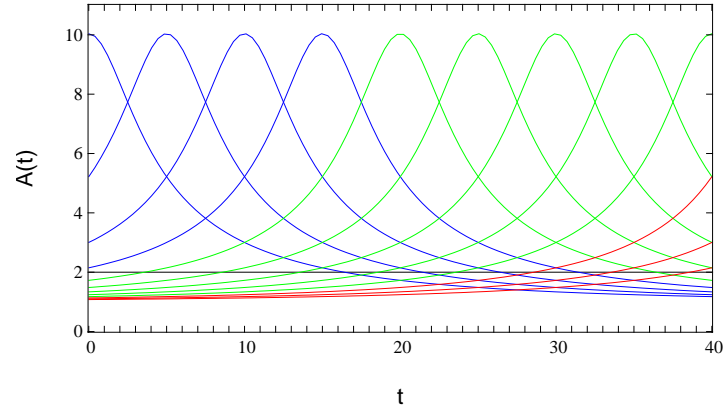
Figure 2.4: Examples for the distributions of events within the time interval of the survey, for the standard definition and the maximum light curve definition. The magnification threshold is chosen as $A_T = 2$. The green light curves are events for both definitions, the blue ones only for the maximum light curve definition, and the red ones only for the standard definition. Of course, in both cases the times, when the events occur are homogeneously distributed within the survey time. The event time, however, is not equal to the time of light curve maximum in the standard definition case. It may happen, the light curve maxima is attained only after the survey has ended (*red curves*).
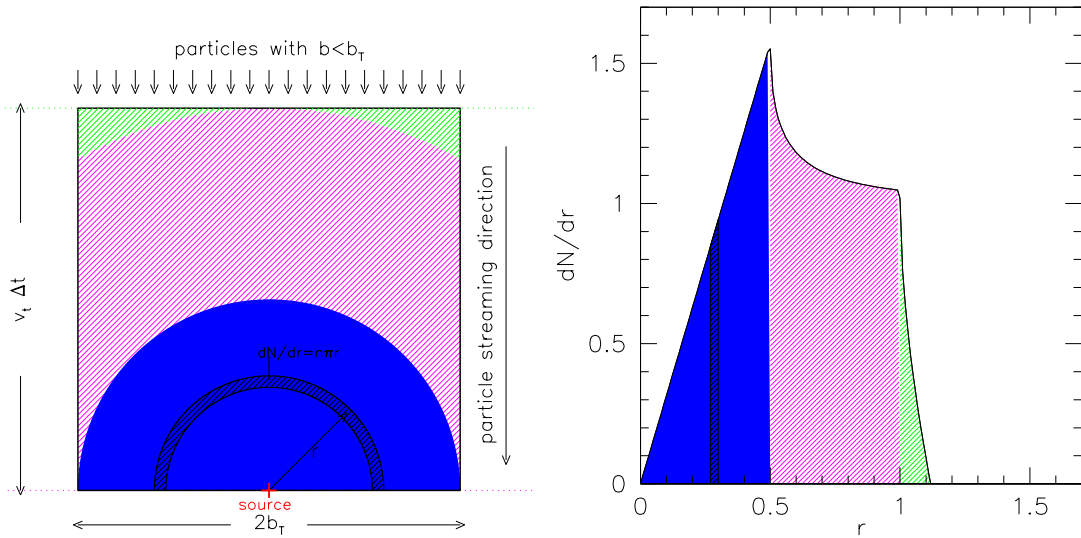
Figure 2.5: These two figures illustrate how the impact parameter distribution and the radial distribution of lenses that become events in the maximum light curve definition are related. In the left panel we choose as an example a coherent particle flow with velocities v_t in one direction. Those particles that have an impact parameter $b \leq b_T$ and will attain their minimum distance to the source within the survey time interval Δt are contained in the black box. Three areas have been shaded with blue, magenta, and green. The same colors have been used in the right panel to show in which part of the radial distribution function the events enter.
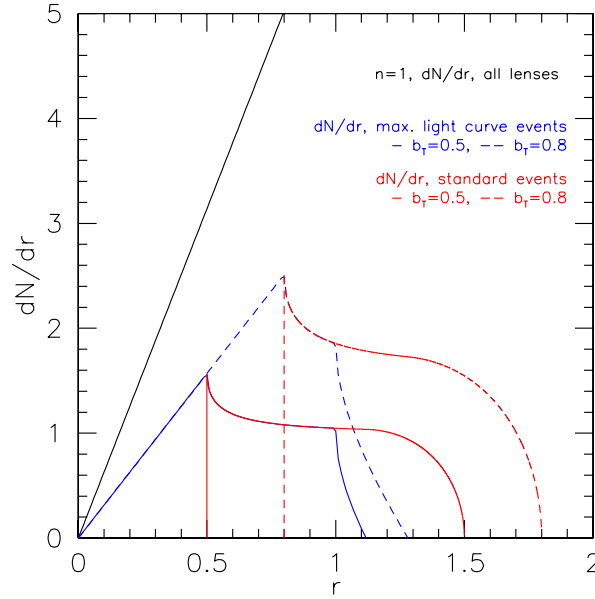
Figure 2.6: Number of lenses per radius interval (*black*) and number of lenses causing events per radius interval. Curves for the standard definition are in red, and for the maximum light curve definition are in blue. Length scales are in arbitrary units, the density is chosen such that it equals $n = 1$ in these units, and the velocities are chosen such that $v_t \Delta t = 1$ holds. The thresholds for the microlensing tube radius and the maximum impact parameter have been chosen as $b_T = 0.5$ (*solid lines*) and $b_T = 0.8$ (*dashed lines*). The integral of the corresponding red and blue curves coincide and give the number of lenses that cause events within Δt. For the standard definition (the locations of) the lenses that cause events with a higher magnification threshold are not all a subset of those with a lower magnification threshold. In addition, lenses that are already within the microlensing tube never will cause any event for the standard definition (implying the lower cutoff). The red and blue curves shown here are straightforwardly obtained analytically (derivation not shown in this chapter).

The blue and red curves show the number of those lenses per radius interval that become events within Δt in the new and the standard definition, respectively. For the standard definition, only lenses with $b_T \leq r \leq b_T + v_t \Delta t$ will become events within Δt, explaining the minimum and maximum radius in Figure 2.6 (*red solid and red dashed curve*, for a threshold of $b_T = 0.5$ and $b_T = 0.8$, respectively).
In the maximum light curve definition lenses within $0 < r < [b_T^2 + (v_t \Delta t)^2]^{1/2}$ can cause events with $b < b_T$, explaining the maximal radius in Figure 2.6 (*blue solid and blue dashed curves*, for the threshold of $b_T = 0.5$ and $b_T = 0.8$, respectively). The relation between the features in the radial distribution of lenses becoming events and the particles motion is shown for the case of a coherent particle stream in Figure 2.5.
One can also see in Figure 2.6 that lenses with the higher magnification threshold (corresponding to $b_T = 0.5$) are a subset of those with the lower magnification threshold ($b_T = 0.8$). In addition, the lenses causing an event within Δt are spatially more confined than for the standard definition: the maximum radius from which a lens can cause an event with an impact parameter b_T within Δt is $[b_T^2 + (v_t \Delta t)^2]^{1/2}$ for a relative velocity of v_t.
Hence, it is obvious that new event definition is more easy to use in simulations, but also more directly

linked to observations. On the other hand, one can guess from Figure 2.6 that the integral of the corresponding blue and red curves in Figure 2.6 agrees. Therefore, the number of events for both definitions is the same.

This implies that for both event definitions, a magnification threshold A_T or impact parameter threshold b_T (for a given lens mass) yields the same events (same number of events and same light curve parameters for the events, with exception of the time of maximum); only the lenses that cause the events are different in both definitions. Since it is not relevant where the lenses that cause events have come from, one can conveniently switch definitions.

2.4.4   Impact Parameter Distribution for Events

For simplicity we consider lenses with one mass, distance, and velocity, for the moment only. The lenses are homogeneously distributed points (in two dimensions) with density n and velocities of v_t (the velocities can have arbitrary directions, but the angular distribution of the velocities must be the same for all the points). The number of lenses per radius interval around the line-of-sight to the source is

$$\frac{dN}{dr}(r) = n\, 2\pi r. \tag{2.28}$$

If r is the source-lens distance at the beginning of the survey and ϕ is the angle that the lens's velocity vector encloses with the lens-source vector at that time, then the configuration will become an event with impact parameter b if $b \leq r \leq \sqrt{b^2 + (v_t \Delta t)^2}$ and $b = r|\sin(\phi)|$ with $\phi \in [-\pi/2, \pi/2]$ holds (see Figure 2.3 and § 2.4.3). Therefore, $\frac{dN}{db}$ can be derived from the spatial distribution of the lenses relative to the source, $\frac{dN}{dr}$, and the distribution of the angles between velocity vector and distance to the source. For the special case in which all lenses have isotropic velocities of v_t, the probability for the angle between radius vector and velocity vector is independent of the location of the lens and equals

$$p_\phi(\phi) := \frac{1}{2\pi}, \quad 0 \leq \phi \leq 2\pi, \tag{2.29}$$

and

$$\begin{aligned}
\frac{dN}{db}(b) &= \int_b^{\sqrt{(v_t\Delta t)^2+b^2}} 2 \int_0^{\pi/2} \frac{dN}{dr}\frac{1}{2\pi}\,\delta(b - r\sin\phi)\,d\phi\,dr \\
&= n \int_b^{\sqrt{(v_t\Delta t)^2+b^2}} 2 \int_0^{\pi/2} r\,\frac{\delta\left(\phi - \arcsin\frac{b}{r}\right)}{\sqrt{r^2-(r\sin\phi)^2}}\,d\phi\,dr \\
&= n \int_b^{\sqrt{(v_t\Delta t)^2+b^2}} \frac{2r}{\sqrt{r^2-b^2}}\,dr = 2n\,v_t\Delta t.
\end{aligned} \tag{2.30}$$

In this equation, the radial integration limits correspond to the minimum and maximum source-lens separation for an event with impact parameter b within Δt, and the δ-function then allows only for those trajectories through r that have the correct angle ϕ for the impact parameter $b = r\sin(\phi)$ of interest. The factor of 2 accounts for integrating from 0 to $\pi/2$ instead of $-\pi/2$ to $\pi/2$ in the angle. In the second line of this equation we have changed the variable in the δ-function from $r\sin(\phi)$ to ϕ and then have carried out the angle integration and finally the r-integration. The quantity $\frac{dN}{db}$ has units of length^{-1}.

Note that $\frac{dN}{db}$ is independent of b; i.e., the impact parameters of the events are uniformly distributed. Of course, in reality, an upper limit $b_{\max}$ will be present, depending on the source brightness, background light and the observing conditions. The integral $\int_0^{b_{\max}} \frac{dN}{db} db = 2n v_t \Delta t \times b_{\max}$ is dimensionless and equals (for the considered line-of-sight) the number of lenses that cause an event above a minimum magnification (corresponding to $b_{\max}$) within Δt.

Equation (2.30) can also be obtained from geometrical arguments: a circle with radius b embedded into a two dimensional plane defines a cross section of $2b$ to streaming particles in that plane, independent of the streaming direction. Therefore, the number of particles passing through that aperture with diameter $2b$ in a time Δt is $n v_t \Delta t 2b$. Hence, equation (2.30) also holds for a coherent particle stream, with any velocity direction. Therefore equation (2.30) is also valid for any probability distribution of the velocity angles.

The number of events per line-of-sight distance D_{ol}, lens mass M, transversal velocity v_t, and impact parameter b follows from equation (2.30) by replacing n with $n(D_{ol}, M, v_t) = n(D_{ol}, M) p_{v_t}(v_t, D_{ol})$:

$$\frac{d^4N}{dD_{ol}\, dM\, dv_t\, db} = 2n(D_{ol}, M) p_{v_t}(v_t, D_{ol}) v_t \Delta t = 2\rho(D_{ol})\xi(M) p_{v_t}(v_t, D_{ol}) v_t \Delta t. \tag{2.31}$$

We now transfer the number N of the events per line-of-sight to the event rate (per line-of-sight), $\Gamma := \frac{N}{\Delta t}$, and write equation (2.31) as

$$\frac{d^4\Gamma}{dD_{ol}\, dM\, dv_t\, db} = 2\rho(D_{ol})\xi(M) p_{v_t}(v_t, D_{ol}) v_t. \tag{2.32}$$

With the relative impact parameter u_0 defined as $u_0 = \frac{b}{R_E(D_{ol}, M)}$ this distribution can be rewritten as

$$\frac{d^4\Gamma}{dD_{ol}\, dM\, dv_t\, du_0} = 2\rho(D_{ol})\xi(M) p_{v_t}(v_t, D_{ol}) v_t R_E(D_{ol}, M), \tag{2.33}$$

which corresponds to the event rate for the standard definition (see de Rujula *et al.* (1991)).[7]

---

[7] de Rujula *et al.*'s (1991) eq. (10) with $d\Gamma \equiv d^4\Gamma$, $D \equiv D_{os}$, $x \equiv D_{ol}/D_{os}$, $r_E[\mu x(1-x)]^{1/2} \propto R_E$, $\rho_0 H(x) \equiv \rho(D_{ol})$, $dn_0/d\mu \equiv \xi(M)$, $u_{\min} \equiv u_0$ yields $d^4\Gamma = 2D_{os} v_t p_{v_t}(v_t) R_E \rho(D_{ol})\xi(M)\, dM\, du_0\, dv_t\, (dD_{ol}/D_{os})$.

2.5   The Source Distributions

In the case of pixel-lensing the parameters of the source cannot be determined. Therefore, we now introduce probability distributions for the source distance D_{os}, velocity $\vec{v}_s$, unlensed flux F_0, color $\mathscr{C}$, and radius R_* (for finite source effects).

2.5.1   The Transverse Lens-source Velocity Distribution

We again assume that the velocity distributions of lenses l and sources s are approximately isotropic around their mean respective streaming velocities (cf. equation (2.27)). The projected velocity dispersion of the source population we call $\tilde{\sigma}_s = D_{ol}/D_{os}\,\sigma_s$. We define $\vec{v}_0 = (v_{0,x}, v_{0,y})$ as the difference between the projected streaming velocities of the source and lens populations. Then, the transverse velocity differences in x and y between a lens and a source, each drawn from their respective distributions, are: $v_{ls,x} := v_{l,x} - v_{s,x} + v_{0,x}$ and $v_{ls,y} := v_{l,y} - v_{s,y} + v_{0,y}$.
Similar to equation (2.27), we obtain for the distribution of the transverse velocities

$$p_{v_t}(v_t, v_0) = \int \delta\left(v_t - \sqrt{v_{ls,x}{}^2 + v_{ls,y}{}^2}\right) p(v_{ls,x})\, p(v_{ls,y})\, dv_{ls,x}\, dv_{ls,y}, \tag{2.34}$$

where $p(v_{ls,x})$ [and $p(v_{ls,y})$ analogously] is given by

$$
\begin{aligned}
p(v_{ls,x}) &= C_l C_s \int_{-\infty}^{+\infty}\int_{-\infty}^{+\infty} \exp\left(-\frac{\tilde{\sigma}_s^2 v_{l,x}{}^2 + \sigma_l^2 v_{s,x}{}^2}{2\sigma_l^2 \tilde{\sigma}_s^2}\right) \delta(v_{ls,x} - (v_{l,x} - v_{s,x} + v_{0,x}))\, dv_{l,x}\, dv_{s,x} \\
&= C_l C_s \int_{-\infty}^{+\infty}\int_{-\infty}^{+\infty} \exp\left(-\frac{\tilde{\sigma}_s^2 v_{l,x}{}^2 + \sigma_l^2 v_{s,x}{}^2}{2\sigma_l^2 \tilde{\sigma}_s^2}\right) \delta(v_{l,x} - (v_{ls,x} + v_{s,x} - v_{0,x}))\, dv_{l,x}\, dv_{s,x} \\
&= C_l C_s \int_{-\infty}^{+\infty} \exp\left(-\frac{(v_{ls,x} - v_{0,x})^2}{2(\sigma_l^2 + \tilde{\sigma}_s^2)}\right) \sqrt{\frac{2\pi \sigma_l^2 \tilde{\sigma}_s^2}{\sigma_l^2 + \tilde{\sigma}_s^2}}\, dv_{ls,x} \\
&= \frac{1}{\sqrt{\sigma_l^2 + \tilde{\sigma}_s^2}\sqrt{2\pi}} \exp\left(-\frac{(v_{ls,x} - v_{0,x})^2}{2(\sigma_l^2 + \tilde{\sigma}_s^2)}\right) \\
&= \frac{1}{\sigma_{ls}\sqrt{2\pi}} \exp\left(-\frac{(v_{ls,x} - v_{0,x})^2}{2\sigma_{ls}{}^2}\right).
\end{aligned}
\tag{2.35}
$$

In the last step we have defined

$$\sigma_{ls} := \sqrt{\sigma_l^2 + \left(\frac{D_{ol}}{D_{os}}\right)^2 \sigma_s^2}, \tag{2.36}$$

which is the combined width of the velocity distribution of the lenses and that of the sources, projected onto the lens plane.
Finally, analogously to equation (2.27), we obtain

$$p_{v_t}(v_t, v_0) = \frac{1}{\sigma_{ls}{}^2}\, v_t \exp\left(-\frac{v_t{}^2 + v_0^2}{2\sigma_{ls}{}^2}\right) I_0\left(\frac{v_0\, v_t}{\sigma_{ls}{}^2}\right), \tag{2.37}$$

with $v_0(x, y, D_{ol}, D_{os})$, $\sigma_l(x, y, D_{ol})$, and $\sigma_s(x, y, D_{os})$.

2.5.2 The Luminosity Function

The luminosity function (LF) $\phi\left(\text{flux}^{-1}\right)$ or $\Phi\left(\text{mag}^{-1}\right)$ is usually defined as the number of stars per luminosity bin. The mean, or so-called characteristic flux of a stellar population is

$$< \mathscr{F} >:= \frac{\int \mathscr{F}\,\phi(\mathscr{F})\,d\mathscr{F}}{\int \phi(\mathscr{F})\,d\mathscr{F}}, \tag{2.38}$$

or, if one instead uses the luminosity function Φ in magnitudes,[8]

$$< \mathscr{F} >:= \frac{\int \mathscr{F}_{\text{Vega}}10^{-0.4\mathscr{M}}\,\Phi(\mathscr{M})\,d\mathscr{M}}{\int \Phi(\mathscr{M})\,d\mathscr{M}}, \tag{2.39}$$

where $\mathscr{F}_{\text{Vega}}$ is the flux of Vega.

We use a luminosity function normalized equal to 1,

$$\int\limits_{0}^{\infty} \tilde{\phi}(\mathscr{F})\,d\mathscr{F} := \int\limits_{-\infty}^{+\infty} \tilde{\Phi}(\mathscr{M})\,d\mathscr{M} := 1, \tag{2.40}$$

as we obtain the amplitude of the LF from the matter density and the mass-to-light ratio of the matter components (bulge, disk) later on.

The luminosity functions in the literature are usually given for stars at a distance of 10 pc. The relations for the source flux F_0 at a distance D_{os} and its flux $\mathscr{F}$ at 10 pc, or its absolute magnitude $\mathscr{M}$ are given in the following two equations, allowing for extinction along the line-of-sight:

$$F_0(\mathscr{F},x,y,D_{\text{os}}) := \mathscr{F} \times \left(\frac{10\,\text{pc}}{D_{\text{os}}}\right)^2 10^{-0.4\,\text{ext}(x,y,D_{\text{os}})}, \tag{2.41}$$

$$F_0(\mathscr{M},x,y,D_{\text{os}}) := \mathscr{F}_{\text{Vega}}10^{-0.4\mathscr{M}} \times \left(\frac{10\,\text{pc}}{D_{\text{os}}}\right)^2 10^{-0.4\,\text{ext}(x,y,D_{\text{os}})}. \tag{2.42}$$

2.5.3 The Number Density of Sources

We characterize different source components (bulge and disk) by an index s with corresponding indices in the density, luminosity, and mass-function of that component. $(M/L)_s$ is the mass-to-light ratio of that component in solar units.

The number density of sources is a function of the mass density, the mass-to-light ratio, and the characteristic flux of each component:

$$n_s(x,y,D_{\text{os}}) := \frac{d^3N_s}{dx\,dy\,dD_{\text{os}}} = \frac{\rho_s(x,y,D_{\text{os}})}{\left(\frac{M}{L}\right)_s \frac{M_\odot}{\mathscr{F}_\odot} < \mathscr{F} >_s}. \tag{2.43}$$

Note that (M/L) is the mass-to-light ratio of the total disk or bulge component, and has to include the mass in stellar remnants or in gas. Therefore, the value of (M/L) is not necessarily equal to the stellar mass-to-light-ratio in the bulge and the disk.

---

[8] With $d\mathscr{M} = -(2.5/\ln 10)\,d\mathscr{F}/\mathscr{F}$ the conversion of the luminosity function from flux to magnitudes becomes $\Phi(\mathscr{M}) = -0.4\ln 10\,\mathscr{F}_{\text{Vega}}10^{-0.4\mathscr{M}}\,\phi\left(\mathscr{F}_{\text{Vega}}10^{-0.4\mathscr{M}}\right)$.

The normalized probability distribution for sources $p_s(D_{\mathrm{os}})$ at distance D_{os} is

$$p_s(D_{\mathrm{os}}) := \frac{\rho_s(D_{\mathrm{os}})}{\int_0^\infty \rho_s(D_{\mathrm{os}})\, dD_{\mathrm{os}}}. \tag{2.44}$$

2.5.4   Including the Color and Radius Information

To use the color information, $\mathscr{C} := \mathscr{M} - \mathscr{M}\mathrm{`}$, we construct a normalized color-flux distribution $p_{\mathrm{cmd}}(\mathscr{M},\mathscr{C})$ from the color-magnitude diagram of stars,

$$\iint p_{\mathrm{cmd}}(\mathscr{M},\mathscr{C})\, d\mathscr{M}\, d\mathscr{C} \overset{!}{=} 1, \tag{2.45}$$

which is related to the luminosity function as

$$\tilde{\Phi}(\mathscr{M}) = \int p_{\mathrm{cmd}}(\mathscr{M},\mathscr{C})\, d\mathscr{C}. \tag{2.46}$$

The radius is related to the luminosity and color as $R_*(\mathscr{M},\mathscr{C})$ (see § 3.5).

2.6 Applications for the Microlensing Regime

In this section we derive the basic microlensing quantities and distributions using the four-dimensional event rate differential derived in § 2.4. We apply the equations to M31 using the M31 model in Chap. 3.

2.6.1 Optical Depth τ

The optical depth τ is defined as the number of lenses that are closer than their own Einstein radius R_E to a line-of-sight. The optical depth τ is therefore the instantaneous probability of lensing taking place, given a line-of-sight and a density distribution of the lenses. For a given source star at distance D_{os}, the optical depth equals the number of lenses within the microlensing tube defined by the Einstein radius $R_E(M, D_{ol}, D_{os})$ (eq. [2.4]) along the line-of-sight:

$$
\begin{aligned}
\tau(D_{os}) &= \int_0^{D_{os}} \int_0^\infty \int_0^\infty \int_0^{R_E} n(D_{ol}, M, v_t) \times 2\pi r\, dr\, dv_t\, dM\, dD_{ol} \\
&= \int_0^{D_{os}} \int_0^\infty \int_0^\infty \rho(D_{ol})\, \xi(M)\, p_{v_t}(v_t, D_{ol}) \int_0^{R_E} 2\pi r\, dr\, dv_t\, dM\, dD_{ol} \\
&= \int_0^{D_{os}} \int_0^\infty \rho(D_{ol})\, \xi(M)\, \pi R_E{}^2\, dM\, dD_{ol} \\
&= \frac{4\pi G}{c^2} \int_0^{D_{os}} \rho(D_{ol})\, D(D_{ol})\, dD_{ol},
\end{aligned}
\tag{2.47}
$$

with $D(D_{ol}) := D_{ol}(D_{os} - D_{ol})/D_{os}$, equal to Paczyński (1986, eq. (9)). Equation (2.47) demonstrates that the optical depth depends on the mass density, but not on the mass function $\xi(M)$ of the lenses. In the past, the optical depth along a line-of-sight to M31 was often calculated by setting D_{os} equal to the distance to the plane of the disk of M31 (Gyuk & Crotts, 2000; Baltz & Silk, 2000). This is like treating the sources for lensing as a two dimensional distribution. It yields fairly adequate results for the optical depth of disk stars but cannot be justified for the bulge stars in M31. We use the source distance probability distribution (equation (2.44) to obtain the line-of-sight distance–averaged optical depth:

$$
< \tau >_s := \int p_s(D_{os})\, \tau(D_{os})\, dD_{os}.
\tag{2.48}
$$

Figure 2.7 shows the average optical depth for the central part of M31 for lenses in the halo of M31 ("halo-lensing"), and for stellar lenses in the bulge and disk of M31 ("self-lensing"). The self-lensing optical depth is symmetric (with respect to the near and far side of M31) and dominates the optical depth in the central arcminute of M31. The halo-lensing optical depth is asymmetric and rises toward the far side of the M31 disk, since there are more halo lenses in front of the disk.

Figure 2.7 (*first row, left*) shows the halo-disk optical depth. The results do not depend so much on the three-dimensional structure of the disk but much more on the halo core radius assumed. We use $r_c = 2\,\mathrm{kpc}$ (see Chap. 3). Gyuk & Crotts (2000) used core radii of $r_c = 1\,\mathrm{kpc}$ and $r_c = 5\,\mathrm{kpc}$ for their Figures 1c and 1d, and our result is in between their results, as expected. Baltz & Silk (2000) have obtained qualitatively similar results using $r_c = 5\,\mathrm{kpc}$, but assuming an M31 distance of 725 kpc and a slightly less massive halo than we do. The optical depth caused by all M31 components is shown
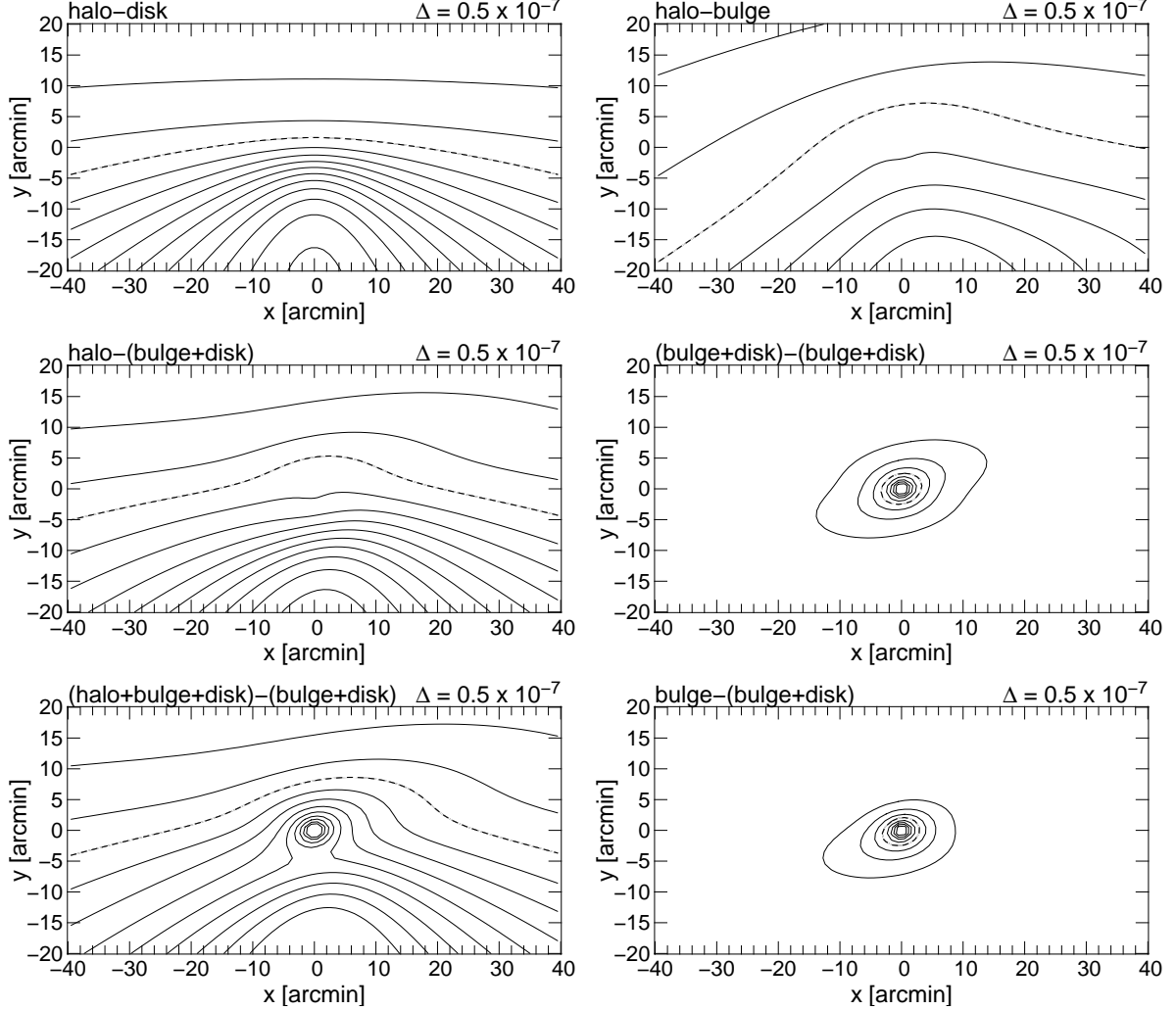
Figure 2.7: Contours of the line-of-sight–averaged optical depth $\langle \tau \rangle_s$ (eq. [2.48]). x and y are given in the intrinsic M31 coordinate system, which is centered on the nucleus of M31 and where the M31 disk major axis is orientated horizontally (P.A. = 38°). Halo lensing of disk sources (*first row left*, a), halo-bulge lensing (*first row right,*), halo-lensing of bulge & disk sources (*second row left*). The average optical depth for self-lensing of sources in M31 is shown in the second row on the right. In the third row, left panel, we show the resulting total optical depth with the contributions of all lenses. The third row, right panel, displays the optical depth due to bulge lenses. The optical depth caused by the MW (not shown), is nearly constant $\tau_{\mathrm{MW}} = 0.78 \times 10^{-6}$. To obtain the values of $< \tau >_s$ we used the model of the luminous and dark matter of M31 presented in Chap. 3. Here and in all following calculations a MACHO fraction in the dark halo of M31 of unity was assumed. The spacing between adjacent contours are shown as inserts in each diagram. The contour lines $< \tau >_s = 2 \times 10^{-6}$ are shown as dashed curve.

in Figure 2.7 (*third row, left*). The result of (Han, 1996, see his Fig. 1) using a halo core radius of $r_c = 6.5$ kpc looks strikingly different. Comparison to Figure 2.7 (*third row, left*) demonstrates that the total optical depth is dominated by bulge lenses in the central part of M31. The last panel of this figure shows the optical depth for bulge-lensing toward M31 sources. The bulge-lensing optical depth had been obtained by (Gyuk & Crotts, 2000, see their Fig. 5), but the values that they obtained are up to a factor of 5 larger than ours (which probably is due to their different M31 model).

2.6.2 Single-star Event Rate

The optical depth is the probability of stars to be magnified above a threshold of 1.34 at any time. Observations, however, usually measure only a temporal change of magnification. Therefore, the event rate, which is the number of events per time interval, is the relevant quantity for observations. The event rate is the integral of equation (2.32) over lens masses, lens distances, relative velocities, and impact parameters b smaller than a threshold $u_T R_E$:

$$
\begin{aligned}
\Gamma_T(D_{os}) &:= \int_0^\infty \int_0^{D_{os}} \int_0^\infty \int_0^{u_T R_E} \frac{d^4\Gamma}{dD_{ol}\,dM\,dv_t\,db}\,db\,dv_t\,dM\,dD_{ol} \\
&= 2u_T \int_0^\infty \xi(M) \int_0^{D_{os}} \rho(D_{ol})\,R_E(D_{ol},M) \int_0^\infty v_t\,p_{v_t}(v_t,D_{ol})\,dv_t\,dD_{ol}\,dM \\
&= 2u_T \frac{\sqrt{4G}}{c} \int_0^{D_{os}} \rho(D_{ol})\,\sqrt{D(D_{ol})} \int_0^\infty \sqrt{M}\,\xi(M) \int_0^\infty v_t\,p_{v_t}(v_t,D_{ol})\,dv_t\,dD_{ol}\,dM \\
&=: u_T \Gamma_1(D_{os}).
\end{aligned}
\tag{2.49}
$$

This had been first evaluated [using a single mass instead of $\xi(M)$] by Griest (1991).[9]
The impact parameter threshold u_T is equivalent to a magnification threshold A_T. Therefore, the number of events with amplifications larger than $A_T(u_T)$ is proportional to the threshold parameter u_T. $\Gamma_1(D_{os})$ is the event rate along a chosen line-of-sight to a distance of D_{os}. Analogously to the optical depth, we also define the line-of-sight distance–averaged single-star event rate

$$
< \Gamma_1 >_s = \int p_s(D_{os})\,\Gamma_1(D_{os})\,dD_{os}
\tag{2.50}
$$

toward M31.
We show these line-of-sight distance–averaged event rates for the halo of M31 and the stellar lenses in the bulge and disk of M31 (self-lensing) in Figure 2.8; the single-star halo-lensing event rate is evidently asymmetric, whereas the single-star self-lensing event rate is symmetric. The levels of the event rates (for each line-of-sight) are of the order $\sim 10^{-5}$ events yr^{-1} (*dashed*), which implies that at least a few times 10^4 source stars are needed to identify one lensing event (even if all lensing events below the threshold $u_T = 1$ could be observed). It can also be seen in Figure 2.8 that only in the

---

[9] Eq. (11): changing his notation with $\Gamma \equiv \Gamma_T$, $v_c \equiv \sqrt{2}\sigma_l$, $L \equiv D_{os}$, $\sqrt{m} \equiv \sqrt{M_0}$, $\frac{\rho_0 A'}{A'+Bx'+x'^2} \equiv \rho(D_{ol})$, $x' \equiv D_{ol}/D_{os}$, $\eta \equiv v_0/(\sqrt{2}\sigma_l)$, $u' \equiv v_t/(\sqrt{2}\sigma_l)$:

$$
\Gamma_T = 4\sqrt{\frac{G}{c^2}} \frac{u_T}{\sqrt{M_0}} \int_0^{D_{os}} dD_{ol}\,\rho(D_{ol})\,\sqrt{D(D_{ol})}\,e^{-v_0^2/(2\sigma_l^2)} \int_0^\infty dv_t\,\frac{v_t^2}{\sigma_l^2}\,e^{-v_t^2/(2\sigma_l^2)}\,I_0\left(\frac{2v_0 v_t}{2\sigma_l^2}\right)
$$

corresponds to our formula setting $\xi(M) = \delta(M - M_0)/M_0$, $\sigma_s = 0$.
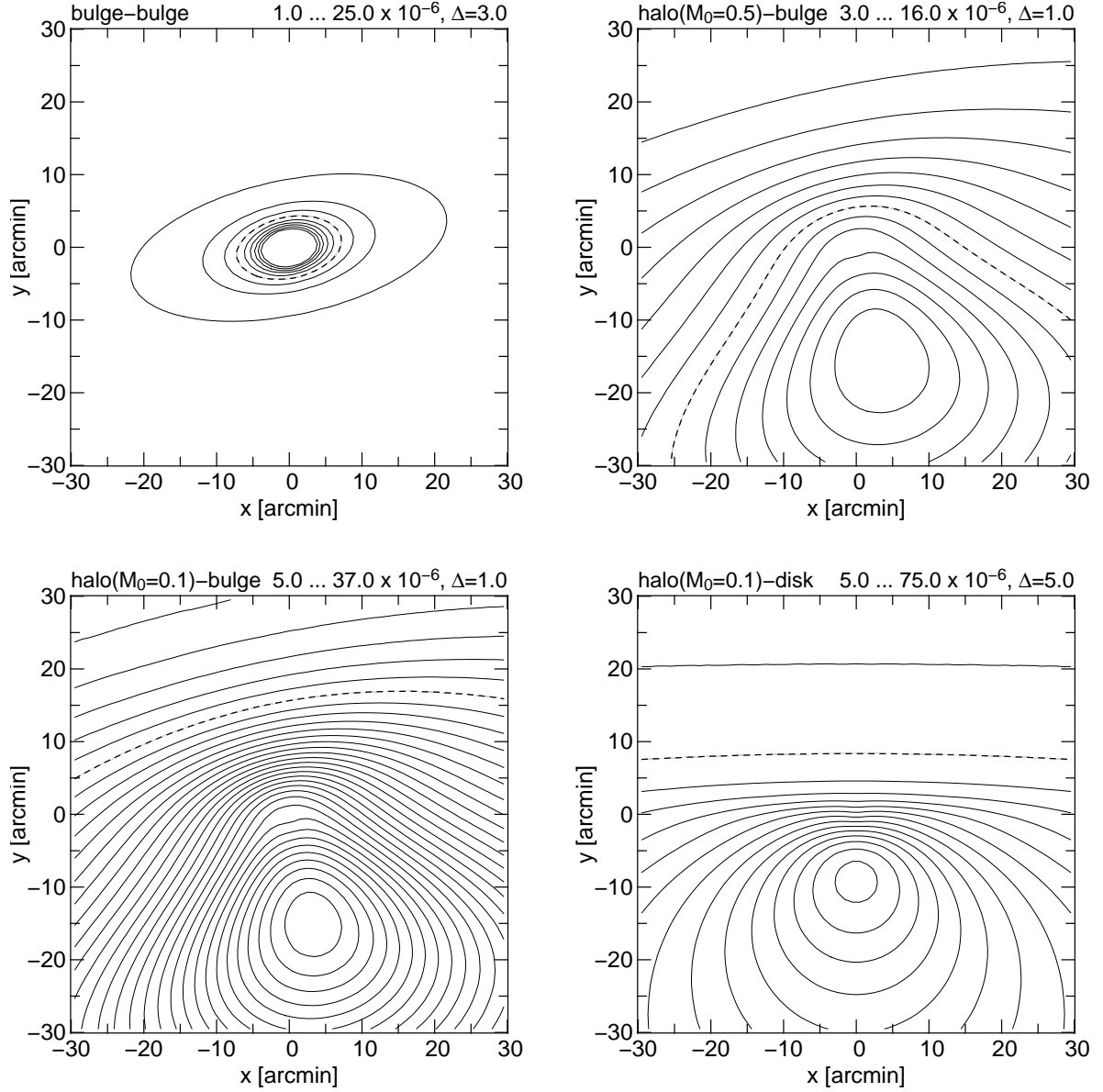
Figure 2.8: Averaged event rate $< \Gamma_1 >_s$ (y^{-1}) toward M31 for bulge-bulge lensing *first row, left*), halo-bulge lensing with $M_0 = 0.5 M_\odot$ (i.e., a mass function $\xi(M) = \delta(M_0 - 0.5 M_\odot)/0.5 M_\odot$) (*first row, right*), halo-bulge lensing with $M_0 = 0.1 M_\odot$ (second row, left), and halo-disk lensing with $M_0 = 0.1 M_\odot$ (second row, right). Contour levels and the spacing between adjacent contours are given on top of each diagram. The dashed line marks the 10^{-5} events yr^{-1} level. Whereas self-lensing is symmetric, halo lensing shows a clear asymmetry. The event rate shows a maximum at the far side of the M31 disk (negative *y*-values). These contours cannot be compared with an experiment since, first, one could certainly not identify all objects with a threshold of $u_T = 1$ or a magnification of 1.34 and second, one has to convolve the single-star event rate with the density of sources. The proper event rate maps in the pixel-lensing regime can be seen in § 2.8.

innermost part ($r \leq 5'$) the self-lensing event rate exceeds the halo-lensing event rate (for a 100% MACHO halo). As mentioned earlier, the optical depth does not depend on the lens-mass distribution (for the same matter density) because the decrease of number of lenses with lens-mass is balanced by the increased area of the Einstein disks around them. However, the events take longer, since larger Einstein radii have to be crossed. For the same optical depth, this then must imply a decrease in event rate: $\Gamma \sim M_0^{-1/2}$, setting $\xi(M) = \delta(M - M_0)/M_0$ in equation (2.49). The decrease of the event rate with increasing mass of the lenses can be seen in Figure 2.8 (*first row, right panel*) and Figure 2.8 (*second row, left panel*).

The relations above give the event rate per line-of-sight or per star. To compare this with measurements of the lensing rate for resolved stars, one has to account for the source density.

2.6.3 Distribution for the Einstein Timescale

Not only the number of lensing events per time and their spatial distribution but also their duration (Einstein time) is a key observable in microlensing surveys. The distribution of the Einstein timescales of the events is

$$
\begin{aligned}
\frac{d^2\Gamma}{dt_{\mathrm{E}}\,du_0} &= \int\limits_0^\infty \int\limits_0^{D_{\mathrm{os}}} \int\limits_0^\infty \frac{d^4\Gamma}{dD_{\mathrm{ol}}\,dM\,dv_{\mathrm{t}}\,du_0} \, \delta\!\left(t_{\mathrm{E}} - \frac{R_{\mathrm{E}}}{v_{\mathrm{t}}}\right) dv_{\mathrm{t}}\,dD_{\mathrm{ol}}\,dM \\
&= \int\limits_0^\infty \int\limits_0^{D_{\mathrm{os}}} \int\limits_0^\infty \rho(D_{\mathrm{ol}})\,\xi(M)\,p_{v_{\mathrm{t}}}(v_{\mathrm{t}})\,2\,v_{\mathrm{t}}\,R_{\mathrm{E}}\,\delta\!\left(t_{\mathrm{E}} - \frac{R_{\mathrm{E}}}{v_{\mathrm{t}}}\right) dv_{\mathrm{t}}\,dD_{\mathrm{ol}}\,dM \\
&= 2\int\limits_0^\infty \int\limits_0^{D_{\mathrm{os}}} \int\limits_0^\infty \rho(D_{\mathrm{ol}})\,\xi(M)\,p_{v_{\mathrm{t}}}(v_{\mathrm{t}})\,v_{\mathrm{t}}\,R_{\mathrm{E}}\,\frac{\delta\!\left(v_{\mathrm{t}} - \frac{R_{\mathrm{E}}}{t_{\mathrm{E}}}\right)}{|R_{\mathrm{E}}/v_{\mathrm{t}}^2|}\,dv_{\mathrm{t}}\,dD_{\mathrm{ol}}\,dM \\
&= \frac{2}{t_{\mathrm{E}}^3} \int\limits_0^\infty \int\limits_0^{D_{\mathrm{os}}} \rho(D_{\mathrm{ol}})\,\xi(M)\,p_{v_{\mathrm{t}}}\!\left(\frac{R_{\mathrm{E}}}{t_{\mathrm{E}}}\right) R_{\mathrm{E}}^3\,dD_{\mathrm{ol}}\,dM.
\end{aligned}
\tag{2.51}
$$

The second line of equation (2.51) is proportional to the equation presented in Han & Gould (1996a).[10] The result is of course independent of the relative impact parameter u_0. If one carries out an (microlensing) experiment with a threshold u_{T}, one obtains with equation (2.51) the Einstein timescale distribution of events as

$$
\frac{d\Gamma_{\mathrm{T}}}{dt_{\mathrm{E}}} = \frac{2u_{\mathrm{T}}}{t_{\mathrm{E}}^3} \int\limits_0^\infty \int\limits_0^{D_{\mathrm{os}}} \rho(D_{\mathrm{ol}})\,\xi(M)\,p_{v_{\mathrm{t}}}\!\left(\frac{R_{\mathrm{E}}}{t_{\mathrm{E}}}\right) R_{\mathrm{E}}^3\,dD_{\mathrm{ol}}\,dM.
\tag{2.52}
$$

This result corresponds to that of Roulet & Mollerach (1997)[11] and Baltz & Silk (2000)[12]. The (normalized) probability distribution for the Einstein timescales becomes

$$
p(t_{\mathrm{E}}) := \frac{1}{\Gamma_{\mathrm{T}}}\frac{d\Gamma_{\mathrm{T}}}{dt_{\mathrm{E}}}.
\tag{2.53}
$$

---

[10] Their eqs. (2.2.6) and (2.2.7) with $f(t_{\mathrm{E}}) \propto p(t_{\mathrm{E}})$, $d_{\min} = 0$, $d_{\max} \equiv D_{\mathrm{os}}$, and $f_M(M) \propto \xi(M)$,

$$
p(t_{\mathrm{E}}) \propto \int \xi(M) \int\limits_0^{D_{\mathrm{os}}} \rho(D_{\mathrm{ol}})R_{\mathrm{E}}(M,D_{\mathrm{ol}},D_{\mathrm{os}}) \int\limits_0^\infty v_{\mathrm{t}}p_{v_{\mathrm{t}}}(v_{\mathrm{t}}) \int\limits_0^\infty \delta\!\left(t_{\mathrm{E}}' - \frac{R_{\mathrm{E}}(M_\odot,D_{\mathrm{ol}},D_{\mathrm{os}})}{v_{\mathrm{t}}}\right) \delta\!\left(t_{\mathrm{E}} - \left(\frac{M}{M_\odot}\right)^{\frac{1}{2}} t_{\mathrm{E}}'\right) dt_{\mathrm{E}}'\,dv_{\mathrm{t}}\,dD_{\mathrm{ol}}\,dM.
$$

[11] Their eq. (31) corresponds to our formula converting their notation to ours $\Gamma \equiv \Gamma/u_{\mathrm{T}}$, $dn/dm \equiv \rho(D_{\mathrm{ol}})\xi(M)$, $T \equiv t_{\mathrm{E}}$, $v^\perp \equiv v_{\mathrm{t}}$, $\int_0^{2\pi} d\gamma v^\perp\,G(v_{\mathrm{dis}}^l)\,G(v_{\mathrm{dis}}^b) \equiv p_{v_{\mathrm{t}}}(v_{\mathrm{t}})$.

[12] Their eq. (9) corresponds to our formula converting their notation to ours $L \equiv D_{\mathrm{os}}$, $t_{\mathrm{E}} \equiv 2t_{\mathrm{E}}$, $\beta_{\mathrm{T}} \equiv u_{\mathrm{T}}$, $v_{\mathrm{c}} \equiv \sqrt{2}\sigma_l$, $x \equiv D_{\mathrm{ol}}/D_{\mathrm{os}}$, $\eta \equiv v_0/\sqrt{2}\sigma_l)$, $v \equiv v_{\mathrm{t}}/(\sqrt{2}\sigma_l)$ and setting $\xi(M) = \delta(M - M_0)/M$, $\sigma_{\mathrm{s}} = 0$.

With this probability distribution the average timescale $\overline{t_E}$ of an event with line-of-sight distance D_{os} can be obtained:

$$
\begin{aligned}
\overline{t_E}(D_{os}) &:= \int_0^\infty t_E \, p(t_E) \, dt_E \\
&= \frac{2u_T}{\Gamma_T} \int_0^\infty \int_0^\infty \int_0^{D_{os}} \rho(D_{ol}) \, \xi(M) \, p_{v_t}\left(\frac{R_E}{t_E}\right) t_E \frac{R_E^3}{t_E^3} \, dD_{ol} \, dM \, dt_E \\
&= \frac{2u_T}{u_T \Gamma_T} \int_0^\infty \int_0^\infty \int_0^{D_{os}} \rho(D_{ol}) \, \xi(M) \, p_{v_t}(v_t) \, R_E^2 \, dD_{ol} \, dM \, dv_t \\
&= \frac{2}{\pi \Gamma_T} \int_0^\infty \int_0^{D_{os}} \rho(D_{ol}) \, \xi(M) \, \pi R_E^2 \, dD_{ol} \, dM \\
&= \frac{2}{\pi} \frac{\tau(D_{os})}{\Gamma_T(D_{os})},
\end{aligned}
\tag{2.54}
$$

which equals the result of Alcock *et al.* (1995).[13]

We instead aim for the line-of-sight distance–averaged mean Einstein timescale [at an arbitrary position (x,y)]. We start from the line-of-sight distance–averaged event rate per Einstein time t_E,

$$
\left\langle \frac{d\Gamma_T}{dt_E} \right\rangle_s = \int p_s(D_{os}) \frac{d\Gamma_T}{dt_E} \, dD_{os}.
\tag{2.55}
$$

Figure 2.9 shows examples for this line-of-sight distance–averaged distribution $\langle d\Gamma_T/dt_E \rangle_s$ for two different positions in the intrinsic M31 coordinate system (see Fig. 2.7), at $(x,y) = (1',0')$ and $(x,y) = (4.46', 4.46') = (1\,\mathrm{kpc}, 1\,\mathrm{kpc})$. The distributions show a strong dependence on the line-of-sight position. The halo-bulge and halo-disk lensing timescales are longer than those of bulge-bulge lensing. An increase in MACHO mass decreases the event rate (see Fig. 2.8), and the timescale of the events becomes longer (see the examples for $M_0 = 0.1\,M_\odot$ and $M_0 = 0.5\,M_\odot$ in Fig. 2.9).

Weighting t_E with this function and integrating over all timescales finally yields the desired mean line-of-sight distance–averaged Einstein timescale of an event:

$$
\overline{\langle t_E \rangle_s} := \frac{\int_0^\infty t_E \left\langle \frac{d\Gamma}{dt_E} \right\rangle_s dt_E}{\int_0^\infty \left\langle \frac{d\Gamma}{dt_E} \right\rangle_s dt_E} = \frac{2}{\pi} \frac{\langle \tau \rangle_s}{\langle \Gamma_T \rangle_s} \neq \langle \overline{t_E} \rangle_s.
\tag{2.56}
$$

Mean Einstein timescales $\overline{\langle t_E \rangle_s}$ are shown for lensing and self-lensing in Figure 2.10. Generally, the minimum of $\overline{\langle t_E \rangle_s}$ is near the M31 center, irrespective of the lens-source configuration. The mean Einstein timescale is smaller for lower MACHO masses, since the Einstein radii become smaller and are faster to cross (compare the two middle panels in Fig. 2.10). The bulge-bulge lensing events (*first panel*) are the shortest. This is caused by the small lens-source distances, which reduce the sizes of the Einstein radii.

2.6.4   The Amplification Distribution

The magnification distribution of the event rate is

$$
\frac{d\Gamma}{dA_0} = \left| \frac{du_0}{dA_0} \right| \frac{d\Gamma}{du_0} = \left| \frac{du_0}{dA_0} \right| \frac{\Gamma}{u_T}.
\tag{2.57}
$$

---

[13] Their eq. (2) with $\hat{t} \equiv 2t_E$.
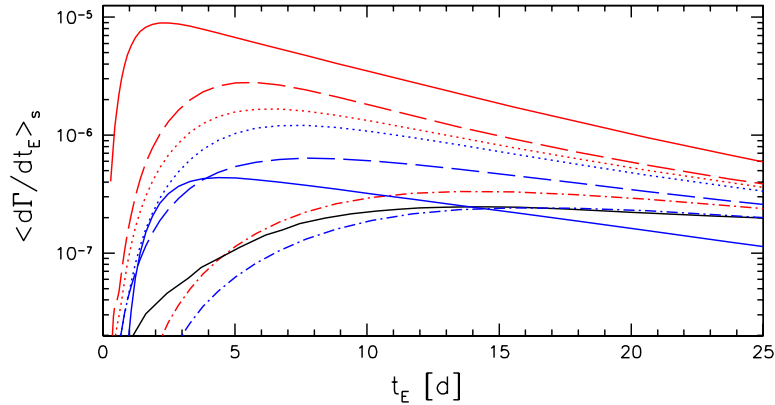
Figure 2.9: Line-of-sight distance–averaged distribution of the event rate with Einstein timescale $\langle d\Gamma/dt_{\mathrm{E}}\rangle_s$ (yr^{-1}) using the model of M31 presented in Chap. 3 and assuming a 100% MACHO halo. Results are shown for two positions in the intrinsic M31 coordinate system (see Figure 2.7), at $(x,y) = (1',0')$ (*red*), and at $(x,y) = (4.46', 4.46')$ (corresponding to $(x,y) = (1\,\mathrm{kpc}, 1\,\mathrm{kpc})$, *blue*). The bulge-bulge Einstein time distribution is shown as solid line. The halo-bulge distributions have been evaluated for a MACHO mass of $M_0 = 0.1\,M_\odot$ (*dotted line*) and $M_0 = 0.5\,M_\odot$ (*dot-dashed line*). The halo-disk lensing case is shown for a MACHO mass of $M_0 = 0.1\,M_\odot$ (*dashed line*). The Einstein time distributions of the event rate differ considerably for halo-disk, halo-bulge and bulge-bulge lensing and also vary significantly with the line-of-sight position. For comparison we also plot the Einstein timescale distribution for M31 halo-lensing derived by Han & Gould (1996a) up to a pre-factor (that we chose equal to 3×10^{-6}) as a black solid curve. Han & Gould (1996a) considered the distributions for the halo-disk and halo-bulge lensing to be similar and not distinguish between them further. They used a MACHO mass of $M_0 = 0.1\,M_\odot$ for their curve. However, it looks more similar to our halo-bulge curve for $M_0 = 0.5\,M_\odot$, and cannot be moved on the halo-bulge or halo-disk for $M_0 = 0.1\,M_\odot$ curve with another choice of the prefactor.

Inserting equation (2.8) makes the result equal to that of Griest (1991).[14]
Transforming equation (2.51) we can write

$$\frac{d^2\Gamma}{dt_{\mathrm{E}}\,dA_0} = \frac{2}{t_{\mathrm{E}}^3}\left|\frac{du_0}{dA_0}\right| \int\limits_0^\infty \int\limits_0^{D_{\mathrm{os}}} \rho(D_{\mathrm{ol}})\,\xi(M)\,p_{v_{\mathrm{t}}}\left(\frac{R_{\mathrm{E}}}{t_{\mathrm{E}}}\right) R_{\mathrm{E}}^3\,dD_{\mathrm{ol}}\,dM. \tag{2.58}$$

using du_0/dA_0 from equation (2.8).

2.6.5 The Distribution for the FWHM Timescale

Although the Einstein timescale t_{E} contains all the relevant physical properties (mass, position, and velocity) of the lens, it is of limited practical use in the case of an ill-determined source flux ("Einstein time - magnification degeneracy", see § 2.3.2). In this case t_{FWHM} is the only properly measurable timescale of a light curve. We obtain the distribution function for t_{FWHM} (neglecting finite-source

---

[14]Eq. (22): with $A \equiv A_0$, $\Gamma' \equiv \frac{\Gamma}{u_{\mathrm{T}}}$, $\frac{d\Gamma}{dA_0} = -\frac{\Gamma/u_{\mathrm{T}}}{\sqrt{2}}\,[A_0(A_0^2-1)^{-1/2}-1]^{-1/2}(A_0^2-1)^{-3/2}$.
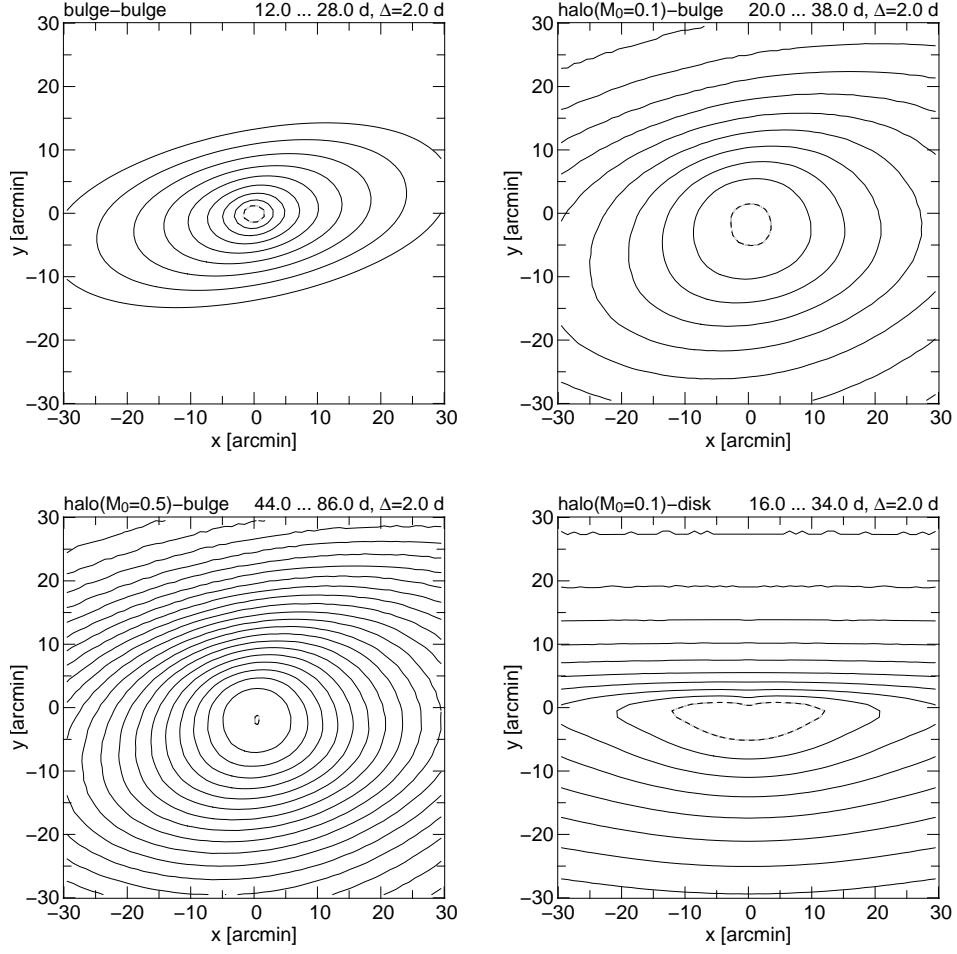
Figure 2.10: Einstein timescale averaged over all sources $\overline{\langle t_E \rangle}_s$ calculated for lines of sights toward the center of M31 using the model of M31 presented in Chap. 3. We show the distributions for bulge-bulge self-lensing (*first row, left*), halo-bulge lensing for lenses of $M_0 = 0.1 M_\odot$ [i.e., a mass function $\xi(M) = \delta(M_0 - 0.1 M_\odot)/0.1 M_\odot$] (*first row, right*), halo-bulge lensing for lenses of $M_0 = 0.5 M_\odot$ (*second row, left*), and halo-disk lensing with $M_0 = 0.1 M_\odot$ (*second row, right*). Contour levels and spacing are shown on top of each diagram. We assume the MACHO fraction in the dark halo to be unity. The dashed line marks the lowest contour level.

effects), starting from § 2.4, using $t_{\text{FWHM}}(v_t, M, D_{\text{ol}}, u_0) = \frac{R_E(M, D_{\text{ol}})}{v_t} w(u_0)$ (see eq. [2.9]):

$$
\begin{aligned}
\frac{d^2\Gamma}{dt_{\text{FWHM}} du_0} &= \int_0^\infty \int_0^{D_{\text{os}}} \int_0^\infty \rho(D_{\text{ol}}) \, \xi(M) \, p_{v_t}(v_t) \, 2v_t R_E \, \delta\left(t_{\text{FWHM}} - \frac{R_E}{v_t} w(u_0)\right) dv_t \, dD_{\text{ol}} \, dM \\
&= 2 \int_0^\infty \int_0^{D_{\text{os}}} \int_0^\infty \rho(D_{\text{ol}}) \, \xi(M) \, p_{v_t}(v_t) \, v_t R_E \, \frac{\delta\left(v_t - \frac{R_E}{t_{\text{FWHM}}} w(u_0)\right)}{\left|-\frac{R_E}{v_t^2} w(u_0)\right|} \, dv_t \, dD_{\text{ol}} \, dM \\
&= \frac{2}{t_{\text{FWHM}}^3} \int_0^\infty \int_0^\infty \rho(D_{\text{ol}}) \, \xi(M) \, w^2(u_0) \, R_E{}^3 \, p_{v_t}\left(\frac{R_E}{t_{\text{FWHM}}} w(u_0)\right) dD_{\text{ol}} \, dM \\
&= \frac{2 w^2(u_0)}{t_{\text{FWHM}}^3} \int_0^\infty \xi(M) \int_0^{D_{\text{os}}} \rho(D_{\text{ol}}) \, p_{v_t}\left(\frac{R_E}{t_{\text{FWHM}}} w(u_0)\right) R_E{}^3 \, dD_{\text{ol}} \, dM.
\end{aligned}
\tag{2.59}
$$

Baltz & Silk (2000) expressed the same relation in an alternative way[15] and already motivated the same change of variables from v_t to t_{FWHM}. Our relation for the FWHM time distribution of the event rate in equation (2.59) does not include any derivative or inversion of $w(u_0)$ and thus is very easy to evaluate numerically. Note that one can use $w(u_0) \approx \sqrt{12}\, u_0$ as high-magnification approximation. Replacing the relative impact parameter u_0 by the maximum amplification A_0 (using eqs. [2.7] and [2.8]) yields an equivalent description of this result:

$$\frac{d^2\Gamma}{dt_{FWHM}\, dA_0} = \frac{2\Psi(A_0)}{t_{FWHM}{}^3} \int\limits_0^\infty \xi(M) \int\limits_0^{D_{os}} \rho(D_{ol})\, p_{v_t}\left(\frac{R_E}{t_{FWHM}}\, \Upsilon(A_0)\right) R_E{}^3\, dD_{ol}\, dM, \tag{2.60}$$

with $R_E(M, D_{ol}, D_{os})$ and $\Psi(A_0)$ as

$$\Psi(A_0) := \left|\frac{du_0}{dA_0}\right| \Upsilon^2(A_0) = 4\sqrt{2}\, \frac{\left[A_0 + (A_0{}^2 - 1)^{1/2}\right]^{1/2} \left[(A_0+1)^{3/2} - A_0(A_0+3)^{1/2}\right]}{(A_0{}^2 - 1)^{7/4}(A_0+3)^{1/2}} \stackrel{A_0 \gg 1}{\approx} \frac{12}{A_0{}^4}, \tag{2.61}$$

where $\left|\frac{du_0}{dA_0}\right|$ was defined in equation (2.8).

Figure 2.11 shows the distribution of events $\left\langle \frac{d^2\Gamma}{d\log(t_{FWHM}/[d])\, d\log A_0} \right\rangle_s$, at the position $(x, y) = (1', 0')$ in the intrinsic M31 coordinate system (see Fig. 2.7), i.e., on the disk major axis.[16]

Small amplifications are favored, which implies a strong dependency of the total number of events on the experimental limit of A_0 (e.g., A_T). Figure 2.11 can be compared with sensitivity regions of current experimental setups for microlensing experiments toward M31. As these are usually only sensitive to t_{FWHM} of larger than 1 day, it is extremely unlikely to detect maximum magnifications larger than 10^3. These high-magnification events can only be routinely detected with combined observations from several sights located on different longitudes, with large telescopes allowing short integration times, or from space. Note that recently after an alert detection and intensive follow-up monitoring, Dong *et al.* (2006) could measure a lensing time-scale of $t_{FWHM} \approx 0.05\,d$ and a magnification of the order 3000.

---

[15] We can derive their expression in eq. (10) with $\eta \equiv \frac{v_0}{\sqrt{2}\sigma_l}$, $v \equiv \frac{v_t}{\sqrt{2}\sigma_l}$, $M \equiv M_0$:

$$\frac{d\Gamma}{dt_{FWHM}} = \int\limits_0^\infty \int\limits_0^{D_{os}} \int\limits_0^\infty \int\limits_0^{u_T R_E} \frac{d^4\Gamma}{dD_{ol}\, dM\, dv_t\, db}\, \delta\left(t_{FWHM} - 2\frac{R_E}{v_t}\, w(u_0)\right) db\, dv_t\, dD_{ol}\, dM$$

$$= \int\limits_0^\infty \int\limits_0^{D_{os}} \int\limits_0^\infty \rho(D_{ol})\, \xi(M)\, v_t{}^2\, p_{v_t}(v_t) \left\{ w'\left[w^{-1}\left(\frac{t_{FWHM} v_t}{2R_E}\right)\right]\right\}^{-1} \theta\left(2\frac{R_E}{t_{FWHM}}\, w(u_T) - v_t\right) dv_t\, dD_{ol}\, dM$$

using $\xi(M) = \delta(M - M_0)/M_0$.

[16] We have now changed to logarithmic units for timescale and magnification, and also converted the probability density according to that.
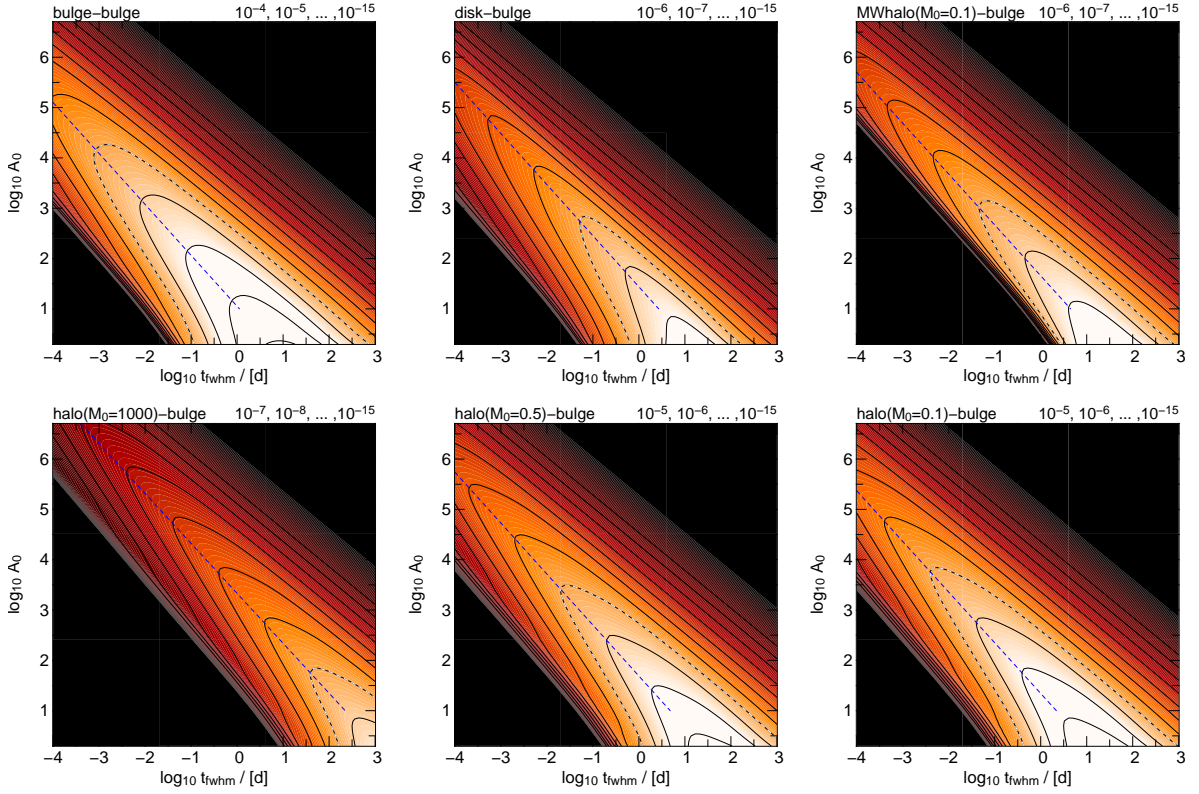
Figure 2.11: Distribution $\left\langle d^2\Gamma/(d\log t_{\mathrm{FWHM}}\, d\log A_0)\right\rangle_s$ (y^{-1}) (i.e., rate per year and line-of-sight) for different lens-source configurations, calculated at the position $(x,y) = (1',0')$ in the intrinsic M31 coordinate system (see Fig. 2.7). The values of timescale and magnification are largely confined to a linear region within the logarithmic timescale-magnification plane. *First row, left panel:* Bulge-bulge lensing; *middle panel:* disk-bulge lensing; *right panel:* MW-halo-bulge lensing for MW lenses with $M_0 = 0.1\,M_\odot$. *Second row, left panel:* Halo-bulge lensing with $M_0 = 1000\,M_\odot$; *middle panel:* halo-bulge lensing with $M_0 = 0.5\,M_\odot$; *right panel:* halo-bulge lensing with $M_0 = 0.1\,M_\odot$. The dashed contour level line marks the 10^{-8} (y^{-1}) level in each diagram. The number of events rises toward smaller amplifications and larger timescales. Small amplifications are strongly favored for all lens-source configurations. The number of high-amplification events rises for smaller t_{FWHM} timescale. Detecting events toward M31 with maximum amplifications of $A_0 > 10^3$ therefore requires an experiment that is particularly sensitive to short timescale events. The dashed blue line shows for each selected timescale the amplification where the distribution is maximal $[\partial \log(A_0) = 0]$.

2.7 Applications for the Pixel-Lensing Regime

The microlensing parameters (F_0, t_E, and u_0) are not directly observable anymore in crowded or unresolved stellar fields. In that case, the two measurable quantities are the full-width timescale t_{FWHM} and the difference flux Δ_F of an event.

We now make use of the luminosity function $\tilde{\Phi}(\mathcal{M})$, the source number density $n_s(x, y, D_{os})$, and the color distribution $p_{cmd}(\mathcal{M}, \mathcal{C})$ of the source stars introduced in § 2.5 and derive the event rate distribution function $\frac{d^2\Gamma}{dt_{FWHM} d\Delta_F}$. This quantity can then be linked to the measured distributions most straightforwardly.[17]

In the first two subsections (§§ 2.7.1 and 2.7.2) we derive the required distributions neglecting finite source effects. However, the high magnifications needed to boost MS stars to large flux excesses go in parallel with finite source effects that make these large flux excesses hardly possible. We show this in detail in § 2.7.3, where we incorporate finite source effects in the calculations.

2.7.1 Changing Variables of Γ to t_{FWHM} and Δ_F

Event Rate per Star with Absolute Magnitude $\mathcal{M}$

We now use the relations $R_E(M, D_{ol}, D_{os})$, $A_0(F_0, \Delta_F)$, $t_{FWHM}(v_t, R_E, b)$, $\Psi[A_0(F_0, \Delta_F)]$, and $\Upsilon[A_0(F_0, \Delta_F)]$ from § 2.3 and the equations $t_{FWHM}(v_t, R_E, F_0, \Delta_F) = \frac{R_E}{v_t} \Upsilon(A_0)$, $\Delta_F(F_0, b, R_E) = F_0 [A(b/R_E) - 1]$ and $\frac{d\Delta_F}{db} = -8 \frac{F_0}{R_E} u_0^{-2} [u_0^2 + 4]^{-3/2}$, and we obtain the event rate per FWHM time, per flux excess, per lens mass and per source star with an absolute magnitude $\mathcal{M}$:

$$\frac{d^4\Gamma}{dt_{FWHM} d\Delta_F dM d\mathcal{M}}$$

$$= \tilde{\Phi}(\mathcal{M}) \int_0^{D_{os}} \int_0^\infty \int_0^\infty \frac{d^4\Gamma}{dD_{ol} dM dv_t db} \delta\left\{\Delta_F - F_0\left[A\left(\frac{b}{R_E}\right) - 1\right]\right\} \delta\left\{t_{FWHM} - \frac{R_E}{v_t} w\right\} db\, dv_t\, dD_{ol}$$

$$= \tilde{\Phi} \int_0^{D_{os}} \int_0^\infty \int_0^\infty \rho\, \xi\, p_{v_t} 2v_t \frac{\delta\left\{b - R_E\left[2A_0(A_0^2 - 1)^{-1/2} - 2\right]^{1/2}\right\}}{\left|\frac{d\Delta_F}{db}\right|} \delta\left(t_{FWHM} - \frac{R_E}{v_t} \omega\right) db\, dv_t\, dD_{ol}$$

$$= 2\tilde{\Phi} \frac{1}{F_0} \frac{du_0}{dA_0} \int_0^{D_{os}} \int_0^\infty \rho\, \xi\, p_{v_t} v_t R_E\, \delta\left(t_{FWHM} - \frac{R_E}{v_t} \Upsilon\right) dv_t\, dD_{ol} \qquad (2.62)$$

$$= 2\tilde{\Phi} \frac{1}{F_0} \frac{du_0}{dA_0} \int_0^{D_{os}} \int_0^\infty \rho\, \xi\, p_{v_t} v_t R_E \frac{\delta\left(v_t - \frac{R_E}{t_{FWHM}} \Upsilon\right)}{\left|-\frac{R_E}{v_t^2} \Upsilon\right|} dv_t\, dD_{ol}$$

$$= 2\tilde{\Phi} \frac{1}{F_0} \frac{du_0}{dA_0} \Upsilon^2 \frac{1}{t_{FWHM}^3} \int_0^{D_{os}} \rho\, \xi\, p_{v_t}\left(\frac{R_E}{t_{FWHM}} \Upsilon\right) R_E^3\, dD_{ol}$$

$$= \frac{2}{t_{FWHM}^3} \tilde{\Phi}(\mathcal{M})\, \xi(M) \frac{\Psi}{F_0} \int_0^{D_{os}} \rho(D_{ol}) R_E^3\, p_{v_t}\left(\frac{R_E}{t_{FWHM}} \Upsilon\right) dD_{ol}.$$

using the luminosity function in magnitudes $\tilde{\Phi}(\mathcal{M})$ and the conversion from absolute magnitudes to intrinsic source fluxes $F_0(\mathcal{M}, D_{os})$ (eq. [2.42]). Equation (2.62) is the transformation of equation (2.32) to the observables relevant in the pixel-lensing regime. It gives the event rate per star with absolute magnitude $\mathcal{M}$ and will be converted to the event rate per area using the density of stars below.

---

[17] Note that this distribution function is different from $d\Gamma/dw_F = d\Gamma/d(\Delta_F t_{FWHM})$ derived by Baltz & Silk (2000) for the flux-weighted timescale $w_F := \Delta_F t_{FWHM}$.

For the special case of highly amplified events, $(A_0 \gg 1)$, the approximations $\Psi \approx 12(F_0/\Delta_F)^4$ and $\Upsilon \approx \sqrt{12}(F_0/\Delta_F)$ can be inserted into equation (2.62).

Event Rate per Area

All previously derived event rates are per star, or per star with a given absolute magnitude $\mathcal{M}$. Observed, however, are event rates per area. These are obtained from the source density distribution along the line-of-sight $n_s(x, y, D_{os})$ and equation (2.62):

$$\frac{d^6\Gamma_{s,l}}{dx\,dy\,dt_{FWHM}\,d\Delta_F\,dM\,d\mathcal{M}} = \frac{2\,\Phi_s(\mathcal{M})\,\xi_l(M)}{t_{FWHM}^3} \int\limits_0^\infty n_s(x,y,D_{os}) \frac{\Psi}{F_0} \int\limits_0^{D_{os}} \rho_l(D_{ol})\,R_E^3\,p_{v_t}\!\left(\frac{R_E\Upsilon}{t_{FWHM}}, v_0\right) dD_{ol}\,dD_{os}, \quad (2.63)$$

where the quantities in the integral have the following functional dependences $F_0(\mathcal{M}, D_{os})$, $\rho_l(x, y, D_{ol})$, $R_E(D_{ol}, M, D_{os})$, $\Psi(A_0(F_0, \Delta_F))$, $\Upsilon(A_0(F_0, \Delta_F))$, $v_0(x, y, D_{ol}, D_{os})$. Equation (2.63) is the event rate per interval of lens plane area, FWHM time flux excess, lens mass and absolute magnitude of the lensed star. For highly amplified events one can replace Ψ and Υ in the integral by $12(F_0/\Delta_F)^4$ and $\sqrt{12}(F_0/\Delta_F)$, respectively.

Different lens (disk, bulge, or halo) and source (disk or bulge) populations are characterized by an index l and s in equation (2.63). For the total event rate Γ_{tot} one has to sum up the contributions of all lens-source configurations:

$$\frac{d^6\Gamma_{tot}}{dx\,dy\,dt_{FWHM}\,d\Delta_F\,dM\,d\mathcal{M}} := \sum_s \sum_l \frac{d^6\Gamma_{s,l}}{dx\,dy\,dt_{FWHM}\,d\Delta_F\,dM\,d\mathcal{M}}. \quad (2.64)$$

The event rate per area is then obtained by multiplying equation (2.64) with the efficiency $\varepsilon(x, y, \Delta_F, t_{FWHM})$ of the experiment and integrating over all lens masses and source magnitudes, and the timescale and flux excess. The probability that one can observe two stars lensed at the same time at the same position is practically zero, since $\int_{\Omega_{psf}} (d^2\Gamma_{tot}/dx\,dy)\,dx\,dy \ll 1$ holds.

We carry out mass and magnitude integration of equation (2.63) for the position $(x, y) = (1', 0')$ in the intrinsic M31 coordinate system (see Figure 2.7), i.e., at a distance of 0.22 kpc along the disk major axis and show the results for bulge-bulge, halo-bulge, and bulge-disk lensing in Figure 2.12. Compared to Figure 2.11 the contours are smeared out in the ΔF-direction, since they come from convolving those in Figure 2.11 with the source luminosity function.

In Figure 2.13 we demonstrate for the halo-bulge lensing case in Figure 2.12 that the "double-wave shape" in the contours in the two left panels of Figure 2.12 indeed is caused by the luminosity function of the PMS stars. We split the source stars into post–main-sequence (PMS) and main-sequence (MS) stars and plot the corresponding contours into the middle and right panels of that figure. The double-wave shape appears only in the PMS figure. Besides that, it becomes obvious that PMS stars cannot be lensed into events with short timescales and small flux excess. This is because the faintest PMS stars in the M31 bulge have an unamplified flux of 8×10^{-9} Jy and thus need an amplification of only a factor of 2 to yield a flux excess of $\Delta_F \approx 10^{-8}$ Jy. Magnifications that small are incompatible with short timescales according to Figure 2.11. In contrast, MS stars need very high amplifications to reach a flux excess comparable to that typical for PMS stars. According to the right panel in Figure 2.13, ultra-short, large excess flux events with MS source stars would be more common [compare, e.g., the contour levels at $\log(t_{FWHM}/[d]) = -3$ and $\log(\Delta F/[Jy]) = -4$] than events with PMS source stars.
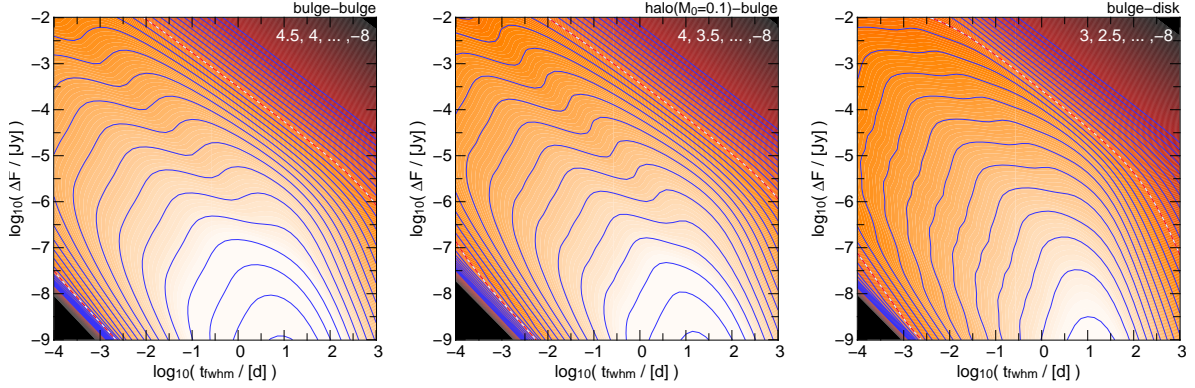
Figure 2.12:   Event rate per area, per FWHM time and per flux excess, $d^4\Gamma/(dx\,dy\,d\log t_{\mathrm{FWHM}}\,d\log\Delta_F)$, obtained from equation (2.63) by mass and magnitude integration. The contours are shown in units of $\mathrm{y}^{-1}\,\mathrm{arcmin}^{-2}$, timescales and flux excess have been inserted in units of days and Jy. The equations are evaluated at $(x,y)=(1',0')$ in the intrinsic M31 coordinate system (see Figure 2.7), i.e., at a distance of $1'$ along the disk major axis. We show bulge-bulge lensing (*left*), halo-bulge lensing with $M_0=0.1\,M_\odot$ lenses, and bulge-disk lensing (*right*). The contour levels are given as inserts in each diagram. The red dashed line marks the $10^{-3}\,\mathrm{y}^{-1}\,\mathrm{arcmin}^{-2}$ level in each diagram, brighter areas correspond to higher values. The double-wave shape of the contours with bulge stars as sources is caused by the shape of the PMS luminosity function of the bulge sources (see Figure 2.13). For the results shown in these panels all sources have been treated as point sources. For finite source effects, see § 2.7.3.
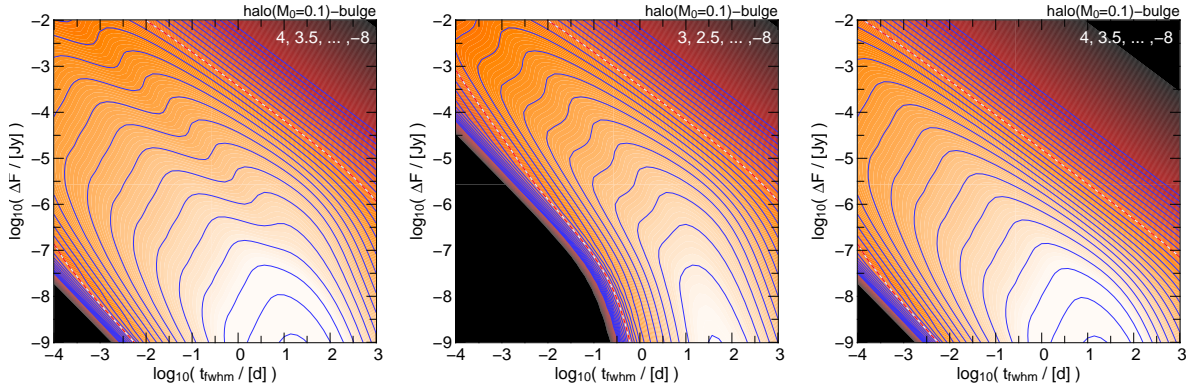
Figure 2.13:   Event rate per area, per FWHM time and per flux excess, $d^4\Gamma/(dx\,dy\,d\log t_{\mathrm{FWHM}}\,d\log\Delta_F)$, for halo-bulge lensing with $M_0=0.1\,M_\odot$ calculated at the position $(x,y)=(1,0)\,\mathrm{arcmin}$. *Left panel:* Distribution for PMS and MS sources. Middle panel: Distribution for PMS sources alone. Right panel: Distribution for MS sources alone. The contour levels are shown as inserts in each diagram. The red line marks the $10^{-3}\,\mathrm{y}^{-1}\,\mathrm{arcmin}^{-2}$ level in each diagram. The double -wave shape of the PMS distribution is due to the two peaks in the PMS luminosity function of the bulge sources (see Figure 3.4 in Chap. 3). For the results shown in these panels all sources have been treated as point sources.

2.7.2 Including Color Information in the Event Rate

The color of a point source remains unchanged during a lensing event, since the lensing amplification does not depend on the frequency of the source light. In practice, microlensing events with blending by nearby stars, and any event with finite source signatures may show chromaticity in the light curve (see e.g. Valls-Gabaud (1995); Witt (1995); Han *et al.* (2000)). The difference imaging technique eliminates all blended light from the lensing light curve. For lensing events without finite source effects the color of the event therefore equals that of the source and can be used to constrain the source-star luminosities.

Replacing $\tilde{\Phi}(\mathcal{M})$ with $p_{cmd}(\mathcal{M}, \mathcal{C})$, and $d\mathcal{M}$ with $d\mathcal{M}\,d\mathcal{C}$ (see § 2.5.4), we obtain

$$\frac{d^7\Gamma_{s,l}}{dx\,dy\,dt_{FWHM}\,d\Delta_F\,dM\,d\mathcal{M}\,d\mathcal{C}} =$$

$$= \frac{2}{t_{FWHM}^3}\,p_{cmd_s}(\mathcal{M}, \mathcal{C})\,\xi_l(M)\int\limits_0^\infty n_s(x,y,D_{os})\,\frac{\Psi}{F_0}\int\limits_0^{D_{os}}\rho_l(D_{ol})\,R_E{}^3\,p_{v_t}\left(\frac{R_E\Upsilon}{t_{FWHM}}, v_0\right)dD_{ol}\,dD_{os}. \tag{2.65}$$

We derive lens mass estimates starting from equation (2.65) in § 2.9. We also demonstrate there that including the color information leads to considerably smaller allowed lens mass intervals than for the case in which color information is ignored (i.e., the case in which lens mass probability functions are derived from eq. [2.63]).

Equation (2.65) allows to reconstruct the mass function of the lenses and the MACHO fraction in the dark halo (see de Rujula *et al.* (1991); Jetzer & Massó (1994); Jetzer (1994); Mao & Paczyński (1996); Han & Gould (1996b); Gould (1996a)). In this way one can obtain the optimal parameterization for the mass function $\xi_l(M)$ using a maximum-likelihood analysis for a set of measured lensing events. If the ingredients for the kernel (i.e., all but the pre-factor $\xi_l(M)$ in eq. [2.65]) are accurately provided by theory and the number of lensing events is large, then the mass distribution can be derived solving the Fredholm integral equation of the first kind. Inversely, a certain ensemble of lenses allows conclusions on the based distribution functions.

2.7.3 Event Rate Taking into Account Finite Source Effects

As described in § 2.3.1 the point-source approximation is no longer valid, if the impact parameter u_0 is smaller than u_0^*, i.e., half the source radius projected onto the lens plane (equation (2.14)). In this case, the maximum amplification and thus the flux excess stays below the value for the point-source approximation, and timescales of events are enlarged (see Eqs. 2.16 and 2.13). Baltz & Silk (2000) already accounted for the upper limit in magnification and obtained the correct value for the total number of events (i.e., events with and without finite source signatures) as a function of magnification threshold. Their approximation, however, is limited to high amplifications and ignores the change of magnification and event timescale.[18] Thus, the flux excess and timescale distributions of the events are not predicted accurately.

---

[18] Baltz & Silk's (2000) eq. (26) with eqs. (20) and (22) can be written in our notation as (see footnote 15)

$$\frac{d\Gamma}{dt_{FWHM}} = \frac{D_{os}}{M_0}\int\limits_{-\infty}^\infty\tilde{\Phi}(\mathcal{M})\int\limits_0^1\theta\left(\left(1 + \frac{R_*^2 c^2}{16GMD_{os}u_T^2}\right)^{-1} - \frac{D_{ol}}{D_{os}}\right)\rho(D_{ol})\int\limits_0^\infty\theta\left(2\frac{R_E}{t_{FWHM}}\sqrt{12}u_T - v_t\right)v_t^2\,p_{v_t}(v_t)$$

$$\times\left\{w'\left[w^{-1}\left(\frac{t_{FWHM}v_t}{2R_E}\right)\right]\right\}^{-1}dv_t\,d\left(\frac{D_{ol}}{D_{os}}\right)d\mathcal{M}.$$

We have shown in § 2.3.1 that finite source effects are likely already for small maximal magnifications and that the timescale changes due to finite source effects can be large. Therefore, we derive precise relations and account for the finite source sizes as follows:

1. Events with $u_0 > u_0^*$, i.e., those for which the finite source sizes are irrelevant, are treated as before; we redo all calculations starting from equation (2.31), and if the impact parameter b is involved in an integral we multiply the integrand with $\theta(b - R_E u_0^*)$; the step function allows only contributions in the integrand, if $b \geq R_E u_0^*$ holds. To see how this transports into the dD_{ol}-integration if the variables are changed from b and v_t to t_{FWHM} and ΔF in the Eqs. 2.62, 2.63 and 2.65

$$\theta(b - R_E u_0^*) = \theta(A_0^* - A_0) = \theta\left(D_{os}\left\{1 + \frac{c^2 R_*^2 \frac{\Delta_F}{F_0}\left(2 + \frac{\Delta_F}{F_0}\right)}{16\,GM\,D_{os}}\right\}^{-1} - D_{ol}\right) = \theta(D_{ol}^* - D_{ol}) \quad (2.66)$$

where we are using the following relations:

$$D_{ol}^* := D_{os}\left(1 + \frac{\Delta_F(2F_0 + \Delta_F)}{C_{D_{ol}^*} D_{os}}\right)^{-1} \approx D_{os}\left(1 + \frac{\Delta_F^2}{C_{D_{ol}^*} D_{os}}\right)^{-1},$$

$$C_{D_{ol}^*} := \frac{16\,F_0^2\,GM}{c^2 R_*^2}\ \left(\text{flux}^2\,\text{length}^{-1}\right).$$

Multiplying the integrand of equations (2.62), (2.63), and (2.65) with equation (2.66) extracts only those light curves, where finite-source effects can be neglected.

2. For events where the finite source sizes are relevant, i.e., events with $u_0 < u_0^*$, we use the approximations for the maximum amplification and the FWHM time given in equations (2.15) and (2.16). This means that we just replace the relations for the impact parameter and the maximum magnification and the FWHM timescale relations of events by equations (2.13) and (2.16) when switching from the point source to the finite source regime. We then can derive the equations for the event rates with finite source effects from equation (2.32) analogously to the point-source approximation, but this time with a step function of $\theta(R_E u_0^* - b)$ in the integrands allowing only small impact parameters. With $A_0^*(D_{ol}, D_{os}, R_*, M)$, $u_0^*(D_{ol}, D_{os}, R_*, M)$ and $v_t = (R_E/t_{FWHM})\Upsilon^*(A_0^*, u_0)$ and $|dt_{FWHM}(v_t)/dv_t| = (R_E/v_t^2)\Upsilon^*$ we obtain:

$$\frac{d^6 \Gamma_{s,l}}{dx\,dy\,dt_{FWHM}\,d\Delta_F\,dM\,d\mathcal{M}} =$$

$$= \int_0^\infty n_s(x,y,D_{os})\,\tilde{\Phi}_s(\mathcal{M}) \int_0^{D_{os}}\int_0^\infty\int_0^\infty \frac{d^4\Gamma}{dD_{ol}\,dM\,dv_t\,db}\,\delta(\Delta_F - F_0(A_0^* - 1))$$

$$\times \delta\left(t_{FWHM} - \frac{R_E}{v_t}\Upsilon^*\right)\theta\left(R_E u_0^* - b\right)\,db\,dv_t\,dD_{ol}\,dD_{os}$$

$$= \int_0^\infty n_s(x,y,D_{os})\,\tilde{\Phi}_s(\mathcal{M}) \int_0^{D_{os}}\rho(D_{ol})\int_0^\infty\int_0^\infty \xi(M)\,p_{v_t}(v_t)\,2v_t \quad (2.67)$$

$$\times \delta(\Delta_F - F_0(A_0^* - 1))\,\frac{\delta(v_t - (R_E/t_{FWHM})\Upsilon^*)}{(R_E/v_t^2)\Upsilon^*}\,\theta\left(R_E u_0^* - b\right)\,dv_t\,db\,dD_{ol}\,dD_{os}$$

$$= \int_0^\infty n_s\,2\,\tilde{\Phi}_s(\mathcal{M}) \int_0^{D_{os}}\rho(D_{ol})\,\xi(M)\,\delta(\Delta_F - F_0(A_0^* - 1)) \int_0^{R_E u_0^*} p_{v_t}\left(\frac{R_E}{t_{FWHM}}\Upsilon^*\right)\frac{R_E^2\Upsilon^{*2}}{t_{FWHM}^3}\,db\,dD_{ol}\,dD_{os}$$

$$= \int_0^\infty n_s(x,y,D_{os})\,\frac{2}{t_{FWHM}^3}\,\tilde{\Phi}_s(\mathcal{M})\,\xi(M)\,\rho(D_{ol}^*)\,\Omega^*\,R_E^3 \int_0^{u_0^*} p_{v_t}\left(\frac{R_E}{t_{FWHM}}\Upsilon^*\right)\Upsilon^{*2}\,du_0\,dD_{os},$$

with

$$\Omega^* := \left| \frac{dD^*_{\mathrm{ol}}(\Delta_F, D_{\mathrm{os}})}{d\Delta_F} \right| = 2C_{D^*_{\mathrm{ol}}} D_{\mathrm{os}}{}^2 (F_0 + \Delta_F) \left(C_{D^*_{\mathrm{ol}}} D_{\mathrm{os}} + \Delta_F (2F_0 + \Delta_F) \right)^{-2}$$

$$\approx 2C_{D^*_{\mathrm{ol}}} D_{\mathrm{os}}{}^2 \Delta_F \left(C_{D^*_{\mathrm{ol}}} D_{\mathrm{os}} + \Delta_F{}^2 \right)^{-2}.$$

We use the values for the source radius, luminosity, and color relations $R_*(\mathscr{M}, \mathscr{C})$ summarized in the Chap. 3 (§§ 3.4 and 3.5). Alternatively a transformation inverting $t_{\mathrm{FWHM}}(b)$ is possible.[19]

Figures 2.14 and 2.15 show contours of the event rate per t_{FWHM} timescale and flux excess, per year and square arcminute, with finite source effects taken into account. We use the same position as before, at $(x, y) = (1', 0')$ in the intrinsic M31 coordinate system (see Figure 2.7) or at a disk major axis distance of $1'$. The upper panels show the distribution for light curves showing no finite source effects (eq. [2.63] with eq. [2.66]), whereas the lower panels show the distribution obtained from mass and source luminosity integration of equation (2.67), i.e., for light curves affected by finite source effects.

The black areas indicate the event parameter space, which is not available to source stars once their real sizes are taken into account: as finite source effects mainly occur at large amplifications, large Δ_F and small t_{FWHM} values are suppressed. Events in the point-source approximation, which fall into the black areas in the upper panels of Figures 2.14 and 2.15, end up with longer timescales and lower excess fluxes (*lower panels*) if the sources sizes are taken into account. The sharp cutoff at large flux excesses arises, since there is an upper limit in Δ_F depending on source luminosity and size (see equation (2.18)) and since the luminosity function of the stars has a steep cutoff at giant luminosities of $\mathscr{M}_R = -0.83\,\mathrm{mag}$ (bulge) and $\mathscr{M}_R = -2.23\,\mathrm{mag}$ (disk). The maxima with vertical contours for finite source effects in the lower panels come from shifting events for which the point-source approximation "just" fails at longer times scales (see eq. [2.16]). Light curves with finite source effects have (depending on their flux excesses) most likely FWHM timescales of about 0.01days, or 15 minutes, and the sources lensed with that timescales are MS stars. The secondary maxima around 1 day and flux excesses of 5×10^{-6} to $2 \times 10^{-5}\,\mathrm{Jy}$ for bulge-bulge, disk-bulge, and $0.1\,M_\odot$ halo-bulge lensing, and of about $10^{-3}\,\mathrm{Jy}$ for $1000\,M_\odot$ halo-bulge lensing, are due to lensing of PMS stars.

In general, the ratio of lensing events with and without finite source signatures is minute for $t_{\mathrm{FWHM}} \gtrsim 0.5\mathrm{d}$ and $\Delta F < 10^{-6}\mathrm{Jy}$, and raises to about an order of unity for bright lensing events with $\Delta F_0 \approx 1.6 \times 10^{-5}\,\mathrm{Jy}$ (corresponding to a magnitude of the excess flux of $m_R = 20.7\,\mathrm{mag}$) for bulge-bulge-lensing and $\Delta F_0 \approx 5 \times 10^{-5}$ ($m_R = 19.5\,\mathrm{mag}$) for halo-bulge lensing with $0.1\,M_\odot$ lenses. We compare the first column, bulge-bulge lensing, with results for the same lens-source configuration in Figure 2.12, which had been obtained assuming the full validity of the point-source approximation. The ratio of these contours is shown in Figure 2.16. The parameter space of interest for current surveys are flux excesses $> 10^{-5}\,\mathrm{Jy}$ (excess magnitude of $m_R = 21.2$) and timescales between 1 and 200 days.

---

[19] Using $b = \left\{ \left[R_{\mathrm{E}} u \left(\frac{A^*_0 + 1}{2} \right) \right]^2 - v_{\mathrm{t}}{}^2 \left(\frac{t_{\mathrm{FWHM}}}{2} \right)^2 \right\}^{\frac{1}{2}}$ and its derivative $\left| \frac{db}{dt_{\mathrm{FWHM}}} \right| = v_{\mathrm{t}}{}^2 \left\{ \left[\frac{2R_{\mathrm{E}}}{t_{\mathrm{FWHM}}} u \left(\frac{A^*_0 + 1}{2} \right) \right]^2 - v_{\mathrm{t}}{}^2 \right\}^{-\frac{1}{2}}$ we obtain

$$\frac{d^6 \Gamma_{s,l}}{dx\,dy\,dt_{\mathrm{FWHM}}\,d\Delta_F\,dM\,d\mathscr{M}} = \int\limits_0^\infty n_s(x, y, D_{\mathrm{os}}) 2\,\tilde{\Phi}_s(\mathscr{M})\,\xi(M) \left| \frac{dD_{\mathrm{ol}}}{d\Delta_F} \right| \rho(D_{\mathrm{ol}}) \int\limits_{v_{\mathrm{t,min}}}^{v_{\mathrm{t,max}}} p_{v_{\mathrm{t}}} v_{\mathrm{t}} \left| \frac{db}{dt_{\mathrm{FWHM}}} \right| dv_{\mathrm{t}}\,dD_{\mathrm{os}}$$

with $v_{\mathrm{t,min}} := \frac{2R_{\mathrm{E}}}{t_{\mathrm{FWHM}}} \sqrt{u \left(\frac{A^*_0 + 1}{2} \right)^2 - u_0^{*2}} \approx \frac{\sqrt{3} R_* D_{\mathrm{ol}}(\Delta_F, D_{\mathrm{os}})}{t_{\mathrm{FWHM}} D_{\mathrm{os}}}$ and $v_{\mathrm{t,max}} := \frac{2R_{\mathrm{E}}}{t_{\mathrm{FWHM}}} u \left(\frac{A^*_0 + 1}{2} \right) \approx \frac{2R_* D_{\mathrm{ol}}}{t_{\mathrm{FWHM}} D_{\mathrm{os}}}$.
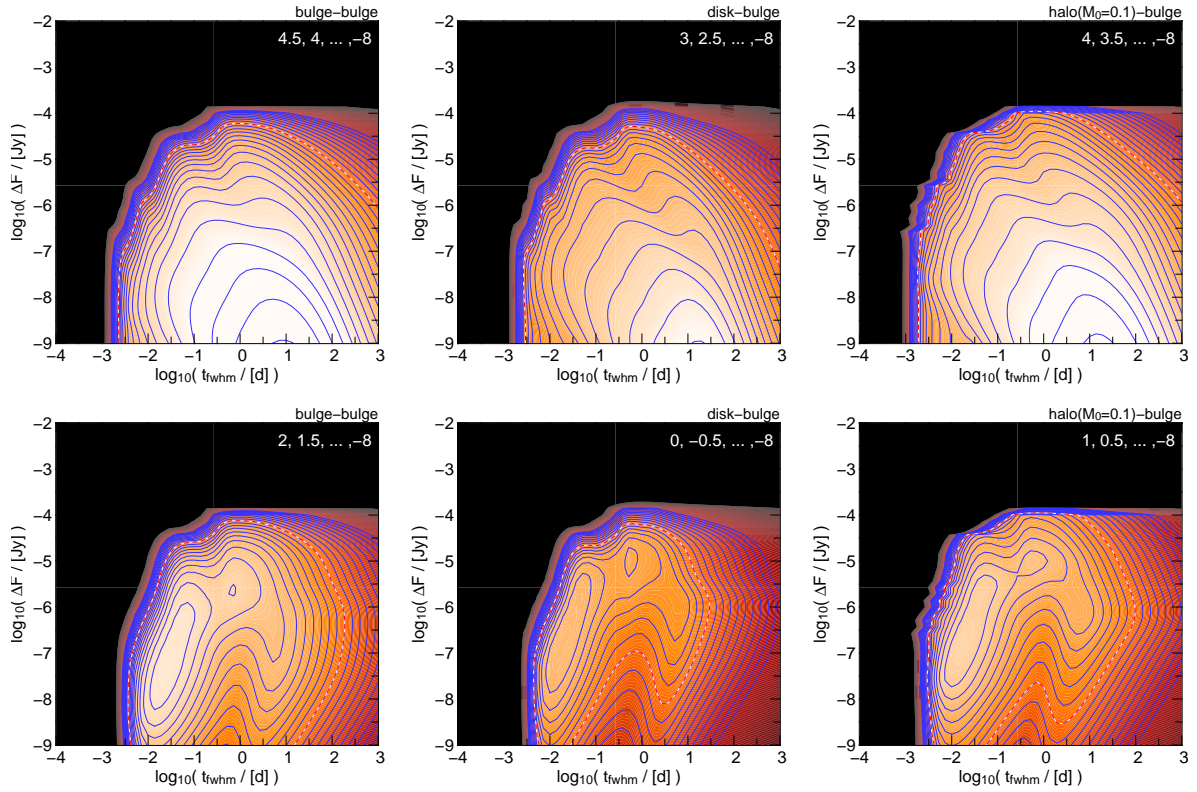
Figure 2.14: $d^2\Gamma/(d\log t_{\mathrm{FWHM}}\, d\log\Delta_F)$ [$\mathrm{arcmin}^{-2}\,\mathrm{y}^{-1}$] at $(x,y) = (1',0')$ in the $\log(\Delta_F)$-$\log(t_{\mathrm{FWHM}})$ plane, for bulge-bulge (*left*), disk-bulge (*middle*), and halo-bulge (*right*) lensing with $0.1\,M_\odot$ MA-CHOs (columns 1-3). The upper panels show the distribution for light curves not affected by the finite source sizes. The contours have been obtained from inserting eq. (2.63) into eq. (2.66) and carrying out the mass and source luminosity integral. The lower panels show the distribution for light curves with finite source signatures (mass and source star luminosity integral of eq. (2.67). The contour levels can be read off from the inserts in each diagram. The dashed line marks the $10^{-3}\,\mathrm{arcmin}^{-2}\,\mathrm{y}^{-1}$ level, areas with brighter colors correspond to higher contour values. Taking into account the finite source sizes implies an upper limit for Δ_F and a lower limit for t_{FWHM} for all light curves, i.e., for light curves with and with out finite source signatures (see text). For the source-lens configurations shown here there are no lensing eventslight curves with excess fluxes $\Delta_F > 5 \times 10^{-4}\,\mathrm{Jy}$. The results shown here have been obtained by taking into account the source sizes of lensed stars.

One can see that the true event rate can differ strongly from that for the point-source approximation depending on the flux excess limit of the survey. The brightest events are preferentially suppressed. This means that taking into account the source sizes is essential for predicting the correct number of lensing events.

Furthermore, one has to be aware that a fair fraction of the brightest lensing events show finite source signatures in their light curves and might be missed when using event filters with a classical lensing event shape in a stringent way. For the detection of finite-source events or even of binary lensing events less stringent thresholds or modified filters are needed, which, however, enhance the risk of a mismatch with variable source detections.
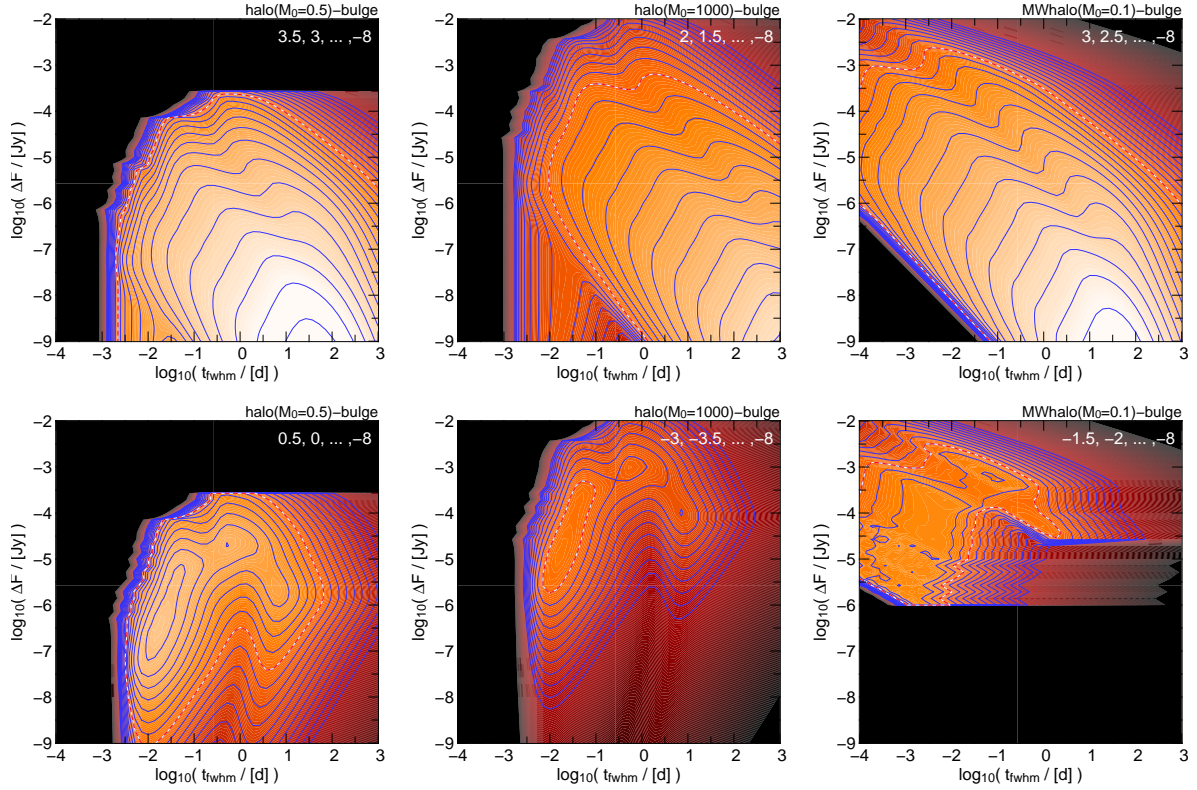
Figure 2.15: Same as Fig. 2.14 for halo-bulge lensing with larger MACHO masses ($0.5\,M_\odot$ and $1000\,M_\odot$ MACHOs in the first and second column) and for Milky Way halo - M31 bulge lensing (for $0.1\,M_\odot$ MACHOs in the third column) As before, the dashed line marks the $10^{-3}\,\mathrm{arcmin}^{-2}\,\mathrm{y}^{-1}$ level in each diagram, and areas with brighter colors correspond to contour higher values. The results shown here have been obtained by taking into account the source sizes of lensed stars.

Finally, Figure 2.15 compares halos with different MACHO masses in its first and second row. An increase in MACHO mass dramatically reduces the event rate and increases the event timescales. This explains the shift in the contours toward longer timescales (compare the change of the A_0-t_{FWHM} contours in Fig. 2.11) and the decrease in the contour levels. For larger MACHO masses, Einstein radii do increase, and one expects finite source effects to become less important: the largest possible flux excess $\Delta_{F,\mathrm{max}}$ for the lensing events indeed increases; the size of the shift is as expected, since the maximum flux excess is proportional to the square root of the MACHO mass according to equation (2.11). The contours in the last row of Figure 2.15 show MW-halo lensing with $0.1\,M_\odot$ MACHOs. Finite source effects are unimportant. Figures 2.14 and 2.15 make it obvious that lensing events above the maximum flux excess predicted for self-lensing would be a clear hint for either massive MACHOs in M31 or MACHOs with unconstrained masses in the Milky Way.

Figure 2.17 shows the distribution for bulge-bulge lensing splits in color space. The selected color intervals are $0.0 < R - I < 0.5$, $0.5 < R - I < 1.0$, and $1.5 < R - I < 2.0$. In the bluest color interval (*first column*) we find MS stars close to the MS turnoff as well as SGB, red clump and some RGB stars. The medium red sample contains MS, RGB. and AGB stars, and the reddest sample (*last row*) contains stars in the RGB and AGB phase and no MS stars. As expected, the timescale of the most likely finite
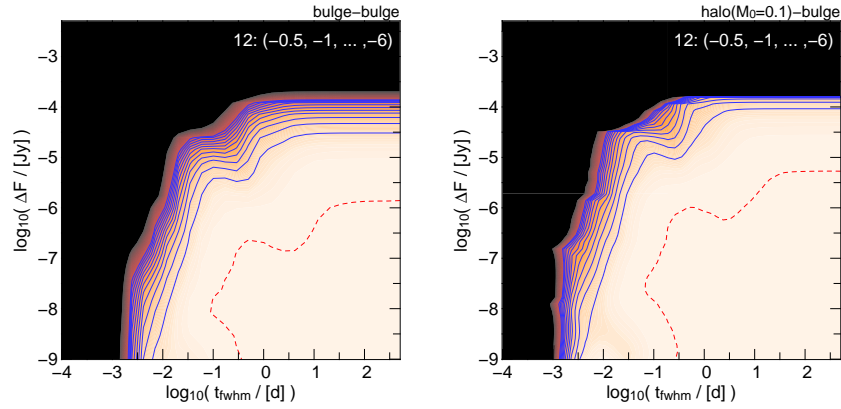
Figure 2.16: Ratio of the event rate distribution for extended sources counting events not showing finite source signatures (equation (2.66) and Figure 2.14) to the event rate assuming pure point sources (equation (2.63) and Figure 2.12), as a function of flux excess and timescale of the events: $\left[d^2\Gamma/(d\log t_{\mathrm{FWHM}}\, d\log\Delta_F)\right]_{\mathrm{finite\ sources}} \Big/ \left[d^2\Gamma/(d\log t_{\mathrm{FWHM}}\, d\log\Delta_F)\right]_{\mathrm{point\ sources}}$ for bulge-bulge (*left*) and $0.1\,M_\odot$ halo-bulge (*right*) lensing at $(x,y) = (1',0')$ in the $\log(\Delta_F)$-$\log(t_{\mathrm{FWHM}})$ plane. The dashed red line marks a ratio of 0.999. The finite source sizes cause a strong suppression of the brightest lensing events relative to the point-source predictions.

source lensing events changes with color: for the bluest color interval MS stars are responsible for the most likely finite source signature events and the event timescales are very short. The secondary maximum is caused by red clump and SGB stars, which are brighter, need less magnification and therefore have longer event timescales. The color interval of $0.5 < R-I < 1.0$ contains the central part of the MS, and RGB and AGB stars. The MS stars are fainter (in R) and have smaller radii than those in the blue sample, and therefore, the maximally probable event caused by the MS stars is at lower flux excess and timescale than that for the bluer sample. The PMS stars are brighter (which enhances the possibility of longer timescale events) and have larger radii (which leads to stronger peak-flux depression by finite source sizes) than in the bluer sample, and therefore, the events have similar brightness but take longer on average. The reddest color interval, $1.5 < R-I < 2.0$ contains the reddest PMS stars and no MS stars. These PMS stars are fainter (in R) and have larger radii than those contained in the $0.5 < R-I < 1.0$ sample, and therefore suffer most strongly from finite source effects causing events with even longer timescales than for the bluer PMS stars.
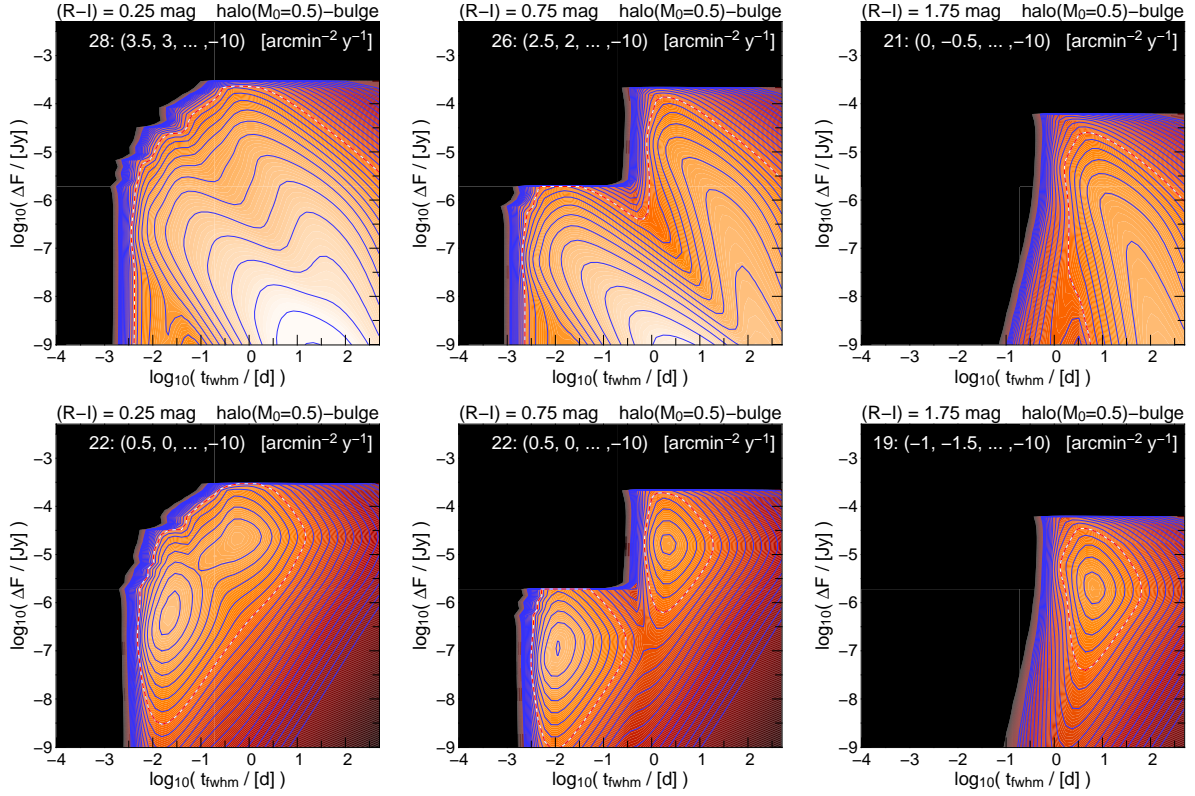
Figure 2.17: Distribution $d^2\Gamma/(d\log t_{\mathrm{FWHM}}\, d\log\Delta_F)$ $[\mathrm{arcmin}^{-2}\,\mathrm{y}^{-1}]$ for $0.5\,M_\odot$ halo-bulge lensing at $(x,y) = (1,0)\,\mathrm{arcmin}$ in the $\log(\Delta_F)$-$\log(t_{\mathrm{FWHM}})$ plane. We show the distribution for bulge sources within different color intervals, $(R-I) \in [0,0.5]\,\mathrm{mag}$ (first column), $(R-I) \in [0.5,1.0]\,\mathrm{mag}$ (second column), and $(R-I) \in [1.5,2.0]\,\mathrm{mag}$ (third column). The upper panels show the distributions for light curves showing no finite source effects, whereas the middle panels show the distributions for light curves with finite source signatures. The lower panels show the sum of both distributions. The contour levels are shown as inserts in each diagram. The dashed line marks the $10^{-3}\,\mathrm{arcmin}^{-2}\,\mathrm{y}^{-1}$ level in each diagram, brighter areas correspond to higher values. See text for more details.

2.8   Application to Experiments: Total Event Rates and Luminosity Function of Lensed Stars

We now apply our results from §§ 2.6 and 2.7 to difference imaging surveys. The goal of this section is to predict realistic event rates that take into account observational constraints (like timescales of events and the signal-to-noise ratios of the light curves, e.g., at maximum). These event rates can be taken for survey preparations or for a first-order comparison of survey results with theoretical models. Exact survey predictions and quantitative comparisons with models can be obtained with numerical simulations of the survey efficiency.

2.8.1   "Peak-Threshold" for Event Detection

In order to identify a variable object at position (x,y), its excess flux Δ_F has to exceed the rms flux $\sigma_F(x,y)$ by a certain factor Q:

$$\Delta_F^{\min}(x,y) = Q\sigma_F(x,y). \tag{2.68}$$

The parameter Q characterizes the significance of the amplitude of a lensing event, but not of the event itself, since that also depends on the timescale (and the sampling) of the event. We will call events characterized by the signal-to-noise ratio at maximum light "peak-threshold-events" in the following (Baltz & Silk, 2000). Considering only the maximum flux excess of an event (and not its timescale) of course can lead to an over-prediction of lensing events, since events might be too fast to be detected. In addition, long timescale events with low excess flux can have many data points with low significance for the excess flux, which all together make a significant lensing candidate. The detectability of events therefore depends on both its amplitude (flux excess at maximum) and its timescale. This is the reason, why we derived the contribution to the event rate as a function of flux excess and FWHM timescale in § 2.7.

The flux excess threshold that a source with intrinsic flux $F_0(\mathcal{M}, D_{\mathrm{os}}, \mathrm{ext}_s)$ must achieve in order to be identified as an event can be translated to thresholds in maximum magnification and relative impact parameter using equations (2.1) and (2.7):

$$A_{\mathrm{T}}(x,y,F_0(\mathcal{M},D_{\mathrm{os}},\mathrm{ext}_s)) := \Delta_F^{\min}(x,y)\,F_0^{-1} + 1 \approx \Delta_F^{\min}(x,y)\,F_0^{-1}, \tag{2.69}$$

$$u_{\mathrm{T}}(x,y,F_0(\mathcal{M},D_{\mathrm{os}},\mathrm{ext}_s)) := \sqrt{\frac{2A_{\mathrm{T}}}{\sqrt{A_{\mathrm{T}}^2 - 1}} - 2} \approx \frac{1}{A_{\mathrm{T}}}; \tag{2.70}$$

in both cases we have also given the high-magnification approximations in the last step.

In contrast to the microlensing regime (where u_{T} is assumed to be constant), u_{T} depends on the local noise value via $\Delta_F^{\min}(x,y)$ and the luminosity $\mathcal{M}$ of the source star being lensed. In Figure 2.18 we show contours of the minimum magnification required to observe an event at a distance of $D_{\mathrm{os}} = 770\,\mathrm{kpc}$, source luminosity of $\mathcal{M}_R = 0\,\mathrm{mag}$ and a signal-to-noise threshold of $Q = 10$ for a survey like WeCAPP in the R band. Since the M31 surface brightness and thus also the rms photon noise increases toward the center, magnifications of 50 or larger are needed in the central part. The M31

Figure 2.18: Contours show the minimum magnifications A_T that stars with $\mathcal{M}_R = 0\,\text{mag}$ at a distance of $D_{os} = 770\,\text{kpc}$ need to exceed the M31 rms flux by a factor of $Q = \left(\frac{S}{N}\right) = 10$ in the R band, for an experiment (with respect to, e.g., pixel size and seeing) like WeCAPP. The contour levels are $A_T = 17, 18, ..., 32$. The dashed line marks the $A_T = 25$ level; the square shows the field observed by WeCAPP given in the intrinsic M31 coordinate system (see Fig. 2.7).

rms photon noise and rms flux within a PSF in the R band had been estimated using equations (2.72) and (2.73) below.

To obtain an upper limit for the event rate, we assume that all events with flux excesses above the peak-threshold can be identified, irrespective of their timescales. In previous event rate estimates the t_{FWHM} timescales have only been considered correctly in Monte-Carlo simulations. Ignoring the event timescales in analytical estimates the event rate predictions are much more alike the upper limit we present here (eq. [2.71]). In this case one can simply use the transformation from minimum flux excess at maximum magnification to the threshold relative impact parameter u_T in equations (2.69) and (2.70) and integrate equation (2.33) over mass, lens distance, and relative velocities, multiplying it with the relative impact parameter threshold $u_T(x, y, F_0(\mathcal{M}, D_{os}, \text{ext}_s))$ and the number density of sources with brightness $\mathcal{M}$, $n_s(x, y, D_{os}) \tilde{\Phi}_s(\mathcal{M})$, and finally integrate along the line-of-sight and source luminosity, ($\S$ 2.5.2):

$$
\begin{aligned}
\frac{d^2\Gamma_{s,l}}{dx\,dy} &= \int_0^\infty \int_0^\infty n_s\, \tilde{\Phi}_s(\mathcal{M}) \int_0^\infty \int_0^{D_{os}} \int_0^\infty \int_0^{u_T(x,y,F_0(\mathcal{M},D_{os},\text{ext}_s))R_E} \frac{d^4\Gamma}{dD_{ol}\,dM\,dv_t\,db}\,db\,dv_t\,dM\,dD_{ol}\,d\mathcal{M}\,dD_{os} \\
&= \int_0^\infty \int_0^\infty n_s(x,y,D_{os})\, \tilde{\Phi}_s(\mathcal{M})\, u_T(x,y,F_0(\mathcal{M},D_{os},\text{ext}_s))\, \Gamma_{1,l}(D_{os})\,d\mathcal{M}\,dD_{os}.
\end{aligned}
\tag{2.71}
$$

In this equation, the subscript "s" indicates the different stellar populations (bulge, disc) and their sum yields the upper limit for the total event rate. This upper limit for the event rate can therefore be also obtained as a product of the single-star event rate $\Gamma_{1,l}$ (equation (2.49)), [using $u_T(x, y, F_0(\mathcal{M}, D_{os}, \text{ext}_s))$] and the number density of sources with luminosity $\mathcal{M}$ on the line of sight. Equation (2.71) is similar to the equations of Han (1996, eq. (2.5)) and Han & Gould (1996a, eq.

(2.2.1)).[20]

Up to now we have not discussed the value of $\sigma_F(x,y)$, i.e., the value of the rms flux that appears in the equations for the detection thresholds. This value can in principle be taken from the error propagation in the reduction process. Due to varying observing conditions (seeing, exposure time of the co-added images per night), the errors can differ from day to day by a factor of up to 10; to obtain predictions for the most typical situation, one therefore should use the median error at each image position of a survey to predict the rms flux $\sigma_F(x,y)$.

Riffeser et al. (2001) showed that using our reduction pipeline (that propagates true errors through all reduction steps) errors in the light curves are dominated by the photon-noise contribution of the background light. Therefore the typical error can be estimated from the surface brightness profile $\mathrm{SB}(x,y)$ of M31 and the typical, i.e., median, observing conditions of the survey. Using analytically predicted rms-values, one can study the impact of the observing conditions on event rates and optimize survey strategies.

To measure the variability of objects one has to perform (psf-)photometry defining the angular area of the psf $\Omega_{\mathrm{psf}} := \pi\,\theta_{\mathrm{psf}}^2/\ln 4$ and the FWHM of the psf θ_{psf}. For a given experimental setup the rms photon noise $\sigma_{\mathrm{photon}}(x,y)$ within an area $\Omega_{\mathrm{psf}}\,[\mathrm{arcsec}^2]$ at a position (x,y) is

$$\sigma_{\mathrm{photon}}(x,y) := \left[\left(10^{-0.4(\mathrm{SB}(x,y)+\kappa\mathrm{AM})} + 10^{-0.4 m_{\mathrm{sky}}} \right) 10^{-0.4(-\mathrm{ZP})}\, t_{\mathrm{exp}}\, \Omega_{\mathrm{psf}} \right]^{1/2}, \qquad (2.72)$$

where $m_{\mathrm{sky}}\,[\mathrm{mag\,arcsec^{-2}}]$ is the sky surface brightness, t_{exp} is the exposure time in seconds, AM is the air mass of the observation, ZP is the photometric zero point of the telescope camera configuration in photons per second and κ is the atmospheric extinction for the observing site.[21]

The rms photon noise can be translated to the rms flux (in Jy) using the flux of Vega, $\mathscr{F}_{\mathrm{Vega}}$, and its magnitude $m_{\mathrm{Vega}} = 0$:

$$
\begin{aligned}
\sigma_F(x,y) &:= \frac{\mathscr{F}_{\mathrm{Vega}}}{t_{\mathrm{exp}}\, 10^{-0.4(m_{\mathrm{Vega}}+\kappa\mathrm{AM}-\mathrm{ZP})}}\, \sigma_{\mathrm{photon}} \\
&= \mathscr{F}_{\mathrm{Vega}} \left[\left(10^{-0.4(\mathrm{SB}(x,y)+\kappa\mathrm{AM})} + 10^{-0.4 m_{\mathrm{sky}}} \right) 10^{0.8\,\kappa\mathrm{AM}}\, 10^{-0.4\mathrm{ZP}}\, \frac{\Omega_{\mathrm{psf}}}{t_{\mathrm{exp}}} \right]^{1/2}.
\end{aligned}
\qquad (2.73)
$$

The last equation shows that the rms flux within an aperture is proportional to $t_{\mathrm{exp}}^{-1/2}$, making the signal-to-noise Q proportional to $t_{\mathrm{exp}}^{1/2}$, as expected for background noise-limited photometry of point-like objects.

The extincted surface brightness profile $\mathrm{SB}(x,y)$ in Eqs. 2.72 and 2.73 can be taken either from very high signal-to-noise measurements of M31 or from analytical models that are constructed to match the observed SFB-profile and dynamics of M31. In the latter case, the extincted surface brightness $\mathrm{SB}(x,y)$-model combines the luminous matter density $\rho_s(x,y,D_{\mathrm{os}})$ with the mass-to-light ratio for each source components (s=bulge,disk) and accounts for Galactic and intrinsic extinction $\mathrm{ext}_s(x,y,D_{\mathrm{os}})$ along the line-of-sight:

$$\mathrm{SB}(x,y) = -2.5\log\left(\mathscr{F}_{\mathrm{Vega}}^{-1} \sum_s \int_0^\infty 10^{-0.4\,\mathrm{ext}_s(x,y,D_{\mathrm{os}})}\, \frac{\rho_s(x,y,D_{\mathrm{os}})}{\left(\frac{M}{L}\right)_s \frac{M_\odot}{\mathscr{F}_\odot}} \left(\frac{10\mathrm{pc}}{D_{\mathrm{os}}} \right)^2 \left(\frac{2\pi}{360\times3600} \right)^2 D_{\mathrm{os}}^2\, dD_{\mathrm{os}} \right), \quad (2.74)$$

where the units are $\mathrm{mag\,arcsec^{-2}}$.

---

[20] With $\beta_{\max}(F_{0,i}) \equiv u_{\mathrm{T}}$, $\Gamma_0 \equiv \Gamma_{1,l}(D_{\mathrm{os}})$, $\frac{\Sigma}{\sum_i \phi(F_{0,i})\,F_{0,i}} \equiv \int_0^\infty n_s\, dD_{\mathrm{os}}$.

[21] We have neglected readout noise of the detector because it is negligible compared to the photon noise.

2.8.2 "Event-Threshold" for Event Detection

Gould & Han (Gould, 1996b; Han, 1996; Han & Gould, 1996a) introduced an "event threshold", where the detectability of events depends on the total excess light of the light curves. They obtained an implicit equation for the threshold u_T of the relative impact parameter,

$$\frac{\zeta(u_T)}{u_T} = \frac{t_{\text{cyc}}\,\sigma_F(x,y)^2}{\overline{t_E}(x,y,D_{\text{os}})\,\pi F_0{}^2} Q_{\text{event}}{}^2, \tag{2.75}$$

where $\sigma_F(x,y)$ is the rms flux at that position and $\overline{t_E}(x,y,D_{\text{os}})$ is the mean Einstein time of the events (equation (2.54)); ζ is defined by $\zeta(u_0) := \frac{\int [A(t)-1]^2\,dt}{\int [(t/t_E)^2+u_0{}^2]^{-1}\,dt}$, $F_0(\mathcal{M},D_{\text{os}},\text{ext}_s)$ is the unlensed source flux and t_{cyc} is the (equidistant) difference between observations.

This equation assumes equidistant sampling of the light curves and is therefore most readily applied to space-based experiments. In addition, it takes into account the mean Einstein timescale of events only, although the relative impact parameter threshold depends on the individual timescale of the event. For realistic event rate estimates, however, one has to to take into account the timescale distributions, as well.

One can in fact obtain an analog relation for flux excess Δ_F and t_{FWHM} timescale of the events (i.e., the actual observables),

$$\Delta_F^{\min 2}\,\tilde{\zeta}\left(\frac{F_0}{\Delta_F^{\min}},t_{\text{FWHM}}\right) = \frac{\sqrt{12}\,t_{\text{cyc}}\,\sigma_F(x,y)^2}{\pi\,t_{\text{FWHM}}} Q_{\text{event}}{}^2, \tag{2.76}$$

with $\tilde{\zeta}(A_0-1,t_{\text{FWHM}}) := \frac{\int [A(t)-1]^2\,dt}{\int (A_0-1)[12(t/t_{\text{FWHM}})^2+1]^{-1}\,dt}$. Equation (2.76) can be numerically inverted to obtain the peak flux threshold $\Delta_F^{\min}(t_{\text{FWHM}},x,y,\mathcal{M})$ as a function of the event timescale. Therefore, it is obvious that the peak threshold and event threshold criteria are related assuming equidistant sampling and that the event threshold criterion is a special case of the peak threshold plus a t_{FWHM} threshold criterion, which is evaluated in equation (2.77) (see § 2.8.3).[22]

2.8.3 Total Event Rate with Excess Flux Threshold $\Delta_F^{\min}$ and Timescale $t_{\text{FWHM}}^{\min}$ Threshold

The upper limit derived in § 2.8.1 still includes numerous events that cannot be detected in finite time resolution experiments. At this point, where not only must the flux excess (maximum magnification or relative impact parameter) of the event be considered, but also the timescale of the event, the transformation of the event rate from the "theoretical quantities" to the "observational quantities" in § 2.7 becomes most relevant. Using equation (2.63) we can simply integrate from the lower limits $\Delta_F^{\min}$ and $t_{\text{FWHM}}^{\min}$ to infinity (or any other value specified by the experiment):

$$\frac{d^2\Gamma_{l,s}}{dx\,dy} := \int\limits_{t_{\text{FWHM}}^{\min}(x,y)}^{\infty} \int\limits_{\Delta_F^{\min}(t_{\text{FWHM}},x,y)}^{\infty} \frac{d^4\Gamma_{s,l}}{dx\,dy\,dt_{\text{FWHM}}\,d\Delta_F}\,d\Delta_F\,dt_{\text{FWHM}} \tag{2.77}$$

---

[22] To be able to roughly compare the event rate predictions of Han & Gould (1996a), who used the event threshold criterion, we can assume $t_{\text{FWHM}}^{\min} \approx t_{\text{cyc}}$ and $\tilde{\zeta} \approx 1$ and obtain $Q \approx 12^{0.25}\pi^{-0.5}Q_{\text{event}} \approx 0.6\,Q_{\text{event}}$.

with

$$\frac{d^4\Gamma_{s,l}}{dx\,dy\,dt_{\text{FWHM}}\,d\Delta_F} := \int\int \frac{d^6\Gamma_{s,l}}{dx\,dy\,dt_{\text{FWHM}}\,d\Delta_F\,dM\,d\mathcal{M}}\,dM\,d\mathcal{M}.$$

The thresholds $t_{\text{FWHM}}^{\min}(x,y)$ and $\Delta_F^{\min}(t_{\text{FWHM}},x,y)$ (see eqs. [2.68] and [2.76]) are set by the experiment and the detection process.[23]

For the WeCAPP experiment (see Table 2.8.3) toward M31 it turned out that the efficiency can easily be evaluated using Monte-Carlo simulations. As in the WeCAPP experiment errors are propagated through all reduction steps (Riffeser et al., 2001); the final errors in the light curve $\sigma(x,y,t_i)$ include the full reduction procedure. For a simple set of detection limits, i.e., $\Delta_F^{\min} \sim \sigma$ and $t_{\text{FWHM}}^{\min} = \text{const}$, the efficiency $\varepsilon(x,y,t_{\text{FWHM}},\Delta_F)$ for a survey can easily be evaluated as a function of the directly observable parameters x, y, t_{FWHM}, and Δ_F (in contrast to the variables t_E and A_0). This and more sophisticated thresholds (as used in Alcock et al. (2001b)) and efficiency simulations for WeCAPP we will present in a forthcoming paper.

Using this efficiency we can generalize equation (2.77) to

$$\frac{d^2\Gamma_{l,s}}{dx\,dy} := \int\int \frac{d^4\Gamma_{s,l}}{dx\,dy\,dt_{\text{FWHM}}\,d\Delta_F}\,\varepsilon(x,y,\Delta_F,t_{\text{FWHM}})\,d\Delta_F\,dt_{\text{FWHM}}. \tag{2.78}$$

As the total event rate depends on the model parameters of the luminous and dark component, precise measurements of the event numbers and event rate's spatial variation can in principle constrain the source and lens densities $[\rho_l(x,y,D_{\text{ol}}),\,n_s(x,y,D_{\text{os}})]$, the lens mass functions $[\xi_l(M)]$, the distribution of the transversal velocities $[p_{v_t}(v_t,v_0(x,y,D_{\text{ol}},D_{\text{os}}))]$, the luminosity function of the sources $[\tilde{\Phi}_s(\mathcal{M})$ or $p_{\text{cmd}_s}(\mathcal{M},\mathcal{C})]$, and finally the MACHO fraction in the halo. There are, of course other valuable parameters, like event duration, flux excess distribution, color of the lensed stars, and finite source effects, which make the lensing analysis much more powerful than the pure counting of events.

Table 2.2 summarizes the event rate predictions for the WeCAPP experiment toward the bulge of M31, using different realistic thresholds[24] for the signal-to-noise threshold necessary to derive "secure" events, and for $t_{\text{FWHM}}^{\min}$. These numbers do not take into account that events cannot be observed when M31 is not visible (one-third of the year), that in the remaining time some – in particular short-term events – escape detections because of observing gaps, and that some of the area is not accessible for identification of lensing events due to intrinsically variable objects. We calculated the predictions for signal-to-noise thresholds of $Q = 10$ and $Q = 6$; these thresholds correspond to flux excess thresholds of $6.2 \times 10^{-6}\,\text{Jy}$ (Q=10) and $3.7 \times 10^{-6}\,\text{Jy}$ (Q=6) in the edges and $2.4 \times 10^{-5}\,\text{Jy}$ (Q=10) and $1.5 \times 10^{-5}\,\text{Jy}$ (Q=6) $20''$ off center (outside saturation) of the WeCAPP field.[25] The $Q > 10$ events are events like those published in the past (e.g., WeCAPP-GL1 and WeCAPP-GL2 have values of $Q \approx 85$ and $Q \approx 16$), whereas $Q = 6$ should be more similar to the medium bright event candidates of MEGA. For the $Q = 10$ cases we have separated events that do not show finite source effects in the light curves ("without fs") from those which show finite source effects ("with fs"). Finite source events are relatively more important for high signal-to-noise, short timescale self-lensing events. In most current pixel-lensing surveys, light curves with finite source effects are not specially searched for and may preferentially get lost in the detection process, unless one allows for a less good fit for bright events.

---

[23] For completeness we can also introduce the color thresholds $\mathcal{C}^{\min}$ and $\mathcal{C}^{\max}$, which may also depend on the experiment and use the distribution derived in eq. (2.65).

[24] This is equivalent to an efficiency $\varepsilon(x,y,\Delta_F,t_{\text{FWHM}}) = \theta(t_{\text{FWHM}} - t_{\text{FWHM}}^{\min})\,\theta(\Delta_F - \Delta_F^{\min}(x,y))$ of the experiment.

[25] A value of $10^{-5}\,\text{Jy}$ correspond to an "excess magnitude" of 21.2 mag in the R band

For the $Q = 6$, $t_{\text{FWHM}} = 2$ days case we split the predictions into the near and far side of M31. Within our field, the predicted halo-bulge asymmetry is small, but the bulge-disk and halo-disk asymmetry are on a noticeable level. (Note that the disk-bulge lensing does show the reversed asymmetry). It has been pointed out in the past (An *et al.* (2004a)) that dust lanes in the M31 disk are an additional source of asymmetry; this is obvious if one considers the spatial distributions of variables found in pixel-lensing experiments (see An *et al.* (2004a), Ansari *et al.* (2004) and Fliri *et al.* (2006)). These can, however, be taken to quantitatively account for extinction, in addition to extinction maps. The values given in our table do not account for the small spatial dependence of extinction and thus place lower limits to the observed far-near asymmetry of the individual lens-source configuration.

The comparison for different timescale thresholds (cases III, IV, and V) shows that (except high mass halo lensing) the majority of events has timescales smaller than 10 days. A clustering of event candidates with short and long timescales as de Jong *et al.* (2004) observed for the MEGA analysis of the POINT AGAPE survey (they obtained 6 candidates with timescales smaller than 10 days and 8 candidates with timescales larger than 20 d) can be hardly explained for the WeCAPP field. This is because, even for supermassive MACHOs, one would expect roughly as many events between 2 and 20 days than above 20 days (compare case III and case V in Table 2.2). de Jong *et al.* (2004) argue that their long-term events arise in the outskirts of M31, where the photon noise is smaller, and could be understood from selection effects. This would still lack to explain the bimodality of timescales. At the moment it is not excluded that these long-term event candidates are still misidentified variable objects.[26] In the last line we add the analogous numbers for halo lensing resulting from Milky Way halo lenses of 0.1 $M_\odot$. The number of MACHO events caused by the MW MACHOs should be roughly one-third of that caused by M31 MACHOs.

Figure 2.19 shows the predictions for the spatial distribution of the lensing events for the WeCAPP survey, evaluated for the $Q = 10$ and $t_{\text{FWHM}} = 1$ day thresholds (column labeled "I" in Table 2.2). One can see that the event rate density becomes maximal close to the M31 center for bulge-bulge and halo-bulge lensing configurations. That seems counterintuitive to the results about the lensing optical depth and single-star event rate in Figures 2.7 and 2.8, where the maximum is attained on the M31 far side, significantly offset from the center. This difference is due to the density of source stars, which rises toward the center much more than the single-star event rate and the detectability of the events drops. As can also be seen in Table 2.2, a far to near side asymmetry (*lower and upper part in the figure*) is not present for bulge-bulge lensing, is modest for halo-bulge lensing, and is stronger for the disk-bulge lensing. This is because the disk effectively cuts the bulge in one part in front and the other behind the disk, and only the stars in the second part can contribute to disk-bulge lensing. The bulge-disk self-lensing shows the opposite far to near side asymmetry and attains its maximum event rate per area in the far side of the disk. The same is true for the halo-disk lensing (main maximum on far side of disk), which shows a secondary maximum close to the M31 center caused by the increase of the disk-star density. The disk-disk lensing event rate per area is symmetric with respect to the near and far side of the disk. The fact that the maximum for bulge-bulge and disk-disk lensing is not located exactly at the M31 center is caused by the increased photon noise combined with finite-source effects.

The total self-lensing (disk-bulge + bulge-disk + bulge-bulge + disk-disk) shows an asymmetry arising from the different luminosity functions and mass functions of the bulge and disk population which leads to different event characteristics for disk-bulge and bulge-disk lensing. Therefore, lens and

---

[26] See de Jong *et al.* (2006) for recent results.
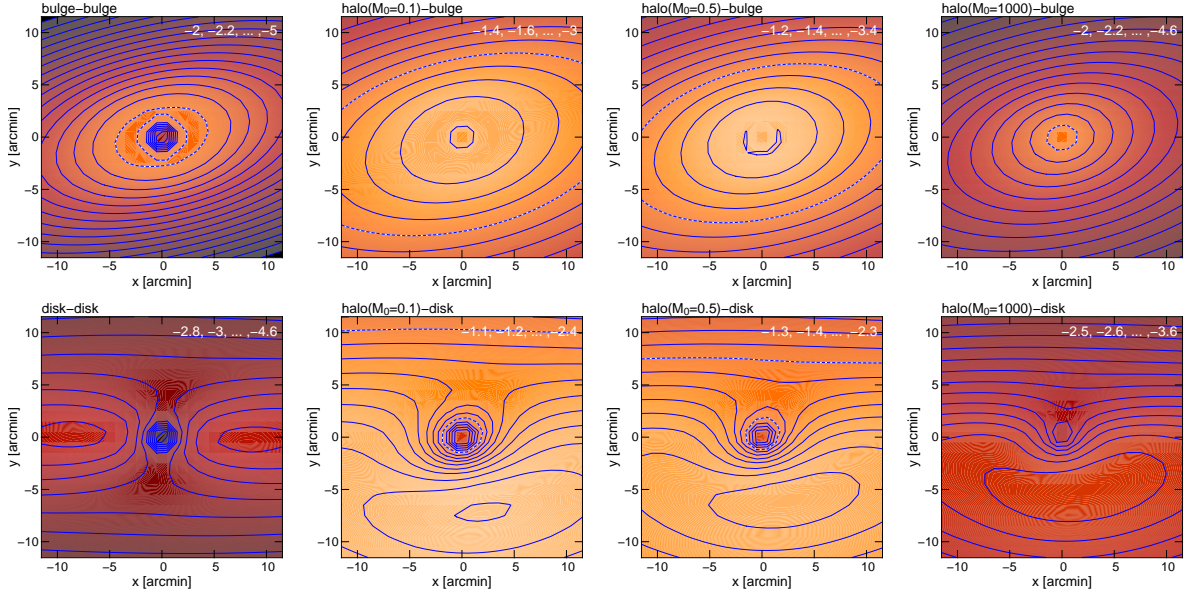
Figure 2.19: Event rate maps in logarithmic units (in units of events $yr^{-1} arcmin^{-2}$) for the WeCAPP survey for $Q = 10$ and $t_{FWHM}^{min} = 1\,d$ (column labeled "I" in Table 2.2). Coordinates are given in the intrinsic M31 coordinate system (see Figure 2.7). The contour levels are shown in inserts in the upper right corners of each diagram. The dashed line marks the $0.01\,ev\,y^{-1}\,arcmin^{-2}$ level in each diagram. The event rate decreases near the center of M31 due to higher noise combined with finite source effects. Note that the maximum lensing (maximum optical depth) region defined by Crotts (1992) and Tomaney & Crotts (1996) is predicted at about $1.5\,kpc$ ($7.5'$) from the nucleus for a simple halo model. For the calculations we have taken into account the finite stellar source sizes; the numbers shown, however, include only those among all events that do not show finite source signatures in their light curves, i.e., those which are usually searched for in lensing experiments.

source populations cannot easily be exchanged. The fact that the near side is closer to us – lensing strength and apparent magnitude of sources change by a few percent – than the far side of M31 plays a minor role for the asymmetry of self-lensing event rates.

The last figure (Fig. 2.20) in this section shows the total event rates $\Gamma_{l,s}(t_{FWHM}^{min}, Q) = \int \int \frac{d^2 \Gamma_{l,s}}{dx dy}\,dx\,dy$ in the WeCAPP field depending on the peak flux threshold and the timescale threshold of the survey. We have taken into account the finite source sizes but show only the rate for those events that do not show any finite source signature in their light curves.

For high signal-to-noise events (e.g., $Q = 20$), all configurations do show more or less flat contours in the t_{FWHM} direction for t_{FWHM} values between 0.1 and 1 days. This indicates that there are relatively few very high signal-to-noise events with timescales around 0.1 days compared to events with timescales of about 1 day. That this is true is confirmed by Figures 2.14 and 2.15, which show that the highest signal-to-noise and thus highest flux excess events occur with timescales between 0.6 and a few days and that events with timescales of about 0.1 days are significantly fainter. Only for smaller flux excesses, the events with timescales of 0.1 days can be as common as events with timescales of a couple of days. This implies that if one can measure only lensing events that have a (S/N) ratio of $Q \geq 10$ in the WeCAPP setup, one cannot greatly increase the number of observed events by increas-
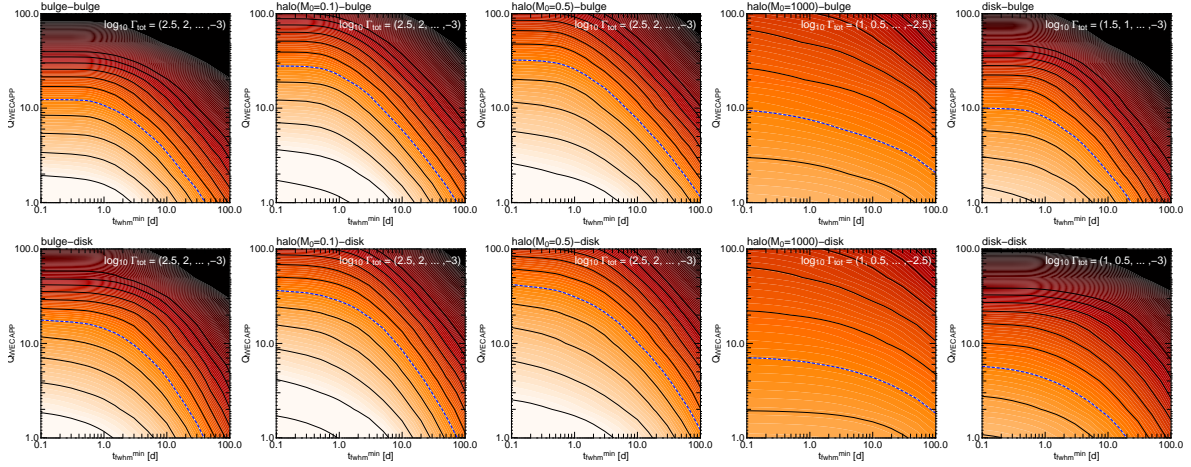
Figure 2.20: Contours of the logarithm of the lensing event rate per year within the $17.2' \times 17.2'$ WeCAPP field as a function of the signal-to-noise threshold Q for the peak-flux excess and as a function of the timescale threshold of the events. For these numbers, eq. (2.77) was integrated over the WeCAPP field, and the noise was estimated for the WeCAPP survey (characterized by Table 2.8.3). We show results for different lens-source configurations, from left to right: bulge-bulge self-lensing, halo-bulge lensing with $0.1\,M_\odot$ lenses, halo-bulge lensing with $0.5\,M_\odot$ lenses, and disk-bulge self-lensing. The blue dashed line marks the 1 event per year level. For the calculations we have taken into account the finite stellar source sizes; the numbers shown, however, include only those among all events that do not show finite source signatures in their light curves, i.e., those which are usually searched for in lensing experiments. For signal-to-noise ratios of $Q > 10$, the rates for events with finite source effects can be of the same order as the rates for events with point-source light curves. For lower signal-to-noise ratios, events with finite source effects become much less important.

ing the sampling (the largest increase for sampling below 1 day would occur for halo-disk lensing). The detectability of events with timescales of hours can therefore be increased effectively only (in the central M31 field), if the noise level of the observations is lowered. It can also be seen in all panels of Figure 2.20 that one expects the number of events to decrease strongly for t_{FWHM}-thresholds larger than several days. The quantitative differences in the different lensing configurations in the subpanels of Figure 2.20 can be easily understood (by combining the dependence of the event rate on event timescale and magnification with the luminosity function of source stars, and accounting for the difference in the importance of finite source effects) and are discussed for the $0.1\,M_\odot$ MACHO bulge and the $0.5\,M_\odot$ MACHO bulge lensing case. Table 2.2 already suggests that these two lensing configurations are very similar for the event numbers that do not show finite source signatures (the $0.1\,M_\odot$ MACHOs do cause more high signal-to-noise finite source events). One expects that the increase of the MACHO mass decreases the total event rate per line-of-sight (fewer lenses) but also increases the events' timescales. On the basis of the event rate per timescale and event magnification (Figure 2.11) one would therefore expect longer timescales but fewer events for the stellar mass MACHO case. This simple picture is altered by the finite source effects, which limit the maximal flux excess and thus signal-to-noise of an event. The question, whether one expects more events for brown dwarf or stellar mass MACHOs depends therefore on the combination of signal-to-noise threshold and timescale threshold.

The predicted event rates rise strongly for lower Q thresholds. This means that if one lowers the
(S/N) threshold – or equivalently increases the signal or decreases the noise level by changing the
experiment – one could dramatically increase the event rates. This can be achieved by an increase
of telescope area and integration time, but much better with a decrease of the PSF of the experiment.
This makes the space experiments most promising. In addition, the comparison of the subpanels in
Figure 2.20 shows that the bulge-bulge lensing rate will profit much stronger from a decrease of the
noise than any other lensing configuration.

Assume that the center of M31 is monitored with the ACS on 30 consecutive days, with three 6 minute
exposures in the F625W band and two 6 minute exposures in the F555W band, which would need one
orbit per day altogether (see more details in Table 2.8.3). Assume furthermore that the background
light has the level of the smoothed M31 SFB isophotes (in reality a fraction of the brightest stars
gets resolved lowering the background light in between the resolved objects). Using that background
level, we predict the event rates with timescales between 1 and 20 days for bulge-bulge self-lensing
and halo-bulge lensing in Table 2.3. If one assumes a halo fraction of about 25% then the halo-lensing
events do not contribute more than 10% relative to the bulge-bulge lensing rate.

Current measurements of extragalactic mass functions reach masses down to 0.6 solar masses (for the
LMC Gouliermis *et al.* (2005)). Microlensing allows a measurement of the low-mass end of the stellar
mass function, while not relying on the luminosity of those low-mass stars. The mass of these stars
becomes visible by their lensing effect on (in general) brighter stars. Therefore, M31 bulge-lensing
combined with space observations makes it possible to test an extragalactic mass function well below
$0.5 M_\odot$.

Parameter	WeCAPP	*HST* with ACS WFC
t_{exp} (s)	500	1000
l_{pixel} (arcsec)	0.5	0.049
Field of view (pixels)	2048×2048	4096×4096
Field of view (arcmin)	17.2×17.2	3.37×3.37
Filter	Johnson R	F625W
ZP (mag)	23.68	25.73 (De Marchi *et al.* (2004), Table 3)
Average sky	20.0	22.5
FWHM of the psf θ_{psf} (arcsec)	1.5	0.12 (Krist (2003), p. 13)
Ω_{psf} (arcsec^2)	5.1	0.033
AM	1.0	0
Atmospheric extinction κ_R	0.1	0
Δt (days)	200	30
$t_{\mathrm{FWHM}}^{\mathrm{min}}$ (days)	1	1
$t_{\mathrm{FWHM}}^{\mathrm{max}}$ (days)	200	20
inner saturation radius (arcsec)	20	0
CCD orientation angle (deg)	45	0

Table 2.1: Observational setups for the WeCAPP survey and a potential experiment using the ACS on
board of *HST*

	I	II	III		IV	V
Q	10	10	6		6	6
$t_{\mathrm{FWHM}}^{\min}$ [d]	1	2	2		10	20
			Near Side	Far Side		
b-b	1.2 + 1.9	0.57 + 0.68	1.4 + 0.98	1.4 + 0.99	0.16 + 0.046	0.026 + 0.0062
h0.1-b	8.2 + 5.4	4 + 1.7	6.3 + 1.6	7.1 + 1.9	0.92 + 0.071	0.16 + 0.0094
h0.5-b	7.4 + 2.7	4.4 + 1	5.5 + 0.72	6.3 + 0.82	1.8 + 0.051	0.47 + 0.0074
h1000-b	0.7 + 0.0013	0.61 + 0.0011	0.51 + 0.00051	0.59 + 0.00056	0.75 + 0.00025	0.6 + 5×10^{-5}
d-b	0.57 + 0.34	0.26 + 0.098	0.89 + 0.16	0.087 + 0.026	0.057 + 0.0029	0.0072 + 0.00031
h_{MW}0.1-b	3.9 + 0.0046	1.9 + 0.0019	2.7 + 0.001	2.7 + 0.001	0.47 + 4×10^{-5}	0.088 + 5×10^{-6}
h_{MW}0.5-b	2.4 + 0.0009	1.5 + 0.0002	1.8 + 0.0001	1.8 + 0.0001	0.76 + 2×10^{-6}	0.23 + 3×10^{-7}
b-d	2.3 + 1.6	1.4 + 0.77	0.43 + 0.22	3.8 + 1.3	0.43 + 0.049	0.082 + 0.0055
h0.1-d	11 + 4.3	6.6 + 2	4.9 + 0.72	12 + 2	2.1 + 0.1	0.5 + 0.014
h0.5-d	8.6 + 1.2	5.8 + 0.65	3.6 + 0.21	9.5 + 0.55	3.1 + 0.069	1 + 0.011
h1000-d	0.61 + 0.00015	0.56 + 0.00014	0.26 + 5×10^{-5}	0.7 + 9×10^{-5}	0.7 + 8×10^{-5}	0.55 + 2×10^{-5}
d-d	0.2 + 0.13	0.14 + 0.075	0.2 + 0.056	0.19 + 0.056	0.095 + 0.018	0.036 + 0.0055
h_{MW}0.1-d	3.1 + 0.0019	2 + 0.00049	2.2 + 0.00025	2.2 + 0.00024	0.95 + 6×10^{-6}	0.3 + 7×10^{-7}
h_{MW}0.5-d	1.9 + 0.00022	1.4 + 0.00013	1.4 + 7×10^{-5}	1.4 + 7×10^{-5}	0.97 + 4×10^{-6}	0.43 + 5×10^{-7}

Table 2.2: Total event rate $\Gamma_{s,l}$ $[\mathrm{y}^{-1}]$ for the WeCAPP experiment for self-lensing and halo-lensing: (d) disk; (b) bulge; (h0.1) halo consisting of 0.1 $M_\odot$ lenses; (h0.5) halo consisting of 0.5 $M_\odot$ lenses (h_{MW} for MW-halo); (h1000) halo consisting of 1000 $M_\odot$ lenses. The numbers give the event rate in events per year integrated over the observed field and applying the following peak-flux signal-to-noise thresholds: (I) $Q = 10$ and $t_{\mathrm{FWHM}}^{\min} = 1\,$day; (II) $Q = 10$ and $t_{\mathrm{FWHM}}^{\min} = 2\,$days; (III) $Q = 6$ and $t_{\mathrm{FWHM}}^{\min} = 2\,$days for the near and far side; (IV) $Q = 6$ and $t_{\mathrm{FWHM}}^{\min} = 10\,$days; (V) $Q = 6$ and $t_{\mathrm{FWHM}}^{\min} = 20\,$days. These (S/N)-limits (at the light curve peak) are more realistic than a flux threshold $\Delta_F^{\min}$, which is constant over the observed field, since the central region shows a strong gradient in the surface brightness and photon noise values. We have also separated events that do not show finite source effects in the light curves from those with finite source effects by a plus sign. Note that light curves with finite source effect signatures might be missed when using event filters with a classical lensing event shape in a stringent way. For the ($Q = 6$, $t_{\mathrm{FWHM}} = 2$) case we split the predictions in those for the near and far side of the M31 (disk and bulge). Within our field, the predicted halo-bulge asymmetry is small, but the bulge-disk and halo-disk asymmetries are on a noticeable level. The comparison for different timescale thresholds (columns labeled "III", "IV", and "V") shows that (except for high-mass halo lensing) the majority of events has timescales smaller than 10 days. A peak of events with timescales of 20 days or larger can only be understood with supermassive MACHOs or miss-identifications of variable objects. In the last line we add the analogous numbers for halo lensing resulting from Milky Way halo lenses of 0.1 $M_\odot$. The MACHO events caused by the MW MACHOs should be roughly one-third of that caused by M31 MACHOs.

Q	6	
$t_{\mathrm{FWHM}}^{\min}$ [d]	1	
	Without fs	With fs
b - b	1350	100
h0.1 - b	620	10

Table 2.3: Total event rates $\Gamma_{s,l}$ $[\mathrm{y}^{-1}]$ for a 30 day, 1-orbit-per day *HST* ACS experiment. The rates are shown for different lens-source configurations: (b) bulge; (h0.1) - halo consisting of 0.1 $M_\odot$ lenses. The numbers give the rate in events per year integrated over the whole ACS field and applying $Q = 6$, $t_{\mathrm{FWHM}}^{\min} = 1$ day and $t_{\mathrm{FWHM}}^{\max} = 20$ days thresholds. "Without fs" describes events, that show no finite source signatures in the light curve; "with fs" gives the number of light curves with finite source signatures.

2.8.4   The Luminosity Function Sensitivity

Whereas the probability for a star to be lensed does not depend on its luminosity, the probability that the event can be detected strongly depends on the luminosity of the source star. This implies that the luminosity function of the source stars of lensing events is biased toward high-luminosity stars. The selection probability of a star with luminosity $\mathcal{M}$, which we call "luminosity function sensitivity", is obtained with equation (2.63) as

$$\frac{1}{\tilde{\Phi}_s(\mathcal{M})}\frac{d^3\Gamma_{s,l}}{dx\,dy\,d\mathcal{M}} = \int\limits_{t_{\mathrm{FWHM}}^{\min}}^{\infty}\int\limits_{\Delta_F^{\min}}^{\infty}\frac{2}{t_{\mathrm{FWHM}}^3}\int\limits_0^{\infty}\xi_l\int\limits_0^{\infty}n_s\frac{\Psi}{F_0}\int\limits_0^{D_{\mathrm{os}}}\rho_l\,R_{\mathrm{E}}{}^3\,p_{v_t}\!\left(\frac{R_{\mathrm{E}}\Upsilon}{t_{\mathrm{FWHM}}},v_0\right)dD_{\mathrm{ol}}\,dD_{\mathrm{os}}\,dM\,d\Delta_F\,dt_{\mathrm{FWHM}},$$

$$(2.79)$$

with the parameters and relations used for $\tilde{\Phi}_s(\mathcal{M})$, $\xi_l(M)$, $n_s(x,y,D_{\mathrm{os}})$, $\rho_l(x,y,D_{\mathrm{ol}})$, $R_{\mathrm{E}}(D_{\mathrm{ol}},M,D_{\mathrm{os}})$, $F_0(\mathcal{M},D_{\mathrm{os}})$, $\Psi(A_0(F_0,\Delta_F))$, $\Upsilon(A_0(F_0,\Delta_F))$. The luminosity function sensitivity gives the event rate per area per source star luminosity bin, normalized by the luminosity function $\tilde{\Phi}_s(\mathcal{M})$. In Figure 2.21 we show results for the luminosity function sensitivity using equation (2.79) for several minimal detectable timescales $t_{\mathrm{FWHM}}^{\min}$ (0, 0.01, 0.1, 1, and 10 days) using the configuration of the WeCAPP and ACS experiments and the model of M31 presented in Chap. 3.

Figure 2.21 shows that the sensitivity strongly increases with decreasing timescale thresholds. Applying no t_{FWHM} threshold for the total event rate (equivalent to evaluating equation (2.71)) overestimates the luminosity sensitivity for faint MS stars. In consequence, the total event rate is overestimated as well. Accounting for the timescale thresholds for microlensing surveys (i.e., using equation (2.77) for the total event rate) suppresses the contribution of faint stars and yields a much more realistic estimate of the total event rate. In Figure 2.21 (*right*) we show the luminosity function of the sources for lensing events, which is obtained as the product of the luminosity function sensitivity and the luminosity function $\tilde{\Phi}_s(\mathcal{M})$. The results differ for an experiment like WeCAPP and an experiment with small PSF noise like the suggested ACS imaging campaign.

An experiment like WeCAPP induces a cutoff of $\mathcal{M}_R \approx 6\,\mathrm{mag}$ in the luminosity of the lensed stars, because one would need magnifications larger than the finite source size magnification limit to obtain an observable flux excess for source luminosities below that value. This cutoff is valid for all lens-source configurations within M31, with the exception of supermassive M31 MACHOs, and it does not hold for lensing by MW MACHOs. With an ACS experiment, the minimum measurable flux excess is much smaller than for WeCAPP, and therefore even the faintest MS stars can act as sources for detectable lensing events (no cutoff in the luminosity function of lensed stars). For events with timescales above 1 day, the luminosity function of lensed stars becomes almost flat for magnitudes brighter than $\mathcal{M}_R \approx 4\,\mathrm{mag}$ (*green curve*).
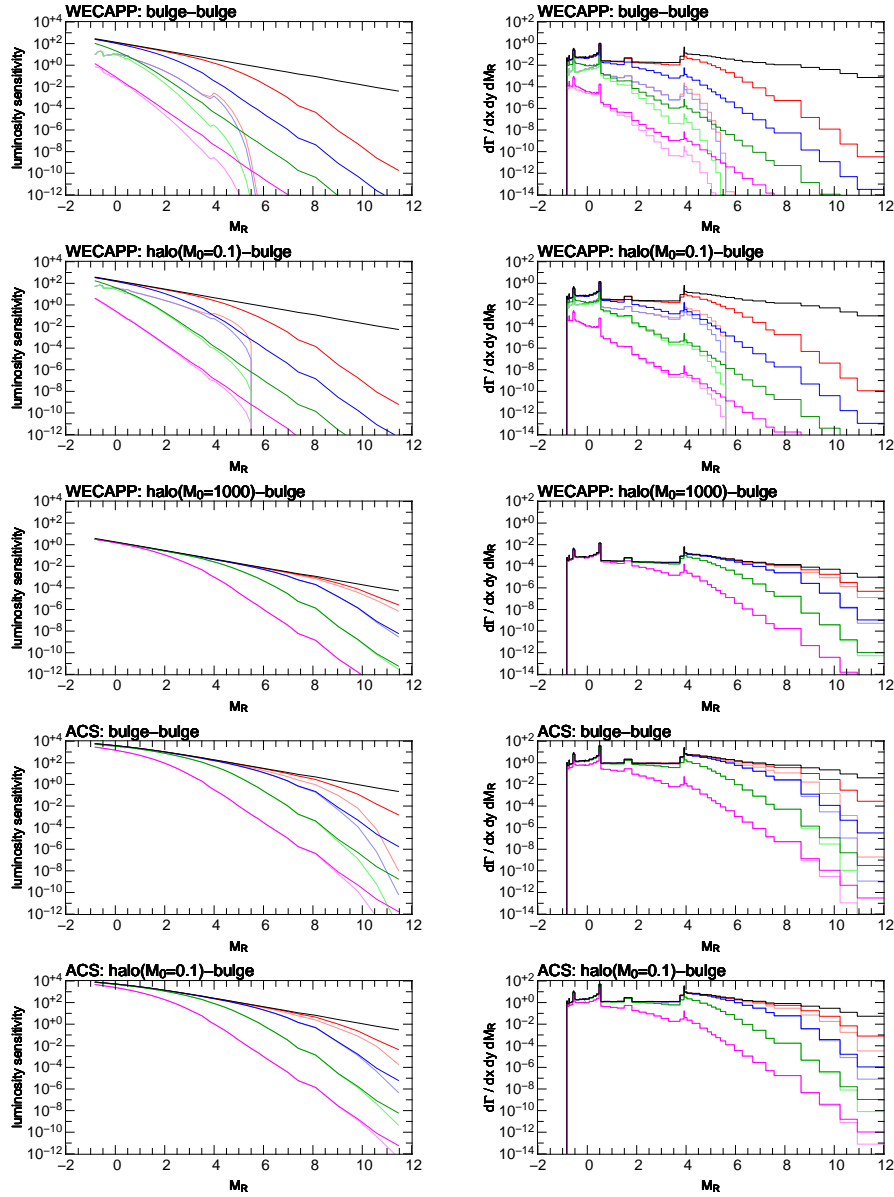
Figure 2.21: *Left panel:* Luminosity function sensitivity (eq. [2.79]) $[\mathrm{arcmin}^{-2}\,\mathrm{y}^{-1}]$ for bulge-bulge, $0.1\,M_\odot$ halo-bulge, $1000\,M_\odot$ halo-bulge lensing in the WeCAPP and ACS experiment (see Chap. 3) with $Q = 12$ at $(x,y) = (1,0)\,\mathrm{kpc}$ (corresponding $\Delta_F^{\min} = 1.7 \times 10^{-5}\,\mathrm{Jy}$ for WeCAPP and $\Delta_F^{\min} = 3 \times 10^{-7}\,\mathrm{Jy}$ for ACS) *Black line:* no t_{FWHM} threshold; *magenta line*: $t_{\mathrm{FWHM}}^{\min} = 10\,\mathrm{days}$; *green line*: $t_{\mathrm{FWHM}}^{\min} = 1\,\mathrm{day}$; *blue line*: $t_{\mathrm{FWHM}}^{\min} = 0.1\,\mathrm{day}$; *red line*: $t_{\mathrm{FWHM}}^{\min} = 0.01\,\mathrm{day}$. The curves for the dark colors have been obtained with the point-source approximation, the curves with the light colors account for the extended source sizes, which further suppresses the luminosity sensitivity (using D_{ol}^* instead of D_{os} as integration limit in eq. [2.79]) . Stars fainter than $\mathscr{M}_R = 5.5\,\mathrm{mag}$ cannot be lensed at all to an event with a signal-to-noise ratio Q larger than 10. *Right panel:* Luminosity function of the sources for lensing events $d^3\Gamma_{s,l}/(dx\,dy\,d\mathscr{M})$ $[\mathrm{arcmin}^{-2}\,\mathrm{y}^{-1}\,\mathrm{mag}^{-1}]$. For $t_{\mathrm{FWHM}}^{\min}$ thresholds of $1\,\mathrm{day}$ that are typical for current experiments the probability to have an MS star among the lensed stars is very low ($< 3 \times 10^{-6}$ for bulge-bulge lensing, $< 3 \times 10^{-5}$ for $0.1\,M_\odot$ halo-bulge lensing, < 0.0002 for $0.5\,M_\odot$ halo-bulge lensing, < 0.2 for $1000\,M_\odot$ halo-bulge lensing).

2.9 The Lens Mass Probability Distribution for Individual Lensing Events

The lens mass probability distribution is one central goal of the analysis of lensing events. We show how this function is extracted from the individual events, depending on whether t_E and A_0 (microlensing), or t_{FWHM} and Δ_F (pixel-lensing) can be measured.

2.9.1 The Lens Mass Probability Distribution, Obtained from the Observable t_E^{meas}

For completeness we recall in this section the classical microlensing formalism, where the intrinsic source flux F_0 is supposed to be known, to derive the mass probability distribution from direct measurements of t_E^{meas} and u_0^{meas}, or equivalently t_E^{meas} and A_0^{meas}.

Starting from the integrand in equation (2.51), without carrying out the mass integral and averaging over all source distances yields

$$\left\langle \frac{d^3\Gamma(M,t_E)}{dM\,dt_E\,du_0} \right\rangle_s = \int p_s \frac{2}{t_E{}^3} \xi(M) \int_0^{D_{os}} \rho(D_{ol})\, p_{v_t}\left(\frac{R_E}{t_E}\right) R_E{}^3\, dD_{ol}\, dD_{os}, \tag{2.80}$$

which can also be converted to

$$\left\langle \frac{d^3\Gamma(M,t_E,A_0)}{dM\,dt_E\,dA_0} \right\rangle_s = \int p_s \frac{du_0(A_0)}{dA_0} \frac{2}{t_E{}^3} \xi(M) \int_0^{D_{os}} \rho(D_{ol})\, p_{v_t}\left(\frac{R_E}{t_E}, D_{ol}\right) R_E{}^3\, dD_{ol}\, dD_{os}. \tag{2.81}$$

In the right-hand side of equation (2.81) the maximum magnification A_0 appears only as a pre-factor (see eq. [2.8]), and the right-hand side of equation (2.80) is independent of the relative impact parameter u_0. This implies that the magnification at maximum or equivalently the relative impact parameter does not enter the mass probability function of the lenses. This is expected, since these quantities depend on the lens-source trajectory but do not contain any information about the lens (unless the impact parameter b could measured by other means). The lens mass probability function thus solely depends on the measured Einstein timescale, and becomes

$$p(M;t_E^{meas}) \sim \left\langle \frac{d^3\Gamma(M,t_E)}{dM\,dt_E\,du_0} \right\rangle_s \Bigg|_{t_E^{meas}} = \int \left\langle \frac{d^3\Gamma(M,t_E)}{dM\,dt_E\,du_0} \right\rangle_s \delta(t_E - t_E^{meas})\, dt_E = \left\langle \frac{d^3\Gamma(M,t_E^{meas})}{dM\,dt_E\,du_0} \right\rangle_s, \tag{2.82}$$

if t_E can be measured without any error.

The measurement error of t_E can be accounted for by replacing the δ-function with the probability for the Einstein time t_E for a measured value of t_E^{meas}. For a Gaussian probability with width $\sigma_{t_E^{meas}}$ one obtains

$$\hat{p}(M;t_E^{meas},\sigma_{t_E^{meas}}) \sim \int \left\langle \frac{d^3\Gamma(t_E,M)}{dt_E\,du_0\,dM} \right\rangle_s g(t_E;t_E^{meas},\sigma_{t_E^{meas}})\, dt_E, \tag{2.83}$$

with

$$g(t;t^{meas},\sigma_{t^{meas}}) := \frac{1}{\sqrt{2}\sigma_{t^{meas}}} \exp\left(-\frac{(t-t^{meas})^2}{2\sigma_{t^{meas}}^2}\right).$$

Our result in equation (2.82) is proportional to the result of Jetzer & Massó (1994)[27] (see also Jetzer, 1994) but differs from the result of Dominik (1998). [28] The lens mass probability function has also been calculated by de Rujula *et al.* (1991) for events with measured maximum magnification A_0^{meas} and Einstein timescale $t_{\mathrm{E}}^{\mathrm{meas}}$. We could not match the result published by them with ours once we converted their notation to ours. [29]

2.9.2 The Lens Mass Probability Distribution, Obtained from the Observable $t_{\mathrm{FWHM}}^{\mathrm{meas}}$ and u_0^{meas}

Now we discuss the case in which the FWHM t_{FWHM} and the relative impact parameter u_0 are the available observables. Starting from the integrand in equation (2.59), without carrying out the mass integral and averaging over all source distances yields

$$\left\langle \frac{d^3\Gamma}{dM\,dt_{\mathrm{FWHM}}\,du_0} \right\rangle_s = \int p_s\, \frac{2\,w^2(u_0)}{t_{\mathrm{FWHM}}^{\;3}}\, \xi(M) \int_0^{D_{\mathrm{os}}} \rho(D_{\mathrm{ol}})\, p_{v_{\mathrm{t}}}\!\left(\frac{R_{\mathrm{E}}}{t_{\mathrm{FWHM}}}\, w(u_0) \right) R_{\mathrm{E}}^{\;3}\, dD_{\mathrm{ol}}\, dD_{\mathrm{os}}. \quad (2.84)$$

The mass probability functions $p(M;t_{\mathrm{FWHM}}^{\mathrm{meas}},u_0^{\mathrm{meas}})$ and $\hat{p}(M;t_{\mathrm{FWHM}}^{\mathrm{meas}},\sigma_{t_{\mathrm{FWHM}}^{\mathrm{meas}}},u_0^{\mathrm{meas}},\sigma_{u_0^{\mathrm{meas}}})$ can then be obtained analogously to equations 2.82 and 2.83. Of course, equations (2.80), (2.81) and (2.84) are equivalent and can be converted into each other as long as t_{FWHM} and u_0, and thus t_{E} are known.

Equation (2.84) nicely illustrates the transition to the pixel-lensing regime: As soon as t_{E} is not an observable anymore (but only t_{FWHM}), the relative impact parameter enters in the integral in equation (2.84), and the mass probability function becomes dependent on the maximum magnification of the source. In pixel-lensing one is often in the situation where the t_{FWHM} is known quite accurately and $u_0(A_0)$ is known to certain limits (if finite source effects and/or space observations can rule out certain magnifications and constrain the magnification interval, equation (2.84) leads to more realistic results than equation (2.80)). In this case, the mass probability function can roughly be obtained with $\hat{p}(M;t_{\mathrm{FWHM}}^{\mathrm{meas}},\sigma_{t_{\mathrm{FWHM}}^{\mathrm{meas}}},u_0^{\mathrm{meas}},\sigma_{u_0^{\mathrm{meas}}})$ including the errors of $t_{\mathrm{FWHM}}^{\mathrm{meas}}$ and u_0^{meas}. But it is not appropriate in

---

[27] Converting Jetzer & Massó (1994) to our notation with $P(\mu,T) \equiv \frac{1}{\xi(M)}\frac{d^2\Gamma(M,t_{\mathrm{E}})}{dM\,dt_{\mathrm{E}}}$, $T \equiv t_{\mathrm{E}}$, $\mu \propto M$, $x \equiv D_{\mathrm{ol}}/D_{\mathrm{os}}$, $\rho_0 H(x) \equiv \rho(D_{\mathrm{ol}})$, $\frac{dn_0(\mu)}{d\mu} \propto \xi(M)$, $r_{\mathrm{E}}^2 \mu x(1-x) \propto R_{\mathrm{E}}^2$, $v_H \equiv \sqrt{2}\sigma$ gives

$$\frac{1}{\xi(M)}\frac{d^2\Gamma(M,t_{\mathrm{E}})}{dM\,dt_{\mathrm{E}}} \propto \frac{M^2}{t_{\mathrm{E}}^4} \int_0^{D_{\mathrm{os}}} dD_{\mathrm{ol}} \left(\frac{D_{\mathrm{ol}}(D_{\mathrm{os}}-D_{\mathrm{ol}})}{D_{\mathrm{os}}} \right)^2 \rho(D_{\mathrm{ol}}) \exp\left(-\frac{R_{\mathrm{E}}^2}{2\sigma^2 t_{\mathrm{E}}^2} \right).$$

[28] Converting Dominik's (1998) eq. (21) to our notation with $\mu \equiv M/M_\odot$, $\omega_0 \equiv u_{\mathrm{T}}$, $x \equiv D_{\mathrm{ol}}/D_{\mathrm{os}}$, $\rho_0 H(x) \equiv \rho(D_{\mathrm{ol}})$, $v_c \equiv \sqrt{2}\sigma_{\mathrm{l}}$, $\zeta \equiv v_{\mathrm{t}}/(\sqrt{2}\sigma_{\mathrm{l}})$, $\tilde{K}(\zeta) \equiv p_{v_{\mathrm{t}}}(v_{\mathrm{t}})\sqrt{2}\sigma_{\mathrm{l}}$, $\frac{dn_0(\mu)}{d\mu} = \alpha\mu^p \equiv \xi(M)$, $r_0\sqrt{x(1-x)} \equiv R_{\mathrm{E}}/\sqrt{M/M_\odot}$ gives

$$\frac{d\Gamma}{dM} = u_{\mathrm{T}} \int \xi(M)\, R_{\mathrm{E}}\, \rho(D_{\mathrm{ol}})\, v_{\mathrm{t}}\, p_{v_{\mathrm{t}}}(v_{\mathrm{t}})\, \delta\!\left(M - t_{\mathrm{E}}^2 v_{\mathrm{t}}^2 \left(\frac{4G}{c^2}\frac{D_{\mathrm{ol}}(D_{\mathrm{os}}-D_{\mathrm{ol}})}{D_{\mathrm{os}}} \right)^{-1} \right) dD_{\mathrm{ol}}\, dv_{\mathrm{t}}.$$

[29] Converting de Rujula *et al.* (1991, eq. (25)) to our notation with $\mu \propto M$, $\tau' \propto t_{\mathrm{E}}$, $\tau \propto t_{\mathrm{E}}^{\mathrm{meas}}$, $u'_{\min} \equiv u_0$, $u_{\mathrm{TH}} \equiv u_{\mathrm{T}}$, $A' \equiv A_0(u_0)$, $A_{\max} \equiv A_0^{\mathrm{meas}}$, $A_{\mathrm{TH}} \equiv A_{\mathrm{T}}(u_{\mathrm{T}})$, $x \equiv \frac{D_{\mathrm{ol}}}{D_{\mathrm{os}}}$, $\rho_0 H(x) \equiv \rho(D_{\mathrm{ol}})$ gives

$$\frac{1}{\xi(M)}\frac{d\Gamma(M)}{dM}\bigg|_{t_{\mathrm{E}}^{\mathrm{meas}},A_0^{\mathrm{meas}}} \propto \int_0^{u_{\mathrm{T}}} du_0 \int\int\int \delta(t_{\mathrm{E}}-t_{\mathrm{E}}^{\mathrm{meas}})\,dt_{\mathrm{E}}\, \delta(A_0^{\mathrm{meas}}-A_0(u_0))\, R_{\mathrm{E}}(D_{\mathrm{ol}})\, \rho(D_{\mathrm{ol}})\, dD_{\mathrm{ol}}\, p_{v_{\mathrm{t}}}(v_{\mathrm{t}})\, dv_{\mathrm{t}}.$$

This equation disagrees in some powers in R_{E} and t_{E} to our result.

this case to convert $t_{\mathrm{FWHM}}^{\mathrm{meas}}$ to $t_{\mathrm{E}}^{\mathrm{meas}}$ (using u_0^{meas}) and then to obtain $\hat{p}(M; t_{\mathrm{E}}^{\mathrm{meas}}, \sigma_{t_{\mathrm{E}}^{\mathrm{meas}}})$ from equation (2.82), since then the error for $t_{\mathrm{E}}^{\mathrm{meas}}$ derived from a measured $t_{\mathrm{FWHM}}^{\mathrm{meas}}$ also depends on u_0^{meas}.

2.9.3 The Lens Mass Probability Distribution, Obtained from the Observables $t_{\mathrm{FWHM}}^{\mathrm{meas}}$, Δ_F^{meas}, and $\mathscr{C}^{\mathrm{meas}}$

Finally, we discuss the situation most relevant for pixel-lensing, i.e., the case where only the flux excess Δ_F, the FWHM timescale t_{FWHM}, and the color of the event $\mathscr{C}^{\mathrm{meas}}$ are determined accurately from the light curve with coordinates x^{meas} and y^{meas}.
With the use of equation (2.65) one obtains

$$
\begin{aligned}
p_{l,s}(M; t_{\mathrm{FWHM}}^{\mathrm{meas}}, \Delta_F^{\mathrm{meas}}, \mathscr{C}^{\mathrm{meas}}) &\sim \Gamma_{l,s}(M, t_{\mathrm{FWHM}}^{\mathrm{meas}}, \Delta_F^{\mathrm{meas}}, \mathscr{C}^{\mathrm{meas}}) \\
&= \xi_l \, \frac{2}{\left(t_{\mathrm{FWHM}}^{\mathrm{meas}}\right)^3} \int\limits_0^\infty p_{\mathrm{cmd}_s} \int\limits_0^\infty n_s \frac{\Psi}{F_0} \int\limits_0^{D_{\mathrm{os}}} \rho_l \, R_{\mathrm{E}}^{\;3} \, p_{v_t} \, dD_{\mathrm{ol}} \, dD_{\mathrm{os}} \, d\mathscr{M},
\end{aligned}
\tag{2.85}
$$

with

$$
\Gamma_{l,s}(M, t_{\mathrm{FWHM}}, \Delta_F, \mathscr{C}) := \int \frac{d^7 \Gamma_{l,s}(x^{\mathrm{meas}}, y^{\mathrm{meas}}, M, t_{\mathrm{FWHM}}, \Delta_F, \mathscr{C}, \mathscr{M})}{dM \, dx \, dy \, dt_{\mathrm{FWHM}} \, d\Delta_F \, d\mathscr{C} \, d\mathscr{M}} \, d\mathscr{M},
$$

ignoring the (tiny) errors for the location of an event.   The functional dependence of the arguments in the integrand are $\xi_l(M)$, $p_{\mathrm{cmd}_s}(\mathscr{M}, \mathscr{C}^{\mathrm{meas}})$, $n_s(x^{\mathrm{meas}}, y^{\mathrm{meas}}, D_{\mathrm{os}})$, $\Psi(A_0)$, $A_0(F_0, \Delta_F^{\mathrm{meas}})$, $F_0(\mathscr{M}, D_{\mathrm{os}}, \mathrm{ext}_s)$, $\rho_l(x^{\mathrm{meas}}, y^{\mathrm{meas}}, D_{\mathrm{ol}})$, $R_{\mathrm{E}}(D_{\mathrm{ol}}, M, D_{\mathrm{os}})$, $p_{v_t}\!\left(\frac{R_{\mathrm{E}} \Upsilon}{t_{\mathrm{FWHM}}^{\mathrm{meas}}}, v_0\right)$, $\Upsilon(A_0)$, and $v_0(x^{\mathrm{meas}}, y^{\mathrm{meas}}, D_{\mathrm{ol}}, D_{\mathrm{os}})$.
Again, as outlined in equation (2.83), one can include the errors of the observables with a Gaussian measurement probability:

$$
\begin{aligned}
&\hat{p}_{l,s}(M; t_{\mathrm{FWHM}}^{\mathrm{meas}}, \sigma_{t_{\mathrm{FWHM}}^{\mathrm{meas}}}, \Delta_F^{\mathrm{meas}}, \sigma_{\Delta_F^{\mathrm{meas}}}, \mathscr{C}^{\mathrm{meas}}, \sigma_{\mathscr{C}^{\mathrm{meas}}}) \\
&\sim \int\int\int \Gamma_{l,s}(M, t_{\mathrm{FWHM}}, \Delta_F, \mathscr{C}) \\
&\qquad \times g(t_{\mathrm{FWHM}}; t_{\mathrm{FWHM}}^{\mathrm{meas}}, \sigma_{t_{\mathrm{FWHM}}^{\mathrm{meas}}}) \, g(\Delta_F; \Delta_F^{\mathrm{meas}}, \sigma_{\Delta_F^{\mathrm{meas}}}) \, g(\mathscr{C}; \mathscr{C}^{\mathrm{meas}}, \sigma_{\mathscr{C}^{\mathrm{meas}}}) \, dt_{\mathrm{FWHM}} \, d\Delta_F \, d\mathscr{C}.
\end{aligned}
\tag{2.86}
$$

If the light curve colors $\mathscr{C}^{\mathrm{meas}}$ can be measured very precisely, the calculations can be simplified using a luminosity distribution taken from the color-magnitude-diagram for a certain population. Mathematically this can be written as

$$
\tilde{\Phi}_{\mathscr{C}^{\mathrm{meas}}}(\mathscr{M}) \propto \int p_{\mathrm{cmd}}(\mathscr{M}, \mathscr{C}) \, \delta(\mathscr{C} - \mathscr{C}^{\mathrm{meas}}) \, d\mathscr{C}.
\tag{2.87}
$$

The modified luminosity distribution $\tilde{\Phi}_{\mathscr{C}^{\mathrm{meas}}}(\mathscr{M})$ replaces p_{cmd_s} in equation (2.85).

2.10 Conclusions and Outlook

Gravitational microlensing is a powerful method to detect compact luminous and dark matter objects in the foreground of stars in nearby galaxies. It can thus be applied to measure the mass function of stellar populations and dark halo objects (MACHOs).

One could infer the mass of an individual lensing object from the lensing light curve directly, if the luminosity of the source, the observer-lens-source distances, and velocities would be known. However, at least the lens distance and velocity are unfortunately almost never known. Hence, distribution functions for the lens and source quantities (see §§ 2.4 and 2.5) have to be used to finally obtain the mass-probability function for individual lensing events.

We used these distribution functions to rederive well-known relations like that for the optical depth, single-star event rate or mean Einstein time of the events. These quantities were taken in the past as "back-of-the-envelope" estimates of lensing frequencies to design microlensing surveys and were evaluated for line-of-sight distances to the plane of M31 only, i.e., simplifying the three dimensional structure of M31. We also accounted for the distance distribution of the sources and obtained the line-of-sight distance-averaged quantities for the optical depth, single-star event rate, and Einstein time instead. We show their values as a function of line-of-sight positions with contour plots in § 2.6. The shape of the total optical depth contours (Fig. 2.7, *third row, left*) obtained in this way deviates from earlier results (in a way that is understood by the simplifications made; Gyuk & Crotts (2000)).

Furthermore, we derived the distribution of the microlensing events rate as a function of FWHM timescale and the magnification of the event. We evaluated this function for a position [i.e., $(x, y) = (1', 0')$] within the WeCAPP field and find the following: the values of timescale and magnification are largely confined to a linear region within the time magnification-FWHM timescale plane (§ 2.6.5, Fig. 2.11); an observing frequency of once per day is sufficient to identify the majority of events with magnification of the order 30–100; and higher magnification events will have smaller timescales on average. Progress in the number of detected lensing events can made by lowering the magnification threshold for the event detection or, less efficiently, by further improving the time sampling. The lowering of the noise per PSF can be best achieved by small PSF and pixel sizes, i.e., by space observations.

We then discussed the pixel-lensing or difference imaging regime, which is the situation where the majority of stars is hardly or not at all resolvable anymore. One then has to include the source luminosity function to account for the additional unknown variable, the intrinsic source flux. With that, we derived the distribution of the lensing events (at a fixed position in the central M31 field) as a function of the two main observables in the pixel-lensing regime, the excess flux and the FWHM timescale. The values of these two quantities are not as confined as those in the magnification-FWHM timescale plane anymore. Due to the broad luminosity function there exists a variety of combinations of magnification and intrinsic source flux which yields the value for the flux excess. Events with high flux excess are dominated by PMS source stars.

It had been noticed before (Gould, 1994b; Auriere *et al.*, 2001) that measuring or excluding finite source effects is useful to tighten constraints on the masses of lensing objects. But finite source effects also change the number and characteristics of events: In the presence of finite source effects, the event timescales are increased and the maximum magnification saturates below the maximum for the point-source approximation (Fig. 2.1). This shifts events to longer timescales, but also suppresses the number of high-magnification events, and therefore the number of observable events. Since events that are ultra-short (of order 0.001 days) in the point-source approximation are mostly high-magnification

events (Figure 2.11), they all do show finite source effects (if the lenses are residing in M31) and thus have larger timescales than 0.001 days if the source sizes are taken into account. This explains the absence of ultra-short events for configurations with lenses in M31 (see Figs. 2.14 and 2.15).

Using equation (2.65) and a flux excess threshold, one can predict the time scale distribution of the events in Figures 2.14 and 2.15. At different locations within M31 the amplitudes of the contours change, and some details of the contours can be changed and moved in the flux excess-FWHM timescale plane. However, in any case shown here one expects many more short-term events with timescales of 1 to several days, than long-term lensing events with timescales of 20 days or longer. Even supermassive MACHOs with $1000 M_\odot$ have about roughly the same number of events within 1 and 20 days as above 20 days. A bimodal distribution of event timescales, with most events between 1 to 5 days, none between 10 and 20 days, and a second group of events with timescales 20 d and above is difficult to understand (compare event candidates of de Jong *et al.* (2004)) on that basis. De Jong et al. argue that their result (many long-term events, and the correlation of the event duration with the distance to the M31 center) can be understood, since the noise level is lower in the outskirts, which would allow the detection of the long timescale events. This does not explain the bimodality in the event timescales (see Figs. 2.14 and 2.15).

Most searches for microlensing were started based on fairly simple calculations of the expected event rates (see Han (1996)). Their event-threshold criterion can be translated to a peak-threshold criterion (see § 2.8.2). This yields about 200 events per year with a minimum signal-to-noise of $Q \approx 6$ at maximum flux, and 15 events with $Q \approx 50$ (for their model survey, assuming 100% efficiency).

The event rates measured up to now in M31 pixel-lensing surveys are below the expectation values for pure self-lensing (using simple estimates of survey efficiencies), while for microlensing surveys toward the LMC and the Galactic bulge the numbers of detected self-lensing events satisfy the predictions. The apparent lack of M31 events can be due to an overestimated detection efficiency or previously overestimated lensing rates. We used the event distributions as function of flux excess and fwhm timescale, and the light distribution of M31 to finally derive the number of halo-lensing and self-lensing events within the WeCAPP field that exceed a given signal-to-noise ratio at the light curve maximum and have timescales of 1 day or larger (see Table 2.2).

For minimum signal-to-noise ratios of $Q = 10$ and a minimum timescale of 1 day one expects about 4.3 (bulge-bulge, disk-bulge, and bulge-disk) self-lensing events per year that have light curves as for point like sources and about 4.0 with finite source signatures in their light curves. For timescales above 2 days these numbers decrease to about 2.4 for point-source and 1.6 finite source signature events per year. Since M31 cannot be observed more the two-thirds of a year, the total efficiency will be not larger than 50% (WeCAPP), even for a survey with good time coverage. This means that there are not much more than a couple of self-lensing events with $Q = 10$ and timescales larger than 2 days in a WeCAPP field per year. A decrease of the "acceptable" (S/N) ratio at maximum light to $Q = 6$ does increase the number of point-source events (roughly) less than a factor of 5 and has little impact on the events with finite source signatures. In addition, at this variation level, a considerable fraction of the area is occupied by intrinsically variable objects, which makes the detection of lensing events even less effective.

These values are much below the already mentioned previous estimates. The identification of the WeCAPP-GL1 and WeCAPP-GL2 event with a signal-to-noise ratio of $Q \approx 85$ and $Q \approx 16$ at peak flux and a FWHM timescale larger than 1 day in the WeCAPP 2000/2001 data is in good agreement with our theoretical expectations. We will present WeCAPP results on lower signal-to-noise events in a forthcoming paper and compare these numbers with expectations in more detail.

The most efficient way to increase the number of lensing events is to lower the noise level. We investigate the number of self-lensing events that can be obtained with a 30 day survey of the M31 center using the ACS on board *HST* (1 orbit of total integration time per day). Since bulge-bulge self-lensing profits more from lowering the noise than the halo lensing (see Figure 2.14), a decrease of the noise level increases the self-lensing relative to the halo lensing. During this campaign we expect of order 120 bulge-bulge self-lensing events with a peak signal-to-noise ratio of 6 and timescales between 1 and 20 days. Halo lensing with $0.1\,M_\odot$ lenses would cause an additional 50 events if the halo is composed of MACHOs by 100%. If the halo fraction is not more than 25%, then the halo-lensing events would drop to a 10% of the total lensing events. The analysis of the lensing events (frequency and timescale) would provide a measurement of the low-mass end of the mass function in the bulge of M31, i.e., the first measurement of the mass function of stars at low masses outside our Galaxy.

Finally, we investigated the luminosity function of the stars that are lensed. The result is very sensitive to the timescale threshold of the survey. MS stars can only be seen if they are highly magnified, which implies (Fig. 2.11) extremely short event timescales. Present day surveys with minimum timescales of one day therefore do not see any main sequence stars (for self-lensing in the central bulge field). One can turn that result around: if one could identify a modestly bright event with $\Delta_F \geq 10^{-5} - 10^{-4}$ Jy with an MS source star and timescale of 1 day or larger within the WeCAPP field (e.g., with spectroscopy by an "instantaneous alert"), it would point to a MACHO. This MACHO would have to be very massive if it was within M31 and could be less massive within the Galaxy.

Another interesting observable is the flux excess of the brightest events. One can infer from equation (2.18) and Figures 2.14 and 2.15 that the inclusion of the source sizes yields to an upper limit of the excess brightness of the events. The value depends on the flux-to-radius ratio of the brightest PMS stars in the lensed population and the mass of the lens, plus some source and lens distance factors. If the radius-luminosity relation of the source population and the luminosity of the brightest PMS stars are known, one can obtain for every event a lower lens mass limit for each source-lens configuration considered.

Chapter 3

A photometric and kinematic model of M31

3.1 Abstract

To calculate lensing event distribution functions for the specific case of M31, we use data from the literature to construct a model of M31, reproducing consistently photometry, kinematics and stellar population.

3.2 Density Distribution

This section contains our models for the bulge, disk and halo density of M31 and comparison with observations. We show that taking a bulge with the same total mass as Kent (1989b) and a disk with the same total mass as Kerins *et al.* (2001) implies mass-to-light ratios for the stellar populations of bulge and disk in good agreement with expectations from population synthesis models. Our bulge model matches the observed surface brightness values of M31 better than previously published analytical models, which is important for the correct self-lensing prediction in the central part of M31. The contributions of the bulge and disk to the rotation curve are almost identical to that shown in Kerins *et al.* (2001), which allows us to assume the same density distribution for the dark halo as they did.

In this section we use the disk major axis coordinate system $(x_0, y_0, z_0$; see Fig. 2.7), which can easily be transformed to the line-of-sight coordinate system using an inclination i of $77°$ of M31 (Stanek & Garnavich, 1998).

3.2.1 Bulge of M31

Our M31 bulge model starts from Table I of Kent (1989b), containing the Gunn-r surface brightness and ellipticity values $\rho_r^{\text{Kent}}(a)$ and $\varepsilon^{\text{Kent}}(a)$ as a function of major-axis distance a to the center of M31. We assumed $50°$ for the position angle of the bulge. Figure 3.1 demonstrates that with

$$\left[\frac{1}{1 - \varepsilon(a)}\right]^2 := 0.254 \frac{a}{\text{arcmin}} + 1.11 \tag{3.1}$$
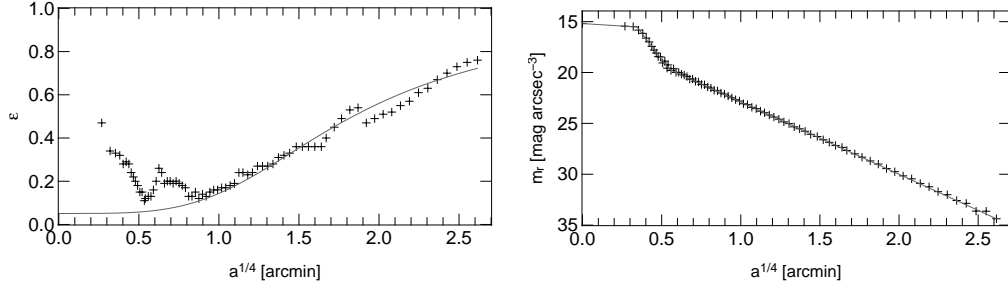
Figure 3.1: (*Left panel, a*) The gray curve shows our approximation for $\varepsilon(a)$ as defined in equation (3.1), and the red crosses are the tabulated values of Kent (1989b); within $0.5'$ and $6'$ the agreement is excellent. (*Right panel, b*) Bulge surface brightness as tabulated by Kent (1989b) is shown with crosses, and our approximation from equation (3.3) as a gray curve.

the ellipticity $\varepsilon(a)$ (*red curve*) becomes an excellent approximation of $\varepsilon_r^{\mathrm{Kent}}(a)$ (*blue crosses*) between $0.5'$ and $6'$.

With this relation we convert (x_0, y_0, z_0) to a by solving the quadratic equation $a^2 = x_0^2 + y_0^2 + (0.254a + 1.11) z_0^2$,

$$a(x_0, y_0, z_0) = \frac{0.254 z_0^2 + \sqrt{0.254^2 z_0^4 + 4\left(x_0^2 + y_0^2 + 1.11 z_0^2\right)}}{2} \qquad \text{[arcmin]}, \tag{3.2}$$

with x_0, y_0, z_0 and a in arcminutes.

The three-dimensionally decomposed spatial brightness density profile of the M31 bulge derived by Kent is well approximated by an $a^{1/4}$ law (see Figure 3.1b). With equation (3.2) the bulge mass density becomes

$$\rho_{\mathrm{bulge}}(x_0, y_0, z_0) := \begin{cases} \rho_0\, 10^{-0.4(0.97 a^{1/4})}, & a \le 0.014', \\ \rho_0\, 10^{-0.4(20.4 a^{1/4} - 6.68)}, & 0.014' < a \le 0.09', \\ \rho_0\, 10^{-0.4(7.1 a^{1/4} + 0.61)}, & a > 0.09', \end{cases} \tag{3.3}$$

where

$$\rho_0 := \left(\frac{M}{L}\right)_{\mathscr{M}} 10^{-0.4\left[\rho_{r,0}^{\mathrm{Kent}} - (r - \mathscr{M}) - \mathrm{ext}_{\mathscr{M}} - d_{\mathrm{mod}} - \mathscr{M}_\odot\right]} \frac{M_\odot}{\mathrm{arcsec}^3} \tag{3.4}$$

is the central mass density derived from the central brightness density in the r band, $\rho_{r,0}^{\mathrm{Kent}} = 15.19\,\mathrm{mag\,arcsec}^{-3}$ (Kent (1989b), Table I), and $(M/L)_{\mathscr{M}}$ is the bulge mass-to-light ratio in a fiducial filter $\mathscr{M}$, and $(r - \mathscr{M}) := m_r - m_{\mathscr{M}}$ is the color of the bulge population; $\mathscr{M}_\odot := -2.5 \log(\mathscr{F}_{\odot\mathscr{M}} / \mathscr{F}_{\mathrm{Vega}\mathscr{M}})$ is the absolute brightness of the Sun in that filter and d_{mod} is the distance modulus to M31.

Kent (1989b) fixes the bulge mass to $4 \times 10^{10}\,M_\odot$, which for $d_{\mathrm{mod}} = 24.19\,\mathrm{mag}$ (690 kpc) and without correcting for dust extinction implies a $(M/L)_r$-ratio of 6.05 (using our analytic approximation for ρ_{bulge}) and $5.5 - 6.6$ (integrating the tabulated values of Kent and estimating the maximal uncertainties due to the coarseness of the table[1]). Using the favored distance to M31 ($d_{\mathrm{mod}} = 770\,\mathrm{kpc}$) and applying

---

[1] We derived the upper and lower limit for the total brightness of the bulge in Kents Table I. By summing over ellipses (with an area $A_i := \pi a_i^2 (1 - \varepsilon_i)$ at semi-major distance a_i, $A_1 = 0$, and with a surface brightness $l_{r,i} := L_{r,\odot} 10^{-0.4(\mu(a_i) - d_{\mathrm{mod}} - \mathscr{M}_{r,\odot})}$, we got $L_{r,\mathrm{tot}}^{\mathrm{min}}/L_{r,\odot} = \sum_{i=2}^{77} l_{r,i}(A_i - A_{i-1})$, and $L_{r,\mathrm{tot}}^{\mathrm{max}}/L_{r,\odot} = \sum_{i=2}^{77} l_{r,i-1}(A_i - A_{i-1})$. These limits lead to a slightly higher $(M/L)_r$ between 5.5–6.6 than the value given by Kent (1989b): $(M/L)_r = 5 \pm 0.5$.

$M_{\text{tot}}/M_\odot$	dist (kpc)	Band $\mathcal{M}$	$(r-\mathcal{M})$	ext$_\mathcal{M}$	$L_{\mathcal{M},\text{tot}}/L_{\mathcal{M},\odot}$	$(M/L)_\mathcal{M}$	Comment
4×10^{10}	690	r	0	0	6.61×10^9	6.05	Kent's model using eq. (3.4)
4×10^{10}	770	R	0.59	0.36	13.5×10^9	2.96	

Table 3.1: This table shows that a bulge mass of $M = 4 \times 10^{10} M_\odot$ as proposed by Kent is a good estimate, even for the more realistic value (770 kpc) for the M31 distance.
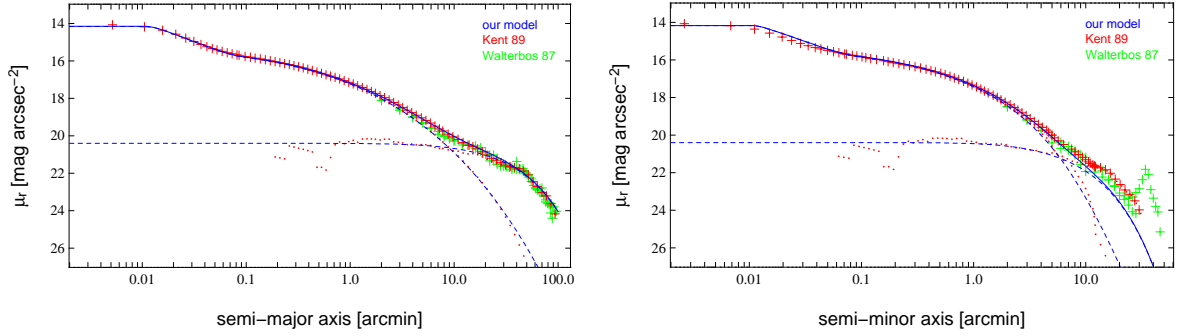
Figure 3.2: Surface-brightness profile of M31 in the r band: red crosses are Kent's r band data for the central region of M31; green crosses are the Walterbos & Kennicutt (1987) data (their Table V) transformed to the r band. The left and right panels show the profiles along semi-major and semi-minor axis, respectively. Kent has decomposed the surface brightness profile into the bulge and disk component (*red dots*). For comparison we have superposed our bulge and disk surface brightness models from Eqs. 3.3 and 3.6. With the exception of spiral arm imprints, they match the observations extremely well.

reasonable extinction values, the dust corrected mass-to-light ratios reduce to lower values (for a constant bulge mass of $4 \times 10^{10} M_\odot$, see Table 3.1).

The R band values were obtained with $R_\odot = 4.42$ mag, $(r - R) = 0.43 + 0.15(B - V) = 0.59$ (Moro & Munari, 2000), and a bulge color of $(B - V) \approx 1.05$ (Walterbos & Kennicutt, 1987).

According to Han (1996) the effect of an asymmetric bulge light extinction caused by the highly inclined M31 disk is negligible. We therefore adopt his values for the mean internal extinctions toward the bulge in the V and I bands of ext$_V = 0.24$ mag and ext$_I = 0.14$ mag and interpolate to the R band which yields ext$_R = 0.19$. With the foreground extinction of ext$_R = 0.17$ (Schlegel *et al.*, 1998) the total extinction becomes ext$_R = 0.36$. In this case, the mass-to-light ratio corresponding to Kent's bulge mass becomes $(M/L)_R = 2.96$ (line 2 in Table 3.1). This value is close to that $[(M/L)_{\text{stellar}} = 2.67]$ one would obtain for a 12 Gyr old, $Z = 2Z_\odot$ metallicity single stellar population (SSP) (see Girardi *et al.* 2002) for a Zoccali *et al.* (2000) mass function (MF) (see §§ 3.3.1 and 3.4).

We conclude that a normalization (equation (3.4)) of

$$\rho_0 = 2.07 \times 10^6 M_\odot\,\text{arcsec}^{-3} = 3.97 \times 10^4 M_\odot\,\text{pc}^{-3}, \tag{3.5}$$

which reproduces Kent's bulge mass of $M = 4 \times 10^{10} M_\odot$, is a reasonable assumption and represents an upper limit for the luminous matter in the bulge.

$M_{\text{tot}}/M_\odot$	dist (kpc)	Band $\mathcal{M}$	$(r-\mathcal{M})$	ext$_\mathcal{M}$	$L_{\mathcal{M},\text{tot}}/L_{\mathcal{M},\odot}$	$(M/L)_\mathcal{M}$	Comment
16×10^{10}	690	gunn r	0	0	$1.4\ldots1.7\times10^{10}$	$11.3\ldots9.6$	for Kent's max. disk mass
3.09×10^{10}	690	gunn r	0	0	1.34×10^{10}	2.31	for Kerins's disk mass
3.09×10^{10}	770	R	0.54	0.68	3.5×10^{10}	0.88	

Table 3.2: This table shows in its last two lines the mass-to-light ratios resulting from the disk mass of Kerins *et al.* (2001), $3.09\times10^{10}\,M_\odot$. The mass-to-light ratio for a realistic amount of extinction (last line), is close to a theoretical $(M/L)_{\text{stellar}}=0.62$ for a 2 Gyr old, solar metalicity SSP disk population (based on Gould *et al.* (1997) and Girardi *et al.* (2002)). Comparing the first and second lines shows that the maximum disk — assumed by Kent (1989b) (first line) — would imply a much too large mass-to-light ratio, which is usually obtained for maximum disk models).

3.2.2 Disk of M31

Like Kerins *et al.* (2001), we model the disk by a sech^2 law,

$$\rho_{\text{disk}}(x_0,y_0,z_0)=\rho_0\exp\left(-\frac{\sigma(x_0,y_0)}{h_\sigma}\right)\text{sech}^2\left(\frac{z_0}{h_z}\right),\tag{3.6}$$

with $\sigma(x_0,y_0)=\left(x_0^2+y_0^2\right)^{1/2}$ being the radial distance in the disk plane inclined by $77°$; the radial scale length $h_\sigma=28.57'$ and the vertical scale lengths $h_z=1.34'$ are equivalent to Kerins *et al.* (2001) values $h_\sigma=6.4\,\text{kpc}$ and $h_z=0.3\,\text{kpc}$ for a M31 distance of 770 kpc. Adopting a central brightness density of the disk in the r band $\rho_{r,0}^{\text{Kent}}=27.39\,\text{mag\,arcsec}^{-3}$ yields a surface brightness profile that matches the data of Kent (1989b) on the major axis and that agrees well with his central surface brightness of $\mu_0=20.4\,\text{mag}$ in the r band. Spiral arms and dust explain the discrepancies at the minor axis (see Figure 3.2). We assumed $38°$ for the position angle of the disk.

As for the bulge, we transform the luminosity density to matter density, using the disk color $(r-\mathcal{M})$, disk extinction ext$_\mathcal{M}$, and disk mass-to-light ratio $\left(\frac{M}{L}\right)_\mathcal{M}$

$$\rho_0=\left(\frac{M}{L}\right)_\mathcal{M}10^{-0.4(\rho_{r,0}^{\text{Kent}}-(r-\mathcal{M})-\text{ext}_\mathcal{M}-d_{\text{mod}}-\mathcal{M}_\odot)}\frac{M_\odot}{\text{arcsec}^3},\tag{3.7}$$

with the absolute brightness of the Sun $\mathcal{M}_\odot$, and the distance modulus d_{mod} to M31.

We normalize equation (3.7) with

$$\rho_0=10.4\,M_\odot\,\text{arcsec}^{-3}=0.2\,M_\odot\,\text{pc}^{-3}\tag{3.8}$$

to obtain the same disk mass as Kerins *et al.* (2001) $M_{\text{disk}}=\int\int\rho\,dz\,d\sigma=4\pi\rho_0 h_z h_\sigma^2=3.09\times10^{10}\,M_\odot$. Table 3.2 demonstrates that this normalization results in a mass-to-light ratio that is expected for the disk population.

With $E(B-V)=0.22$ (Stephens *et al.*, 2003) we obtain ext$_V=3.1E(B-V)=0.682$ for the extinction in the M31 disk. This translates to ext$_R=0.748\,\text{ext}_V=0.51$ (Binney & Merrifield, 1998). Adding the foreground extinction, ext$_R=0.17$ (Schlegel *et al.*, 1998), we obtain ext$_R=0.68$ for the total extinction for sources residing in the disk of M31. Using that extinction, the M31 distance of 770 kpc and the central luminosity density of $\rho_{R,0}^{\text{Kent}}=26.86\,\text{mag\,arcsec}^{-3}$ [obtained from $\rho_{r,0}^{\text{Kent}}$ and $r-R=0.53$ for a disk color $(B-V)\approx0.7$; Walterbos & Kennicutt (1987)], we get a disk luminosity of $L_{R,\text{tot}}/L_{R,\odot}=3.5\times10^{10}$. For the disk mass of Kerins *et al.* (2001), our $(M/L)_R$ ratio becomes 0.88.
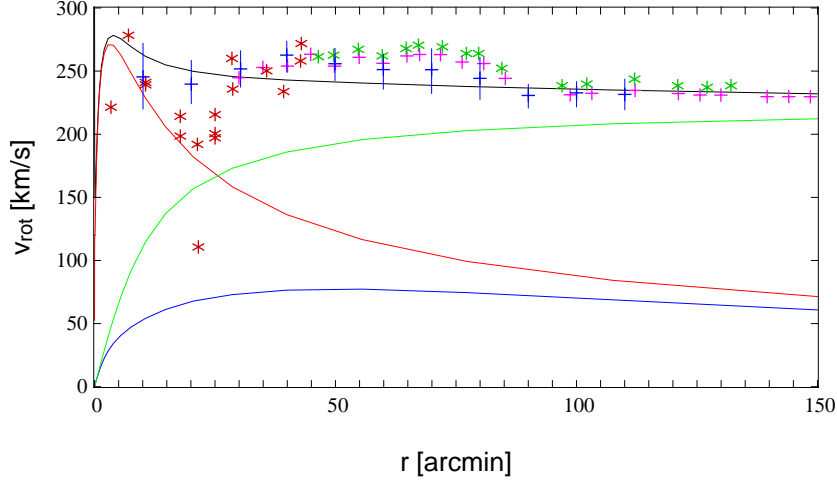
Figure 3.3: Overall rotation curve of our model (*black curve*) and its contributions of the bulge (*red*), disk (*blue*), and halo (*green*). These rotation curves match with Fig. 3*b* in Kerins *et al.* (2001). In red crosses we show the data points derived from CO measurements of Loinard *et al.* (1995); in green, HI measurements from Brinks & Burton (1984); in blue, averaged data points from Widrow *et al.* (2003) (based on Kent (1989a), and Braun (1991)); in magenta, the data points of Kerins *et al.* (2001) (based on Kent (1989b)).

This mass-to-light ratio is well consistent with a theoretical $\left(\frac{M}{L}\right)_{\text{stellar}} = 0.61$ for a 2 Gyr old, solar metallicity SSP disk population (based on Gould *et al.* (1997) and Girardi *et al.* (2002)).

We also summarize the maximum disk model of Kent (1989b) in Table 3.2 (*first row*). This model implies a 4 times higher $(M/L)_r$-ratio, which is hard to reconcile with population synthesis models. Note that the results from Han & Gould (1996a) are not easy to compare with ours: they used a double exponential disk with $\rho_0 = 0.35\,M_\odot\,\text{pc}^{-3}$, $h_z = 0.4$ kpc, and $h_\sigma = 6.4$ kpc corresponding to a disk mass of $7.2 \times 10^{10}\,M_\odot$. At the same time their bulge is also more massive than ours ($4.9 \times 10^{10}\,M_\odot$).

3.2.3 Halo of M31

Our density models for the bulge and disk differ only slightly (e.g., in the central region) from that of Kerins *et al.* (2001). The contributions to the rotation velocity resulting from the different populations are therefore very much the same as in the Kerins *et al.* (2001) model. This implies that we can use the halo density distribution from Kerins *et al.* (2001) to obtain a halo model consistent with the observed M31 rotation curve. This halo density distribution is that of an isothermal sphere with a core radius of $r_{\text{c}} = 2$ kpc:

$$\rho_{\text{halo}}(x_0, y_0, z_0) = \frac{\rho_0}{1 + (r/r_{\text{c}})^2}, \quad r \leq 200\,\text{kpc}, \tag{3.9}$$

with $r = (x_0^2 + y_0^2 + z_0^2)^{1/2}$, $r_{\text{c}} = 2$ kpc, and $\rho_0 = 0.23\,M_\odot\,\text{pc}^{-3}$. Figure 3.3 shows the overall rotation curve of our model.

In the model of Han & Gould (1996a) the core radius of the halo is much larger ($r_{\text{c}} = 6.5$ kpc) to compensate for their higher disk and bulge mass in order to match the rotation curve of M31.

3.2.4 Halo of the Milky Way

The halo of the Milky Way (MW) is also modeled as a cored isothermal sphere,

$$\rho_{\mathrm{MW}}(D_{\mathrm{ol}}) = \frac{\rho_0}{1 + (r/r_{\mathrm{c}})^2}, \quad r < 200\,\mathrm{kpc}, \tag{3.10}$$

where we choose a core radius of $r_{\mathrm{c}} = 2\,\mathrm{kpc}$ as used in Han & Gould (1996a) and Gyuk & Crotts (2000).
The central density is taken from (Han & Gould, 1996a):

$$\rho_0 = 0.0079\,M_\odot\,\mathrm{pc}^{-3} \left[1 + \left(\frac{r_\odot}{r_{\mathrm{c}}} \right)^2 \right] = 0.1343\,M_\odot\,\mathrm{pc}^{-3}. \tag{3.11}$$

We convert the Galactocentric distance r to our line-of-sight coordinate system according to

$$r(D_{\mathrm{ol}}) = \sqrt{r_\odot^2 - 2r_\odot D_{\mathrm{ol}} \cos(l)\cos(b) + {D_{\mathrm{ol}}}^2}, \tag{3.12}$$

using the M31 Galactic coordinates $l = 121.14988°$, $b = -21.61707°$ and the solar Galactocentric distance $r_\odot = 8\,\mathrm{kpc}$ (Bahcall *et al.*, 1983).

3.3 The Mass Function

3.3.1 The Mass Function for the bulge and disk sources

For the M31 bulge we take the mass function (MF) $\xi \sim M^{-1.33}$ of Zoccali *et al.* (2000), which was derived for the Galactic bulge. The MF is cut off at $0.01\,M_\odot$ at the lower end and at the MS turnoff $1.01\,M_\odot$ at the upper end for a 12 Gyr old SSP with $Z = 2Z_\odot$.
We describe the disk with a Gould MF, $\xi \sim M^{-2.21}$, which has a flattening $\xi \sim M^{-0.56}$ below $0.59\,M_\odot$ (Gould *et al.*, 1997). We cut the disk MF at 0.01 and $1.71\,M_\odot$ (2 Gyr old SSP with $Z = Z_\odot$), respectively. Of course, the number of stars with a given mass changes for different cut off values or for alternative mass functions (e.g., Chabrier (2003)). The investigation of halo-lensing and self-lensing rates for different MFs is not a subject of that chapter.

3.3.2 The Mass Function for the Halo

The mass function $\xi(M)$ for the potential MACHO population residing in the halo of M31 is of course unknown. In this chapter we simply assume that the halo consists of one mass objects M_0 only,

$$\xi(M) = \frac{\delta(M - M_0)}{M_0}, \tag{3.13}$$

satisfying the normalization constraint

$$\int M\,\xi(M)\,dM = 1. \tag{3.14}$$

3.4 The Luminosity Function and CM Diagram

We use a stellar LF obtained from isochrones of the Padova database of stellar evolutionary tracks and isochrones given by Girardi *et al.* (2002) (based on Marigo & Girardi (2001)).
The luminosity function can be extracted from the mass function $\xi(M)$ discussed in § 3.3.1. Using the mass-magnitude relation provided by theoretical stellar isochrones each mass bin $[M_i, M_{i+1}]$ of stars is connected to a absolute brightness bin $[\mathcal{M}_i, \mathcal{M}_{i+1}]$:

$$\int_{\mathcal{M}_i}^{\mathcal{M}_{i+1}} \Phi(\mathcal{M})\, d\mathcal{M} \stackrel{!}{=} \int_{M_i}^{M_{i+1}} \xi(M)\, dM \tag{3.15}$$

and therefore,

$$\Phi(\mathcal{M}) \approx \frac{\int_{M_i(\mathcal{M}_i)}^{M_{i+1}(\mathcal{M}_{i+1})} \xi(M)\, dM}{\mathcal{M}_{i+1} - \mathcal{M}_i} \qquad \mathcal{M}_i \leq \mathcal{M} \leq \mathcal{M}_{i+1}. \tag{3.16}$$

For the bulge we assumed a 12 Gyr old SSP with $Z = 2Z_\odot$ (isoc_z040s.dat[2]), which leads to good results for the stellar content of the bulge (C. Maraston 2004, private communication).
For the disk we used for simplicity a 2 Gyr old SSP with $Z = Z_\odot$ (isoc_z019m.dat; see footnote 2) leading to acceptable results for the disk data shown in (Williams (2002); fields INNER, NGC224-DISK, NGC224-POS2, G287, G11, G272, G87, K108, and G33).
With the mass function $\xi(M)$ and the luminosity function $\Phi(\mathcal{M})$ we obtain the mass-to-light ratio

$$\left(\frac{M}{L}\right)_{\mathcal{M}} = \frac{\int_{M_{\min}}^{M_{\max}} M\,\xi(M)\, dM \,/M_\odot}{\int_{-\infty}^{+\infty} \mathcal{F}_{\mathrm{Vega}} 10^{-0.4\mathcal{M}} \Phi(\mathcal{M})\, d\mathcal{M} \,/\mathcal{F}_\odot} = \frac{\int_{M_{\min}}^{M_{\max}} M\,\xi(M)\, dM \,/M_\odot}{<\mathcal{F}> \int_{-\infty}^{+\infty} \Phi(\mathcal{M})\, d\mathcal{M} \,/\mathcal{F}_\odot}. \tag{3.17}$$

For a bulge MF as in § 3.3.1 we get a characteristic flux $<\mathcal{F}_R> = 0.20\mathcal{F}_\odot$, yielding a $(M/L)_R$ in the R band of $(M/L)_R = 2.67$ and a $(B-V) = 1.14$ mag. For a disk MF as in § 3.3.1 we get a characteristic flux $<\mathcal{F}_R> = 0.67\mathcal{F}_\odot$, yielding a $\left(\frac{M}{L}\right)_R$ in the R band of $(M/L)_R = 0.61$ and a $(B-V) = 0.88$ mag. Note that other values of $M_{\min}$ and $M_{\max}$ give different mass-to-light ratios, as the decrease of $M_{\min}$ increases only the mass of the population, but not its luminosity. We show the LF for the bulge population in Figure 3.4, along with the stellar radii data (see § 3.5). Note that the faint cutoff of $\Phi(\mathcal{M})$ affects the characteristic luminosity $<\mathcal{F}>$ but at the same time the normalization of $\tilde{\Phi}(\mathcal{M}) = \Phi(\mathcal{M})/\int \Phi(\mathcal{M})d\mathcal{M}$. Therefore, the number of bright stars, $\mathcal{F}_{\mathrm{tot}} <\mathcal{F}>^{-1} \int_{\mathrm{bright}} \tilde{\Phi}(\mathcal{M})d\mathcal{M}$, is nearly not affected by changing the faint cutoff.
Using equation (2.43) we calculate the projected densities of bulge and disk stars brighter than $\mathcal{M}_R \leq 0$ mag and show the results in Figure 3.5; basically at any position monitored by WeCAPP there is more than one bright star per square arcsec each from bulge and disk. This demonstrates that crowding in the central bulge is very severe even for the brightest stars with $\mathcal{M}_R \leq 0$ mag and even if image PSFs are small.

---

[2] See Girardi *et al.* (2002) and http://pleiadi.pd.astro.it.
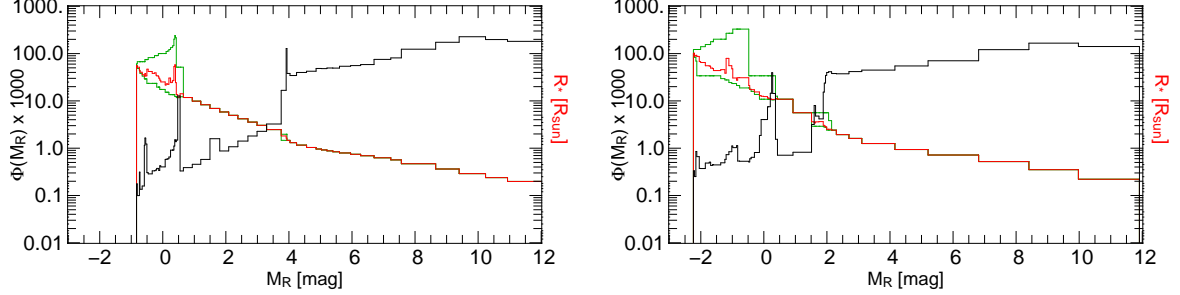
Figure 3.4: Theoretical LF in the *R* band $\tilde{\Phi}_R(\mathscr{M})$. *Left*: bulge for a 12 Gyr old SSP of 2 $Z_\odot$ metalicity. *Right*: disk for a 2 Gyr old SSP of 1 $Z_\odot$ metalicity. In red and green we show the values of the stellar radii obtained with § 3.5 and the theoretical luminosities for the stars of the model SSP. The red line shows the average radius $\overline{R}_*$ according to equation (3.19). In green we give the minimal and maximal radii of stars (reflecting the different values in color space) in the particular magnitude range. The LF was scaled by a factor of 1000 to show the two different histograms with the same scaling. The unit of the LF is number of stars per magnitude, the radii distribution is given in solar radii.
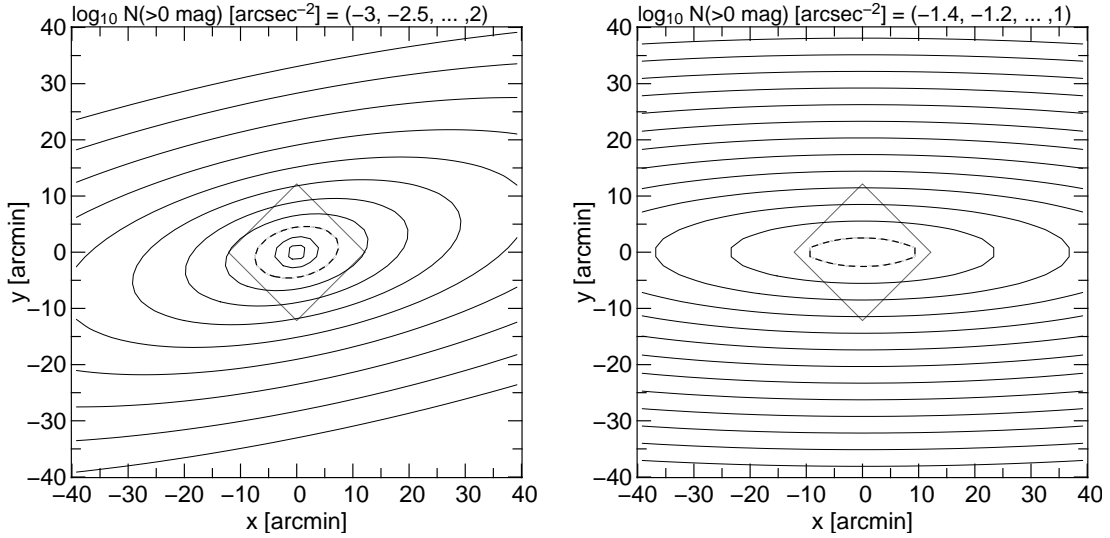
Figure 3.5: Number density of bulge stars (*left*) and disk stars (*right*) brighter than $\mathscr{M}_R \leq 0$ mag in units of stars arcsec^{-2}. The contours show the values of $d^2N/(dx\,dy)\big|_{\mathscr{M}_R \leq 0} = \int_{-\infty}^0 \int_0^\infty \tilde{\Phi}(\mathscr{M})\, n_s(x, y, D_{os})\, dD_{os}\, d\mathscr{M}$ and were obtained from the number density and luminosity functions of the bulge and disk component of M31. The WeCAPP field, a square of $17.2'$, is shown as a box. The dashed contour outline a density of the $\mathscr{M}_R \leq 0$ stars of 10 stars/arcsec^2 and demonstrate that one cannot resolve even giants in the central M31 field for the majority of ground-based data. The coordinates are that of the intrinsic M31 system (see Figure 2.7).

3.5 Radius-Brightness Relations for Stars

For the inclusion of finite source effects one needs the radius-brightness relation of stars. The radius can easily be correlated to the brightness (and to the luminosity function) using $\log(L_i)$ and $\log(T_{\text{eff},i})$ given in the theoretical stellar isochrones (see § 3.4)

$$R_*(\mathcal{M}_i, \mathcal{C}_i) = \frac{10^{[\log L_i + \log L_{i+1}]/4}}{\sqrt{4\pi\sigma_{\text{B}}}\, 10^{\log T_{\text{eff},i} + \log T_{\text{eff},i+1}}} \qquad \mathcal{M}_i \leq \mathcal{M} \leq \mathcal{M}_{i+1}, \mathcal{C}_i \leq \mathcal{C} \leq \mathcal{C}_{i+1}. \tag{3.18}$$

If we want to account for finite source effects without having any color information, e.g., equation (2.63), we use a color-averaged source radius $\overline{R}_*$,

$$\overline{R}_*(\mathcal{M}) = \int p_{\text{cmd}}(\mathcal{M}, \mathcal{C}) R_*(\mathcal{M}, \mathcal{C}) \, d\mathcal{C}, \tag{3.19}$$

and replace $R_*(\mathcal{M}, \mathcal{C})$ with $\overline{R}_*(\mathcal{M})$ in Eqs. 2.66 and 2.67 (see Figure 3.4).

3.6 The Velocity Distributions for the M31 Components

The random velocity components of bulge, disk, and halo are assumed to be of Gaussian shape with dispersions taken from Kerins *et al.* (2001):

$$\begin{aligned} \sigma_{\text{bulge}} &= 100\,\text{km s}^{-1}, & \sigma_{\text{disk}} &= 30\,\text{km s}^{-1}, \\ \sigma_{\text{halo}} &= 166\,\text{km s}^{-1}, & \sigma_{\text{MW-halo}} &= 156\,\text{km s}^{-1}. \end{aligned} \tag{3.20}$$

In addition, we account for rotation in bulge and disk of $v_{\text{rot,bulge}} = 30\,\text{km s}^{-1}$ and $v_{\text{rot,disk}} = 235\,\text{km s}^{-1}$ (Kerins *et al.*, 2001). In a previous work Han & Gould (1996a) used $\sigma_{\text{halo}} = 170\,\text{km s}^{-1}$ for the halo, but a value of $\sigma_{\text{bulge}} = 156\,\text{km s}^{-1}$ for the bulge and disk (based on Lawrie (1983)).
In the following two sections we derive the relative source-lens velocity v_0 taking into account rotation of the source and lens objects and the observers motion. The combination of all contributions results in one movement depending on

$$v_0(D_{\text{os}}, D_{\text{ol}}, v_{\text{rot,l}}, v_{\text{rot,s}}, v_{\odot-\text{M31}}). \tag{3.21}$$

3.6.1 Additional Rotation for Lenses and Sources

The additional rotation of the lens system $v_{\text{rot,l}}$ (for bulge and disk lenses) and/or of the source system $v_{\text{rot,s}}$ changes the relative velocity v_0. For the calculation of the effect we first have to transform the positional components of a lens located at $(x, y, z := D_{\text{ol}} - d_{\text{m31}})$ along the line-of-sight to the components (x_0, y_0, z_0) in the M31 system. In the internal system the position is given by

$$x_0 = x, \quad y_0 = y\cos i - z\sin i, \quad z_0 = y\sin i + z\cos i, \tag{3.22}$$

with inclination angle $i = 77°$ and the distance to M31 $d_{\text{m31}} = 770$ kpc. Projecting on the base $\rho = (x_0^2 + y_0^2)^{1/2}$, the rotation angle can be expressed as $\omega = \arccos(x_0/\rho) = \arcsin(y_0/\rho)$.
Reprojecting the components of the rotation velocity v_x and v_{yz} (calculated for a clockwise rotation)

$$v_x = v_{\text{rot}}\sin\omega = -\frac{y_0}{\sqrt{x_0^2 + y_0^2}}\, v_{\text{rot}}, \quad v_{yz} = \sqrt{v_{\text{rot}}^2 - v_x^2} = \frac{x_0}{\sqrt{x_0^2 + y_0^2}}\, v_{\text{rot}}, \tag{3.23}$$

to the y- and z- plane yields[3]

$$v_y = v_{yz} \cos i, \quad v_z = v_{yz} \sin i, \tag{3.24}$$

which depends on the position along the line-of-sight (x, y, z). To combine this velocity vector (v_x, v_y, v_z) with all other velocities (see § 3.6.2) it has to be projected to the lens plane.

3.6.2   Observer's Motion

Finally, we have to account for the transversal velocity of M31 v_{M31} arising from the observers motion against M31. A hypothetical star on a circular orbit at solar distance (local standard of rest, LSR) has velocity $v_l(R_\odot) = 220 \pm 15 \, \mathrm{km \, s^{-1}}$. The Sun is moving with $v_\odot = 16.5 \, \mathrm{km \, s^{-1}}$ relative to the LSR toward the directions $l = 53°$, $b = 25°$ (Binney & Tremaine, 1987). For simplicity we neglect the contributions to the Galactic height (see Figure 3.6) and calculate the transversal velocity of M31 as

$$v_{\odot - M31} \approx (220 \, \mathrm{km \, s^{-1}}) \sin(l_{M31} - 90°) + 16.5 \, \mathrm{km \, s^{-1}} \sin(121° - l_{LSR}) = 129 \, \mathrm{km \, s^{-1}}, \tag{3.25}$$

with the Galactic coordinates of M31 $l_{M31} = 121.2°$ and $b_{M31} = -21.6°$. The relative velocity between the velocity distribution of the lenses and the sources is calculated by projecting $v^p_{\odot - M31}$ to the lens plane

$$v^p_{\odot - M31} \approx \frac{D_{os} - D_{ol}}{D_{os}} 129 \, \mathrm{km \, s^{-1}}. \tag{3.26}$$

For lenses residing in M31 this motion is negligible compared to the rotation described in § 3.6.1.
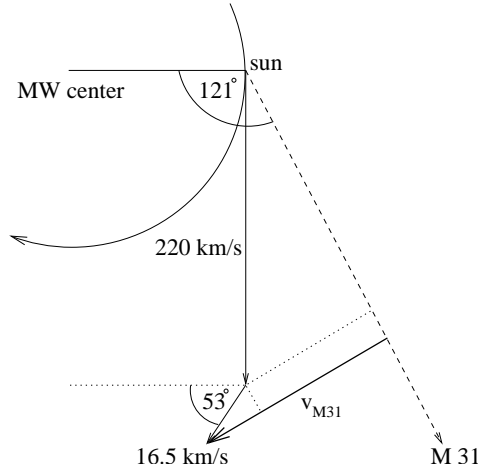
Figure 3.6: Geometry of the Galaxy-M31 system. A star at solar distance is assumed to move on a circular orbit with a rotational velocity of $220 \, \mathrm{km \, s^{-1}}$ (local standard of rest, LSR). M31 is located at Galactic coordinates $l_{M31} = 121.2°$ and $b_{M31} = -21.6°$. The Sun has a velocity of $16.5 \, \mathrm{km \, s^{-1}}$ relative to the LSR. The transversal velocity of M31 is shown as v_{M31}.

---

[3] The relations are valid for the first quadrant, else the sign has to change.

Chapter 4

The Wendelstein Calar Alto Pixellensing Project (WeCAPP)

This section includes the main parts of the published paper Riffeser *et al.* (2001) with modifications for the full 8 years data set.

4.1 Abstract

We present WeCAPP, a long term monitoring project searching for microlensing events toward M31. Since 1997 the bulge of M31 was monitored in two different wavebands with the Wendelstein 0.8 m telescope. From 1999 to 2002 we extended our observations to the Calar Alto 1.23 m telescope. Observing simultaneously at these two sites we obtained a time coverage of more than 60% during 13 months of these 3 years, reaching 90% during 4 month. To check thousands of frames for variability of unresolved sources, we used the optimal image subtraction method (OIS) by Alard & Lupton (1998). This enabled us to minimize the residuals in the difference image analysis (DIA) and to detect variable sources with amplitudes at the photon noise level. Thus we can detect microlensing events with corresponding amplifications $A > 10$ of red clump giants with $\mathcal{M}_I = 0$.

4.2 Telescopes and Instruments

The Wendelstein 0.8 m telescope has a focal length f of 9.9 m, which results in an aperture ratio $f/D = 12.4$. Starting in September 1997 we used a TEK CCD with 1024×1024 pixels of $24\,\mu$m corresponding to 0.5 arcsec on the sky. With this CCD chip we were able to cover $8.3 \times 8.3\,\text{arcmin}^2$ of the bulge of M 31. To increase the time sampling of our observations we started to use the Calar Alto 1.23 m telescope ($f = 9.8$ m, $f/D = 8.0$) in 1999. The observations were partly carried out in service mode. Six different CCD chips were used. Three of these CCDs cover a field of $17.2 \times 17.2\,\text{arcmin}^2$ and were used to survey the whole bulge for lensing events. A detailed overview of the properties of each CCD camera used for WeCAPP is given in Table 4.1.

Most of the sources for possible lensing events in the bulge of M 31 are luminous red stars i.e. giants and supergiants. Consequently the filters used in our project should be sensitive especially to these kind of stars. We chose therefore R and I filters for our survey. At Wendelstein we used the R2 ($\lambda \simeq$ 650 nm, $\Delta\lambda \simeq$ 150 nm) and Johnson I ($\lambda \simeq$ 850 nm, $\Delta\lambda \simeq$ 150 nm) wavebands. To be as consistent

Site	Campaign	CCD	Size	[arcsec/px]	Field [arcmin^2]	days in R	days in I	total days
We	1997/1998	TEK#1	1K × 1K	0.49	8.3 × 8.3	36	32	37
We	1998/1999	TEK#1	1K × 1K	0.49	8.3 × 8.3	33	28	33
We	1999/2000	TEK#1	1K × 1K	0.49	8.3 × 8.3	65	59	67
CA	1999/2000	SITe2b_17	2K × 2K	0.50	17.2 × 17.2	31	31	32
CA	1999/2000	SITe2b_11	2K × 2K	0.50	17.2 × 17.2	1	1	1
CA	1999/2000	SITe18b_11	2K × 2K	0.50	17.2 × 17.2	23	22	23
CA	1999/2000	TEK7c_12	1K × 1K	0.50	8.6 × 8.6	21	17	21
CA	1999/2000	TEK13c_15	1K × 1K	0.50	8.6 × 8.6	5	4	5
CA	1999/2000	LOR11i_12	2K × 2K	0.31	10.75 × 10.75	9	10	13
	1999/2000					*129*	*123*	*134*
We	2000/2001	TEK#1	1K × 1K	0.49	8.3 × 8.3	77	70	77
CA	2000/2001	SITe2b_17	2K × 2K	0.50	17.2 × 17.2	108	89	108
	2000/2001					*156*	*138*	*156*
We	2001/2002	TEK#1	1K × 1K	0.49	8.3 × 8.3	101	92	105
CA	2001/2002	SITe2b_17	2K × 2K	0.50	17.2 × 17.2	129	119	130
	2001/2002					*190*	*175*	*193*
We	2002/2003	TEK#1	1K × 1K	0.49	8.3 × 8.3	45	43	46
We	2003/2004	TEK#1	1K × 1K	0.49	8.3 × 8.3	57	53	58
We	2004/2005	TEK#1	1K × 1K	0.49	8.3 × 8.3	26	18	26
total						**672**	**610**	**683**

Table 4.1: Observations and properties of all CCD cameras used during WeCAPP at Wendelstein (We) and Calar Alto (CA) Observatories, respectively. All CCDs have a pixel size of $24\,\mu$m, except the Loral which has $15\,\mu$m pixels. During the 8 years period the bulge of M31 was observed on 683 days.

as possible with the data obtained at Wendelstein, the Calar Alto observations were carried out with the equivalents filters, R2 ($\lambda \simeq 640$nm, $\Delta\lambda \simeq 150$nm) and Johnson I ($\lambda \simeq 850$nm, $\Delta\lambda \simeq 150$nm). Since June 2000 we are using the newly installed filters Johnson R ($\lambda \simeq 640$nm, $\Delta\lambda \simeq 160$nm) and Johnson I ($\lambda \simeq 850$nm, $\Delta\lambda \simeq 150$nm) at Calar Alto.

Despite of the combination of different telescopes, CCDs, and slightly different filter systems we observed no systematic effects in the light curves depending on these parameters.

4.3 Observing Strategy

To follow the suggestion of Tomaney & Crotts (1996) and Han & Gould (1996a) we chose the field with the maximal lensing probability, pointing to the far side of the M 31 disk. The main fraction of the field is covered by the bulge of M 31 with the nucleus of M 31 located at one corner of the field (Fig. 4.1).

As gravitational lensing is achromatic, the amplification of the source is the same in different wavebands. However, as shown in several papers (e.g. Valls-Gabaud, 1994; Witt, 1995; Han *et al.*, 2000) blending on the one hand and differential amplification of an extended source on the other hand can lead to a chromatic, but still symmetric, lensing light curve. Under certain circumstances chromatic light curves permit to constrain the physical properties of the source-lens system (e.g. Gould & Welch, 1996; Han & Park, 2001). Variable stars will generally change colour in a different way. Our observation cycle therefore comprises 5 images in the R band and 3 images in the I band lasting about 45 min including readout time. Stacking these images with an average exposure time of 150 sec in R and
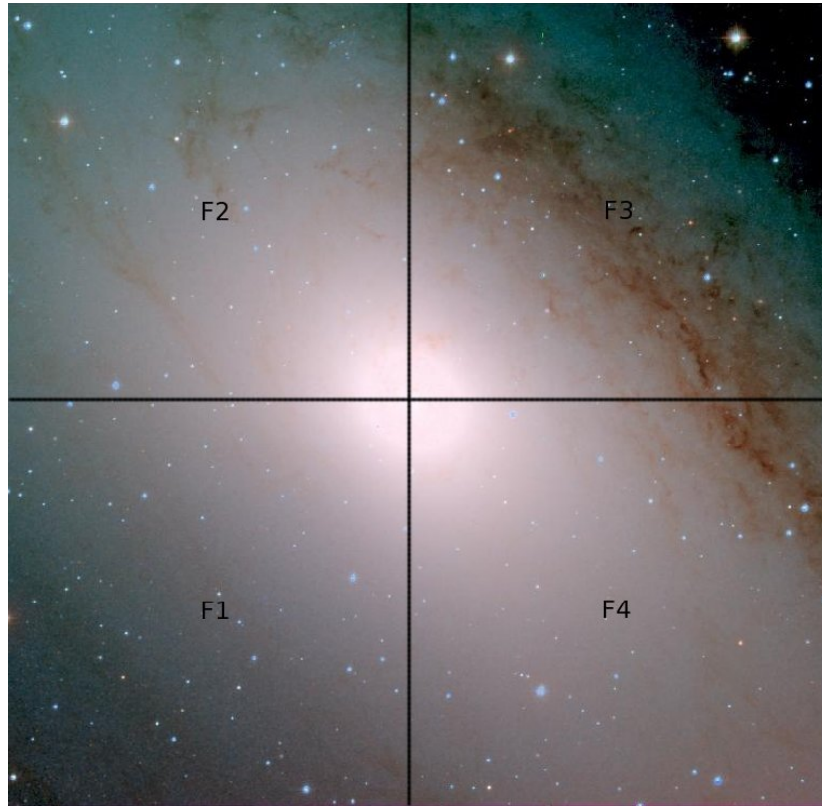
Figure 4.1: M31 composite image (*V*-, *R*-, and *I*-band) of the observed fields F1 to F4, taken at Calar Alto Observatory during the campaign 2000/2001. The black lines mark the positions of fields F1 to F4. Field F1 was observed during all eight campaigns from September 1997 until March 2005.

200 sec in I results in a magnitude limit between $(20.8 - 22.1)$ mag in R and $(19.1 - 20.4)$ mag in I for a point source on the background of M 31 and a signal-to-noise ratio $(S/N) = 10$ in over 95 % of the frame. The background of M 31 typically has a surface brightness between $(18.7 - 21.2)$ mag/arcsec^2 in R and $(16.8 - 19.3)$ mag/arcsec^2 in I. The cycles were repeated as often as possible during one night, usually at least twice. As we had to avoid saturation of stars in the observed field we made exposure times dependent of the actual seeing, whereas exposure times in the I bands where generally longer.

4.4 The Data

We began our observations at Wendelstein with a test period in September 1997, observing on 37 nights until March 1998. The second observational period lasted from 1998 October 22nd until 1999 March 24th. During the first Calar Alto campaign we received two hours of service observations on 95 of 196 allocated nights (1999 June 27th - 2000 March 3rd). From November 1st until November 14th we were able to observe during the whole night. In parallel we continued our observations at Wendelstein on 221 nights, of which 67 were clear. In this way we achieved an overall time coverage for the 1999/2001 season of 134 nights (53% of 252 nights). During season 2000/2001 (from 2000

Filter	We 1997/1998	We 1998/1999	We 1999/2000	CA 1999/2000
R	2.76	1.45	1.40	1.49
I	2.59	1.44	1.32	1.44

Table 4.2: Median values of the FWHM of the PSF, given in arcsec, for the images taken during WeCAPP in the R and I band at Wendelstein and Calar Alto Observatories.

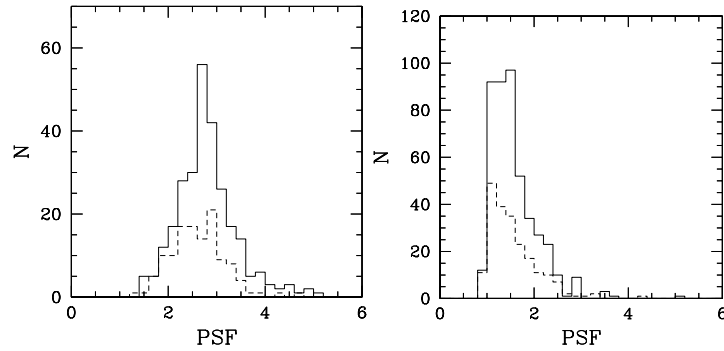Figure 4.2: Histograms of the Full Width Half Maximum (FWHM) of the point spread function (PSF) of the frames taken at Wendelstein Observatory during the 1997/1998 campaign (*left panel*) and the 1998/1999 campaign (*right panel*). Frames in the R band are marked by a solid line, frames in the I band by a dashed line. The lower limit of the PSF is restricted by a pixel size of 0.5 arcsec.

June 23th - 2001 March 4th) we observed on 156 nights (61% of 255 nights), during season 2001/2002 (from 2001 July 3rd - 2002 April 6th) on 193 nights (69% of 278 nights), during season 2002/2003 (from 2002 June 1st - 2003 March 10th) on 46 nights (16% of 283 nights), during season 2003/2004 (from 2003 June 6th - 2004 March 15th) on 58 nights (20% of 283 nights), and finally during season 2005/2005 (from 2004 Sep. 5th - 2005 March 4th) on 26 nights (14% of 180 nights).

During the 1997/1998 test campaign conditions at the Wendelstein telescope were improved significantly. A newly installed air conditioning system reduced dome seeing to a low level. Further improvements like fans just above the main mirror finally lead to a leap in the image quality obtained with the telescope. Figure 4.2 which presents the PSF statistics of Wendelstein images from the 1997/1998 and 1998/1999 campaigns respectively illustrates this fact. In general Wendelstein shows a marginally better PSF distribution than Calar Alto (see Figs. 4.2 and 4.3). Table 4.2 shows the PSF median values for the images taken during WeCAPP at both sites.

Figure 4.4 shows the time sampling we reached with WeCAPP during the first 3 years. Because of time loss during the upgrades of the telescope, time coverage of the 1997/1998 campaign is only fragmentary. About the same applies to the following campaign, this time due to a camera shutdown and another time consuming project. Finally time coverage of the first joint campaign of Wendelstein and Calar Alto is good, last but not least due to the often opposite weather situation in Spain and Germany. Fig. 4.5 shows the intensive observations during 3 years of simultaneous Wendelstein and Calar Alto observations. Note that the last 3 years with poor time coverage were mainly used to detect long-periodic variable stars.
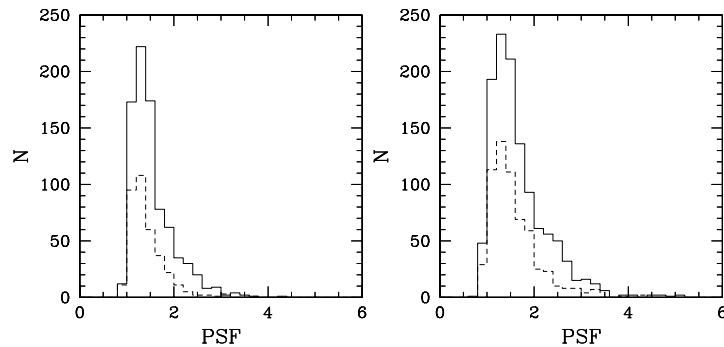
Figure 4.3: Histograms of the FWHM of the frames taken during the 1999/2000 campaign at Wendelstein (*left panel*) and Calar Alto Observatory (*right panel*). Frames in the R band are marked by a solid line, frames in the I band by a dashed line. Note that the pixel sizes of the CCD cameras used correspond to 0.5 arcsec on the sky.
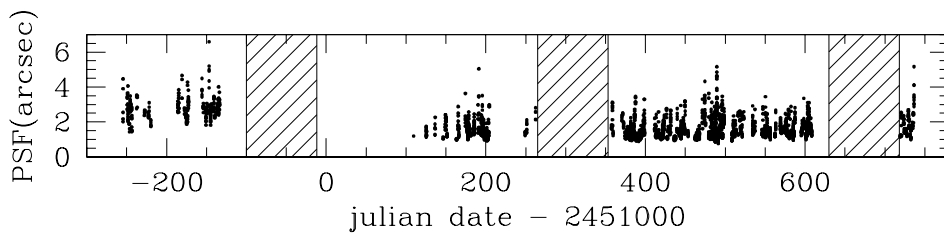
Figure 4.4: Illustration of PSF vs. time coverage during three years of WeCAPP. Shaded regions mark the periods of time when M 31 was not observable.
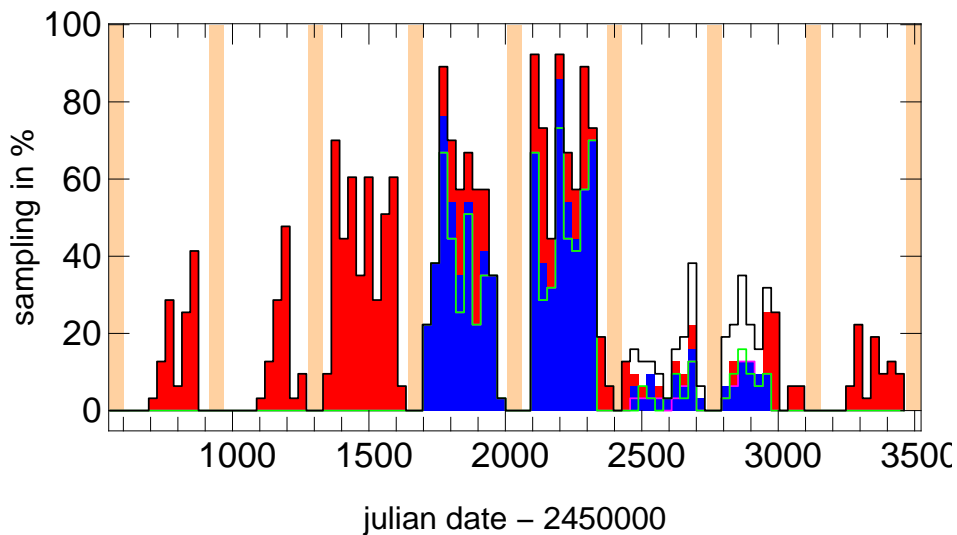
Figure 4.5: Illustration of the sampling given in percentage of observed days per month. *red areas:* field F1, *magenta:* F2, *blue areas:* field F3, *green:* F4, *black:* total. During the season 1999/2000 time sampling up to 70% was reached. During the seasons 2000/2001 and 2001/2002 the monthly time sampling reached up to 89% and 92%, respectively.

4.5   Results

We present a small sample of light curves to show the efficiency of the method. All light curves were observed over more than three years from 1997 until 2000. Time spans when M 31 was not observable are marked by shaded regions. Because of bad dome seeing conditions and an inappropriate autoguiding system errors were largest during the first Wendelstein campaign 1997/98. During the second period 1998/99 we were able to decrease the FWHM of the PSF by a factor of two, thus the photometric scatter is also clearly smaller. During the third period 1999/2000 we observed simultaneously at Calar Alto and Wendelstein and got data points for 53 % of the visibility of M 31.
A good estimate for the average noise present in the area Ω_{PSF} of a PSF is $N = 0.1 \times 10^{-5}$Jy. The light curves of variable stars presented in the Figs. 4.6 through 4.15 indicate a typical scatter which is in good agreement with the above estimate. This means that a red clump giant with a brightness of $M_I = 0$ (Grillmair et $al.$, 1996, Fig. 7) and a colour of $(R-I) = 0.5$ (Lejeune et $al.$, 1998) has to be amplified by a factor of 10 to be detected with a peak signal-to-noise ratio of $(S/N) = 3$ in our survey. The brightest RGB stars with a $M_I = -3.5$ and a colour of $(R-I) = 1$ need an amplification of 1.6 only.
Up to now we detected around 24000 variable sources in a 17×17 arcmin^2 field (Fliri et $al.$, 2006). A preliminary analysis of the light curves shows that we have found the whole range of variable stars including novae and other types of eruptive variables, Cepheids, semi-regular, Mira-type and other longperiodic variables.
In Fig. 4.6 we present one of the δ-Cephei variable stars in the R′ and I′ bands, Fig. 4.7 shows the R′ light curve of this star convolved with its period, which was determined to 15.76 ± 0.01 days. Figure 4.8 presents the light curve of a nova previously published by Modjaz & Li (1999). It's the brightest variable source detected in our M 31-field. Figure 4.9 is an example for an eruptive variable star, which could be mistaken as a microlensing event, if the time coverage were insufficient. Figures 4.10 to 4.14 display light curves of variable stars, which were classified as longperiodic in a preliminary analysis. Finally we present the light curve of a RV Tauri star in Fig. 4.15.

4.6   Summary

We presented an overview of the Wendelstein Calar Alto Pixellensing Project (WeCAPP). Observing simultaneously at two sites (Wendelstein and Calar Alto) we obtained a time coverage of 53% and 61% during the observed periods and up to 70% and 89% during the best month. Our best season was 2001/2002 with a 69% time coverage over the observed period, reaching around 90% during the 3 months (July 2001, October 2001, January 2002). This comes from a lucky coincidence that weather is correlated such, that observing conditions are hardly ever bad at both observatories at the same time. We demonstrated that despite observing at different sites with different instruments all data can be used for optimal image subtraction following Alard & Lupton (1998). This method can be applied for very crowded fields like M31 and gives residual errors at the photon noise level. A red clump giant of $\mathcal{M}_I = 0$ mag, which is amplified by a factor of 10 by a microlensing event, can be detected with our data. We showed how the data are reduced and how light curves are extracted. For illustration we presented a small sample of light curves. In future publications we will present a full catalogue of variable sources which we found in our M31 field, including potential MACHO light curves.
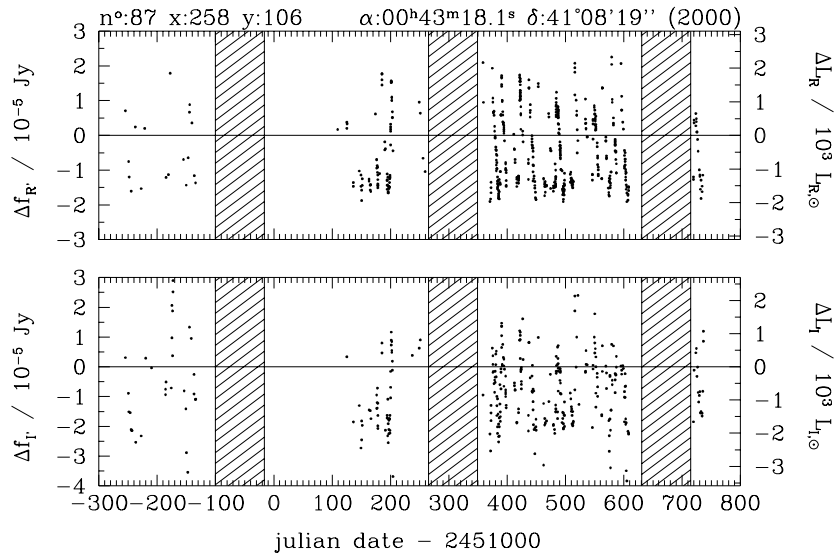
Figure 4.6: Light curve of a δ-Cephei variable star, upper panel: R$'$ band, lower panel: I$'$ band.
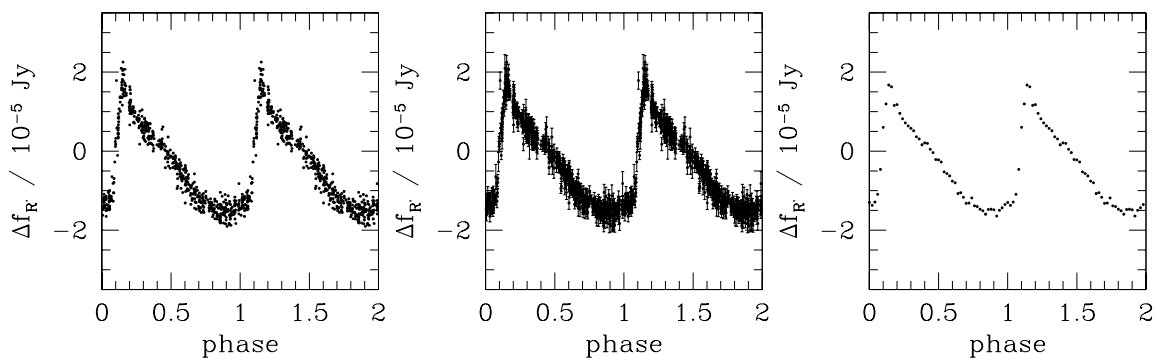
Figure 4.7: Light curve of the δ-Cephei star of Fig. 4.6 in the R$'$ band, convolved with its period of $P = 15.76 \pm 0.01$ d. Plotted without (left panel) and with (centre panel) 1σ error bars, which represent fully propagated errors through all reduction steps. Right panel: Binned R$'$ light curve of this star.
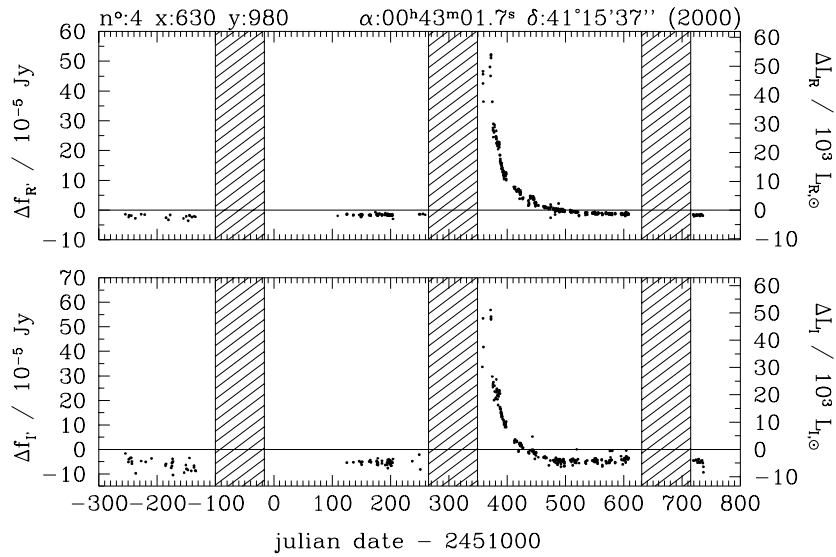
Figure 4.8: Light curve of a nova, representing the brightest variable source detected in our M 31-field. This nova was previously published by Modjaz & Li (1999). Upper panel: R'-Band, lower panel: I'-Band.
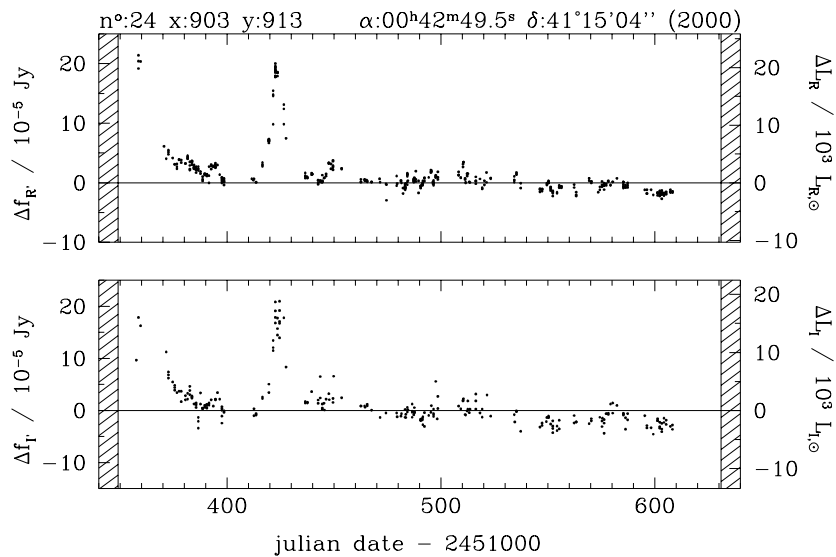
Figure 4.9: Light curve of an eruptive variable, which could be mistaken as a microlensing event, if the time coverage were insufficient. Upper panel: R' band, lower panel: I' band.
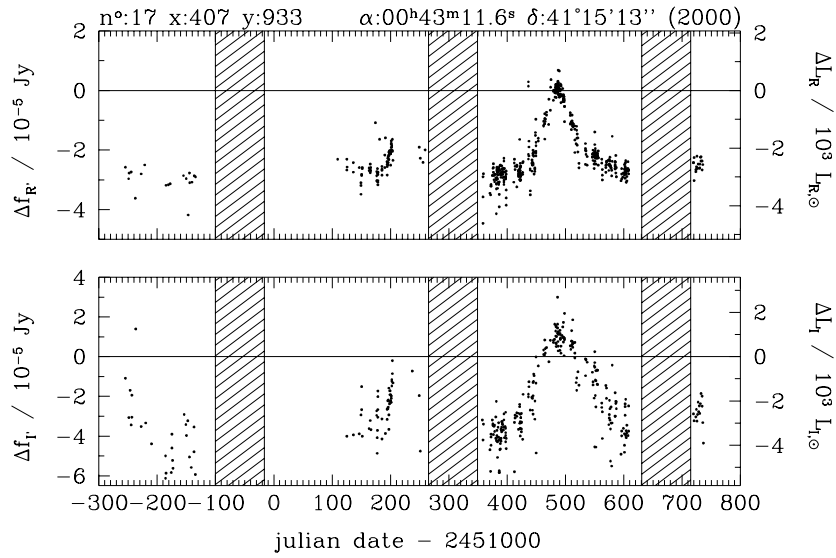
Figure 4.10: Light curve of a longperiodic variable. Upper panel: R′ band, lower panel: I′ band. Note, that insufficient time coverage could result in a false identification of this variable as a microlensing event.
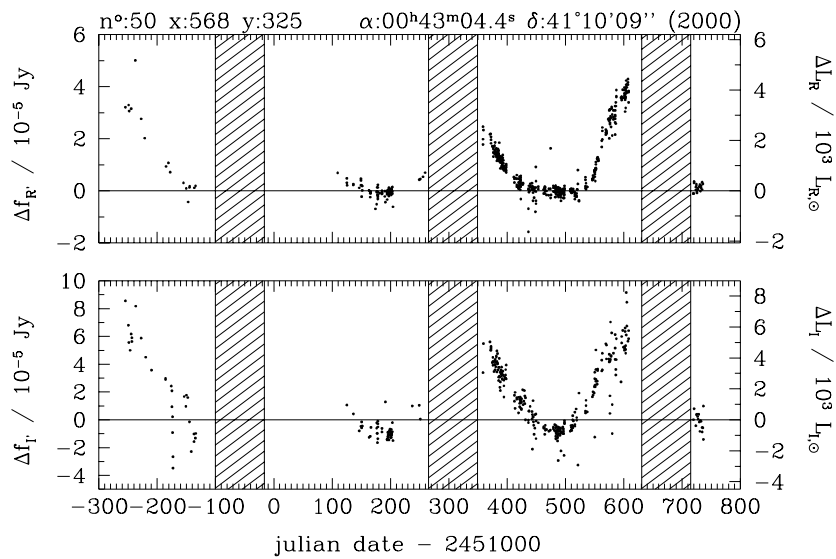
Figure 4.11: Light curve of a longperiodic variable star. Upper panel: R′ band, lower panel: I′ band.
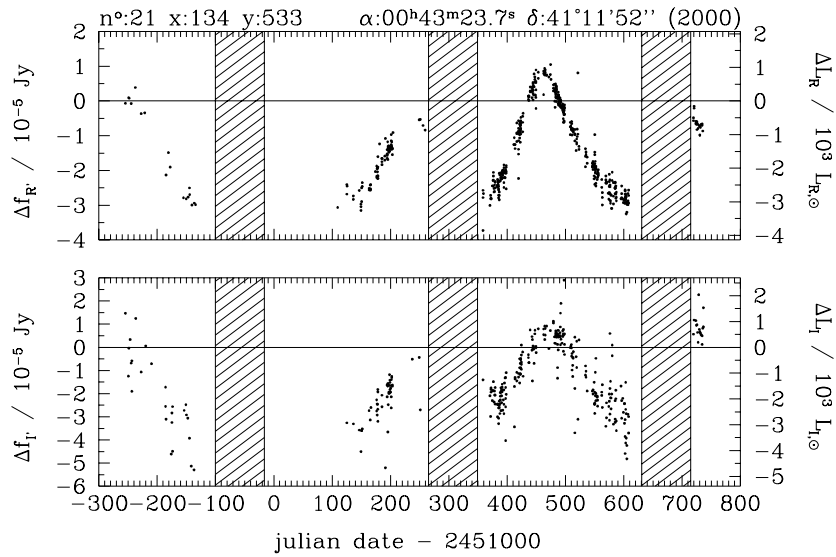
Figure 4.12: Light curve of a longperiodic variable star. Upper panel: R′ band, lower panel: I′ band.
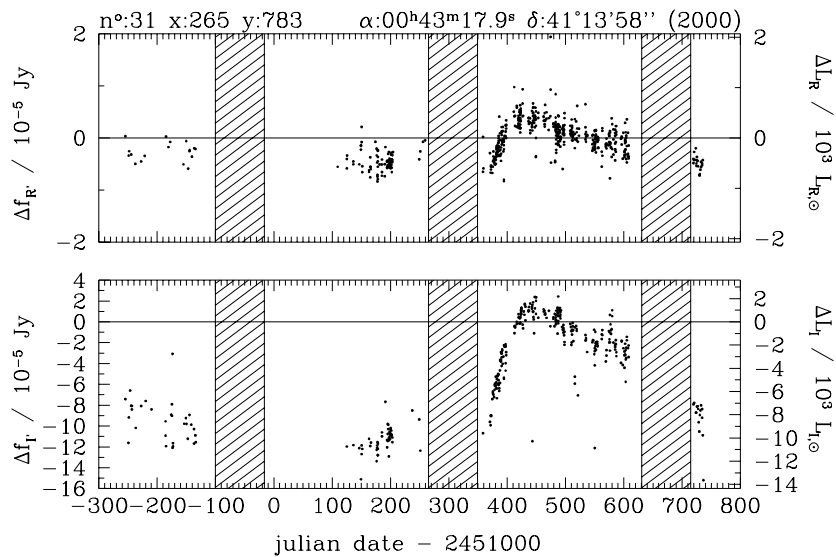
Figure 4.13: Light curve of a longperiodic variable star with a very large variation in the I′ band. Upper panel: R′ band, lower panel: I′ band.
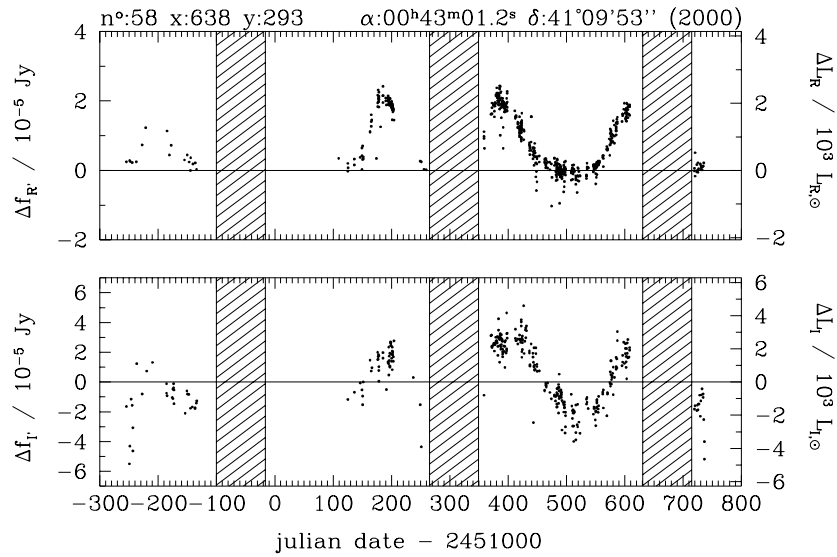
Figure 4.14: Light curve of a longperiodic variable. Upper panel: R' band, lower panel: I' band.
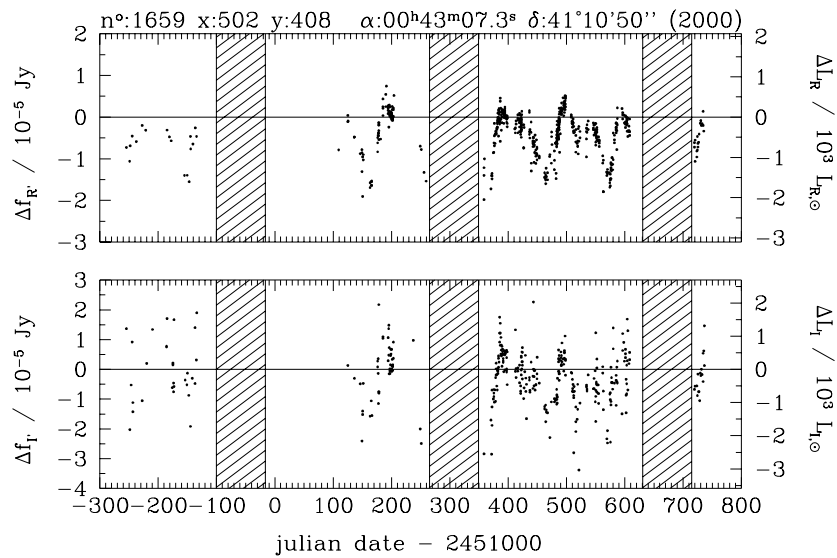
Figure 4.15: Light curve of a RV Tauri star in the R' (upper panel) and I' (lower panel) bands. Due to the optimal time coverage, the typical double-wave shape with alternating deep and shallow maxima of the light curves of this class of variable stars is uncovered.

Chapter 5

Optimal image analysis

5.1 Abstract

The largest technical challenge of the WeCAPP project is the photometry of variable sources in the highly crowded center of M31. The so called "difference imaging analysis" (DIA) allows to identify variable sources and to measure their excess flux relative to a reference image; at the same time this technique is (up to their photon noise) "insensitive" to the presence of non-variable sources. The application of the DIA requires an optimal reduction of images since they have to be 'equal' before subtraction except for their variable sources. To achieve that optimal reduction a lot of new data reduction tools have been developed, which are partly described already in Gössl & Riffeser (2002) and partly presented in this chapter for the first time.

We present a reduction pipeline for CCD (*charge-coupled device*) images which was built to search for variable sources in highly crowded fields like the M 31 bulge and to handle extensive large time series databases. We describe all steps of the standard reduction in detail with emphasis on the realization of per pixel error propagation: Bias correction, treatment of bad pixels, flatfielding, and filtering of cosmic rays. The problems of conservation of the PSF (*point spread function*) and error propagation in our image alignment procedure as well as the detection algorithm for variable sources are discussed: We build difference images via image convolution with a technique called OIS (*optimal image subtraction*, Alard & Lupton, 1998), proceed with an automatic detection of variable sources in noise dominated images and finally apply a PSF-fitting, relative photometry to the sources found. The complete per pixel error propagation allows us to give accurate errors for each measurement.

5.2 Introduction

Astronomical imaging in optical wavebands is performed nearly exclusively with *charge-coupled devices*[1] today. Despite the numerous advantages of modern CCDs, their images still have to be corrected for a couple of disturbing influences and effects before one can base advance in science on them. Here, we will focus on the problems arising with optical, ground based imaging and time-series observations to find and measure variable sources either hidden in a bright background (e.g. a variable star in its host galaxy) or a crowded field or even in a combination of both.

---

[1] The history of CCDs in astronomy and a basic description of them can be found in McLean (1997); Buil (1991); Jacoby (1990); Mackay (1986).

The search for variable objects with common photometry methods becomes very ineffective in crowded fields because of blending. Phillips & Davis (1995) show algorithms for registering, matching the point spread functions (PSFs), and matching the intensity scales of two or more images in order to detect transient events. Tomaney & Crotts (1996) propose a method called *Difference Image Analysis* (DIA) where the point spread function (PSF), describing the projection of a point source onto the image plane, is matched by calculating a convolution kernel in Fourier space. This method has been applied to Galactic microlensing (Alcock *et al.*, 1999) as well as for microlensing in M 31 (Crotts *et al.*, 1999a). A new method for *Optimal Image Subtraction* (OIS) of two images has been designed by Alard & Lupton (1998). They derive an optimal kernel solution from a simple least-squares analysis using all pixels of both images. This method has been used successfully in different projects (OGLE, Wozniak, 2000; MOA, Bond *et al.*, 2001; DIRECT, Mochejska *et al.*, 2001; etc.).
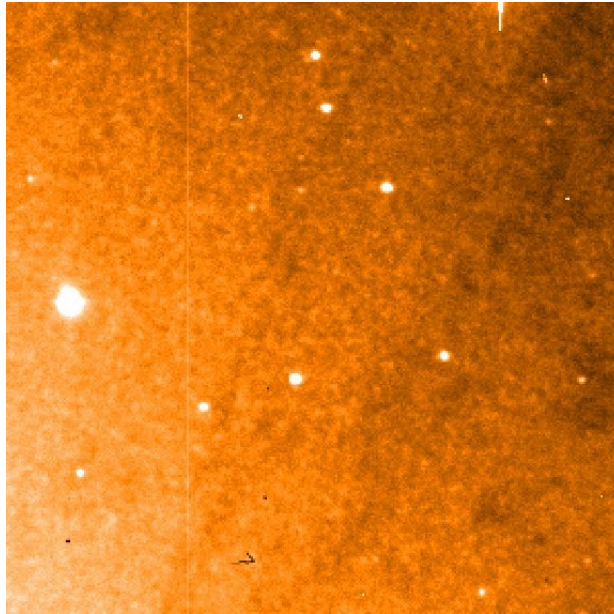
Figure 5.1: Example of a raw image. This is a 300×300 pixel region within a raw CCD image showing a part of the M 31 bulge taken at the Calar Alto 1.23 m telescope, Feb. 3rd, 2001. (WeCAPP project, Riffeser et al. 2001.)

5.3 Overview

Our pipeline combines all reduction steps from de-biasing of the images until the final measurements of the light curves in one software package, including full error propagation from the first reduction step to the last:

   i) standard CCD reduction including de-biasing, flatfielding and filtering of cosmics

  ii) image position alignment using a 16 parameter interpolation for non-integer pixel positions

 iii) stacking of frames

iv) photometric alignment

v) PSF matching using OIS (Optimal Image Subtraction), a method proposed by Alard & Lupton (1998)

vi) generation of difference images

vii) detection of variable sources

viii) PSF-photometry of the variable sources

We have to consider all properties of raw CCD images (Tab. 5.1) before we can establish a reliable difference image analysis. When estimating photometric errors all these effects and their errors have to be taken into account in addition to the photon noise induced by the imaged objects. For each pixel, all sources of errors (photon noise, read-out noise, flatfield errors, saturation) have to be included and propagated through all steps of the datareduction.

origin of phot. error	property of error
detector:	photosensitive area and additional "borders" (prescan, postscan, overscan), geometric variation of pixel size and edge pixels, pixel sensitivity variations and pixel defects (cold pixel, hot pixel, trap), sub-pixel quantum efficiency variations, charge transfer efficiency (CTE), linearity range and saturation level.
electronics:	bias, gain, ADC width, sampling (of charges), thermal noise.
instrument:	dust in optics and optic distortions, optical scale and detector pixel size (and their ratio to the typical seeing – spatial sampling), file format (e.g. FITS - Flexible Image Transport System, see Wells *et al.* (1981); Greisen *et al.* (1981); Grosbol *et al.* (1988); Harten *et al.* (1988); Ponz *et al.* (1994)), and information beyond raw image (header keywords).
environment:	signals originating from particle events (cosmic rays), varying meteorological observing conditions (seeing), and other atmospheric effects like sky illumination (moon) and extinction.

Table 5.1: Properties of errors of raw CCD images and their origin.

5.4   Name convention

Our image names contain object, filter, date, instrument, and number separated by underscores, i.e.

- *m31*, *sky*, *dom*, *bia*, as object abbreviations

- *r*, *i*, as filter abbreviations

- *YYMMDD* as date format

- *TWS*, *S27* as instrument abbreviations

- a 3 digit number to account for different observations in the same night

Each reduction process adds a specific letter, i.e. *a* for adding images. The reduction letters are separated from the raw name by a "–". This name convention is unambiguous, for example
`dabtcbedb-m31_i_991222_TWS_027.fits`

5.5   Standard reduction

This chapter describes the standard reduction for individual object and calibration frames. All effects of Tab. 5.1, which can be corrected in single images, will be discussed. We show how to account for saturation and carry out bias subtraction, dark and shutter correction, marking bad or low count pixels, and include these steps into the error budget of each pixel.
For the first steps we use the mupipe-program `biasredux`[2].

5.5.1   Saturation and blooming

Ideally CCDs have a range within which photons are linearly converted to ADUs (Analog Digital Units). For large photon- and thus electron numbers the conversion to ADUs becomes non-linear and saturates. The saturation is set by the maximum charge a CCD pixel can contain, before charges flow into neighboring pixels, which is called blooming.
We keep track of pixels with counts above the linear range by marking them. The linearity threshold is 64000 ADUs for the MONICA-CCD[3]. Blooming occurs close to saturated pixels, but bloomed pixels do not necessarily have to exceed the linear or saturation threshold themselves. Since the blooming
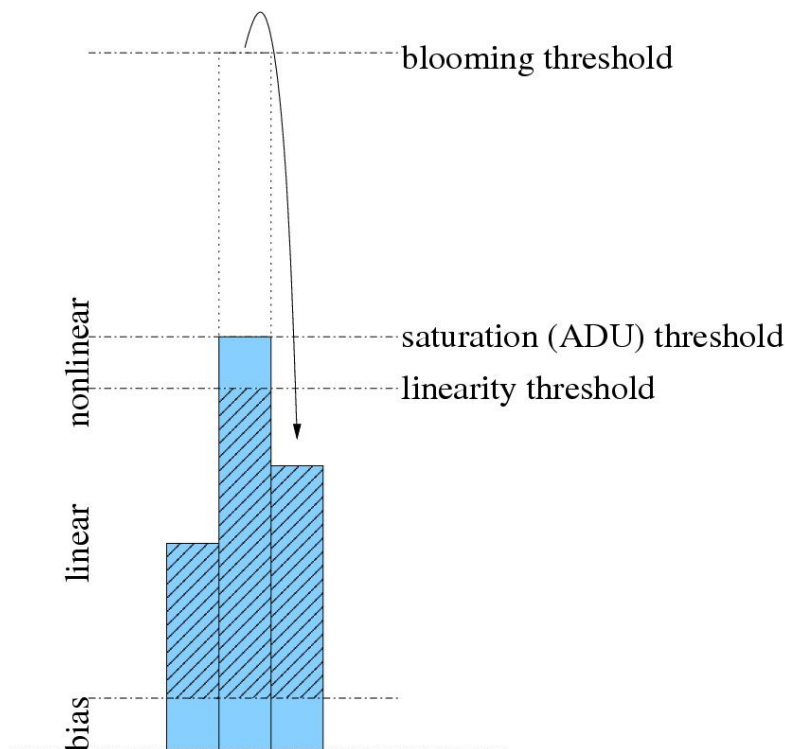

Figure 5.2: Different intensity intervals for a CCD. Our reduction pipeline extracts the scientifically relevant part (lined parts) and marks all other interval.

---

[2] `biasredux -g $GAIN -m $MASK -h $SHUTTER -r $OVERSCAN -s $SATURATE -t $HIGHTRESH -l $LOWTHRESH $SKYFLAT`
[3] the camera mounted on the 80 cm telescope on the Wendelstein

level is normally set (depending on the gain) high above the largest possible ADU level (2^{16} for actual CCD devices), we define "bloomed" pixels as those reaching this highest ADU level. We are even more conservative and fix this saturation level to 65000 ADUs. Since this blooming goes either in x or in y direction (depending on the CCD design), a certain number of neighbor pixels in one of these directions has to be removed to exclude blooming pixels: for calibration images we use 10 pixels (to remove also part of the underlying stars), for science frames only 1 (to keep as much information as possible).

We perform this step in first place, because only these raw frames contain the unchanged information regarding blooming and saturation (after bias subtraction this information would be changed).

5.5.2 Bias correction

Each CCD has a bias level, i.e. a minimum ADU level which is generated also if no photons were detected. This originates from the offset voltage of the CCD ADC (analog-digital converter) which is set to have only positive current. The bias level can be different depending on CCD hardware and is also temperature dependent. Therefore each frame can have slightly different bias levels, which can be hardly derived in an science frame directly.

To remove it we use the overscan or prescan regions[4]: these regions are not exposed and therefore in an ideal case they directly show the bias level. This can be checked by so-called bias frames, where the image is not exposed but instantaneously (after cleaning) read-out.

Sometimes also some features are present due to CCD defects (We check the reproducibility by looking for patterns in a mean bias image):

- If these patterns in the bias frame are varying on short time scales, or there is no pattern at all (just thermal noise), we subtract only the $\kappa\sigma$-clipped mean of a suitable part of the overscan (i.e. a part of the overscan, which is identical in exposed frames and in dark, not exposed frames). Since the bias is an additive constant and usually a small number the $\kappa\sigma$-clipped mean ($\kappa \approx 6$, to get rid of cosmics) will be more accurate than the median.

- Real bias frames show some offset between overscan, prescan and bias on the exposeable frame. If the bias patterns are stable in time, to account for the offset and for these features a so-called "masterbias" frame is created. For this purpose many overscan corrected bias frames are combined using $\kappa\sigma$-median-clipping to reduce the intrinsic electronic noise (which is always present). This masterbias frame describes the "true" bias frame of images up to an additive constant (due to overscan correction). This additive constant can be obtained from the overscan of each image and of the masterbias. The levels of the two overscans are again derived by $\kappa\sigma$-clipping.

$$\text{bias}_{\text{image}} = \text{masterbias} + (\text{overscan}_{\text{image}} - \text{overscan}_{\text{masterbias}}) \tag{5.1}$$

For the MONICA-CCD the bias voltage is contaminated by an antenna signal: instruments at Wendelstein are exposed to high MHz to GHz radiation caused by the "Mobilfunk" in vicinity of the observatory. We succeed to reduce the impact of this radiation by shielding the CCD detector by a cooper ton.

We account for three types of errors, which can occur when the bias is subtracted:

---

[4] The overscan is the part of the CCD, which is physically present but not exposed, prescan is called the part which is virtually read-out but not physically present.
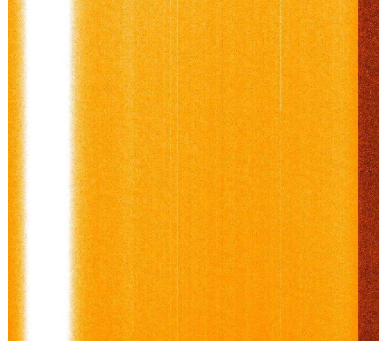
Figure 5.3: Typical bias image of a 2k × 2k CCD detector. The lower right side marks the overscan region. The bright (white) vertical stripe marks a bias defect.

- statistical error: The readout noise is due to thermal noise of the amplifier, and, if present, of the dark current.

- systematic error: Unreproducible bias patterns may result from bad CCD electronics or insufficient electronic shielding (Strong immission may even penetrate an excellent shielding).

- numerical error: Error resulting from the numerical determination of the bias level.

5.5.3 Generation of the error frame

The error in each pixel can easily derived from the number statistics of photons. Since our CCD frames already consist of ADUs we have to know the conversion factor between ADUs and photons the so-called gain. It is usually larger than one and converts more than one photons into one ADU count. In case of the MONICA CCD we derived the gain to be 3.37. A simple method to derive the gain is to use images with bright sky level correct them for pixel-to-pixel variations and to derive the standard deviation in a flat area. The relation between gain, error and ADUs can than written

$$\sigma_{\text{ADU}} \cdot \text{gain} = \sqrt{\text{ADU} \cdot \text{gain}} \tag{5.2}$$

using Gaussian approximation of the Poisson noise. In reality the gain is different in each pixel, but the variations should be small and not relevant for further reduction.

For simplicity we transform all images to photon level, because then the error frame can be easily compared to the noise and the telescope zero point (ZP), which is usually given in photons per sec.

All saturated or bloomed pixels marked in th first step are now set to -1 in the error frame.

Our error frames are similar to a data-quality mask as used in many pipelines, but differ in that their values are not representative flags but actually numerical errors, with the exception of saturated and bad pixels which are represented by simple flags (-1, 0).

Each pixel (x, y) in an image I has an initial error $\delta_I(x, y)$ resulting from the photon noise, the bias noise (i.e. readout noise) plus the error in determination of the bias level:

$$\delta_I(x, y) = \sqrt{\frac{\text{counts}_I(x, y) - \text{bias}_I}{\text{gain}_I} + \sigma_{\text{bias}_I}^2 + \frac{\sigma_{\text{bias}_I}^2}{n_{\text{bias}_I}}} \, , \tag{5.3}$$

where

counts$_I$	=	flux of pixel (x, y) in image I in ADU,
bias$_I$	=	bias of the image,
gain$_I$	=	$\frac{\text{photons}_I}{\text{ADU}}$ = conversion factor,
σ_{bias_I}	=	we use the $\kappa - \sigma$-clipped RMS ($\kappa = 6$) of a suitable part of the overscan as an estimation for the bias noise (i.e. readout noise),
n_{bias_I}	=	number of pixels actually used for the bias determination.

If we use a small clipping factor ($\kappa < 3$) for the determination of the bias noise, σ_{bias_I} will be underestimated and therefore has to be corrected by a factor $1/C_C$ where

$$C_C = \text{erf}(\kappa/\sqrt{2}) = \frac{1}{\sqrt{2\pi}} \int_{-\kappa}^{\kappa} e^{-\frac{1}{2}\hat{\kappa}^2} d\hat{\kappa} \,. \tag{5.4}$$

Reproducible bias patterns can be determined with an accuracy only limited by the applied numerical precision, so their error may be neglected.

We mark saturated pixels in the error frame by setting them to minus one, which will be dominant in any error propagation from now on to prevent the use of saturated pixels.

5.5.4 Dark correction

It is important to know how many ADUs are created on a CCD even without having any shutter opened. Our CCD does not show any dark current on a relevant level, and therefore dark correction turned out not to be necessary.

5.5.5 Shutter

The opening and closing of the shutter of each camera implies a position dependent exposure time[5]. For science frames exposures are large compared to the shutter opening time and shutter effects could be neglected. This is not the case for calibration frames taken during dusk and dawn with short exposure times (due to the high sky brightness).

If the shutter movements show a predictable time dependency, the flatfields can be cleaned from the two-dimensional shutter pattern as proposed by Surma (1993).

To test this effect the movement of the shutter and the measurement of the exposure time has to be understood. Fig. 5.4 shows a simplified configuration of the relevant time scales for the MONICA CCD. As soon as the command for beginning the exposure (written to the image header) is sent the shutter starts to open and the center is immediately exposed, while the exposure of the edges starts on half way, as the shutter moves out of the image. As soon as the command for the exposure end is send the shutter starts to close, but takes approximately half way to reach the exposed CCD part.

---

[5] Assuming an average flatfield charge per pixel of $160\,000$ electrons the shutter pattern will exceed one σ photon noise, if the exposure time is shorter than 400 times the shutter movement time (opening plus closing) of a non photometric shutter. E.g. for an iris type shutter and a total shutter movement of $10\,\text{ms}$ the exposure time has to exceed $4\,\text{s}$ just to have the additional shutter error not bigger than the photon noise. Since the shutter movement is a systematic effect, the combination of many short time flatfields will even enhance that error by increasing their fraction of all used flats and therefore amplifying their impact on the resulting flatfield.
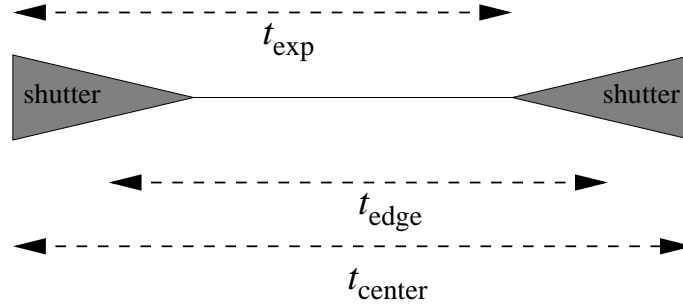
Figure 5.4: Simplified shutter model: t_{exp} is the exposure time written in the header of the image (from opening signal to closing signal), t_{center} is the exposure time for the central part of the images, t_{edge} is the exposure time for regions near the edges of the images.

Therefore for the Wendelstein CCD camera t_{exp} is approximately equal the exposure time of the CCD edges t_{edges}. The exposure time of the center is nearly that time longer the shutter takes to open/close. With this simplified model we are able to derive the shutter correction using calibration exposures in the dome[6].

Our aim is to extract the time S which has to be added to the (header-)exposure time to get the real exposure time due to the shutter movement depending on different CCD positions (x, y).

Then the flux per unit time $I_1(x, y)$ reaching the shutter and the measured intensity $I(x, y)$ behind the shutter are connected by

$$I(x, y) = t_{exp} \cdot I_1(x, y) + S(x, y) \cdot I_1(x, y) \tag{5.5}$$

A shutter correction $S(x, y)$ can be created by comparing long integration flats to short integration flats[7]. $S(x, y)$ has to be added to the exposure time to correct for the shutter effect.

We define a long integration flat $t_L \gg S$ with

$$I_L = t_L \cdot I_1 + S \cdot I_1 \quad . \tag{5.6}$$

Since this implies a constant light source, we interpolate (average) two short exposures before and after the long exposure. Then I_1 of the long exposure is nearly in between (for slightly varying light and consecutive exposures) of

$$I_S = (t_S \cdot I_1' + S \cdot I_1' + t_S \cdot I_1'' + S \cdot I_1'')/2 \approx t_S \cdot I_1 + S \cdot I_1 \tag{5.7}$$

Although long and short exposure could be divided and the unknown intrinsic flux I_1 would cancel out

$$\frac{I_S}{I_L} = \frac{t_S + S}{t_L + S} \quad \Rightarrow \quad S = \frac{t_S \cdot I_L - t_L \cdot I_S}{I_S - I_L} = \frac{t_L \cdot I_S - t_S \cdot I_L}{I_L - I_S} \tag{5.8}$$

this is not recommendable since I_S would be quite noisy (short exposure). Averaging over a sample of $(I_S/I_L)_i$ can solve this problem, but still the division enlarges the noise.

---

[6] Note that the shutter in reality does not open with the same movement as closing, neither the movement has constant velocity. Also the estimate that that the shutter reaches the edges of the CCD at half of his way is only an rough simplification.

[7] For MONICA on short exposures a six-petal shutter is blocking light from the CCD.
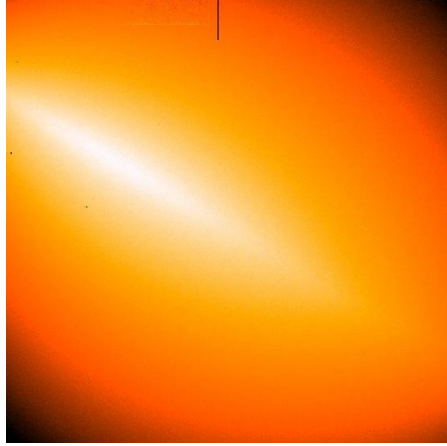
Figure 5.5: Real shutter pattern: bright areas mark regions where the shutter opened first, dark areas where $S(x,y)$ is small.

Alternatively we motivate transforming

$$\frac{I_S}{t_S} - \frac{I_L}{t_L} = \frac{t_S \cdot I_1 + S \cdot I_1}{t_S} - \frac{t_L \cdot I_1 + S \cdot I_1}{t_L} = \frac{t_L - t_S}{t_S t_L} S \cdot I_1 \tag{5.9}$$

to

$$S = \left(\frac{I_S}{t_S} - \frac{I_L}{t_L} \right) \frac{t_S t_L}{t_L - t_S} \frac{1}{I_1} = \frac{t_L \cdot I_S - t_S \cdot I_L}{t_L - t_S} \frac{1}{I_1} \tag{5.10}$$

For a sample of N exposures we then can write

$$S \approx \frac{t_L \cdot \sum I_S - t_S \cdot \sum I_L}{t_L - t_S} \frac{t_L}{\sum I_L} \tag{5.11}$$

assuming $t_L \gg S$ and $I_1 \approx \frac{\sum I_L}{N t_L}$.
Having derived the shutter frame $S(x,y)$ in this way we can correct the science frames and calibration frames using

$$I_1(x,y) \cdot t = \frac{t}{t + S(x,y)} I(x,y) \tag{5.12}$$

The advantage of this method is that images have not to be normalized, because depending on the normalization region different results are achieved!

5.5.6 Bad pixels

We investigate flatfields and darks with a large spread of exposure times and counts to identify cold pixels, traps, coating defects, and hot pixels.
We obtained all nonlinear pixels by dividing two high signal-to-noise domeflat frames, where the first flat results from a combination of low count images (e.g. 1000 ADUs) and the second one from high count images (e.g. 50000 ADUs). Pixels with values deviating more than 5 σ (using propagated error

frames) from expected values were added to the bad pixel mask. Since each CCD chip undergoes aging, the mask has to be modified at least once per year. This mask is used in the reduction process to set the values of all non-linear pixels in all frames and their error frames to zero. The value of zero ADUs is not treated as an algebraic number, but as a flag for "no photometric information" in the following.

5.5.7 Photosensitive region

Since the overscan and prescan are not needed any more, the frame is trimmed to its exposed part. We also exclude bad rows and columns at the CCD boundary; in some CCDs the first row is broken or the edges of the photosensitive area are up to 20% larger in effective size than average pixel. For MONICA images we extract the area within $x = 51, \ldots, 1073\,\mathrm{px}$ and $y = 19, \ldots, 1039\,\mathrm{px}$.

5.5.8 Low counts pixels

We also exclude all pixels with "low" counts from contributing to our data for several reasons:

- bad pixels can have developed since the last bad pixel mask was generated (aging)

- each CCD has a non linear range due to a bad *charge transfer efficiency* (CTE) at low pixel charges[8]

The "low count rate" level was set to 10 ADUs (i.e. marginally above the bias) for science frames and high values of up to 1500 ADUs for calibration frames.
Like the defective pixels (Sect. 5.5.6) those pixels will be estimated later (Sect. 5.10.1), where it is possible.
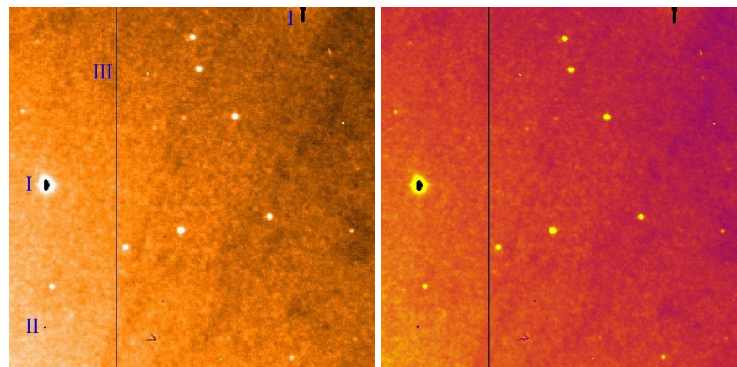
Figure 5.6: Bias corrected and bad pixel masked image (*left*) and error frame (*right*), composed of photon noise and bias noise: Masked pixels are saturated and blooming affected pixels (I) and CCD defects (hot and cold pixels (II) and a bad column (III)). Before subtraction the bias level of individual frames is estimated from the overscan region and a masterbias ($\kappa\sigma$-median-clipped mean of multiple bias frames).

---

[8] Since we do not have to deal with short exposures of bright objects in empty fields this procedure does not result in ignoring the vast majority of pixels in a dataset. When dealing with empty, low count backgrounds we propose to follow e.g. McLean (1997) and to add a *"fat" zero* by preflashing the CCD.

5.6 Flatfield correction

In the "flatfield correction" step so-called "flatfield" images are built (e.g. from bright sky images obtained during dusk or dawn) and used to correct for pixel-to-pixel variations and for the absorption of the instrument including filters and dust. We separate this step from the "standard reduction" since a lot of points have to be taken into account, which make human-eye-control necessary.

5.6.1 Flatfielding philosophy

In order to normalize the apparent photon sensitivity of all pixels in a single CCD frame, a calibration image (flatfield image) has to be built. In an ideal case this would be the image of an extended, homogeneous, flat, and white object at infinity. The apparent photon sensitivity results from geometric size, coating, and electronic properties of each single pixel, and, in addition, from the inherent properties of the optics, and finally dust in the optics. Since it is not feasible to get close to the ideal case using dome flats, we improved the methods to extract the relevant information from skyflats. The daylight sky would be ideal case for flatfield images, but it is much too bright. Therefore getting skyflats is restricted to dusk and dawn. The superiority of twilight flatfields over dome flatfields is well known and e.g. discussed in Buil (1991); Mackay (1986). Nevertheless, domeflats and twilight flats can be used effectively in combination as described in Sect. 5.6.8.

5.6.2 Absorption and distortion

It is important to distinguish between spatially varying absorption in the instrument and field distortion. Both effects produce a flatfield which is not 'flat', but affect point sources in a different way:
In the case of absorption the PSF shape remains the same, but the PSF amplitude is reduced and fewer photons arrive at the CCD, which is then corrected by the flatfield.
In the case of field-distortion the photon number arriving at the CCD remains the same but is spread over a larger area (the PSF gets distorted). Dividing by the flatfield increases the flux within the PSF. Therefore after correcting the frames the zero-point (ZP) is not constant over the image. For this reason for distorted images the distortion has to be corrected not conserving the flux! Note that normally distortion is accompanied by absorption.

5.6.3 Observation strategy for flatfields

Accurate flatfields are most important to avoid systematic photometric errors. To minimize the noise of skyflats a (possibly large) sample of flatfields are exposed and combined. We require at least five flatfield images per used filter, fulfilling following constraints:

- The individual flatfield images should have count levels as high as or higher than a typical single science image of the same night (see Sect. 5.6.4 and 5.6.8). Nevertheless, flatfields with fewer counts are preferred relative to having less than five flatfields.

- Exposure times should be adjusted in that way to have high signal to noise in all skyflats, which often requires experienced observers or self-adjusting flat field imaging software. At least exposures have to be long enough to avoid residuals of the shutter but short enough to avoid saturation.

- Flatfields should be taken in "blank fields" (i.e. fields with a small number of bright stars).

- The telescope should be (roughly) focused to minimize the number of pixels affected by stars. This is difficult for dusk flatfields, because one cannot make a focus series of a star before starting with the flat series for obvious reasons. Also guiding is important to minimize the area contaminated by stars.

- For dusk/dawn skyflats the telescope position has to be moved slightly to avoid overlapping of stars. We use some small pointing offsets, so that the $\kappa\sigma$-clipped median of the series are clean of stars for all pixel positions. We have found an offset of $30''$ to be sufficient.

- Diffuse light contamination (i.e. reflections from inside the dome) has to be avoided. Otherwise this results in a mixture of dome and sky flat with improper illumination[9].

With the Tyson & Gal (1993) twilight formula one can easily estimate, that it is impossible to obtain five flatfield images (following from above constraints) for more than one filter, if the CCD wipe and readout time exceeds three minutes. We have found that in this case it is better to take flat series for one filter per twilight only and to alternate the filters for each twilight period, instead of combining several suboptimal flatfield series.

5.6.4   The importance of error propagation – an analytic example

We show that the errors from flatfield calibration (Sect. 5.6) can dominate the total error of a reduced science frame.

Given the pre-reduced science images with photon counts of $I(x,y)$ and a photon noise dominated total error of $\delta_I(x,y) \approx \sqrt{I(x,y)}$ and a flatfield $F(x,y)$, the flatfield corrected pixel stack can be written as

$$\tilde{I}(x,y) = \sum_{j=1}^{n_I} \frac{I_j(x,y)}{F(x,y)} \approx n_I \, \frac{I(x,y)}{F(x,y)} \tag{5.13}$$

where the last step assumes that $I := I_l \approx I_k$ for $l \neq k$ holds. See Tab. 5.2 for common components of formulae used throughout this section.

We show for 3 cases how the flatfield errors enter the error of flatfielded and stacked science frames:

i) If one assumes that the flatfield values are of order one and if one ignores the flatfield error the pixel error of the stacked images becomes

$$\delta_{\tilde{I}}(x,y) \approx \delta_I(x,y) \, \sqrt{n_I} \, . \tag{5.14}$$

---

[8] Our blank fields are clean of bright stars within the field of view of the cameras used (less than 17×17 arcmin^2). Since we also use only small, 1m-class telescopes there is no considerable light contamination beyond the $30''$ limit of moderately bright stars or galaxies at average flatfield exposure times.

[9] One can check the impact of this light pollution effect by turning on a weak dome light while taking an image in a new moon night. We have improved considerably the situation at the Wendelstein telescope by painting the interior dome surface black.

(x,y)	$=$	pixel coordinates,
$I(x,y)$	$=$	value of pixel (x,y) in image I (in photons),
$\delta_I(x,y)$	$=$	corresponding absolute error,
$\tilde{I}, \hat{I}, \bar{I}$	$=$	sequence of indicators, that some reduction step has been applied to I,
n_I	$=$	integer number of e.g. images of type I,
σ	$=$	the root mean square of a sample.

Table 5.2: Common components for the notation of formulae.

ii) Let $\delta_F(x,y)$ be the flatfield error, and $\xi(x,y) := \frac{\delta_I(x,y)}{I(x,y)} \Big/ \frac{\delta_F(x,y)}{F(x,y)}$ be the ratio of the relative errors between the flatfield and a single science image. The propagated pixel error depends on the individual signal-to-noise ratios of the images and the flatfield, and on dithering.

If spatially undithered images are stacked the flatfield error $\delta_F(x,y)$ always enters the same physical position in the I/F ratio and flatfield error part of the stack is not an independent error. It is like stacking first and flatfielding later:

$$\delta_{\tilde{I}}(x,y) \approx \delta_I(x,y) \sqrt{n_I \left(1 + \frac{n_I}{\xi^2}\right)} . \tag{5.15}$$

iii) With spatially dithered (and digitally realigned) images we get (by neglecting errors of the alignment procedure)

$$\delta_{\tilde{I}}(x,y) \approx \delta_I(x,y) \sqrt{n_I \left(1 + \frac{1}{\xi^2}\right)} , \tag{5.16}$$

because independent flatfield pixels add to the pixel error of the stack.

An example: We consider an extended and bright object (e.g. the M 31 bulge), and twilight flatfields. Here we get $1 < \xi < 3$ because of the difficulties in getting twilight flats discussed in Sect. 5.6. In a dithered $n_I = 5$ stack this yields an up to 41% error increment and even a 145% increment in an undithered $n_I = 5$ stack, both compared to the simple estimate of Eq. 5.14, i.e. with respect to the Poissonian noise in the images before flatfield division.

The per pixel propagation of errors gets even more important when performing multi-pixel approximations, as we do in some parts of our data reduction pipeline for the difference image analysis. When performing e.g. PSF-fitting one can enhance the accuracy by including the appropriate error weights as stated in Sect. 5.15.2.

5.6.5   Calibration images ("masterflats") from domeflats and science frame

One standard approach to extract a so-called "masterflat" is to use dome flats and science frames: If the illumination of the science frames can be extracted (under the assumption that they have the true illumination with $\mathrm{sky}_{\mathrm{moon}}(x,y) = \mathrm{const}$), the multiplicative correction for a domeflat to a masterflat is[10]

   i) illumination := **combine** $(\mathrm{science}_i - \mathrm{bias})$

  ii) pixelvariations := **combine** $(\mathrm{domeflat}_j - \mathrm{bias})$

 iii) correction := **smooth** $\left(\frac{\mathrm{illumination}}{\mathrm{pixelvariations}} \right)$

  iv) masterflat $=$ pixelvariations $\times$ correction

The combination of domeflats allows a high-signal to noise for the pixel variations. But since domeflats never have the right illumination, they have to be corrected.
The combining and smoothing function can be executed, e.g. by medianing or clipping and respectively by polynomial approximation or spline interpolation.
Note that for twilight (skylight) flats the "true illumination" may be hidden by the observed sky gradient: $\mathrm{illumination}(x) \times s_0 + s_x x + s_y y$ (see next Sec. 5.6.6).

5.6.6   Measuring the true illumination

Wrong illumination in the skyflats may destroy photometry: for example using the illumination gradient from science images for the flatfielding procedure, flattens all science frames. This can be wrong since flatfielding corrects multiplicative terms, but skylight is an additive feature. Therefore using different gradients in the flatfields for different measurements leads to large systematic offsets on the CCD.
To check for the true illumination we suggest a very simple method:
Assuming that the illumination gradient is only linearly depending on x and y, we can rotate the field by $180°$ (12 h for HA) between two images. Normalizing and adding these two images results in images where the skylight illumination gradient cancels out. These method can only be applied to domeflat field or night-sky-blank-fields, since dusk/dawn-skylight normally has a changing gradient in time. Applying to blank-fields the night sky has not to change during the two observations. Therefore cloudy night sky is not very useful. Applying to domeflats a homogeneous illumination inside the dome is needed; intensity variation of the light source is not dramatic since the domeflats are normalized before adding. For telescopes with RA-DEC mounting the field can only be rotated if the declination is fixed at $\delta = 90°$. Note that the exposure time should be long enough (≥ 30 sec) so that shutter effects are negligible. The method can be verified for different telescope angles in HA, but always two images rotated by $180°$ have to be combined. For different combinations the result has to be the same, else the method is not usable.

---

[10]If the bias is unknown but constant, one can nevertheless extract the domeflat (if exact calibration lamps were used and exact exposure times t_i are accessible) making pairwise differences of differently exposed domeflats: $\mathrm{dom}_1(x) = t_1 \mathrm{dom}(x) + \mathrm{bias}(x)$, $\mathrm{dom}_2(x) = t_2 \mathrm{dom}(x) + \mathrm{bias}(x) \Rightarrow \mathrm{bias}(x) = \frac{t_2 \mathrm{dom}_1(x) - t_1 \mathrm{dom}_2(x)}{t_2 - t_1}$

5.6.7   Bringing calibration flat frames to the same illumination

The prereduced flat frames, which are used for the flat frame combination, must have the same (not stringently the correct) illumination. We use the program `compare` in the mupipe pipeline to transform an image f to the same illumination as an image f_{ref}:

- $d(x,y) = f_{\mathrm{ref}}(x,y)/f(x,y) \rightarrow \mathrm{norm}_d$

- $d_{\mathrm{norm}}(x,y) = d(x,y)/\mathrm{norm}_d$

- $d_{\mathrm{norm}}(x,y) \overset{\mathrm{clipping}}{\rightarrow} d'_{\mathrm{norm}}(x,y) \overset{\mathrm{fitting}}{\rightarrow} d_{\mathrm{poly}}(x,y)$

- $f_{\mathrm{corrected}}(x,y) = f(x,y) \times d_{\mathrm{poly}}(x,y)$

We explain our algorithm comparing two frames: The idea is to divide the reference image by the second image, normalize this, and then to extract a smoothed illumination ratio. The difficulty is again to remove residual stars in the image, the dust should have already disappeared by the previous division. We used a modified clipping filter on the divided frame to remove outliers in both directions: if a pixel value exceeds/under-runs the 3rd lowest/highest pixel in a circular area with a radius of 10 by a factor four times larger than the propagated error, this pixel is rejected. This leads to a very strict rejection. The resulting frame has still enough pixels to fit a polynomial of order 4 with 25 free parameters. This polynomial fit is then used to correct for the wrong illumination in the second frame

5.6.8   Flat frame combination with κ-σ-clipping

The final flatfield frame is combined of individual flats following this standard recipe:

i) We follow the steps described in Sect. 5.5.1 to 5.5.8 for the individual flatfield images to build appropriate flats I and their correspondent error image δ_I.

ii) Then we normalize all flats by dividing them with the median C_I of a central area of the CCD

$$F_l = I_l/C_I \,. \tag{5.17}$$

We determine the median only in the central quarter of the full frame in order to minimize the impact of differential illumination gradients when combining the flats[11].

iii) To get rid of stars, cosmics, and differential illumination we build a $\kappa\sigma$-clipped mean of the normalized flat frames F

$$\tilde{F}(x,y) = \frac{\sum\limits_{F}^{n_{\mathrm{used}}} F(x,y)}{n_{\mathrm{used}}} \,. \tag{5.18}$$

For each pixel the outliers are excluded by $\kappa\sigma$-clipping, but we use the median instead of the mean as reference for the selection procedure because the median is less sensitive to occasional

---

[11] The gradient due to vignetting within this central area is median level $\pm$ 3% in our images. A higher gradient may still be acceptable as long as it is guaranteed that the "normalization median" lies within a well populated region of the normalization region's distribution.

outliers; the mean of the remaining pixel values yields the final calibration factor. We got the best results (least residuals) with $\kappa = 1.0$, which will preserve no more than two flats for most pixels. With only five single flats for combination a larger κ would leave residuals at the 3% level.

iv) We control the result of step iii) by inspecting all control frames $F_{\text{control}} = F/\tilde{F}$. They should neither show any signal < 1, like holes or shadows around stars[12], nor illumination gradients. Both effects would indicate residuals still left in the median flatfield.

v) Now we exclude those flats which cause residuals, and repeat the procedure in step iii) and iv), until there are no residuals left in the control images. If this would lead into having too few flats, we add the median flats of the days before and/or after to the median procedure.

vi) Since the pixel-to-pixel sensitivity variations are often exclusively due to the CCD itself and therefore only a weak function of time, one can enhance a flatfield (i.e. improve its signal-to-noise ratio) by combining the high spatial frequency, pixel-to-pixel variation of several twilight periods (or of very high signal-to-noise domeflats) with the smoothed flatfield for the observed night, whose low spatial frequency information can change from night to night due to dust shadows etc.

 (a) We smooth each median flat pixel within a box smaller than the typical projected size of the short-time-scale variation due to dust: Each pixel (x_0, y_0) is smoothed according to

$$\tilde{F}_s(x_0, y_0) = \frac{\sum\limits_{x,y}^{\text{box}} \tilde{F}(x,y)}{n_{\text{box}}} \text{ , where} \tag{5.19}$$

 n_{box} = number of pixels in the smooth box.

 (b) The pure pixel-to-pixel variation is given by

$$\tilde{F}_p(x,y) = \tilde{F}(x,y)/\tilde{F}_s(x,y) \text{ .} \tag{5.20}$$

 (c) The pixel-to-pixel variation flats are now combined by building a $\kappa\sigma$-clipped, median referenced mean as shown in step iii):

$$\hat{F}_p(x,y) = \frac{\sum\limits_{\tilde{F}_p}^{n_{\text{used}}} \tilde{F}_p(x,y)}{n_{\text{used}}} \text{ .} \tag{5.21}$$

 (d) The enhanced flatfield for the night can now be calculated via $\hat{F}(x,y) = \tilde{F}_s(x,y)\,\hat{F}_p(x,y)$.

This procedure has only been applied, if the observational circumstances will lead to a gain in the signal-to-noise ratio of the resulting flatfield. A comparable technique has been used to build high quality HST flatfields (Ratnatunga *et al.*, 1994).

---

[12] Since the contamination of a flatfield image with stars or cosmics always creates an additional signal, the origin of residuals in the control frames can be identified: Residuals with a signal > 1 are correctly removed features of an individual flat. Residuals with a signal < 1, which also should be perceivable in multiple control frames, must originate from the median flatfield.

vii) It is possible to check the gain (after a change of detector or an observational gap) using following correlation:

$$\text{gain} = \frac{1}{C_I \, \sigma^2_{F/\tilde{F}}} \quad \left(= \frac{C_I}{\sigma^2_{I/\tilde{F}}} \right) \text{, where} \qquad (5.22)$$

$$
\begin{aligned}
F, C_I, \tilde{F} &= \quad \text{see steps 2 and 3,} \\
\sigma_{F/\tilde{F}} &= \quad \text{RMS of all pixels of a control image } F/\tilde{F}, \\
\sigma_{I/\tilde{F}} &= \quad \text{RMS of an alternative control image } I/\tilde{F}.
\end{aligned}
$$

This is only an approximation neglecting the readout noise and assuming identical pixel sensitivities.

viii) All data frames are divided by the finally accepted flatfield: $\tilde{I}(x,y) = I(x,y)/\hat{F}(x,y)$.

We are still considering options to build a full automated flatfield evaluation procedure analyzing the control images.

The whole flatfielding procedure can also be performed by standard astronomical data reduction software but without error propagation.

Error propagation for κ-σ-clipping method

The statistical error is propagated as follows; all approximations are only given to illustrate the impact of the respective reduction step and assume a normalized flatfield flux ≈ 1 and negligible pixel-to-pixel and image-to-image variation of the error:

i) Normalization, error of pixel (x,y) in normalized flat F:

$$\delta_F(x,y) = F(x,y) \sqrt{ \left(\frac{\delta_I(x,y)}{I(x,y)} \right)^2 + \left(\frac{\delta_{C_I}}{C_I} \right)^2 } , \qquad (5.23)$$

where
$$
\begin{aligned}
F(x,y) &= \quad \text{flux of pixel } (x,y) \text{ in normalized flat } F, \\
I(x,y) &= \quad \text{flux of pixel } (x,y) \text{ in bias corrected flat } I, \\
\delta_I(x,y) &= \quad \text{error of pixel } (x,y) \text{ in bias corrected flat } I \text{ defined in Eq. 5.3,} \\
C_I &= \quad \text{normalization factor, see Sect. 5.6.8, step 2,} \\
\delta_{C_I} &= \quad \sigma_{\text{med}}/\sqrt{n_{\text{med}}} = \sqrt{ \left[\sum_{x,y}^{n_{\text{med}}} (C_I - I(x,y))^2 \right] / (C_I n_{\text{med}})^2 }, \\
&= \quad \text{for the error of normalization factor we use a standard error of the median} \\
n_{\text{med}} &= \quad \text{number of pixels used to build the median.}
\end{aligned}
$$

An uniform CCD, homogeneously illuminated flatfields, and a suitable (large) tailored area for the determination of C_I altogether will lead to a negligible δ_{C_I}, which can be seen via

$$\delta_F(x,y) \approx \frac{\delta_I(x,y)}{C_I} \sqrt{1 + \frac{1}{n_{\text{med}}}} \text{, assuming } \delta_{C_I} \approx \frac{\delta_I(x,y)}{C_I \sqrt{n_{\text{med}}}} \quad \text{and} \quad C_I \approx I(x,y) . \quad (5.24)$$

If one uses $\kappa\sigma$-clipping then σ_{med} has to be corrected with Eq. 5.4 as shown in Sect. 5.5.3.

ii) Building of median flatfield, error of pixel (x,y) in median flat $\tilde{F}$:

$$\delta_{\tilde{F}}(x,y) = \frac{\sqrt{\sum_{F}^{n_{\text{used}}} \delta_F^2(x,y)}}{\text{erf}\left(\frac{\kappa}{\sqrt{2}}\right) \sqrt{n_{\text{used}} \, n_{\text{total}}}} \overset{\kappa=1}{\approx} \delta_F \sqrt{\frac{2}{n_{\text{total}}}} \overset{\kappa>3}{\approx} \frac{\delta_F}{\sqrt{n_{\text{total}}}} \text{ , where} \tag{5.25}$$

n_{used}	=	remaining number of flats after clipping used for a specific median clipped mean pixel,
n_{total}	=	total number of flats used for clipping,
$\text{erf}\left(\frac{\kappa}{\sqrt{2}}\right)$	=	see Eq. 5.4, and
κ	=	clipping factor.

Ignoring the effect of using preselected, $\kappa\sigma$-clipped pixels to calculate the mean calibration pixel would lead to a significant misestimation of the resulting error for small κ. The assumption of normal distributed values is crude but still fair.

iii) The error of the flatfield enhancement (if applied):

(a) The error of a smoothed pixel (x_0, y_0) built by averaging independent pixels is

$$\delta_{\tilde{F}_s}(x_0, y_0) = \sqrt{\sum_{x,y}^{\text{box}} \delta_{\tilde{F}}^2(x,y)} \Big/ n_{\text{box}} \approx \frac{\delta_{\tilde{F}}}{\sqrt{n_{\text{box}}}} \; . \tag{5.26}$$

(b) The error for the pixel-to-pixel flatfield is given by

$$\delta_{\tilde{F}_p}(x,y) = \tilde{F}_p(x,y) \sqrt{\left(\frac{\delta_{\tilde{F}}(x,y)}{\tilde{F}(x,y)}\right)^2 + \left(\frac{\delta_{\tilde{F}_s}(x,y)}{\tilde{F}_s(x,y)}\right)^2} \approx \delta_{\tilde{F}} \sqrt{1 + \frac{1}{n_{\text{box}}}} \tag{5.27}$$

(c) Combining the pixel-to-pixel flats yields (as in step ii)

$$\delta_{\hat{F}_p}(x,y) = \frac{\sqrt{\sum_{\tilde{F}_p}^{n_{\text{used}}} \delta_{\tilde{F}_p}^2(x,y)}}{\text{erf}\left(\frac{\kappa}{\sqrt{2}}\right) \sqrt{n_{\text{used}} \, n_{\text{total}}}} \overset{\kappa=1}{\approx} \delta_{\tilde{F}_p} \sqrt{\frac{2}{n_{\text{total}}}} \overset{\kappa>3}{\approx} \frac{\delta_{\tilde{F}_p}}{\sqrt{n_{\text{total}}}} \tag{5.28}$$

(d) The error of the enhanced flatfield can be calculated with

$$\delta_{\hat{F}}(x,y) = \hat{F}(x,y) \sqrt{\left(\frac{\delta_{\tilde{F}_s}(x,y)}{\tilde{F}_s(x,y)}\right)^2 + \left(\frac{\delta_{\hat{F}_p}(x,y)}{\hat{F}_p(x,y)}\right)^2} \overset{\kappa>3}{\approx} \delta_{\tilde{F}} \sqrt{\frac{1}{n_{\text{box}}} + \frac{1 + 1/n_{\text{box}}}{n_{\text{total}}}} \tag{5.29}$$

iv) Flatfield division, error of pixel (x,y) in flatfield calibrated image $\tilde{I}$:

$$\delta_{\tilde{I}}(x,y) = \tilde{I}(x,y) \sqrt{\left(\frac{\delta_I(x,y)}{I(x,y)}\right)^2 + \left(\frac{\delta_{\hat{F}}(x,y)}{\hat{F}(x,y)}\right)^2} \approx \sqrt{\delta_I^2 + (\delta_{\hat{F}} \, I)^2} \tag{5.30}$$

Minor systematic errors are neglected here:

average flux	flat skylight image						
[10^3 ADU]	1	10	20	30	40	50	60
$\overline{\delta_I}$	1.826	0.577	0.408	0.333	0.289	0.258	0.236
f 10	1.937	0.716	0.582	0.528	0.500	0.482	0.469
l 20	1.916	0.656	0.507	0.445	0.411	0.389	0.373
a 30	1.910	0.636	0.479	0.413	0.376	0.352	0.335
t 40	1.907	0.625	0.465	0.396	0.358	0.332	0.314
s 50	1.905	0.619	0.456	0.386	0.346	0.320	0.301
60	1.903	0.614	0.450	0.379	0.338	0.312	0.292
~ 30	1.911	0.640	0.485	0.420	0.382	0.359	0.343

Table 5.3: Normalized standard deviation of flatfielded artificial skylight images [%]: $\overline{\delta_I}$ denotes a perfect flat, with noise exclusively induced by the skylight image, i.e. the naive error; rows 10 to 60 in respect to the $\overline{\delta_I}$ row illustrate the impact on the error budget for different flux levels of the median of five flatfield calibration image; ~ 30 shows the realistic case of five artificial dithered flats containing stars and cosmics.

- The flatfield response of a CCD is a strong function of color. This results in a systematic error when calibrating stars with colors different from the sky on an image, and gets worse if the compared objects have very different colors.

- The geometric distortion introduced with the variation of CCD pixel size is ignored in our flatfielding procedure. A position estimate will have a systematic error according to this, if determining positions of objects in undersampled images (e.g. due to extraordinary good observing conditions and therefore very sharp PSFs).

- Since we ignore the individual geometric sizes of CCD pixels the integrated photometry of a flatfielded image may be corrupted (not exceeding 0.5% in a single pixel of our images).

All those errors could be compensated, but will have at most a minor (but detectable) influence on our data because of OIS, relative profile fitting photometry, dithered image stacks and error propagation (Sect. 5.12, 5.12.1, and 5.15.2).

Measured errors in flatfields

We show the impact of error propagation by flatfielding artificial skylight images where both (flatfields and images) consist of different flux levels. Tab. 5.6.8 gives the measured relative errors i.e. the normalized standard deviation of the image. The realistic ~ 30k counts flatfields case compared to the naive $\overline{\delta_I}$ case (Eq. 5.3 without any further correction for flatfielding) gives an underestimation of 5% to 30% compared to the true errors. For the very low counts (but clean of stars and cosmics) case the underestimation is even 50%. The mean propagated error estimate, calculated as shown in Sect. 5.6, always differs less than 2% from the measured error.

5.6.9   Flatfield combination with double κ-σ-clipping method with neighbor rejection

For the latest version of the pipeline we improved these basic ideas using following algorithm[13]:

i) First step is to evaluate the normalization factor n_i of each frame with its error σ_n. For this purpose we use $\kappa - \sigma$ clipping ($\kappa = 3$, and with the median as start value) of a preferably flat region in the flat images (pixel area 167:350,217:291 for MONICA).

ii) After normalization, each pixel stack is clipped for extreme outliers (cosmics, stars with high counts) exceeding a value of 5σ the error weighted average of the stack. If we would use a smaller κ, more outliers resulting from pure noise would be removed. Around each masked pixel an area of 5x5 pixels is also masked (neighbor rejection). This removes very efficiently the stars in the whole frame.

iii) To remove also deviations smaller than 5σ, the clipping procedure is repeated, but now with a $\kappa = 3$.

iv) After all outlying pixel are marked in all images, we combine them by simply adding the un-normalized frames, since in this case the signal-to-noise is maximized.

v) After that the pixel stack is normalized by the sum of the normalization factors of the used pixels. This results in a normalized master sky flat (see Fig. 5.7).
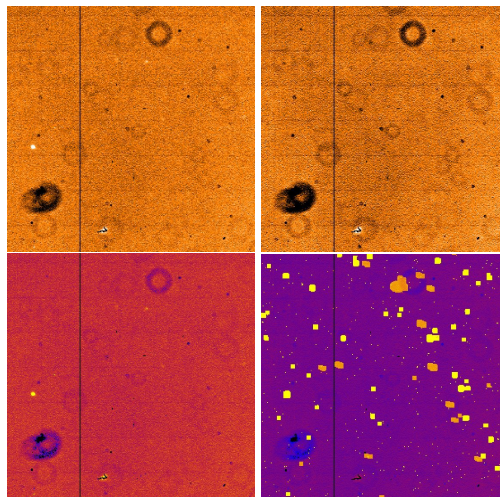
Figure 5.7: Flatfield combination with double κ-σ-clipping method with neighbor rejection. *Left:* single twilight sky flatfield; *right:* final combined flatfield; *top:* images; *bottom:* corresponding error images. To achieve a high S/N for the combined flatfield we first calculate in each pixel the error weighted mean of normalized and illumination corrected twilight flatfields. After rejecting 5×5 pixel around pixels exceeding the mean by more than $5\sigma_{xy}$, the final calibration image is built with a $3\sigma_{xy}$ clipping of the remaining pixels.

---

[13] mupipe program `masterflat`

5.6.10 Test with artificial images

We tested our method with numerically simulated flats and show results for 5 simulated flats containing stars in Fig. 5.8. A comparison between our final method with some more simple methods is shown in Fig. 5.9. For our final method described in Sec. 5.6.9 all stellar residuals can be made to dissappear. At the same time small flat field errors (see Fig. 5.10) can be achieved.
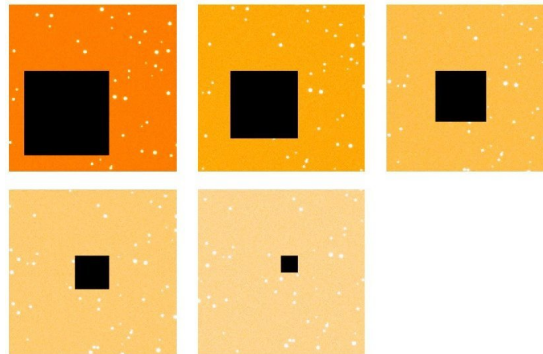
Figure 5.8: Five simulated flatfields with varying brightness, and different marked bad flag regions. Note that the flatfields are shifted against each other.
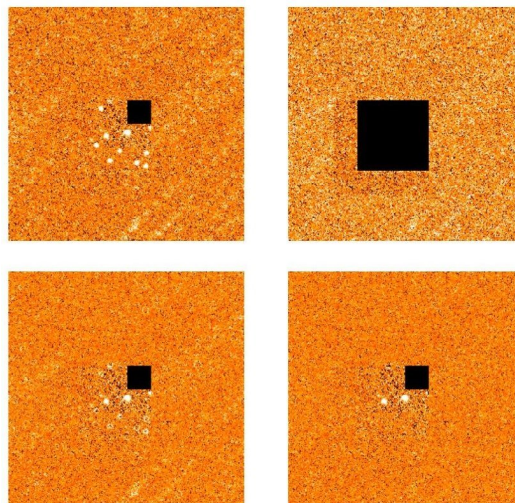
Figure 5.9: Comparison of different methods for flatfield combination; *upper left panel:* medianing of the 5 images; *upper right panel:* κ-σ-clipping with $\kappa = 1$; *lower left panel:* $> 5\sigma_{xy}$ error clipping, $3\sigma_{xy}$ error clipping and averaging; *lower right panel:* $> 5\sigma_{xy}$ error clipping, $3\sigma_{xy}$ error clipping, neighbor rejection and averaging. If one applies the last method all residuals of stars disappear. For the two stars left information of only one image is present.
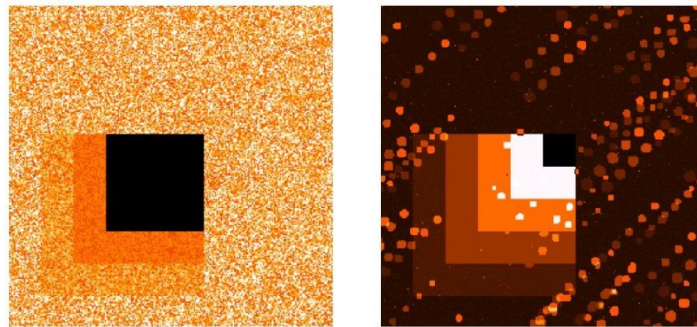
Figure 5.10: Error frames of the combined flat: *left:* κ-σ-clipping with $\kappa = 1$; *right:* with $> 5\sigma_{xy}$ error clipping, $3\sigma_{xy}$ error clipping, neighbor rejection and averaging. The errors for the double clipping method with neighbor rejection are much smaller in respect to the error of a simple clipping method.

5.7 Filtering of cosmic rays with Gaussian filter

There are two major reasons, why we have to correct for the image contamination by particle events (so called *cosmics*): We use small, two 1m-class telescopes for our observational projects (e.g. Riffeser *et al.*, 2001) and therefore we integrate for half an hour or longer. We want to find variable sources and measure light curves for every pixel of an observed field. So we have at least to identify individual cosmics in single frames automatically, or better clean the images of cosmics and account for the error this procedure might introduce in a stack of images.

5.7.1 Common and literature filters

Existing filtering techniques for particle events either rely on median stacking of multiple well aligned images (i.e. see Windhorst *et al.*, 1994) or compare each pixel value with the median of its neighbors and define pixels with a sharpness ratio above a deliberately set value as cosmic. The first approach does not work at all if there are no multiple images available or the sample of images to be stacked has different observational features (variable sky, extinction or PSF). Aligning images will always spread and diffuse cosmics and therefore obscure them. The latter technique gets into trouble with noisy images, undersampled images and multiple-pixel cosmics for obvious reasons.

Trainable cosmic classifiers i.e. as described in Salzberg *et al.* (1995) have the advantage of also being applicable to undersampled data but rely on subjectively defined training sets which are difficult to create for a large spread of different telescope, camera, and detector configurations in addition to the wide range of observing conditions. An interesting idea is presented in Rhoads (2000). Since this method relies on an accurate PSF and sky determination and the author does not refer to possible problems in heavily crowded fields we do not use it. Furthermore, this technique is in principle only sensitive to single pixel events, which we found to be not the common case. In fact most cosmics seem to have a major-to-minor axis ratio[14] greater than two. Multiple-pixel events, which can be filtered with our technique (see below) in one pass, can only be detected iteratively and with decreasing efficiency with the Rhoads technique.

5.7.2 Gaussian filter

We apply a straightforward Gaussian filter to every single image[15]: We fit five-parameter Gaussians to all local maxima of an image. If the width along one axis of the fitting function is smaller than a threshold (which has to be adapted to the PSF) and, in addition, the amplitude of the fitting function exceeds the expected noise by a factor (which has to be chosen depending on the additional noise caused by crowding, see Sect. 5.7.3 for details), we replace the pixels with the fitted surface constant, where the fitting function exceeds this constant by more than two times the expected photon noise. In the following we describe the algorithm in detail:

i) Because of code speed improvements which rely on some symmetries in the fitting function the tested cosmic candidate has to be in the center of a 7×7 pixel array. In order to be applicable also on the first and last three rows and columns we add a border surrounding the exposed frame

---

[14] We have checked this with the control output of our filter code. It gives the major and minor axis full width half maximum of the Gaussian fit function for every cosmic replaced.

[15] using the mupipe program `cosmic`

filled with zero value pixels. Since we do not want to lose too much of the images when shifting them later we enlarge the images not only with a three pixels but with a 20 pixels border.

ii) Now, first we search for all local maxima (x_0, y_0) in the image, but ignore those with either a large error[16] $\left(\delta^2(x_0, y_0) > \gamma^2 \, \frac{\text{signal}(x_0, y_0)}{\text{gain}} \right)$ or more than two saturated neighbors[17] or with less than four (of eight possible) valid neighbors[18].

iii) Then we perform a propagated error weighted, least-squares fit, assuming a five-parameter, two-dimensional Gaussian fitting function centered on these local maxima (x_0, y_0) coordinates in 7×7 pixel subarrays: We determine a surface constant C, an amplitude A, a rotation angle α, a major and a minor axis full width half maximum (x_{fwhm} and y_{fwhm}) of the fitting function f_{gauss} giving the flux of a pixel (x, y)

$$f_{\text{gauss}}(x, y) = C + A \exp\left[-4\ln 2 \left(\frac{x'^2}{x_{\text{fwhm}}^2} + \frac{y'^2}{y_{\text{fwhm}}^2} \right) \right],$$

where

$$x'(x, y) = (x - x_0)\cos\alpha + (y - y_0)\sin\alpha,$$
$$y'(x, y) = (y - y_0)\cos\alpha - (x - x_0)\sin\alpha.$$

iv) All Gaussians with an amplitude of t_{limit} times the propagated error of the center pixel and a full width half maximum in one axis smaller than a limiting $\text{FWHM}_{\text{cosmic}}$ are defined as *cosmic*:
$(A > t_{\text{limit}} \, \delta(x_0, y_0)) \wedge [(x_{\text{fwhm}} < \text{FWHM}_{\text{cosmic}}) \vee (y_{\text{fwhm}} < \text{FWHM}_{\text{cosmic}})]$

v) We have to perform a sanity check on the fitting function: The surface constant C and the amplitude A must be positive; $\bar{\chi}^2$ of the fit must be close to unity[19]:

$$C > 0 \wedge A > 0 \wedge \bar{\chi}_{\text{fit}}^2 \simeq 1 \tag{5.31}$$

where

$$\bar{\chi}_{\text{fit}}^2 = \frac{\sum_{x,y}^{\text{fitbox}} \left(\frac{f(x,y) - \tilde{I}(x,y)}{\delta_{\tilde{I}}^2(x,y)} \right)^2}{n_{\text{dof}}}, \tag{5.32}$$

$$n_{\text{dof}} = (7 \times 7) - 5. \tag{5.33}$$

---

[16] We found $\gamma \approx 3$ to be an empirically suitable factor.

[17] Cosmics candidates close to saturated pixels need a special treatment, see step 9. Because we always consider the possibility of blooming (see Sect. 5.5.1), only for pixels with at least three saturated marked pixels (of the eight possible neighbors) one pixel (of the four directly adjacent) is really saturated.

[18] The Gaussian fit of step 3 gets unstable when fewer than half of the pixels adjacent can be used in the fitting algorithm.

[19] This corresponds to a compatible fitting function and correct error weights.

vi) Now we mark pixels (x, y) where the Gaussian fitting function f_{gauss} gives a value larger than the assumed signal plus two times the assumed photon noise

$$f_{gauss}(x, y) > C + 2\sqrt{\frac{C}{\text{gain}}}.$$

vii) The new error of the substituted pixels is set to

$$\sqrt{\delta_{\bar{I}}^2(x, y) + \bar{\chi}_{\text{fit}}^2 \, \frac{C}{\text{gain}}} \; , \text{ where} \tag{5.34}$$

$$\begin{aligned}
\delta_{\bar{I}}(x, y) &= \text{propagated old error of pixel,} \\
\bar{\chi}_{\text{fit}} &= \text{accuracy of the Gaussian fitfunction} \\
&\quad (\bar{\chi} \approx 1 \text{ for a perfect fit}).
\end{aligned}$$

This will be large enough to prevent an incautious use of the replaced pixels in the following.

viii) We then repeat this procedure for the areas with cosmics found beginning with step ii) until no more cosmics are found.

ix) Finally we try to find and replace cosmics near saturated pixels with a similar, just in some details more sophisticated technique: The Gaussian fit starts centered on the saturated region but the center position is added to the list of free parameters. We ignore the saturated region for the fitting and the replacement procedure. For overall stability reasons we have to use stronger constraints for the sanity check. Since pixels saturated due to cosmics will not be treated at all, because they are flagged as "dominant bad pixels", step 9 might be readjusted, if dealing with shallow-well CCDs; saturated regions can be replaced, but then saturated objects may be mistaken for a cosmic.

We found that a $t_{\text{limit}} = 8.0$ and a $\text{FWHM}_{\text{cosmic}} = 1.5$ works fine in any well sampled image. However, in some extraordinary good seeing images (with an average stellar PSF FWHM ≤ 2.0 pixels) we had to specify a limiting $\text{FWHM}_{\text{cosmic}} = 1.3$ to avoid to cancel stars. All fixed fitting and substitution constants were adjusted in order to get an accurate and reliable filter for cosmic rays for all our images. The sensitivity parameters t_{limit} and $\text{FWHM}_{\text{cosmic}}$ nevertheless have to be adjusted to the observational and object properties to reach the best compromise between false alarm and false detection rate (Sect. 5.7.3).

5.7.3 Errors with Gaussian filter for cosmic rays

Empirical tests on real images have been done by comparing the number of cosmics found in exposed images with that found in dark frames and visually examining both the unfiltered image and the difference of the unfiltered and the filtered image (e.g. for effects on bright stars etc.).
In addition we have tested the reliability of our Gaussian filter with five simulated cases (Tab. 5.4): A pure skylight image, a simple field with 500 stars plus 10 saturated and bloomed stars (N_{sat}) and two different sky levels, a crowded field with 100 000 stars, and a highly crowded field with 200 million stars; the positions of stars and cosmics as well as the flux and the orientation of cosmics follow uniform deviates; the flux of stars follows an exponential deviate, which sufficiently matches the

field	sky level	stars		cosmics	
		number	max. flux	number	max. flux
empty	500	–	–	500	80 000
a) simple + low sky	500	500	30 000	500	80 000
		(+10)	(200 000)		
b) simple + high sky	5000	500	30 000	500	80 000
		(+10)	(200 000)		
crowded	500	100 000	1000	500	80 000
high	500	$200 \cdot 10^6$	10	500	80 000

Table 5.4:   Parameters to creste test images for the cosmic rays detection algorithm: the level of background sky [ADU], numbers and maximum fluxes [ADU] of stars and cosmics.

luminosity function in our fields. Stars have a PSF FWHM of 2.6 pixel. The images are processed with our standard reduction pipeline (Sect. 5.5) using a median of five simulated flatfields with an average flux level of 30 000 ADU per flatfield and the filter parameters of Sect. 5.7.2 unless stated otherwise (detection thresholds $t_{limit} = 8$, $FWHM_{cosmic} = 1.5$).

We determine the false alarm rate by filtering the clean test images without any cosmics (Tab. 5.5): For 10^6 pixels with about 30 000 to 100 000 local maxima 0.3 to 1×10^5 tests are performed. So the false alarm rate is given by the ratio of false occurances to number of tests. To determine the detection rate we put 500 artificial cosmics with flat deviates in space, form, and energy into the test images (Tab. 5.5): We identify and count the cosmics found. To get an accurate estimate of the performance these numbers still have to be compared with the photon noise, the noise induced by the object density, and the filter parameters.

The highest false alarm rate occurs for the crowded field. Here the total pixel-to-pixel variation of the image (photon noise plus objects' signal) exceeds the pure photon noise by a factor of 25. In the highly crowded field this excess is only a factor of 11 and can be compensated by setting $t_{limit} = 10$. The false alarm $\propto N_{sat}$ in the simple, high sky field is due to the unawareness of saturation[20] because of missing saturation tags without error propagation. Our tests show a false alarm rate $< 0.2\%$ in any (error propagated) case. We found that our fields are resembled closer by the smooth simple-and-high-sky field than by the crowded and even the highly crowded test fields. Therefore we are sure the false alarm rate does not exceed 0.01% in our real images. However, a false alarm resulting in deleting a true source will not lead to wrong photometry because of the high error assigned to replaced pixels (Sect. 5.7.2). Under certain circumstances (bad sampling, small stacks) it may lead to large error bars, but the result is still reliable within those.

The expected detection rate (97% to 99%) is achieved nearly with all test images including error propagation. Even without error propagation the detection rate is still very close to the expected one. The worst case is again the (not extremely) crowded field where the object induced noise exceeds the photon noise by far. Here the expected rate is missed by $0.008 = 4$ (of 500) cosmics.

---

[20] As stated in Sect. 5.7.2 saturated pixels need a special treatment.

error propagation	with			without		
detection rates	false alarm	detection rate		false alarm	detection rate	
empty	$< 10^{-5}$	0.992	†	$< 10^{-5}$	0.992	†
a) simple	$< 10^{-5}$	0.992	†	$\sim 10^{-5}$	0.988	
b) simple	$\sim 10^{-5}$	0.982	†	$\propto N_{\mathrm{sat}}$	0.978	
crowded	$1.80 \cdot 10^{-3}$	0.978		$2.27 \cdot 10^{-3}$	0.972	
high	$0.34 \cdot 10^{-3}$	0.976	†	$0.36 \cdot 10^{-3}$	0.964	
high[a]	$\sim 10^{-5}$	0.970	†	$\sim 10^{-5}$	0.958	

Table 5.5: Performance of Gaussian filter for cosmic ray events for the test configurations of Tab. 5.4: The false alarm and the detection rates with and without error propagation frames; † indicates that the detection rate matches the expected rate.
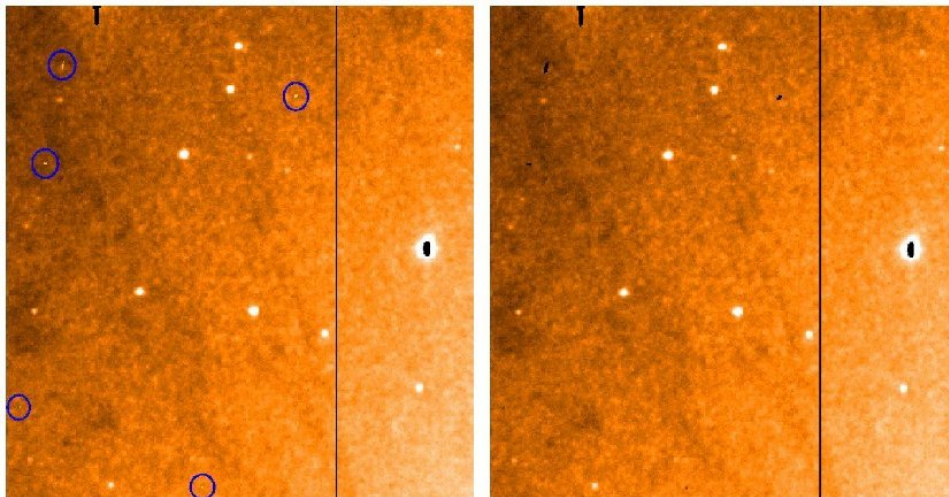

Figure 5.11: Gaussian filter for cosmic rays. *Left:* flatfielded and rotated image; *right:* image after rejection of cosmic ray events. We fit five-parameter Gaussians to all local maxima of an image. If the width along one axis of the fitting function is smaller than a threshold and the amplitude of the fitting function exceeds the expected noise by a certain factor we mask the pixels

5.8   Position alignment

Up to now our reduction pipeline can be applied to any image regardless of its scientific application. When images are shifted (to be stacked later on) without great care, the PSF can change and even the PSF-flux can be altered. It is however important to conserve the PSF, because the image convolution that we adopt in the differential photometry later on relies crucially on it.

The alignment of images is done in a four step procedure:

   i) First we determine the coordinates of reference objects in every image,

   ii) then we calculate the coordinate transformation to project an image onto the reference frame,

   iii) subsequently we project the images into the reference frame coordinate grid and

   iv) finally we stack the images.

5.8.1   Position of reference stars by PSF-fitting

In order to obtain the coordinates of reference objects in all images we perform interactively a 6-parameter Gaussian fit. We begin with the reference frame: About 20 stars with a high signal-to-noise ratio and well distributed over the frame would be sufficient but we use 50, because stars close to the frame border may be missing on some images. We continue with selecting at least one reference object in every image manually, the rest will be found automatically[21]. The lists with the reference objects in the reference frame and the first reference object of the original images are used to recognize the reference objects in each image, to determine their position, and finally to calculate the projection parameters.

5.8.2   Translation of image coordinates – determination of a linear projection

With the telescopes and cameras used in our observing campaigns, we found a linear relation to be sufficient. We easily match 50 stars all over a $17' \times 17'$ field within $1/20\,''$ rms. Since there is no significant optical field distortion, it was not necessary to use a non linear relation. We determine a 2×2 linear matrix and a two-dimensional translation vector

$$\begin{pmatrix} x' \\ y' \end{pmatrix} = \begin{pmatrix} a_{11} & a_{12} \\ a_{21} & a_{22} \end{pmatrix} \begin{pmatrix} x \\ y \end{pmatrix} + \begin{pmatrix} t_1 \\ t_2 \end{pmatrix} \tag{5.35}$$

with a least-squares fit. It matches the positions of reference stars in the reference system with the positions in the unshifted image with this six-parameter relation.

5.8.3   Accuracy of the linear projection

The projection (Sect. 5.8.2) was tested with two simulated, not perfectly aligned (shifted, rotated and rescaled) frames. It was calculated to match the position of 70 bright stars in these frames. The position differences are always below 0.05 pixels (Fig. 5.12). This reflects the accuracy limit[22] set by the size of the corresponding fit box (20×20 pixels).

---

[21] In case the imaging device would provide an accurate World Coordinate System (WCS) information of all reference stars could be found automatically.

[22] Spatially extremely undersampled images, leading to peak-shaped PSFs, still can restrict this principle accuracy limit to one pixel, but this was not a required test case.
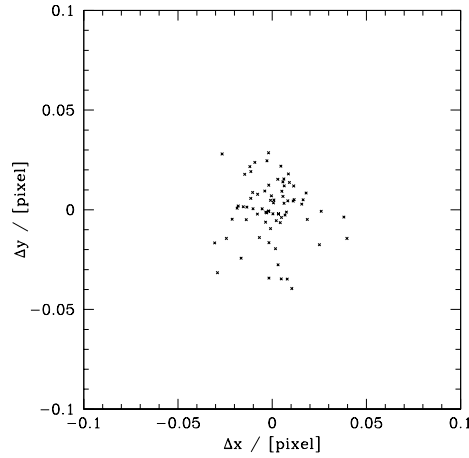
Figure 5.12: Accuracy of the linear projection: position differences ($\Delta x = x'_1 - x_2$, $\Delta y = y'_1 - y_2$) of 70 stars after projecting the coordinates of one frame (x_1, y_1) to the other frame (x_2, y_2).

5.8.4 Drizzling

The technique of Variable-Pixel Linear Reconstruction or *drizzling* (Fruchter & Hook, 1997; Hook & Fruchter, 1997; Mutchler & Fruchter, 1997) offers the possibility to add images while preserving both the flux and the PSF. In undersampled images one might even enhance the resolution and therefore gain signal to noise. Unfortunately this technique requires some image properties to be applicable and these are very difficult to obtain with ground-based telescopes: There must be no variations in sky, extinction and PSF, and there should be a uniform spatial sampling in the sub-pixel pointing. If those requirements are missed, the flux will still be preserved, but the PSF may get very distorted. So aperture photometry might still work very well, but since we use PSF convolution and a PSF-dependent photometry, developed an alternative way with fewer observational constraints.

5.8.5 Interpolating pixels conserving PSF

Our translation algorithm preserves PSF in unstacked and sometimes undersampled frames. We found that a 16-parameter, 3rd-order polynomial interpolation with 16 pixel base points does satisfy to our needs. A 2nd-order polynomial still smoothes the images, whereas a 4th-order polynomial does no better PSF conservation compared to the 3rd-order polynomial. Since the number of parameters of the polynomial is matched with the input base points, no least-squares fit is needed; the polynomial can be calculated analytically.

The flux interpolation for non-integer-value coordinates (x, y) is calculated with a polynomial

$$p(x,y) = \sum_{i=0}^{3} \sum_{j=0}^{3} a_{ij} x^i y^j \text{ , where} \tag{5.36}$$

i, j = index for subscript, and exponent for superscript. For a region with 4×4 pixels this yields 16 linear equations

$$p(x_k, y_k) = \tilde{I}(x_k, y_k) \text{ , where } 1 \leq k \leq 16, \tag{5.37}$$

so the coefficients $a_{ij} = a_{ij}(\tilde{I}(x_k,y_k))$ can be calculated by solving the matrix equation. The error is calculated using Gaussian error propagation

$$\delta_p(x,y) = \sqrt{\sum_{i=0}^{3}\sum_{j=0}^{3}(x^iy^j)^2\,\delta_{a_{ij}}^2}\ , \text{ where} \tag{5.38}$$

$$\delta_{a_{ij}} = \sqrt{\sum_{k=1}^{16}\left(\frac{\partial a_{ij}(\tilde{I}(x_k,y_k))}{\partial \tilde{I}(x_k,y_k)}\,\delta_{\tilde{I}}(x_k,y_k)\right)^2}\ .$$

5.8.6   Interpolating pixels conserving the flux

In our latest version of the reduction pipeline we implemented an interpolation routine[23], which conserves the flux and does not destroy the shape of the PSF (see Fig. 5.13).

spline fitting   flux conservation   interpolating integral
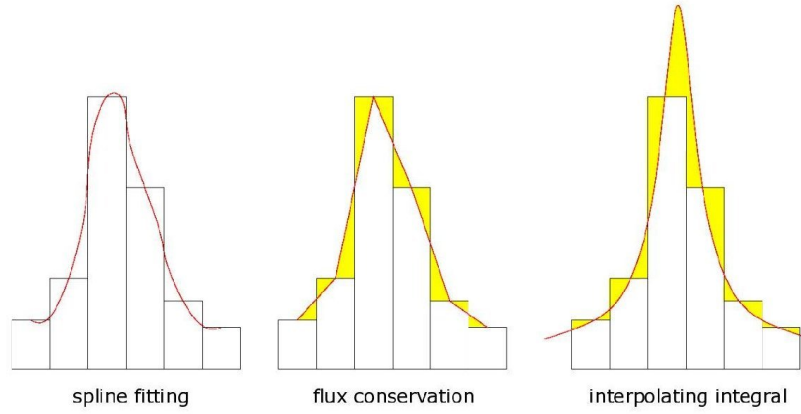
Figure 5.13: Different interpolation methods.

The flux interpolation for non-integer-value coordinates (x,y) is calculated with a polynomial

$$p(x,y) = \sum_{i=0}^{n-1}\sum_{j=0}^{n-1}a_{ij}x^iy^j\ , \text{ where} \tag{5.39}$$

i,j are the index for subscript and exponent. For a region with $n \times n$ pixels this yields n^2 linear equations from the constraint that each measured pixel value arises from an integration over one pixel

---

[23] mupipe program `divvy`

$$\tilde{I}(x_k, y_k) = \int\limits_{x_k}^{x_k+1} \int\limits_{y_k}^{y_k+1} p(x,y)\, dx\, dy \qquad\qquad \text{where } 1 \leq k \leq n^2,$$

$$= \sum_{i=0}^{n-1}\sum_{j=0}^{n-1} a_{ij} \int\limits_{x_k}^{x_k+1} \int\limits_{y_k}^{y_k+1} x^i y^j\, dx\, dy$$

$$= \sum_{i=0}^{n-1}\sum_{j=0}^{n-1} a_{ij} \frac{\left((x_k+1)^{i+1}-x_k^{i+1}\right)\left((y_k+1)^{j+1}-y_k^{j+1}\right)}{(i+1)(j+1)}\, dx\, dy$$

$$= \sum_{i=1}^{n}\sum_{j=1}^{n} \tilde{a}_{ij} \left((x_k+1)^i - x_k^i\right)\left((y_k+1)^j - y_k^j\right) \tag{5.40}$$

In this way the coefficients $\tilde{a}_{ij} = \tilde{a}_{ij}(\tilde{I}(x_k, y_k))$ are calculated by solving the matrix equation. As we want to obtain an interpolation value for the central pixel we allow only odd values for n for the box-size.

We found that a 25-parameter, 5$^{\text{th}}$-order polynomial interpolation with 25 pixel base points gives good results. Interpolating pixels at the edges or near marked pixels, the box size is automatically decreased. After deriving the coefficients for each pixel the integration is done by dividing each pixel into a subgrid, evaluating the interpolated flux in each subpixel, applying the transformation from Sec. 5.8.2 and summing all subpixels on the new grid [24].

Since the subpixel grid is finite, the number of summed pixels on the new grid depends on the transformation. Therefore we count how many subpixels contributed to the new pixel grid and divide the previous image with that. For a subpixel grid of 32 x 32, counting the amount of subpixel in the new pixels, does not deviate more than 3% from 32^2 (see Fig. 5.14).

The error is redistributed without interpolating, simply by dividing the error pixel into a subgrid and redistributing it over the new grid.
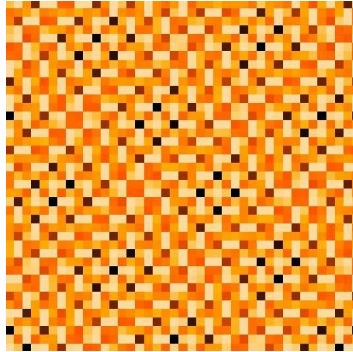

Figure 5.14: Number of subpixels redistributed over the new grid. Colors are shown with cut levels $(100 \pm 3)\%$. Since we are using a linear transformation, the pattern reflects the symmetries of the transformation.

---

[24] For future work an analytic integration could be useful and may be less time consuming than summing over subpixels.

5.8.7 Errors visible after alignment – a snapshot

To give an impression of error features which would be neglected by just considering the cleaned image, but still visible in a propagated error image, we present image and error image of one hour total integration with a small telescope of the dwarf galaxy EGB 0427 +63 (Fig. 5.15). Despite the fact that the images were dithered there are still features of the flatfield (dust rings) visible as well as the impact of CCD defects and a huge amount of cosmics.
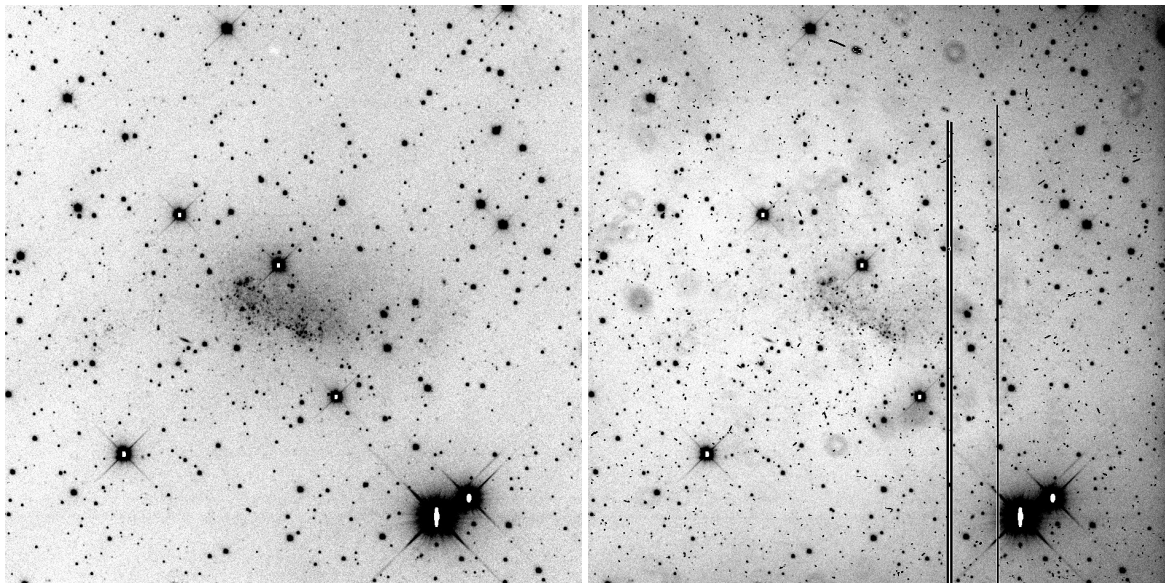
Figure 5.15: The dwarf galaxy EGB 0427 +63: One hour observation with the 0.8 m Wendelstein telescope, 20 best seeing and lowest sky images of four nights were stacked; *left*: image; *right*: error image. For bright objects, the dominant error is the noise of the photons of the source. This implies, that high noise regions generally coincide with regions of large error (of course, the signal to noise ratio is largest for bright objects). So, as expected, the error image looks fairly similar to the science image. the ring like features at low level in the error image are caused by dust grains on the Dewar window.

5.9 Photometric Alignment

Photometric alignment is crucial for a precise comparison of data taken under different observing conditions: There are several effects which make these data differ by multiplicative and additive terms:

- moon and skylight cause an additive term that can usually be modelled as linear function

- atmospheric extinction depends on the airmass of the observation and can be modelled as a color dependent multiplicative factor

- optics (e.g. focus, a non linear optical plane) create non-linear multiplicative deformations

- a non-optimal telescope baffle allows an additive non-uniform sky

- depending on the angle the effective primary size (and therefore the total light) is variing (multiplicative)

- the concentration of light comes from multiple refelections between optical surfaces like filter, dewer window, and chip surface. Therefore light rays distant from the optical axis are only partially arriving at the CCD (additive)

- skyflats normally are not flat and therefore, doing flatfield correction, a non-constant function is divided

- reflections and scattering light add as nonlinear terms

There are several ways to disentangle between these effects and to align them[25] to a reference image $R_{\mathrm{meas}}(x,y)$:

$$I^{\mathrm{photom.\,aligned}}(x,y) = a(x,y) \times I_{\mathrm{meas}}(x,y) + b(x,y) \approx R_{\mathrm{meas}}(x,y)\,. \tag{5.41}$$

For simplicity we call the additive term the 'background' b and the multiplicative the 'absorption' a.

5.9.1 Constant background and absorption terms

Assuming a constant scaling factor a for different exposure times and atmospheric extinction and a constant background sky light b, these constants are determined in a simple way. We first remove all bright stars from our field and replace them by a plane representing the surrounding background level. Each pixel value in $I^{\mathrm{photom.\,aligned}}$ and R_{meas} is replaced with the median count rates within 21×21 pixel subsections, which eliminates any PSF differences. We finally take these images and estimate a and b by solving the least-squares problem.
The error frame is calculated using Gaussian error propagation

$$\delta_{I^{\mathrm{photom.\,aligned}}}(x,y) = \sqrt{I_{\mathrm{meas}}{}^2(x,y)\,\delta_a^2 + a^2\,\delta_{I_{\mathrm{meas}}}^2(x,y) + \delta_b^2}\,. \tag{5.42}$$

---

[25] using the mupipe program `skycalc`

5.9.2   Spatially varying background and absorption terms

In this section we use a polynomial fitting routine to evaluate $a(x,y)$ and $b(x,y)$.
We have two possibilities to extract the information we need as input for the algorithms described in the following section.

- Relative photometry of resolved stars allows to evaluate $a(x_i, y_i)$ and $b(x_i, y_i)$ at various positions. We choose the same method as in Sec. 5.12.1 (difference image analysis), to evaluate the relative terms for each star (in a region 50×50 pixels) separately. The interpolation can than be done with averaging, medianing or a polynomial approximation (see WESPS project, Koppenhöfer, priv. comm.)

- For extended objects like the galaxy M31 we can use the galaxy profile itself to evaluate $a(x,y)$ and $b(x,y)$.

Our algorithm writes as follows:
We want to transform the measured I_{meas} so that $I^{\mathrm{photom.\,aligned}}$ is equal to the measured reference R_{meas} combining a non-linear factor (shutter, flatfield) $a_{\mathrm{NL}}(x,y)$ with a polynomial parameterization[26].
We assume that this polynomial parameterization is valid and can be determined in a specific (central) part of the image and allow for an extended non-linear solution for the rest of the frame fixing either the multiplicative or the additive parameters.
Note that for higher order than linear the problem is slightly degenerate between multiplicative and additive parameters and we recommend to allow only for linear terms for background and absorption.

Polynomial parameterization

We model the 'background' term with a gradient since that is a good description for the night sky. A multiplicative gradient arises from skyflats, which can also have a gradient. For this reason we divide by the linear multiplicative term after adding the background.

$$
\begin{aligned}
R_{\mathrm{meas}}(x,y) &= \tfrac{1}{a_R(x,y)}\left(R(x,y)+b_R(x,y)\right) \\
I_{\mathrm{meas}}(x,y) &= \tfrac{1}{a_I(x,y)}\left(I(x,y)+b_I(x,y)\right)
\end{aligned}
\tag{5.43}
$$

The 'background' and 'absorption' are described by polynomials (of order n), $b(x,y) = \sum\limits_{i=0}^{n}\sum\limits_{j=0}^{n-i} b_{ij}\, x^i y^j$

and $a(x,y) = \sum\limits_{i=0}^{n}\sum\limits_{j=0}^{n-i} a_{ij}\, x^i y^j$.
For a specific (central) region ideally holds $I(x,y) \approx R(x,y)$ and we can write

$$
\begin{aligned}
a_I(x,y)\cdot I_{\mathrm{meas}}(x,y) &\approx a_R(x,y)\cdot R_{\mathrm{meas}}(x,y) - b_R(x,y) + b_I(x,y) \\
\left(\sum\sum a_{ij,I}\, x^i y^j\right)\cdot I_{\mathrm{meas}}(x,y) &\approx \left(\sum\sum a_{ij,R}\, x^i y^j\right)\cdot R_{\mathrm{meas}}(x,y) - \left(\sum\sum b_{ij,R}\, x^i y^j\right) + \left(\sum\sum b_{ij,I}\, x^i y^j\right) \\
\left(1 + \sum\sum \tfrac{a_{ij,I}}{a_{00,I}}\, x^i y^j\right)\cdot I_{\mathrm{meas}}(x,y) &\approx \left(\sum\sum \tfrac{a_{ij,R}}{a_{00,I}}\, x^i y^j\right)\cdot R_{\mathrm{meas}}(x,y) + \sum\sum \tfrac{b_{ij,I}}{a_{00,I}}\, x^i y^j - \sum\sum \tfrac{b_{ij,R}}{a_{00,I}}\, x^i y^j \\
L(x,y)\cdot I_{\mathrm{meas}}(x,y) &\approx M(x,y)\cdot R_{\mathrm{meas}}(x,y) + N(x,y)
\end{aligned}
\tag{5.44}
$$

---

[26]The true images $R(x,y)$ and $I(x,y)$ cannot be derived by simple comparison of images.

with polynomials defined as

$$
\begin{aligned}
L(x,y) &:= 1 + l_x x + l_y y + \dots \\
M(x,y) &:= m_0 + m_x x + m_y y + \dots \\
N(x,y) &:= n_0 + n_x x + n_y y + \dots
\end{aligned}
\tag{5.45}
$$

Solving the linear equation

$$
L(x,y)I_{\mathrm{meas}}(x,y) - M(x,y)R_{\mathrm{meas}}(x,y) - N(x,y) \approx 0
\tag{5.46}
$$

provides the parameters l_x, l_y, m_0, m_x, m_y, n_0, n_x, n_y,... .
The transformed image becomes

$$
I^{\mathrm{photom.\,aligned}}(x,y) = \frac{1}{M(x,y)}\left(L(x,y)I_{\mathrm{meas}}(x,y) - N(x,y)\right) \quad .
\tag{5.47}
$$

Non-linear multiplicative terms

Often the linear correction works only in the central part of the images. Near the edges non-linear effects $a_{\mathrm{NL}}(x,y)$ have to be taken into account, which may arise from optics (distortion), while the linear part $a(x,y)$ comes from a skyflat gradient.
Therefore we assume a non-linear correction $a_{\mathrm{NL}}(x,y)$ of $I_{\mathrm{meas}}(x,y)$ witch together with the previously evaluated linear parameters leads to an image $\tilde{I}_{\mathrm{NL}}^{\mathrm{photom.\,aligned}}(x,y)$ which is "very similar" to $R_{\mathrm{meas}}(x,y)$

$$
\tilde{I}_{\mathrm{NL}}^{\mathrm{photom.\,aligned}}(x,y) := \frac{1}{M(x,y)}\left[L(x,y)a_{\mathrm{NL}}(x,y)I_{\mathrm{meas}}(x,y) - N(x,y)\right] \approx R_{\mathrm{meas}}(x,y)
\tag{5.48}
$$

solving for $a_{\mathrm{NL}}(x,y)$ leads to

$$
a_{\mathrm{NL}}(x,y) = \frac{M(x,y)\cdot R_{\mathrm{meas}}(x,y) + N(x,y)}{L(x,y)\cdot I_{\mathrm{meas}}(x,y)}
\tag{5.49}
$$

To derive a smooth nonlinear correction for the whole image we evaluate Eq. 5.48, bin the $a_{\mathrm{NL}}(x,y)$-field, then perform a cubic spline interpolation.

Non-linear additive terms

Restricting the multiplicative solution to the linear terms allows to correct for higher order sky using

$$
\tilde{I}_{\mathrm{NL}}^{\mathrm{photom.\,aligned}}(x,y) = I^{\mathrm{photom.\,aligned}}(x,y) + b_{\mathrm{NL}}(x,y)
\tag{5.50}
$$

with

$$
b_{\mathrm{NL}}(x,y) := R_{\mathrm{meas}}(x,y) - I^{\mathrm{photom.\,aligned}}(x,y)
\tag{5.51}
$$

Subtracting the linearly transformed image $I^{\mathrm{photom.\,aligned}}$ from R_{meas} and binning offers the possibility of fitting the non-linear sky by simple cubic spline interpolation.

Applications

We show how to apply the general transformation in some special cases depending on the optical properties of the telescope. If the properties are understood, the optimal method can easily be selected.

- **constant central absorption**

  If we can assume a "perfect" reference frame free of absorption and background, $R_{\text{meas}}(x,y) \approx R(x,y)$ and constant multiplicative terms in a specific region, the linear parameterization for sky gradient $b + b_x x + b_y y$ can be easily evaluated:

  We insert

  $$
  \begin{aligned}
  a_R(x,y) &= 1 \quad b_R(x,y) = 0 \\
  a_I(x,y) &= \tfrac{1}{a} \quad b_I(x,y) = \tfrac{b}{a} + \tfrac{b_x}{a}x + \tfrac{b_y}{a}y
  \end{aligned}
  \tag{5.52}
  $$

  into Eq. 5.45 and write Eqs. 5.47, 5.48 and 5.49 as

  $$
  \begin{aligned}
  I_{\text{meas}}(x,y) &\approx a R_{\text{meas}}(x,y) + b + b_x x_{\text{c}} + b_y y_{\text{c}} \\
  a_{\text{NL}}(x,y) &\approx \tfrac{a R_{\text{meas}}(x,y) + b + b_x x + b_y y}{I_{\text{meas}}(x,y)} \\
  \bar{I}_{\text{NL}}^{\text{photom. aligned}}(x,y) &= \tfrac{1}{a}\left[a_{\text{NL}}(x,y)I_{\text{meas}}(x,y) - b - b_x x - b_y y\right] \quad .
  \end{aligned}
  \tag{5.53}
  $$

  With this simple example it can be easily shown that it is more convenient to apply the multiplicative non-linear correction directly to the measured frames[27]

  Here we are able to correct with a variable absorption but with a linear intrinsic sky.

- **constant sky**

  Now we assume that only the skyflats induced a gradient and that the sky in the science frames is roughly constant. For science frames during moon light this is obviously not the case.

  We can also assume a linear gradient correction L_R for the reference image and obtain

  $$
  \begin{aligned}
  a_R(x,y) &:= 1 + \tfrac{m_x}{a}x + \tfrac{m_y}{a}y \quad b_R(x,y) := 0 \\
  a_I(x,y) &:= \tfrac{1}{a}(1 + l_x x + l_y y) \quad b_I(x,y) := \tfrac{b}{a}
  \end{aligned}
  \tag{5.54}
  $$

  We use Eq. 5.45 to write Eqs. 5.47, 5.48 and 5.49 as

  $$
  \begin{aligned}
  (1 + l_x x_{\text{c}} + l_y y_{\text{c}})I_{\text{meas}}(x,y) &\approx (a + m_x x_{\text{c}} + m_y y_{\text{c}})R_{\text{meas}}(x,y) + b \\
  a_{\text{NL}}(x,y) &\approx \tfrac{(a + m_x x_{\text{c}} + m_y y_{\text{c}}) R_{\text{meas}}(x,y) + b}{(1 + l_x x_{\text{c}} + l_y y_{\text{c}}) I_{\text{meas}}(x,y)} \\
  \bar{I}_{\text{NL}}^{\text{photom. aligned}}(x,y) &= \tfrac{1 + l_x x_{\text{c}} + l_y y_{\text{c}}}{a + m_x x_{\text{c}} + m_y y_{\text{c}}} a_{\text{NL}}(x,y)I_{\text{meas}}(x,y) - \tfrac{b}{a + m_x x_{\text{c}} + m_y y_{\text{c}}} \quad .
  \end{aligned}
  \tag{5.55}
  $$

- **constant absorption and nonlinear sky**

  In the WeCAPP experiment different telescopes and different CCD-chips were used and with a drastically varying image quality. In some of these cases non-linear effects are large, in particular near the edges of the frames. Images taken through clouds can show a halo of scattered

---

[27] Using the factor for non-linear correction independently from sky can lead to erroneous results: With $R_{\text{meas}}(x,y) = R(x,y)$, $I_{\text{meas}}(x,y) = a \cdot I(x,y) + b$, $I_{\text{meas}}(x,y) \approx aR(x,y) + b$, $\bar{I}_{\text{NL}}^{\text{photom. aligned}}(x,y) = a \cdot a_{\text{NL}}(x,y) \cdot I(x,y) + b$, and $R(x,y) \approx \bar{I}_{\text{NL}}^{\text{photom. aligned}}(x,y) \Rightarrow a_{\text{NL}}(x,y)$ the nonlinear term writes as $a_{\text{NL}}(x,y) = \tfrac{I_{\text{meas}}(x,y) - b}{aI(x)} \approx \tfrac{I_{\text{meas}}(x,y) - b}{aR_{\text{meas}}(x)}$ With $a_{\text{NL}}(x,y) \ll 1$ the enumerator $I_{\text{meas}}(x,y) - b$ for its evaluation can be negative leading to a negative (and wrong) $a_{\text{NL}}(x,y)$.

light around M31. Mathematically this can be treated as broad wings of the PSF. In practice the easiest procedure is to treat this object light as sky background, which then has to be described by non-linear terms.

For this reason we decided to fix the absorption in a central region in a first step fitting simultaneously a polynomial of order 3 for the background

$$
\begin{aligned}
a_R(x,y) &= 1 \quad b_R(x,y) = 0 \\
a_I(x,y) &= \tfrac{1}{a} \quad b_I(x,y) = \tfrac{1}{a}\left(\sum_i^3 \sum_j^{3-i} b_{ij}\,x^i y^j\right)
\end{aligned}
\tag{5.56}
$$

and write Eqs. 5.47, 5.48 and 5.51 as

$$
\begin{aligned}
I_{\mathrm{meas}}(x,y) &\approx a R_{\mathrm{meas}}(x,y) + \left(\sum_i^3 \sum_j^{3-i} b_{ij}\,x^i y^j\right) \\
b_{\mathrm{NL}}(x,y) &\approx a R_{\mathrm{meas}}(x,y) + \left(\sum_i^3 \sum_j^{3-i} b_{ij}\,x^i y^j\right) - I_{\mathrm{meas}}(x,y) \\
\tilde{I}_{\mathrm{NL}}^{\mathrm{photom.\ aligned}}(x,y) &= \tfrac{1}{a}\left[I_{\mathrm{meas}}(x,y) - \left(\sum_i^3 \sum_j^{3-i} b_{ij}\,x^i y^j\right)\right] + b_{\mathrm{NL}}(x,y)
\end{aligned}
\tag{5.57}
$$

Equations 5.57 describe the photometric alignment for all WeCAPP-data. The fitting can be easily done by the algorithms of the difference imaging technique described in Sec. 5.12.

5.10 Reconstruction of bad pixel areas

5.10.1 Approximation of bad pixels by interpolation of pixel values in the same frame

Up to this step we have flagged values for pixels with unreliable photometry as "zero", and used the same flag also in the error frame. These pixels with value and error set to zero will now be replaced. We use a distance and error weighted linear approximation of the closest neighbors. The fitting box is selected as small as possible with the restriction that more than 2/3 of the fitting box pixels minus the central pixel must be valid pixels and the fit box may not be larger than an arbitrary limit which we set according to the spatial resolution of a specific imaging system. If even the largest possible box does not apply to the first criterion the pixel is considered as isolated and not replaced at this point. Each replaced pixel (x_0,y_0) of an image $\tilde{I}$ gets an error calculated from the individual pixel errors of the fitting box

$$
\delta_{\tilde{I}}(x_0,y_0) = \bar{\chi}_{\mathrm{fit}}\,\frac{\displaystyle\sum_{x,y}^{n_{\mathrm{used}}} \delta_{\tilde{I}}(x,y)}{n_{\mathrm{used}}}\ ,\ \text{where}
\tag{5.58}
$$

$n_{\mathrm{used}} = $ number of pixels used for fit, and

$\bar{\chi}_{\mathrm{fit}} = $ defined according to Eq. 5.32.

A larger fitting box has fewer close base points and therefore raises the uncertainty of the linear approximated substitute, so we use an average error of the input parameters times the quality of the fit ($\bar{\chi}_{\mathrm{fit}}$) and not only the error of the calculated value ($\propto 1/n_{\mathrm{used}}$). Like in Sect. 5.7.2, step vii this prevents an incautious use of the replaced pixels in the following.

5.10.2   Replacing with values from similar images

A more sophisticated way is to replace missing pixels with values from comparable images. In addition to the same geometrical and photometric alignment 'comparable images' must have a similar PSF. We test this calculating the χ^2 between the analytical PSF of the two images. The image with the smallest χ^2 is used to replace bad pixels. If no image fulfills the criterion, the stacked value remain marked with zero. This is also the case for saturated pixels, since the PSF-differences are highest in the central part of stars, and the systematic error for replacing would be very high. Since a correct error propagation needs the information about the combined images and their weights, the replacing is done in one step together with stacking[28]. This is explained in the next section.

5.11   Stacking with weighting

To avoid saturation of Galactic foreground stars and the nucleus of M 31 in our field, exposure times were limited to a few hundred seconds. Therefore one has to add several frames taken in one cycle to obtain an acceptable signal-to-noise ratio (S/N). Usually we stacked 5 frames in the R band and 3 frames in the I band according to the criteria of comparable PSF and comparable sky. Frames with very high background levels or very large PSFs were not added if they reduced the detectability of faint variable sources. Consequently the number of images to be stacked was not fixed, coaddition of frames was performed in a way to get a maximum (S/N) ratio for faint point sources in the stacked frame.

Single exposures are never taken under the same observing conditions: the sky levels, the seeing and the zeropoints may differ slightly. To obtain an optimal signal-to-noise ratio (S/N) in a final combined frame weighting factors can be used to stack single images.

In the following we derive the weight α for stacking of two images (denoted by index 1 and index 2) which can be easily generalized to a large number of images. We characterize the PSF by σ_1 and σ_2 and define that inside σ there is a fraction p of the total signal (p can also be optimized so that the (S/N) is largest):

$$S_1 = p^{-1} f_1 \qquad S_2 = p^{-1} f_2 \qquad S = S_1 + \alpha S_2 \tag{5.59}$$

$$N_1 = p^{-1}\sqrt{f_1 + \bar{e}_1^2 \cdot \sigma_1^2 \pi} \qquad N_2 = p^{-1}\sqrt{f_2 + \bar{e}_2^2 \cdot \sigma_2^2 \pi} \qquad N = \sqrt{N_1^2 + \alpha^2 N_2^2} \tag{5.60}$$

where f_1 and f_2 are the fluxes of an object without sky (signal), and $\bar{e}_1$ and $\bar{e}_2$ are the average errors not including the signal (e.g. from sky). and where S and N is the signal and the noise of the combined image. This transforms to:

$$\left(\frac{S}{N}\right) = \frac{S_1 + \alpha S_2}{\sqrt{N_1^2 + \alpha^2 N_2^2}} \tag{5.61}$$

The value of α for which the S/N is largest is

$$\frac{\partial \left(\frac{S}{N}\right)}{\partial \alpha} = (S_1 + \alpha S_2)\left(-\frac{1}{2}\right)\left(N_1^2 + \alpha^2 N_2^2\right)^{-3/2} 2\alpha N_2^2 + S_2 \left(N_1^2 + \alpha^2 N_2^2\right)^{-1/2} \stackrel{!}{=} 0 \quad , \tag{5.62}$$

---

[28] use the `mupipe`-program `subby`

$$(S_1 + \alpha S_2)\alpha N_2^2 = S_2 \left(N_1^2 + \alpha^2 N_2^2\right) \quad , \tag{5.63}$$

$$\alpha N_2^2 S_1 + \alpha^2 N_2^2 S_2 = S_2 N_1^2 + \alpha^2 N_2^2 S_2 \quad , \tag{5.64}$$

$$\alpha = \frac{S_2 N_1^2}{S_1 N_2^2} = \frac{f_2}{f_1} \frac{f_1 + \bar{e}_1^2 \cdot \sigma_1^2 \pi}{f_2 + \bar{e}_2^2 \cdot \sigma_2^2 \pi} \quad . \tag{5.65}$$

For faint, sky-dominated objects (with $f_1 \ll \bar{e}_1^2 \cdot \sigma_1^2 \pi$ and $f_2 \ll \bar{e}_2^2 \cdot \sigma_2^2 \pi$) Eq. (5.65) transforms into

$$\alpha \approx \frac{f_2}{f_1} \frac{\bar{e}_1^2}{\bar{e}_2^2} \frac{\sigma_1^2}{\sigma_2^2} \quad , \tag{5.66}$$

whereas for bright stars, which are not dominated by the sky noise ($f_1 \gg \bar{e}_1^2 \cdot \sigma_1^2 \pi$ and $f_2 \gg \bar{e}_2^2 \cdot \sigma_2^2 \pi$), Eq. (5.65) transforms into

$$\alpha \approx 1 \quad . \tag{5.67}$$

As the majority of the objects in the WeCAPP are very faint point sources (and therefore dominated by the sky-noise) Eq. (5.66) is used for the weighting-parameter α.

We derive the fluxes f_i and the width of the PSF σ_i from a bright star[29], and the errors by medianing a small region in the error frames. The weighting factor[30] for the 1$^{\text{st}}$ frame α_1 was set to one. The factors for the remaining $N-1$ images is given by Eq. (5.66) relative to this image. The final stacked frame I is then obtained[31] from the single frames I_i as

$$I = \frac{\sum_{i=1}^{N} \alpha_i I_i}{\sum_{i=1}^{N} \alpha_i} \quad . \tag{5.68}$$

The error can then be written as

$$\delta_I = \frac{\sqrt{\sum_{i=1}^{N} \alpha_i^2 I_i^2}}{\sum_{i=1}^{N} \alpha_i} \quad . \tag{5.69}$$

Note that the replacement of marked pixels can easily be carried out at that point by setting the weights for those pixels to $\alpha_i = 0$. Since we normalize the sum with the total weight each pixel gets the correct value.

How our pipeline finds "similar images" has been described in Sec. 5.10.2.

---

[29] using the `mupipe`-program `starphot`
[30] using the `mupipe`-program `weight`
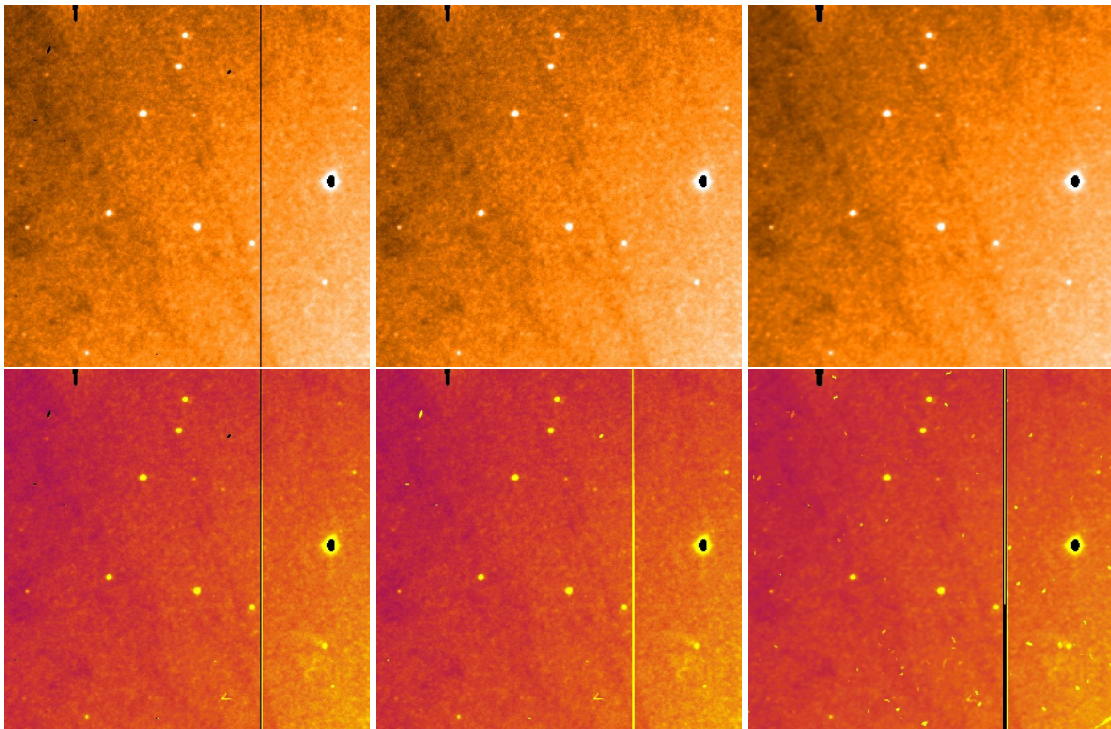[31] using the `mupipe`-program `adder`

Figure 5.16: Photometric Alignment, reconstruction of bad pixels and stacking. *Left:* position and photometrically aligned image; *middle:* with bad pixels replaced; *right:* stacked image; *top:* science images; *bottom* corresponding error image. Images are shifted onto a reference grid using a flux and PSF conserving algorithm. The shifted images are photometrically calibrated using the profile of the M31 bulge. Bad pixels (except saturated) are replaced with pixels of the most similar image, but accounted for in the error image. The final stack is built by maximizing its S/N ratio using the error images and the PSF width for the calculation of weighting factors.

5.12 Difference image analysis

In order to extract light curves of variable sources from the data we use a method called Difference Image Analysis (DIA), proposed by Ciardullo *et al.* (1990) and first implemented by Tomaney & Crotts (1996) in a lensing study.

The idea of DIA is to subtract two positionally and photometrically aligned frames which are identical except for variable sources. The resulting difference image should than be a flat noise frame, in which only the variable point sources are visible.

The crucial point of this technique apart from position registration is the requirement of a perfect matching of the point spread functions (PSFs) between the two frames.

In order to obtain an optimal kernel k we implemented OIS as proposed by Alard & Lupton (1998). This least-squares fitting method determines k by decomposing it into a set of basis functions and solving for the best least square solution.

5.12.1 Convolution and differential background subtraction

One advantage of OIS is that differential background variations can be fit simultaneously with the PSF between the frames. Including a background term the convolution equation, which transforms the PSF with smaller FWHM of the reference frame R to the PSF of an image I, is of the form

$$I(x,y) \approx R(u,v) \otimes K(u,v) + bg(x,y) = \tilde{R}(x,y) \ , \tag{5.70}$$
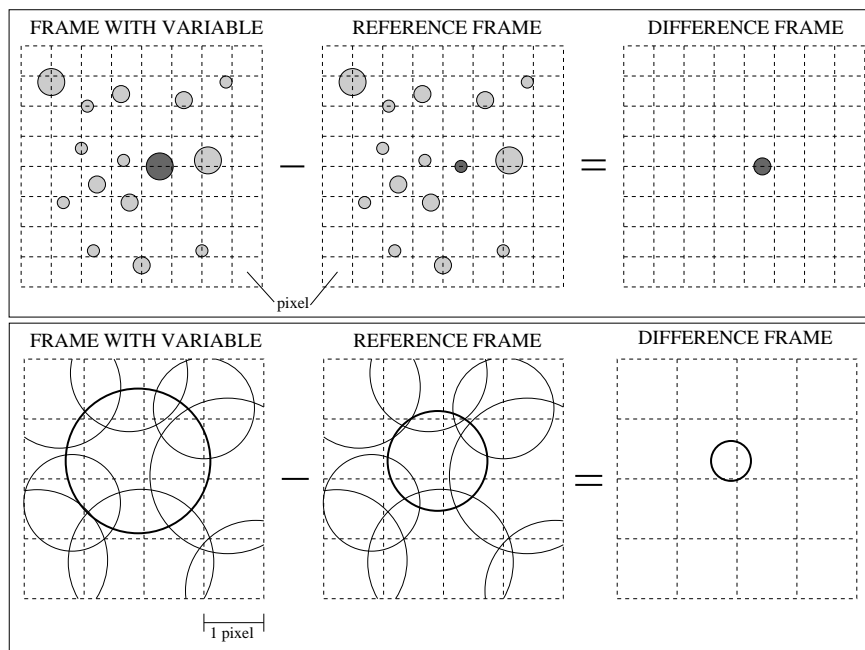

Figure 5.17: Principle of difference imaging, *upper panel:* example for subtracting images with resolved objects from each other, *lower panel:* the method works the same in highly crowded fields (where individual stars cannot be resolved anymore)
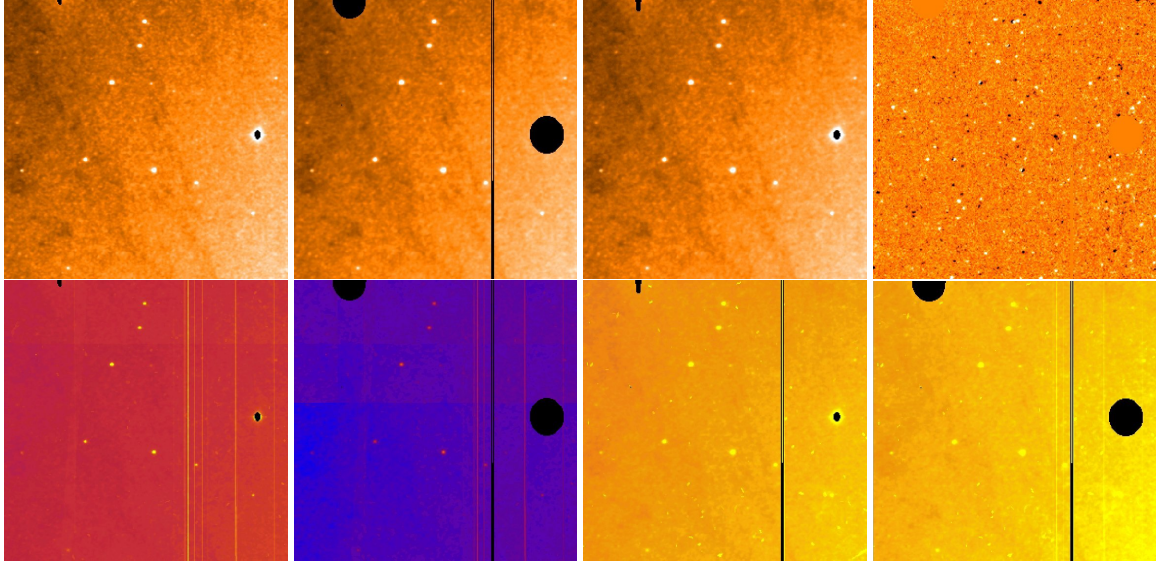
Figure 5.18: Difference image analysis: *From left to right*: reference frame, convolved reference frame, image of particular epoch, difference image; *top:* images; *bottom*: corresponding error images. For the difference photometry a high S/N reference frame with narrow PSF is convolved to the broader PSF of each science frame. The convolution kernel is obtained by a least squares linear fitting procedure with 52 free parameters (OIS). The difference frame (built by subtracting the convolved reference frame from the science frame) shows a large number of positive and negative point sources.

where $(R \otimes K)(x,y) = \sum_{u,v} R(x+u,y+v)K(u,v)$.

The convolution kernel $K(u,v)$ and the background term $bg(x,y)$ are decomposed into basis functions

$$K(u,v) = \sum_{i=1}^{n} a_i B_i(u,v) \text{ , and}$$

$$bg(x,y) = \sum_{i=n+1}^{n+n_{bg}} a_i x^{p_i} y^{q_i} \text{ ,}$$

where n is the total number of coefficients of $K(u,v)$ and n_{bg} is the corresponding number for the background term $bg(x,y)$. The exponents p_i and q_i are integers.

$K(u,v)$ is determined by solving the least-squares problem:

$$\chi^2 = \sum_{x,y} \frac{1}{\sigma_{x,y}^2} [(R \otimes K)(x,y) + bg(x,y) - I(x,y)]^2 \qquad (5.71)$$

$$\overset{!}{=} \min .$$

By setting $\frac{\partial \chi^2}{\partial a_j} \overset{!}{=} 0$ these equations transform into

$$\sum_i a_i \sum_{x,y} \frac{1}{\sigma_{x,y}^2} C_i(x,y) C_j(x,y) \tag{5.72}$$

$$= \sum_{x,y} \frac{1}{\sigma_{x,y}^2} I(x,y) C_j(x,y) \text{ , where}$$

$$C_i(x,y) = \begin{cases} R(u,v) \otimes B_i(u,v) & i = 1,\ldots,n \\ x^{p_i} y^{q_i} & i = n+1,\ldots,n+n_{bg} \end{cases} \tag{5.73}$$

The problem is reduced to the solution of the following matrix equation for the a_i coefficients

$$\sum_i a_i M_{ij} = V_j \quad , \qquad \underline{\underline{M}}\, \underline{a} = \underline{V} \quad , \tag{5.74}$$

where the matrix elements are defined according to

$$M_{ij} = \sum_{x,y} \frac{1}{\sigma_{x,y}^2} C_i(x,y)\, C_j(x,y) \text{ ,} \tag{5.75}$$

$$V_j = \sum_{x,y} \frac{1}{\sigma_{x,y}^2} I(x,y)\, C_j(x,y) \text{ .} \tag{5.76}$$

We use Gaussians modified with polynomials of order p as a kernel model as proposed by Alard & Lupton (1998)

$$K(u,v) = \sum_i a_i B_i(u,v) =$$

$$= \sum_l e^{-\frac{u^2+v^2}{2\sigma_l^2}} \sum_{j=0}^{p_l} \sum_{k=0}^{p_l-j} a_{ljk}\, u^j v^k \text{ .}$$

We limit the number use a combination of three Gaussians with different widths σ multiplied with polynomials up to 6th order. This leads to the following 49 parameter decomposition of $k(u,v)$:

$$\begin{aligned} \sigma_1 = 1 &: e^{-\frac{u^2+v^2}{2\sigma_1^2}} \left(a_1 + \cdots + a_{22}u^6 + \cdots + a_{28}v^6 \right) \\ \sigma_2 = 3 &: e^{-\frac{u^2+v^2}{2\sigma_2^2}} \left(a_{29} + \ldots + a_{39}u^4 + \ldots + a_{43}v^4 \right) \\ \sigma_3 = 9 &: e^{-\frac{u^2+v^2}{2\sigma_3^2}} \left(a_{44} + \cdots + a_{47}u^2 + a_{48}uv + a_{49}v^2 \right) \end{aligned} \tag{5.77}$$

Additionally 3 parameters are used to fit the background

$$bg(x,y) = a_{50} + a_{51}x + a_{52}y \text{ .} \tag{5.78}$$

To cope with the problem of a PSF varying over the area of the CCD we divide the images in sub-areas of 141 x 141 pixels each. In all sub-areas a locally valid convolution kernel is calculated. As we have chosen the kernel to have 21 x 21 pixels we therefore effectively use 161 x 161 to derive $k(u,v)$. Differential refraction causes a star's PSF to depend on its color (Tomaney & Crotts, 1996, chap. 4.4).

However these second order effects are negligible for our data set and do not lead to residuals in the difference images.

For all bad pixels (marked as 0) the convolution is not done, these pixels remain flagged with a zero. The calculation of the matrix M_{ij} is the most time consuming part of the convolution. The matrix M_{ij} of the reference frame R is calculated once and can be used for all images. To enable this timesaving approach we take the error $\sigma_{x,y}$ which enters the calculations always from the error frame of R ($\sigma_{x,y} = \delta_R(x,y)$). Therefore only the calculation of the vector V_j has to be done for each image/reference frame pair.

Bad pixels in the frame I would lead to an error if they are not marked in the frame R. To compensate this the calculation of the matrix is redone for these pixels and then subtracted from the original matrix.

After the convolution the difference frame D is computed by subtracting the $\tilde{R}$ frame from the I frame

$$D = I - \tilde{R} \,. \tag{5.79}$$

The error frames are

$$\delta_{\tilde{R}}(x,y) = \sqrt{\sum_{u,v} K_{u,v}^2 \, \delta_{x+u,y+v}^2} \quad \text{and} \tag{5.80}$$

$$\delta_D(x,y) = \sqrt{\delta_{\tilde{R}}^2(x,y) + \delta_I^2(x,y)} \,. \tag{5.81}$$

As we are performing DIA we have to choose a reference frame R which will be subtracted from all other coadded frames i and which determines the baseline of the light curve. OIS shows best results for a small PSF and a high (S/N) reference frame. Therefore, the best stacked images were coadded once more. Our actual R band reference frame comprises 28 images taken at 2 different nights resulting in a total exposure time of 4400 seconds and a PSF of a FWHM of ≈ 1 arsec (= 2 pixels for all CCDs except one at Wendelstein and Calar Alto). For the I band we coadded 37 frames (i.e. 5 stacked frames taken at 5 different nights) which results in a total exposure time of 5190 seconds and a FWHM of ≈ 1 arsec. As we are continuing collecting data the process of constructing the ultimate reference frame has not finished yet. Each night of high quality data collected at one of the two sites will improve the reference frame further. Figure 5.19 shows a typical difference image obtained by using our implementation of OIS.

5.12.2   Testing the accuracy of the convolution

We tested the accuracy of the convolution with 19 pairs of simulated frames: The reference frames with a FWHM of the stellar PSF of 2.4 pixel and five times more flux than the comparison frames with a FWHM of 3.0, both with of order 100 000 stars and different background levels. According to Sect. 5.12 the reference frames are convolved to match the PSF and the background level of the comparison frames. The convolved frames are subtracted from the comparison frames and the result is divided by the expected RMS errors, as derived from error propagation. This gives the ratio of expected photon noise and measured noise. The histogram of such a ratio frame matches a Gaussian with $\sigma = 1$ almost perfectly, which means that the expected photon noise fits the measured noise. This shows that the OIS method can be applied to very crowded fields like M 31 and gives residual errors at the photon noise level (Fig. 5.20).
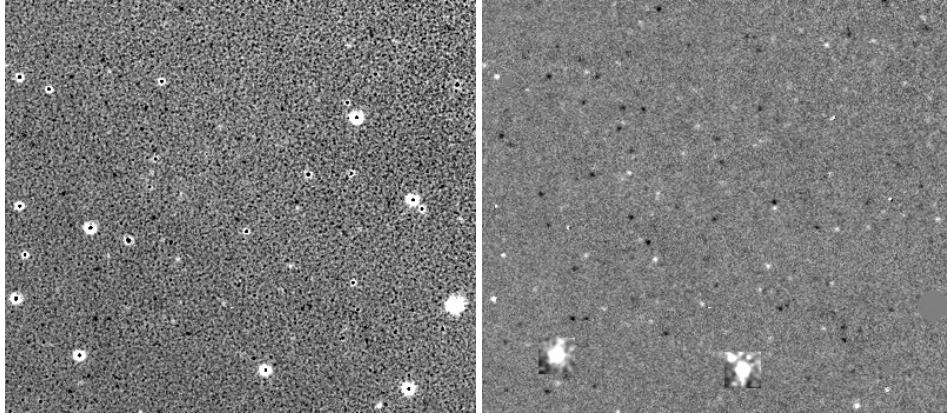
Figure 5.19: Difference images of a part of the M31 bulge ($3.25 \times 2.82\,\mathrm{arcmin}^2$), centered at 6.6 arcmin distance from the nucleus. *Left panel:* difference frame without OIS. Because of the relatively large residuals from stars no identification of faint variable stars is possible. *Right panel:* difference frame with OIS. Bright and dark spots are variable sources. The two boxes represent stars not subtracted in order to provide information on the PSF.
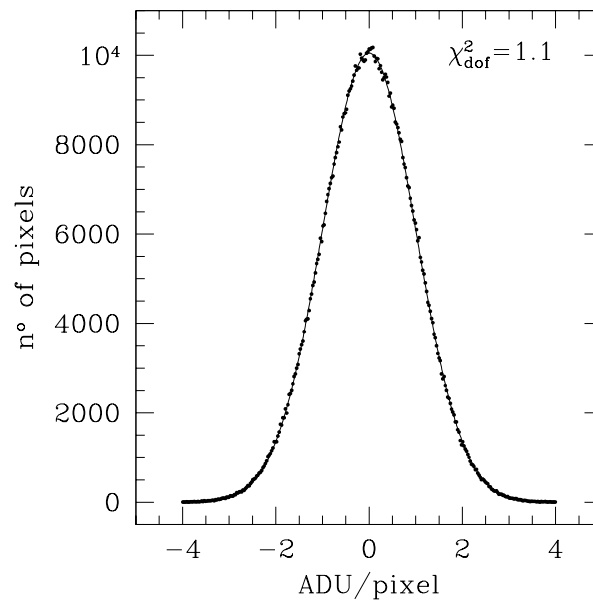

Figure 5.20: Histogram of the pixel values of a simulated difference image divided by the expected RMS errors. The solid curve is a Gaussian with $\sigma = 1$. We calculate the reduced chi-square $\bar{\chi}^2$ of 19 different simulated images in the range between -3 and 3. The median is 1.1, which means that expected and measured errors match almost perfectly and that the residuals in the OIS are at the photon noise level.

5.13   Removing the fringe pattern

Atmospheric sky light lines can produce so-called fringing patterns on CCD images: Since CCDs are very thin to achieve high quantum efficiencies in UBV, some atmospheric lines can have a wavelength with integer multiples of the CCD thickness. This acts like a Fabry-Perot-interferometer and produces a wave like additive structure on the CCD. This source of night sky is nearly independent of moon-light and can be seen mostly in nights without moon, otherwise the photon noise of the moonlight exceeds the signal of the fringe patterns. For the Wendelstein CCD Camera "MONICA" the thickness of the CCD correlates with lines in the I-Band. If the images of a single night are dithered with too small offsets relative to each other the patterns become visible in our difference images. As this additive light strongly influences the light curve measurements of faint sources, we developed an algorithm to extract the fringe pattern and to remove it from the difference images. We use the following seven steps to remove the fringe pattern:

i) The images are smoothed using the median of a circular area with radius 10 pixels in R and 6 pixels in the I-band[32]

ii) The smoothed image is subtracted from the difference images[33] Note that some (bright) variable sources may influence the smoothing of the images so that the subtracted image consists of a combination of fringe pattern and "smeared out" variable sources.

iii) Therefore we detect all variable sources in the corrected difference image[34]

iv) produce an image with artificial sources derived from the difference image[35]

v) and subtract this artificial source image from the original difference image

vi) This difference image without sources is then smoothed again with a smoothing radius of 10 px in the R-band (8 px in the I-band)

vii) and subtracted from the original difference image

This procedure ensures that the variable sources do not influence the fringe pattern map (see Fig 5.21). Note that "better looking" results are achieved with smaller smoothing-radii, but also the risk of removing variable sources is strongly increased.

---

[32] using the mupipe program `smoothfits`
[33] using the mupipe program `subtractfits`
[34] using the mupipe program `psffind`
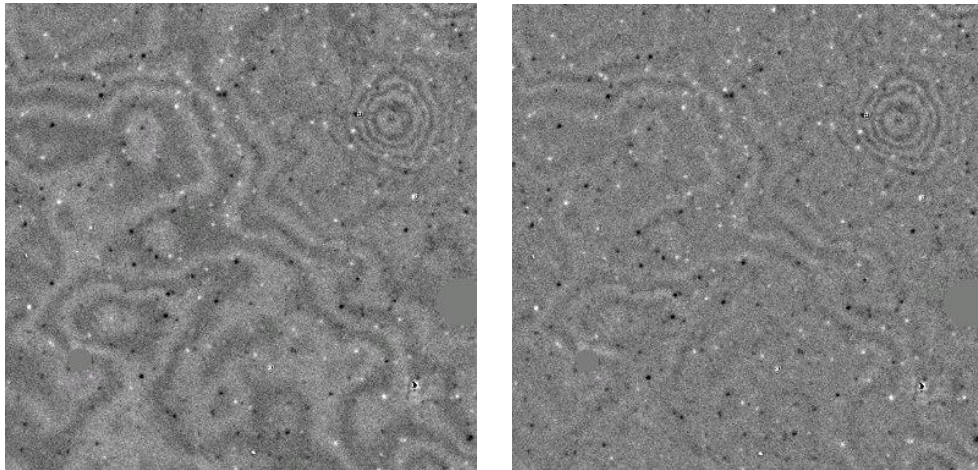[35] using the mupipe program `psfphot`

Figure 5.21: Removing the fringe pattern. *Left*: difference image before de-fringing. *right:* difference image after de-fringing. The result is not perfect but the level of fringing is highly reduced. "Better looking" results are achieved with smaller smoothing-radii, but also the risk of removing variable sources is strongly increased.

5.14   Detection of variable objects

5.14.1   Fast source detection on the integer pixel grid

To detect sources in the difference images we fit a rotated Moffat function (Moffat, 1969) to all local maxima in a binned science frame. Real sources are filtered by rejecting sources with an amplitude less than 5 times the background noise.

We developed a standard star finding algorithm to detect sources in the difference images: We smooth the image by replacing each pixel with the mean of five pixels of a cross shaped area and tag all local maxima. Then we fit a simplified Moffat function (Moffat, 1969) $A\left[1 + s(x^2 + y^2)\right]^{-2.5}$ to these local maxima in the unsmoothed image. After excluding all bad fits we fit a rotated Moffat function to the remaining maxima:

$$f_{\mathrm{moffat}}(x, y) = A\left[1 + (s_x x')^2 + (s_y y')^2\right]^{-\beta} , \qquad (5.82)$$

where
$$\begin{aligned} x' &= (x - x_0)\cos\alpha + (y - y_0)\sin\alpha, \\ y' &= (y - y_0)\cos\alpha - (x - x_0)\sin\alpha. \end{aligned}$$

α denotes the rotation angle, A the amplitude and the pair x_0, y_0 the central coordinates of a stellar PSF. The rise of the wings of the PSF is given by the parameter β, whereas s, s_x, and s_y specify the width of the function.

We include the errors taken from the error frame in the nonlinear least squares fit considering the error frame to weight the count rates obtained in the frames.

Minimum and maximum expected FWHM of the PSF and minimum and maximum of β have to be chosen according to observational conditions. To distinguish between noise and real sources a threshold factor t, is introduced; t gives the ratio of the parameter A and the background noise. All sources below a certain threshold (i.e. $t = 5$ for the WeCAPP project) are regarded as noise. Because difference images can comprise negative sources the images are inverted after one detection cycle. The whole detection procedure is then redone on this inverted frame.

5.14.2   Source detection on a subpixel grid

Using the algorithms presented in Sec. 5.15.3 we designed a simple source detection algorithm for subpixels: All sources where the flux exceeds the error by a threshold t and where the χ^2 is smaller than a threshold value, are extracted from the image and saved into tables[36] of variable sources.

---

[36] using the mupipe program `psfind`

5.15 Photometry

5.15.1 Comparing between PSF-photometry and aperture-photometry

We discuss the differences between PSF-photometry and aperture-photometry in this section. We define the normalized PSF as $\tilde{g}(r)$ and the discrete version as $g_i(\vec{r}_i)$, the measured star $\tilde{p}(r)$ or p_i The photon noise is given by $\tilde{\sigma}(r) = \sqrt{\tilde{p}(r) + B} \approx \sqrt{F\tilde{g}(r) + B}$ or by σ_i for a pixel coordinate $\vec{r}_i$.

Aperture-photometry

After subtracting the background the flux is measured inside an aperture a and extrapolated to infinity using the normalized PSF $\tilde{g}(r)$ or g_i:

$$F(a) = \frac{\sum\limits_{i}^{r_i < a} p_i}{\sum\limits_{i}^{<a} g_i} = \frac{\int\limits_{0}^{a} \tilde{p}(r) 2\pi r\, dr}{\int\limits_{0}^{a} \tilde{g}(r) 2\pi r\, dr} \tag{5.83}$$

$$\sigma_F(a) = \frac{\sqrt{\sum\limits_{i}^{r_i < a} \sigma_i^2}}{\sum\limits_{i}^{<a} g_i} = \frac{\sqrt{\int\limits_{0}^{a} \tilde{\sigma}^2(r) 2\pi r\, dr}}{\int\limits_{0}^{a} \tilde{g}(r) 2\pi r\, dr} \quad . \tag{5.84}$$

For a Gaussian PSF $\tilde{g}(r) \sim e^{-\frac{r^2}{2\sigma_{\text{PSF}}^2}}$ the aperture with largest signal-to-noise is that with $a \approx \frac{2}{3}\text{FWHM}_{\text{PSF}}$ (see Fig. 5.22).
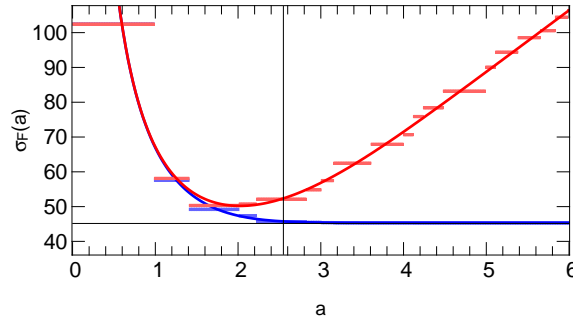

Figure 5.22: The dependency of the photometry accuracy on the aperture a of the two different methods for a Gaussian PSF ($F = 10$, $B = 100\,[\text{px}^{-2}]$, $\text{FWHM}_{\text{PSF}} = 3\,\text{px}$): *light blue*: PSF-photometry with discrete pixels, *blue*: integral PSF-photometry (pixel size $\to 0$), *light red*: aperture-photometry with discrete pixels, *red*: integral aperture-photometry (pixel size $\to 0$). For large apertures PSF-photometry converges to $\sqrt{B \cdot \pi \text{FWHM}_{\text{PSF}}^2 / \ln 4} = 45.16$. The optimal aperture for aperture-photometry is $a \approx \frac{2}{3}\text{FWHM}_{\text{PSF}}$, but the accuracy is always larger than the best value for PSF-photometry. The vertical line mark $\text{FWHM}_{\text{PSF}}/\sqrt{\ln 4}$, the effective aperture, where the noise inside contributes to the error of the PSF-photometry.

PSF-photometry

PSF-photometry consists of fitting a high-signal-to-noise PSF (extracted from stars), to the single sources (after subtracting the background).

In the following we show how to derive the error σ_F for the measured flux in the case of PSF-photometry by minimizing the χ^2:

$$\chi^2 = \sum_i^{r_i < a} \frac{(F \cdot g_i - p_i)^2}{\sigma_i^2} = \int_0^a \frac{(F \cdot \tilde{g}(r) - \tilde{p}(r))^2}{\tilde{\sigma}^2(r)} 2\pi r \, dr \tag{5.85}$$

$$\alpha(a) \equiv 2\pi \int_0^a \frac{\tilde{g}^2(r)}{\tilde{\sigma}^2(r)} r \, dr \tag{5.86}$$

$$\beta(a) \equiv 2\pi \int_0^a \frac{\tilde{g}(r)\,\tilde{p}(r)}{\tilde{\sigma}^2(r)} r \, dr \tag{5.87}$$

$$F(a) = \frac{\beta(a)}{\alpha(a)} = \frac{\int_0^a \frac{\tilde{g}(r)\,\tilde{p}(r)}{\tilde{\sigma}^2(r)} r \, dr}{\int_0^a \frac{\tilde{g}^2(r)}{\tilde{\sigma}^2(r)} r \, dr} \approx \frac{\int_0^a \frac{\tilde{g}(r)\,\tilde{p}(r)}{\tilde{p}(r)+B} r \, dr}{\int_0^a \frac{\tilde{g}^2(r)}{\tilde{p}(r)+B} r \, dr} \overset{\tilde{p}(r) \approx F\tilde{g}(r)}{\approx} F \tag{5.88}$$

$$\sigma_F(a) = \sqrt{\frac{1}{\alpha(a)}} = \sqrt{\frac{1}{2\pi \int_0^a \frac{\tilde{g}^2(r)}{\tilde{\sigma}^2(r)} r \, dr}} \approx \sqrt{\frac{1}{2\pi \int_0^a \frac{\tilde{g}^2(r)}{\tilde{p}(r)+B} r \, dr}} \tag{5.89}$$

For a Gaussian PSF $\tilde{g}(r) \sim e^{-\frac{r^2}{2\sigma_{\mathrm{PSF}}^2}}$, small fluxes $F \ll B$ and large apertures the error of the flux measurement σ_F converges to

$$\lim_{a \to \infty} \sigma_F(a) = \sqrt{B \cdot 4\pi\sigma_{\mathrm{PSF}}^2} = \sqrt{B \cdot \frac{\pi\,\mathrm{FWHM}_{\mathrm{PSF}}^2}{\ln 4}}; \tag{5.90}$$

with $\mathrm{FWHM}_{\mathrm{PSF}} = 2\sqrt{\ln 4}\,\sigma_{\mathrm{PSF}}$.

Therefore $2\sigma = \mathrm{FWHM}_{\mathrm{PSF}}/\sqrt{\ln 4}$ marks the effective aperture, where the noise inside still contributes to the error of the PSF-photometry (see Fig. 5.22).

5.15.2 PSF photometry on the integer grid of each pixel

Photometry of the detected (variable) sources is performed by a profile fitting technique. We first fit a Moffat profile (Moffat, 1969) to several reference stars in the CCD field. These stars should be

bright and isolated. They also have to be unsaturated in any of the images. In the second step we fit the Moffat profile obtained from the reference stars to all variable sources with the amplitude of the sources being the only free parameters. To determine the flux of the source we finally integrate the count rates over the area of the (now fully known) analytical function of the PSF. This minimizes the contamination from neighboring sources. The fitting error of the amplitude is derived according to Eq. 5.89. See Figs. 5.23 and 5.24 for the results of the profile fitting photometry.
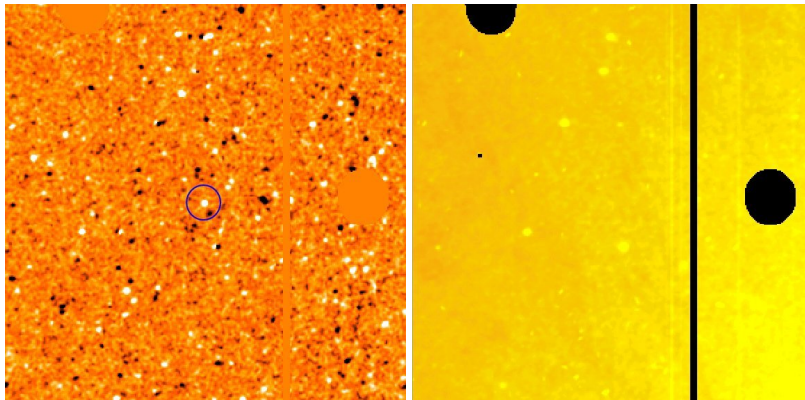
Figure 5.23: *Left:* profile fitting photometry (cuts: $-5 \cdot 10^{-6}$ Jy, $+5 \cdot 10^{-6}$ Jy); *right:* corresponding error frame (cuts: $+0.6 \cdot 10^{-6}$ Jy, $+1.2 \cdot 10^{-6}$ Jy). Fluxes for the variable sources are extracted using PSF-photometry in each pixel: The PSF of a high S/N star in the convolved reference frame is fit in a small region around each pixel in the difference image. This reduces the influence of neighboring variable sources to a low level. Therefore we are able to extract light curves for each pixel of the difference frame.

Errors in interpolations – PSF-fitting photometry

We performed PSF-fitting photometry in simulated images as described in Sect. 5.15.2 using a Moffat fitting function (Eq. 5.82) on bright stars, and (together with OIS, using a high signal-to-noise reference image) on faint variable sources in a crowded and a highly crowded field. We found that per pixel propagated errors compared to estimated errors greatly enhanced the reliability of any fit. Extensive testing with simulated images comprising different observational features shows that this is especially due to the treatment of defective pixels, cosmics and saturation (pixel defects). If we want to avoid the labor of full error propagation we nevertheless have to use masks to get rid of these pixel defects. But then long time series will diminish our field, because the defects will spread (due to dithering, minor misspointing, different detectors, random position defects etc.). Furthermore, the $\bar{\chi}^2$ (Eq. 5.32) of a fit has a valid meaning only for fully propagated errors: $\bar{\chi}^2 \approx 1$ implies a correct measurement within purely noise induced errors and correctly flagged pixel defects; $\bar{\chi}^2 > 1$ indicates systematic errors beyond noise and corrected pixel defects like blending of variable sources, missed or wrongly treated pixel defects. Renouncing full error propagation will shift e.g. bad flatfields from the recognized, high noise category to the undiscovered systematics regime. The calculated error will not change, because we consider $\bar{\chi}^2$ for the final error budget, but we would lose the chance to investigate those cases. If one cannot prove the origin of the uncertainties in a measurement, one can neither be sure of the measurement itself nor of the postulated accuracy.
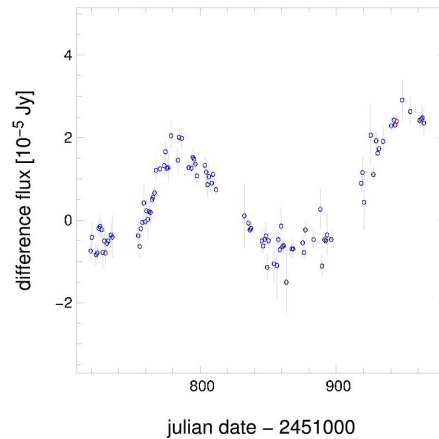
Figure 5.24: Final light curve of a long periodic, semi-regular variable star (marked in the center of Fig. 5.23). The red circle displays the epoch of the sample images in Fig. 5.23. The source shows a difference flux of $3.0(\pm0.2)\cdot10^{-5}$ Jy measured on a background of $11\cdot10^{-5}$ Jy / arcsec^2.

5.15.3 PSF photometry on a subpixel grid of each pixel

Subtracting the background of the convolved reference frame

The aim of producing convolved reference frames is not only to create the difference frame, but also to extract a high signal-to-noise PSF. All bright foreground stars are usable to extract a PSF. The problem in the case of M31 is that each single star has a different background due to the galaxy profile. Therefore our first step is to extract a smooth galaxy profile for each image and to subtract this from the convolved reference frame. This gives a flattened frame with median zero where all bright foreground stars are present with their positive PSF.
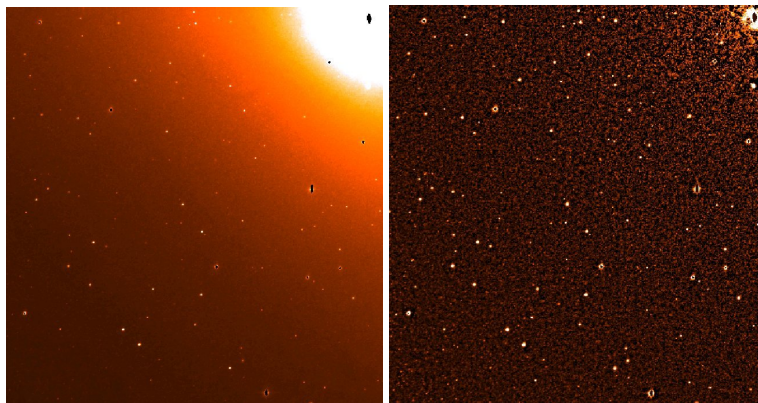

Figure 5.25: Subtracting the background. *Left:* original M31 R-band image ($8\times8\,\mathrm{arcmin}^2$), *right:* image after subtracting the model for the M31 light

Extracting an optimal PSF

After subtracting the galaxy background, a lot of stars can be used to measure the median PSF-shape. For this purpose we fit the center of light for the used stars and combine the stars to a high signal-to-noise PSF.

A straightforward combination-method is to divide each star into a subgrid and combine the stars by shifting them to a common grid, stacking, and normalizing. For a large number of stars the resulting PSF shows nearly no pixelization.

A more sophisticate combination-method is to create the subgrid according to Sec. 5.8.6 using a flux conserving integral interpolation. This provides a smooth PSF also for a small number of reference stars.
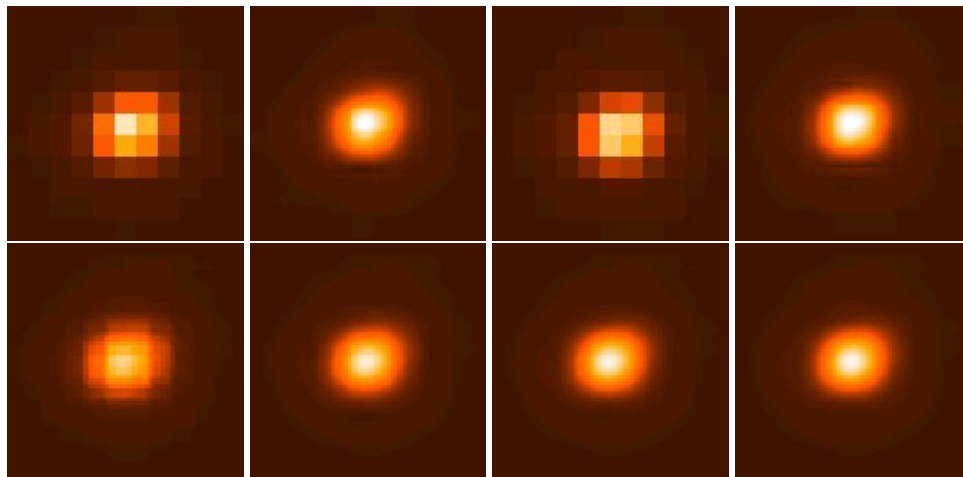

Figure 5.26: Extracting an optimal PSF. *Upper panel:* two stars and their interpolated PSF (order 3), *lower panel:* extracted PSF from 7 stars, created with different interpolation orders, *from left to right:* order 0 to 3.

PSF-photometry on a subgrid

At this point we define the $n \times n$ pixel subgrid. Due to the finite pixel size the PSF located on a special subgrid point can look quite different from the smooth PSF. Therefore we sum up the smooth PSF centered on each subgrid point over the intervals of the surrounding pixels. This results in n^2 different PSFs for each subpixel point.

The last step is to fit the resulting n^2 PSFs to all pixels of the image using the PSFs centered on each pixel subgrid point and to evaluate a χ^2. The minimum of the χ^2 of all subgrid-points of a pixel then defines the most probable PSF-center and the amplitude and thus the flux of the PSF at that pixel position.

Doing this for all pixels we are able to create a new image (of the same size) where each pixel represents a good photometry at that position.

As the fit also provides an error for each pixel, we can also create a corresponding error image.

At positions in the image where no sources are present, the resulting flux derives from the noise value and its errors at this position.

5.16 Photometric calibration of the reference image

As the coadded images are normalized to the reference frame it is not necessary to calibrate each image separately. Only the reference frame is calibrated once.

5.16.1 Calibration with an A0V star

To calculate R-band magnitudes in our R band-data, we determined the instrumental zeropoint Z_R and the atmospheric extinction coefficient κ_R:

$$R = -2.5 \log \frac{\text{phot}_R}{t\,[\text{sec}]} - \kappa_R\,\text{AM} - Z_R \quad , \tag{5.91}$$

where t is the exposure time and AM is the airmass.[37]

Aperture photometry with 7 different Landolt standard stars (Landolt, 1992) observed at different airmasses was performed for a photometric night at Calar Alto Observatory. With these stars the extinction κ_I for the night was calculated to $\kappa_R = 0.073 \pm 0.005$. To determine the zeropoint for the R band we used an A0V-star, Feige 16, with the colors $(B-V) = -0.012$, $(U-B) = 0.009$, $(V-R) = -0.003$, $(R-I) = 0.002$, and a visual magnitude of $V = 12.406$ mag. The zeropoint was determined according to Eq. 5.91 to $Z_R = -23.05 \pm 0.02$ mag and used to calculate the magnitudes for the reference frame. This zeropoint is not valid for Wendelstein.

In the following, we only give fluxes for the sources in our filter system, because the intrinsic magnitudes and colors of our unresolved sources cannot be determined with sufficient accuracy.

We show the light curves in flux differences according to

$$\Delta_{FR} = F_{0R,\text{Vega}} \frac{\Delta\,\text{phot}_R}{t\,[\text{sec}]} 10^{0.4\,\kappa_R\,\text{AM}} 10^{-0.4 Z_R} \tag{5.92}$$

with $F_{0R,\text{Vega}} = 3124$ Jy from an integration over the CCD-filter system.

The same transformations were done for our I band, corresponding to Johnson I (Calar Alto), with $\kappa_I = 0.025 \pm 0.005$, $Z_I = -21.82 \pm 0.03$ mag and $F_{I,\text{Vega}} = 2299$ Jy.

5.16.2 Calibration including color terms

The standard method for the filter calibration is described in Walker (1990), Bessell (1995) and Landolt (1992).

The brightness of a star is measured by counting photons per time $\tilde{R}_i = -2.5 \log \frac{\text{phot}}{t_i\,[\text{sec}]}$

$$\tilde{R} = \tilde{R}_i - \kappa_R\,\text{AM}_i \qquad \tilde{I} = \tilde{I}_i - \kappa_I\,\text{AM}_i \tag{5.93}$$

The extinction coefficient κ is evaluated by imaging a star at least two times with different air mass AM_i under photometric conditions (where the extinction coefficient κ is assumed to be stable and not depending on the sky position) and extrapolating to $\text{AM} = 0$.

---

[37] Note that in Riffeser *et al.* (2001) the given zeropoint is $\text{ZP}_{R'} \equiv -\left(Z_R + 2.5\log\frac{\text{phot}}{\text{ADU}}\right)$ with phot/ADU $= 2.6$ for CA.

The transformation to the standard system is done

$$
\begin{cases}
R = \tilde{R} + \mathscr{Z}_{\tilde{R}} + \alpha_{R,1}(\tilde{R} - \tilde{I}) + \alpha_{R,2}(\tilde{R} - \tilde{I})^2 + \dots \\[2mm]
I = \tilde{I} + \mathscr{Z}_{\tilde{I}} + \alpha_{I,1}(\tilde{I} - \tilde{R}) + \alpha_{I,2}(\tilde{I} - \tilde{R})^2 + \dots \\[2mm]
(R - I) = (\tilde{R} - \tilde{I}) + \alpha_{RI,0} + \alpha_{RI,1}(\tilde{R} - \tilde{I}) + \alpha_{RI,2}(\tilde{R} - \tilde{I})^2 + \dots
\end{cases}
\tag{5.94}
$$

This system is useful for measurements of stars and calibration.
The transformation from the standard system to the local system writes as

$$
\begin{cases}
\tilde{R} = R + Z_R + a_{R,1}(R - I) + a_{R,2}(R - I)^2 + \dots \\[2mm]
\tilde{I} = I + Z_I + a_{I,1}(I - R) + a_{I,2}(I - R)^2 + \dots \\[2mm]
(\tilde{R} - \tilde{I}) = (R - I) + a_{RI,0} + a_{RI,1}(R - I) + a_{RI,2}(R - I)^2 + \dots
\end{cases}
\tag{5.95}
$$

This system allows a reasonable comparison between different telescopes (instruments) based on the coefficients.

We derive the transformations between the coefficients combining the linear transformation of the two systems

$$
\begin{aligned}
R &= \tilde{R} - Z_R - a_{R,1}(R - I) \\[2mm]
&= \tilde{R} - Z_R - a_{R,1}[\tilde{R} + \mathscr{Z}_{\tilde{R}} + \alpha_{R,1}(\tilde{R} - \tilde{I}) - \tilde{I} - \mathscr{Z}_{\tilde{I}} - \alpha_{I,1}(\tilde{I} - \tilde{R})] \\[2mm]
&= \tilde{R} - Z_R - a_{R,1}(\mathscr{Z}_{\tilde{R}} - \mathscr{Z}_{\tilde{I}}) - a_{R,1}(1 + \alpha_{R,1} + \alpha_{I,1})(\tilde{R} - \tilde{I})
\end{aligned}
\tag{5.96}
$$

$$
\begin{cases}
\mathscr{Z}_{\tilde{R}} = -Z_R - a_{R,1}(\mathscr{Z}_{\tilde{R}} - \mathscr{Z}_{\tilde{I}}) \\[2mm]
\alpha_{R,1} = -a_{R,1}(1 + \alpha_{R,1} + \alpha_{I,1})
\end{cases}
\Rightarrow
\begin{cases}
Z_R = -\frac{\mathscr{Z}_{\tilde{R}} + \alpha_{I,1}\mathscr{Z}_{\tilde{R}} + \alpha_{R,1}\mathscr{Z}_{\tilde{I}}}{1 + \alpha_{R,1} + \alpha_{I,1}} \\[3mm]
a_{R,1} = -\frac{\alpha_{R,1}}{1 + \alpha_{R,1} + \alpha_{I,1}}
\end{cases}
\Rightarrow
\begin{cases}
\mathscr{Z}_{\tilde{R}} = -\frac{Z_R + a_{I,1}Z_R + a_{R,1}Z_I}{1 + a_{R,1} + a_{I,1}} \\[3mm]
\alpha_{R,1} = -\frac{a_{R,1}}{1 + a_{R,1} + a_{I,1}}
\end{cases}
\tag{5.97}
$$

For the WeCAPP we derived the calibration for Calar Alto 1.23 m telescope in Riffeser *et al.* (2001) with $\kappa_R = 0.073 \pm 0.005$ and $\kappa_I = 0.025 \pm 0.005$ (see also Sec. 5.16.1)

- $Z_R = -23.05 \pm 0.02 \, \text{mag}$ and $\mathscr{Z}_{\tilde{R}} = -(Z_R + a_{I,1}Z_R + a_{R,1}Z_I)/(1 + a_{R,1} + a_{I,1}) = 23.11 \, \text{mag}$

- $Z_I = -21.82 \pm 0.03 \, \text{mag}$ and $\mathscr{Z}_{\tilde{I}} = -(Z_I + a_{R,1}Z_I + a_{I,1}Z_R)/(1 + a_{R,1} + a_{I,1}) = 22.17 \, \text{mag}$

- $a_{R,1} = -0.06$ and $\alpha_{R,1} = -a_{R,1}/(1 + a_{R,1} + a_{I,1}) = 0.045$

- $a_{I,1} = 0.38$ and $\alpha_{I,1} = -a_{I,1}/(1 + a_{R,1} + a_{I,1}) = -0.29$

Note that the color terms of the Calar Alto are quite similiar to Wendelstein, only the zeropoints differ by $\sim 1\,\mathrm{mag}$, which reflects the difference in size of the telescope mirrors.
Combining the color transformation of Eq. 5.94 and Eq. 5.95

$$(\tilde{R}-\tilde{I}) = (R-I) - \sum_j a_{RI,j} \left((\tilde{R}-\tilde{I}) + \sum_i \alpha_{RI,i}(\tilde{R}-\tilde{I})^i \right)^j \tag{5.98}$$

and accounting only for the first order coefficients

$$(R-I) = (\tilde{R}-\tilde{I}) - a_{RI,0} - a_{RI,1}\left[(\tilde{R}-\tilde{I}) + \alpha_{RI,0} + \alpha_{RI,1}(\tilde{R}-\tilde{I}) \right]$$
$$= (\tilde{R}-\tilde{I}) - (a_{RI,0} + a_{RI,1}\alpha_{RI,0}) - a_{RI,1}(1+\alpha_{RI,1})(\tilde{R}-\tilde{I}) \tag{5.99}$$

we calculate the transformation of the color coefficients between the two systems

$$\begin{cases} \alpha_{RI,0} = -(a_{RI,0} + a_{RI,1}\alpha_{RI,0}) \\ \alpha_{RI,1} = -a_{RI,1}(1+\alpha_{RI,1}) \end{cases} \Rightarrow \begin{cases} a_{RI,0} = -\alpha_{RI,0} + \frac{\alpha_{RI,1}\alpha_{RI,0}}{1+\alpha_{RI,1}} = -\frac{\alpha_{RI,0}}{1+\alpha_{RI,1}} \\ a_{RI,1} = -\frac{\alpha_{RI,1}}{1+\alpha_{RI,1}} \end{cases} \Rightarrow \begin{cases} a_{RI,0} = -\frac{\alpha_{RI,0}}{1+\alpha_{RI,1}} \\ 1 + a_{RI,1} = -\frac{1}{1+\alpha_{RI,1}} \end{cases} \tag{5.100}$$

The parameters $\alpha_{RI,1}$ and $\alpha_{RI,0}$ can easily be measured using a set of different stars with $(R-I)_j$

$$(R-I) = (1+\alpha_{RI,1})(\tilde{R}-\tilde{I}) + \alpha_{RI,0}$$
$$(\tilde{R}-\tilde{I}) = \frac{1}{1+\alpha_{RI,1}}(R-I) - \frac{\alpha_{RI,0}}{1+\alpha_{RI,1}}$$
$$(\tilde{R}-\tilde{I}) = -(1+a_{RI,1})(R-I) - a_{RI,0}$$
$$(\tilde{R}-\tilde{I}) = \beta(R-I) - a_{RI,0} \tag{5.101}$$

solving for the two parameters $\beta := -(1+a_{RI,1})$ and $a_{RI,0}$. Normally the linear relation is acceptable inside a certain color range. If the relation is non-linear higher order terms are needed. Note that for an A0V star (where $R=I$) the color shift can easily derived as

$$a_{RI,0} = (\tilde{R}-\tilde{I})_{\mathrm{A0V}} \tag{5.102}$$

For completeness we mention also a common combined color systems based on 3 filters and 9 free parameters:

$$R = \tilde{R} + \mathscr{Z}_{\tilde{R}} + \alpha_{R,1}(\tilde{R}-\tilde{I}) + \beta_{R,1}(\tilde{R}-\tilde{V})$$
$$(R-I) = (\tilde{R}-\tilde{I}) + \alpha_{RI,0} + \alpha_{RI,1}(\tilde{R}-\tilde{I}) + \beta_{RI,1}(\tilde{R}-\tilde{V})$$
$$(R-V) = (\tilde{R}-\tilde{V}) + \alpha_{RV,0} + \alpha_{RV,1}(\tilde{R}-\tilde{I}) + \beta_{RV,1}(\tilde{R}-\tilde{V}) \tag{5.103}$$

5.17   Implementation

All algorithms are implemented in C++. Each individual reduction step is represented by a commandline program. The pipeline is a simple shell script or Makefile. We take part in the development of a Little Template Library (LTL) which provides very fast and easy to use methods for I/O (i.e. FITS or ASCII), array operations, statistics and Linear Algebra as well as for commandline flags and configuration file parameters.

5.18   Applications

A paper about the application of this image reduction pipeline on a massive imaging campaign of a part of the M 31 Bulge is published (Riffeser *et al.*, 2001). Parts of the reduction pipeline have also been successfully applied to MUNICS data (cosmic-filtering of MOSCA spectra and CAFOS images; Drory *et al.*, 2001) and VLT FORS data (cosmic-filtering and image alignment of revised FDF frames, A. Gabasch, priv. comm.; image alignment and OIS in the center part of NGC 4697 using a difference image built of narrow on-band and off-band line images, Méndez *et al.*, 2001).
Recently the pipeline was also used in Gössl *et al.* (2006), Snigula *et al.* (2004), Pietsch *et al.* (2005), Teodorescu *et al.* (2005), Snigula *et al.* (2006), Gössl *et al.* (2006), Fliri *et al.* (2006), Scholz & Eislöffel (2004b), Moehler *et al.* (2004a), Scholz & Eislöffel (2004a), Moehler *et al.* (2004b), Puzia *et al.* (2004), Snigula *et al.* (2004), Feulner *et al.* (2003) and Heidt *et al.* (2003).

5.19   Summary

WeCAPP (Riffeser *et al.*, 2001) searches for variable objects in the M31 bulge and has collected 100 GB of inhomogeneous raw data. Available data reduction software was not able to comply with the highly variable observing conditions (varying seeing, skylight background, and flatfield quality; different cameras, CCDs, and telescopes) and yet give consistent measurements with reliable error estimates. Therefore we had to develop our own reduction pipeline for CCD images to search for variable sources in highly crowded fields like the M31 bulge.
We describe all steps of the standard reduction including per pixel error propagation: Bias correction, treatment of bad pixels, flatfielding, and filtering of cosmic ray events.
We mask saturated (and blooming affected) pixels, as well as CCD-defects (hot, cold pixels etc.). We subtract the bias level of individual frames estimated from the overscan region and a masterbias ($\kappa\sigma$-clipped mean image of multiple bias level corrected bias frames).
We put a great emphasis on the importance of per pixel propagated errors. The initial error estimate for each pixel in every image is calculated from the pixel's photon noise , the bias noise of the image (clipped RMS of the overscan), and the uncertainties of bias level and bias pattern determination.
We have demonstrated the need of good flatfield calibration images and developed the procedure to obtain them. To achieve a high signal-to-noise ratio (S/N) for a combined flatfield of an epoch we first calculate in each pixel the error weighted mean of normalized and illumination corrected twilight flatfields. After rejecting all 5×5 pixels regions where the center pixel exceeds this mean by more than 5σ, the final calibration image is built by 3σ clipping of the remaining pixels.
We also presented a robust filtering technique for cosmic rays applicable to single images, if we are not undersampled. We fit five-parameter Gaussians to all local maxima of an image. Sources with a width

along one axis of the fitting function smaller than a threshold (which has to be adapted to the PSF size) and, in addition, an amplitude of the fitting function exceeding the expected noise by a certain factor (which has to be chosen according to the additional noise i.e. due to crowding) correspond to cosmics. We mask the pixels, where the fitting function exceeds the fitted surface constant by more than two times the expected photon noise.

We utilize a flux and PSF (point spread function) conserving alignment procedure and a signal-to-noise maximizing stacking method. Images are translated to a reference grid using a flux and PSF conserving algorithm. The shifted images are photometrically calibrated using the profile of the M31 bulge. Bad pixels (except saturated) are replaced with pixels of the most similar image, but accounted for in the error image. The final stack is built by maximizing its S/N ratio using the error images and the PSF width for the calculation of weighting factors.

We discussed all image reduction issues of finding variable objects and measuring their variations in highly crowded fields: optimal image subtraction (OIS), detection for variable sources, and relative photometry of variable sources by a profile fitting technique.

For the difference photometry (Alard & Lupton, 1998) a high S/N reference frame with a narrow PSF is convolved to the broader PSF of each science frame. The calculation of the convolution kernel is performed by a least squares linear fitting procedure optimizing 52 free parameters (OIS). The difference frame (build by subtracting the convolved reference frame from the science frame) shows a large amount of positive and negative point sources.

Fluxes for the variable sources are extracted using PSF-fitting photometry in each pixel: The PSF of a high S/N star in the convolved reference frame is fit to a small region around each pixel in the difference image (Fig. 5.23). This reduces the influence of neighboring variable sources to a low level. Therefore we are able to extract light curves for each pixel of the difference frame (Fig. 5.24).

The complete per pixel error propagation allows us to give accurate errors for each measurement.

Chapter 6

Macho or self-lensing: analysis of microlensing events

6.1 Abstract

We show light curves for all WeCAPP microlensing candidates identified up to now. We analyze all WeCAPP, POINT-AGAPE, MEGA and other events toward M31 and derive probability functions for the lens masses. We also obtain the relative probabilities for lensing by MACHOs in the halo and lensing by bulge or disk stars (self-lensing). We demonstrate the importance of accounting for finite source sizes for the events with largest flux excesses. We show, that there are several events that cannot be caused by stellar lenses, based on our model. We compare the number and characteristics of the measured events with the expectations for MACHO-lensing and self-lensing, derived from a self-consistent M31-model.
We conclude that most likely halo masses are of order ~ 0.2 solar masses, and that the halo fraction has to be 30% to make for each event halo-lensing as likely as self-lensing.

6.2 Introduction

Studies of the Microlensing effect in our local group shall primarily constrain the fraction of compact halo dark matter (MACHOS, see Paczyński (1986)). In addition to lensing by a potential MACHO component there will be lensing of (background) stars by (foreground) stars. These self-lensing events define a lower limit to the number of lensing events that have to be identified in a survey. The comparison of the expected self-lensing and the observed event rate provides a consistency check for the lens model (depending on stellar population content, stellar dynamics and density distribution of the stars) and for the survey efficiency estimate (see Alcock *et al.* (2001b) for MACHO, and Tisserand (2005); Afonso *et al.* (2003a) for EROS and Calchi Novati *et al.* (2005) for POINT-AGAPE and de Jong *et al.* (2006) for MEGA). One can use the known characteristics of lensing and self-lensing events to design surveys that will be dominated by self-lensing. These self-lensing-surveys can measure the faint end mass function of stellar populations (see Riffeser *et al.* (2006) for a proposed ACS campaign to measure the bulge mass function in M31).
One can obtain the most likely MACHO-mass fraction and its confidence limits from the analysis of all lensing events found in a survey (using number, spatial distribution, time scale distribution etc.)

only after the selection criteria and the survey efficiency have been taken into account. The survey efficiency depends on the event characteristics (location, color, time scale and flux excess, finite source effects etc.) and on the sampling and photometric quality of observations. Including precise values for the survey efficiency can completely change the interpretation of a survey. Paulin-Henriksson & Calchi Novati (2004) concluded that there is no hint for Machos toward M31 in the INT data set, whereas the same collaboration claimed with Calchi Novati *et al.* (2005) that there is a fairly strong evidence based on new efficiency estimates of the same survey.

Instead of comparing the expected and observed events one can analyze the observables of individual lensing events; these are flux excess at maximum magnification, full width half maximum ime, color, location and presence/absence of finite source signatures in the light curve (see Riffeser *et al.* (2006) for more details). One can ask for the relative probability of halo lensing and self lensing and derive probability distributions for the lens masses causing that event.

In this chapter we first summarize those M31 lensing event candidates toward M31 that will be investigated here. Then we derive the mass probability functions for all four self-lensing scenarios (bulge and disk stars as sources and lenses), and do the same for all Macho-lensing scenarios (where Galactic and M31 Machos are lensing M31 bulge and disk stars).

6.3   Microlensing candidates obtained by AGAPE, POINT-AGAPE, MEGA, NMS survey teams

In 1994 two projects, AGAPE (Ansari *et al.*, 1997) and Columbia/VATT (Tomaney & Crotts, 1996; Crotts & Tomaney, 1996), started pixellensing surveys toward M31. A lot of microlensing event candidates in M31 have been published after 1996 (Crotts & Tomaney, 1996; Uglesich *et al.*, 1997, 1998, 1999; Crotts *et al.*, 2003). They are formally well fit by a ML light curve (see candidates of Calchi Novati *et al.* (2002)). But many of them lack dense sampling and have large event time scales, which both makes a misinterpretation of long-periodic variables as lensing candidates likely. Indeed, all 5 candidates of Calchi Novati *et al.* (2002) had to be withdrawn for that reason later-on (Calchi Novati *et al.*, 2003).

We do consider AGAPE-Z1 (Ansari *et al.*, 1999) as the first reliable M31 lensing candidate: its light curve is that of a short time scale, bright event, which makes a variable source very unlikely. Candidates reported by the POINT-AGAPE Auriere *et al.* (2001); Paulin-Henriksson *et al.* (2003, 2002); Calchi Novati *et al.* (2005), MEGA (de Jong *et al.* (2004, 2006)) and WeCAPP (Riffeser *et al.*, 2003) consortia should also be reliable, if selected conservatively, since these three consortia analyze data collected with good time sampling.

We have summarized the observational properties of AGAPE-Z1 and event candidates of POINT-AGAPE, MEGA and NMS in Tab. 6.1.

Nevertheless four of these candidates (MEGA-4, MEGA-5, MEGA-6, MEGA-12) have turned out to be variable stars and thus have been withdrawn meanwhile (compare list of MEGA event candidates from de Jong *et al.* (2004) with de Jong *et al.* (2006)). In our analysis we treat withdrawn, reliable and less reliable lensing event candidates the same, since the analysis of missidentified events infact might be useful to judge questionable candidates. Some of the events summarized in Tab. 6.1 have been identified in in more than one survey (like POINT-AGAPE-N1, POINT-AGAPE-N2, POINT-AGAPE-S3, POINT-AGAPE-S4 which correspond to MEGA-16, MEGA-7, WeCAPP-GL1, MEGA-11, respectively.)

We analyse in Sec. 6.9 each event as reported in the publication and use the slightly different results for time scale, flux excess and color to evaluate the robusteness of the mass probability function with respect to observational errors.

For completeness we report in Tab. 6.2 parameters derived from the light curves. The large error bars show the difficulties to estimate the degenerate parameters t_E and u_0 (see Sec. 2.3.2 for the description of observables and degenerate light curve parameters). For this reason we analyze the lensing events without use of that quantities, but with use of the observables in Tab. 6.1.

	α (2000)	δ (2000)	$\Delta\Theta$	t_{FWHM} [d]	$\Delta r'$	$v'-r'$	$r'-i'$	t_0 (JD-2450000)	χ^2/N
				de Jong *et al.* (2004)					
ML 1	0:43:10.54	41:17:47.8		4.2 ± 4.3	22.2 ± 1.1		1.1 ± 1.5	1453.1 ± 0.1	
ML 2	0:43:11.95	41:17:43.6		4.6 ± 0.6	21.6 ± 0.3			1427.08 ± 0.08	
ML 3	0:43:15.76	41:20:52.2		2.6 ± 2.2	21.8 ± 1.2		0.4 ± 1.5	1813.06 ± 0.05	
ML 4	0:43:04.08	41:26:15.6		29.1 ± 1.0	22.8 ± 0.2		0.8 ± 0.3	1822.7 ± 0.2	
ML 5	0:44:48.95	41:22:59.3		9.4 ± 4.1	22.9 ± 0.8		0.4 ± 1.0	1791.1 ± 0.2	
ML 6	0:44:50.97	41:24:42.4		22.9 ± 0.7	22.6 ± 0.2			1470.3 ± 0.2	
ML 7 = N2	0:44:20.89	41:28:44.6		21.6 ± 0.7	19.3 ± 0.2		1.4 ± 0.2	1464.2 ± 0.06	
ML 8	0:43:24.53	41:37:50.4		27.4 ± 0.9	22.7 ± 0.2		0.8 ± 0.2	1456.1 ± 0.2	
ML 9	0:44:46.80	41:41:06.7		3.8 ± 1.6	21.8 ± 0.8		0.4 ± 1.0	1785.3 ± 0.2	
ML 10	0:43:54.87	41:10:33.3		46.8 ± 4.4	22.2 ± 0.3		1.0 ± 0.3	1467.7 ± 0.4	
ML 11 = S4	0:42:29.90	40:53:45.6		2.0 ± 0.3	20.5 ± 0.2		0.3 ± 0.2	1881.6 ± 0.05	
ML 12	0:41:26.90	40:49:42.1		131.0 ± 9.4	23.2 ± 0.3		1.0 ± 0.3	1829.6 ± 0.6	
ML 13	0:43:02.49	40:45:09.2		22.8 ± 3.8	23.3 ± 0.3		0.5 ± 0.4	1430.3 ± 0.5	
ML 14	0:43:42.53	40:42:33.9		28.1 ± 1.4	22.5 ± 0.2		0.3 ± 0.4	1848.1 ± 0.3	
				de Jong *et al.* (2006)					
ML 1	0:43:10.54	41:17:47.8		5.4 ± 7.0	21.8 ± 0.4		0.6	1453.1 ± 0.1	1.12
ML 2	0:43:11.95	41:17:43.6		4.2 ± 0.7	21.51 ± 0.06		0.3	1427 ± 0.1	1.06
ML 3	0:43:15.76	41:20:52.2		2.3 ± 2.9	21.6 ± 0.1		0.4	1813.03 ± 0.03	1.14
ML 7 = N2	0:44:20.89	41:28:44.6		17.8 ± 0.4	19.37 ± 0.02		1.5	1464.8 ± 0.1	1.98
ML 8	0:43:24.53	41:37:50.4		27.5 ± 1.2	22.3 ± 0.2		0.6	1456.3 ± 0.3	0.82
ML 9	0:44:46.80	41:41:06.7		2.3 ± 0.4	21.97 ± 0.08		0.2	1784.9 ± 0.1	1.02
ML 10	0:43:54.87	41:10:33.3		44.7 ± 5.6	22.2 ± 0.1		1.1	1468.9 ± 0.4	1.28
ML 11 = S4	0:42:29.90	40:53:45.6		2.3 ± 0.3	20.72 ± 0.03		0.2	1881.43 ± 0.04	1.03
ML 13	0:43:02.49	40:45:09.2		26.8 ± 1.5	23.3 ± 0.1		0.8	1434 ± 0.3	0.75
ML 14	0:43:42.53	40:42:33.9		25.4 ± 0.4	22.5 ± 0.1		0.4	1848.9 ± 0.1	1.11
ML 15	0:43:09.28	41:20:53.4		16.1 ± 1.1	21.63 ± 0.08		0.5	2538.5 ± 0.1	1.23
ML 16 = N1	0:42:51.22	41:23:55.3		1.4 ± 0.1	21.16 ± 0.06			1406.38 ± 0.02	0.93
ML 17	0:41:55.60	40:56:20.0		10.1 ± 2.6	22.2 ± 0.1		0.4	2553.7 ± 0.2	0.79
ML 18	0:43:17.27	41:02:13.7		33.4 ± 2.3	22.7 ± 0.1		0.5	2536.9 ± 0.4	1.13
				Ansari *et al.* (1999)					
AGAPE Z1	0:42:41.47	41:16:39.1	$42''$	5.3 ± 0.2	17.9			-375.5	2.4
				Auriere *et al.* (2001); Paulin-Henriksson *et al.* (2003, 2002)					
PA-99-N1 = ML 16	0:42:51.42	41:23:53.7	$7'52''$	1.80 ± 0.22	20.8 ± 0.13	1.2 ± 0.2		1406.37 ± 0.06	0.9
PA-99-N2 = ML 7	0:44:20.81	41:28:45.2	$22'03''$	21.75 ± 0.20	19.0 ± 0.2	1.0 ± 0.1		1464.06 ± 0.10	3.1
PA-00-S3 = GL1	0:42:30.51	41:13:04.9	$4'00''$	2.18 ± 0.14	18.8 ± 0.2		0.6 ± 0.1	1850.85 ± 0.02	1.1
PA-00-S4 = ML 11	0:42:29.97	40:53:47.1	$22'31''$	2.09 ± 0.11	20.7 ± 0.2		0.0 ± 0.1	1881.40 ± 0.07	0.7
				Calchi Novati *et al.* (2005)					
PA-99-N1 = ML 16	0:42:51.19	41:23:56.3	$7'53''$	$1.83^{+0.12}_{-0.11}$	20.83 ± 0.10	1.2 ± 0.2		1406.35 ± 0.05	1.1
PA-99-N2 = ML 7	0:44:20.92	41:28:44.8	$22'04''$	$22.16^{+0.12}_{-0.12}$	19.10 ± 0.10	1.0 ± 0.1		1464.2 ± 0.10	9.3
PA-00-S3 = GL1	0:42:30.27	41:13:00.6	$4'06''$	$2.303^{+0.074}_{-0.062}$	18.80 ± 0.20		0.6 ± 0.1	1850.9 ± 0.02	2.1
PA-00-S4 = ML 11	0:42:29.98	40:53:46.1	$22'33''$	$1.96^{+0.09}_{-0.10}$	20.7 ± 0.20		0.0 ± 0.1	1881.4 ± 0.07	0.9
PA-00-N6	0:42:10.70	41:19:45.4	$7'16''$	$1.77^{+0.57}_{-0.60}$	$20.78^{+0.18}_{-0.31}$		$0.51^{+0.25}_{-0.43}$	1883.8 ± 0.07	1.0
PA-99-S7	0:42:42.56	41:12:42.8	$3'28''$	$4.10^{+0.85}_{-0.73}$	20.80 ± 0.10	0.79 ± 0.14		1457.71 ± 0.14	1.3
PA-00-S5	0:41:14.54	40:48:37.7	$32'$	~ 1 see [1]	brighter 20.31		~ 0	1794.5 ± 1	>10
				Belokurov *et al.* (2005)					
Level1-1	0:42:02.3	40:54:35	$22'94$	3.4 ± 0.5				2163.8 ± 0.2	
Level1-2 = GL1, S3	0:42:30.3	41:13:01	$4'08$	2.3 ± 0.1				1850.9 ± 0.0	
Level1-3 = S4	0:42:30.0	40:53:46	$22'54$	2.0 ± 0.1				1881.4 ± 0.1	
Level2-1	0:42:57.7	40:45:37	$30'64$	35.8 ± 3.8				2146.1 ± 1.2	
Level2-2	0:42:59.5	41:14:17	$3'40$	33.1 ± 2.1				1439.1 ± 0.5	
Level2-3	0:42:23.9	41:12:06	$5'57$	50.7 ± 5.4				1523.2 ± 2.9	
				Joshi *et al.* (2005)					
NMS-E1	0:43:33.3	41:06:44	$15'28$	59 ± 2	20.1		1.3 ± 0.2	1908 ± 1	1.3

Table 6.1: Microlensing candidates obtained by AGAPE, POINT-AGAPE, MEGA, NMS survey teams. Positions (α and δ) and other parameters (projected separation from the center of M31, full-width-half-maximum time t_{FWHM}, flux excess, colors, time of event, quality of the Paczynski fit) of microlensing events in M31. AGAPE Z1 was reported by Ansari *et al.* (1999), the POINT-AGAPE events (PA-) by Auriere *et al.* (2001); Paulin-Henriksson *et al.* (2003, 2002); Calchi Novati *et al.* (2005); Belokurov *et al.* (2005), MEGA events (ML) by de Jong *et al.* (2004, 2006). Note that some the MEGA candidates have been withdrawn meanwhile, and some of the Belokurov-POINT-AGAPE candidates are doubtful (Calchi Novati, priv. comm.). The NMS-E1 can also easily be explained by a variable source.

	t_E (days)	u_0	$F_{0,r}$ (ADU/s)	$F_{0,g}$ (ADU/s)	$F_{0,i}$ (ADU/s)	A_0
			de Jong *et al.* (2006)			
ML 1			0.1 ± 0.3			
ML 2			3.4 ± 1.7			
ML 3			0.08 ± 0.21			
ML 7 = N2			6.8 ± 0.4			
ML 8			20.4 ± 22.9			
ML 9			0.9 ± 0.4			
ML 10			1.4 ± 0.5			
ML 11 = S4			1.5 ± 0.4			
ML 13			9.2 ± 10.8			
ML 14			146 ± 182			
ML 15			7.0 ± 2.2			
ML 16 = N1			2.6 ± 0.7			
ML 17			0.5 ± 0.3			
ML 18			13.7 ± 16.3			
			Ansari *et al.* (1999)			
AGAPE Z1	60					40
			Paulin-Henriksson *et al.* (2003)			
PA-99-N1 = ML 16	9.74 ± 0.70					$17.54^{+1.33}_{-1.15}$
PA-99-N2 = ML 7	$91.91^{+4.18}_{-3.83}$					$13.33^{+0.75}_{-0.67}$
PA-00-S3 = GL1	$12.56^{+4.53}_{-3.23}$					$18.88^{+8.15}_{-5.89}$
PA-00-S4	$128.58^{+142.61}_{-72.27}$					211^{+16456}_{-120}
			Calchi Novati *et al.* (2005)			
PA-99-N1 = ML 16	$8.3^{+4.5}_{-2.7}$	$0.070^{+0.046}_{-0.030}$	$1.17^{+0.76}_{-0.49}$	$0.35^{+0.24}_{-0.15}$		$14.3^{+9.4}_{-6.1}$
PA-99-N2 = ML 7	$71.1^{+4.1}_{-3.7}$	$0.1014^{+0.0070}_{-0.0067}$	$10.87^{+0.77}_{-0.83}$	$3.57^{+0.28}_{-0.25}$		$9.9^{+0.68}_{-0.65}$
PA-00-S3 = GL1	$10.4^{+2.5}_{-2.3}$	$0.070^{+0.024}_{-0.017}$	$8.9^{+3.3}_{-2.1}$		$11.7^{+4.0}_{-2.9}$	$14.3^{+4.9}_{-3.5}$
PA-00-S4	$135^{+??}_{-76}$	$0.0042^{+0.056}_{-??}$	$0.11^{+0.15}_{-??}$		$0.07^{+0.10}_{-??}$	$200^{+3200}_{-??}$
PA-00-N6	$8.3^{+10.5}_{-4.1}$	$0.07^{+0.13}_{-0.052}$	$1.40^{+2.6}_{-0.95}$		$1.7^{+3.2}_{-1.2}$	14^{+26}_{-11}
			Belokurov *et al.* (2005)			
Level1-1	10.1 ± 1.8		8.8 ± 3.1		4.9 ± 1.8	8.99 ± 3.128
Level1-2 = GL1, S3	11.2 ± 2.6		8.2 ± 2.3		10.6 ± 3.0	15.62 ± 4.350
Level1-3 = S4	146.6 ± 174.2		0.1 ± 0.1		0.1 ± 0.1	259.48 ± 312.411
Level2-1	36.3 ± 28.0		3.2 ± 4.9		2.2 ± 3.4	2.57 ± 2.407
Level2-2	11.1 ± 1.4		257.9 ± 127.4		–	1.06 ± 0.032
Level2-3	21.4 ± 5.2		102.3 ± 84.5		295.8 ± 243.2	1.15 ± 0.122

Table 6.2: Main characteristics (Einstein time, impact parameter, source brightness, and amplification) of the published microlensing candidates. See Sec. 2.3 for the definitions. Note that the AGAPE-results reported here are the results of the paczinski fit alone, even when extra information is available, as is the case for PA-99-N1 and PA-99-N2.

6.4 The first two microlensing candidates of the WeCAPP survey: WeCAPP-GL1 and WeCAPP-GL2

This section includes the published letter Riffeser *et al.* (2003).

6.4.1 Abstract

In Riffeser *et al.* (2003) we report the detection of the first two microlensing candidates from the Wendelstein Calar Alto Pixellensing Project (WeCAPP). Both are detected with a high signal-to-noise ratio and were filtered out from 4.5 million pixel light curves using a variety of selection criteria. Here we only consider well-sampled events with timescales of $1 \, \mathrm{day} < t_{\mathrm{FWHM}} < 20 \, \mathrm{days}$, high amplitudes, and a low χ^2 of the microlensing fit. The two-color photometry (R, I) shows that the events are achromatic and that giant stars with colors of $(R - I) \approx 1.1 \, \mathrm{mag}$ in the bulge of M31 have been lensed. The magnification factors are 64 and 10, which are obtained for typical giant luminosities of $M_I = -2.5 \, \mathrm{mag}$. Both lensing events lasted for only a few days ($t_{\mathrm{fwhm}}^{\mathrm{GL1}} = 1.7 \, \mathrm{days}$ and $t_{\mathrm{fwhm}}^{\mathrm{GL2}} = 5.4 \, \mathrm{days}$). The event GL1 is likely identical with PA-00-S3 reported by the POINT-AGAPE project. Our calculations favor in both cases the possibility that MACHOs in the halo of M31 caused the lensing events. The most probable masses, $0.08 \, M_\odot$ for GL1 and $0.02 \, M_\odot$ for GL2, are in the range of the brown dwarf limit of hydrogen burning. Solar mass objects are a factor of 2 less likely.

6.4.2 Introduction

Microlensing experiments are an ideal method to search for dark objects within and between galaxies. A large number of microlensing events have been detected toward the Galactic bulge, constraining the number density of faint stars in this direction (Alard, 1999; Afonso *et al.*, 1999; Alcock *et al.*, 2000b; Udalski *et al.*, 1992). Toward the LMC, only 13-17 microlensing events have been reported so far (Alcock *et al.*, 2000a). If all these events are attributed to $0.5 \, M_\odot$ MACHOs, the associated population of dark objects would contribute up to the 20% level to the dark matter content of the Milky Way (Alcock *et al.*, 2000b). However, both the relatively large size of the LMC relative to its distance and the nature of the lenses have cast doubt on this interpretation. It is indeed likely that a large fraction of the microlensing events toward the LMC are due to self-lensing of stars within the LMC (see Lasserre *et al.* (2000); Evans & Kerins (2000), and references therein).

Studying microlensing events toward M31 allows us to separate self-lensing and halo lensing in a statistical way since the optical depth for halo lensing is larger on the far side of M31. In M31, individual stars cannot be resolved, and one therefore has to use the pixellensing technique (Crotts, 1992; Baillon *et al.*, 1993) to follow the variability of sources blended with thousands of other sources within the same pixel. First detections of possible microlensing events were reported by several pixellensing experiments (Crotts & Tomaney, 1996; Ansari *et al.*, 1999; Auriere *et al.*, 2001; Paulin-Henriksson *et al.*, 2002, 2003; Calchi Novati *et al.*, 2003). But since the candidate nature of only five of these events is convincing, no conclusions concerning the near-far asymmetry or the most likely dark matter lensing masses could be drawn yet.

The Wendelstein Calar Alto Pixellensing Project (WeCAPP; Riffeser *et al.* 2001) started in 1997 with test observations. Since 1999, the bulge of M31 was monitored continuously during the time of visibility of M31. The analysis of our 4 yr data will allow not only the identification of very short duration events (e.g., in the fourth year, data of the combined field have been taken on 83% of possible

nights) but also the separation of long-duration microlensing events from long periodic variables like Mira stars. For this Letter, we analyzed the short-duration events ($t_{\mathrm{FWHM}} < 20\,\mathrm{days}$) within one season of Calar Alto data and restricted the detection to high signal-to-noise ratio (S/N), high-magnification events. We report our first two microlensing candidates of that type.

6.4.3   Observations and data reduction

WeCAPP monitors the central region of M31 in a $17.2 \times 17.2\,\mathrm{arcmin}^2$ field with the $1.23\,\mathrm{m}$ telescope of the Calar Alto Observatory. In addition, a quarter of this field, pointing toward the far side of the M31 disk along the southeast minor axis, was observed with the $0.8\,\mathrm{m}$ telescope of the Wendelstein Observatory. The data analysis and candidate selection reported in this Letter are based on the season from 2000 June 23 to 2001 February 25 and are restricted to the Calar Alto data only. During this period, M31 was observed during 43% of all nights. Observations were carried out in R and I filters close to the Kron-Cousins system. We estimate the systematic error in the $(R - I)$ color to be $\leq$ 0.05 mag.

We have developed a pipeline based on the work of Gössl & Riffeser (2002) and A. Riffeser, J. Fliri, & C. A. Gössl (2004, in preparation) that performs the standard CCD reduction, position alignment, photometric alignment, stacking of frames, matching of the point-spread function (PSF) using optical image subtraction (Alard & Lupton, 1998), and the generation of difference images. For the data presented here, all data within one night are co-added, yielding one difference image per night. The reduction package includes full error propagation for each pixel through all reduction steps. In this way, all data points are properly taken into account in the search for variables.

6.4.4   Selection criteria

We investigate only pixels that have more than 10 data points in R and I, which applies to 85% of the $2K \times 2K$ field. For each pixel, we define a flux baseline by the iterative $3\,\sigma$ clipping of all outliers with higher flux. All pixels that have at least three successive (positive) $3\,\sigma$ deviations from this baseline are considered as variables. We fitted the microlensing light curve for high-amplification events (Gould, 1996b) simultaneously to the R- and I-band pixel light curves for every variable. The fit has six free parameters: the full width at half-maximum t_{FWHM} and the time t_0 of maximum amplification (these two parameters are the same for both filters), amplitude $F_{\mathrm{eff},R}$, color $F_{\mathrm{eff},I}/F_{\mathrm{eff},R}$, and baseline levels c_R and c_I. Variables with a reduced $\chi_R^2 > 1.3$ or $\chi_I^2 > 1.3$ are discarded. In this way, we exclude light curves that are not achromatic or that are not symmetric. We also exclude events with $t_{\mathrm{FWHM}} > 20\,\mathrm{days}$, which can be confused with long periodic variables like Mira stars, as long as only one season of data is investigated. In addition, all candidates that do not have at least one significant data point ($3\,\sigma$ deviation from the baseline) within t_{FWHM} of the time of maximum amplification are rejected. We further define the sampling quality for the falling and rising parts of each light curve within $(t_0 - 15\,\mathrm{days}, t_0)$ and $(t_0, t_0 + 15\,\mathrm{days})$; within these time intervals, we require a sampling of the area under the light curve of at least 20% on one side and of at least 5% on the other side (Table 6.3). Here, we only present the two microlensing candidates that have amplitudes 10 times larger than the median error of the light curve (see Fig. 6.1). Both candidates fit perfectly with a symmetric microlensing light curve. Ruling out systematic offsets for the points and errors on the trailing side of GL2 (which is strongly proved by the six single images of that night in each filter), a nonmicrolensing light curve of a variable source hardly fits the data points of GL2. Both microlensing candidates are

Table 6.3: Selection criteria for 2000/2001 data

Criterion	Number
Analyzed light curves	4492250
Light curves with > 10 data points	3835407
Three successive $3\,\sigma$ in R **or** I	517052
$\chi_R < 1.3$ **and** $\chi_I < 1.3$	186039
1 day $< t_{\text{FWHM}} < 20$ days	9497
$3\,\sigma$ light point inside t_{FWHM}	1829
Sampling: $\text{side}_1 > 20\%$, $\text{side}_2 > 5\%$	256
$F_{\text{eff}} > 10\ \text{median}_{\text{error}}$ in R **and** I	15
Candidates	2

detected in several pixels (11 for GL1 and 4 for GL2) inside the PSF of the position of the lensed object. This explains the reduction from 15 events to two events in the last line of Table 6.3. The amplification light curves were obtained by calculating the total flux within the PSF area of each microlensing event.

For both candidates, the selection criteria exclude variable stars like Miras, novae, or dwarf novae. Extracting lensing events with less good time sampling or lower amplitude or events located close to other variables requires refined selection criteria. These will be discussed in a future paper that will also include a test of the detection efficiency and false detection rate with Monte Carlo simulations.

6.4.5 Microlensing candidates

The parameters of both lensing candidates are summarized in Table 6.4. Their light curves are shown in Figure 6.1. GL1, the highest S/N lensing event candidate in our sample, lies $4.^{\text{m}}1$ to the southwest of the nucleus of M31. GL2 is $4.^{\text{m}}4$ to the northwest of the nucleus. Our data have been astrometrically calibrated using bright foreground stars observed with the *Hubble Space Telescope* by Jablonka *et al.* (1999) and with ground-based observations by Magnier *et al.* (1992). Our two calibrations agree within $0.''5$ in declination and $0.''7$ in right ascension, consistent with the astrometric accuracy of $0.''8 - 1.''0$ of the Magnier et al. catalog. After we had detected GL1 and GL2, we cross-checked with events reported by the POINT-AGAPE survey for the same period of time and the same field in M31 (Paulin-Henriksson *et al.*, 2003). It appears that GL1 is likely identical with PA-00-S3, which occurred at the same time (Fig. 6.1). Because POINT-AGAPE did not provide a flux calibration of their data, we had to assume a scaling factor for the amplitude. The zero point in time was not adjusted. The data points from WeCAPP and POINT-AGAPE complement each other nicely and make GL1 the best pixellensing event found so far in M31. GL2 also falls in the observing period covered by POINT-AGAPE, but their time sampling around the event is poor. This may be the reason why GL2 was not detected.

The parameters of the lensing fit are degenerate for high magnifications (Gould, 1996b), i.e., for amplitudes $A_0 \gg 1$ that correspond to impact angles much smaller than the Einstein angle θ_{E}. In this case, for the light curve, we obtain $F_0\,[A(t) - 1] \rightarrow F_{\text{eff}}\,[(12/t_{\text{FWHM}}{}^2)(t - t_0)^2 + 1]^{-1/2}$, with F_0 being the intrinsic flux of the source and $F_{\text{eff}} = F_0/u_0 \approx F_0 A_0$, where u_0 is the impact angle in units of the Einstein angle.
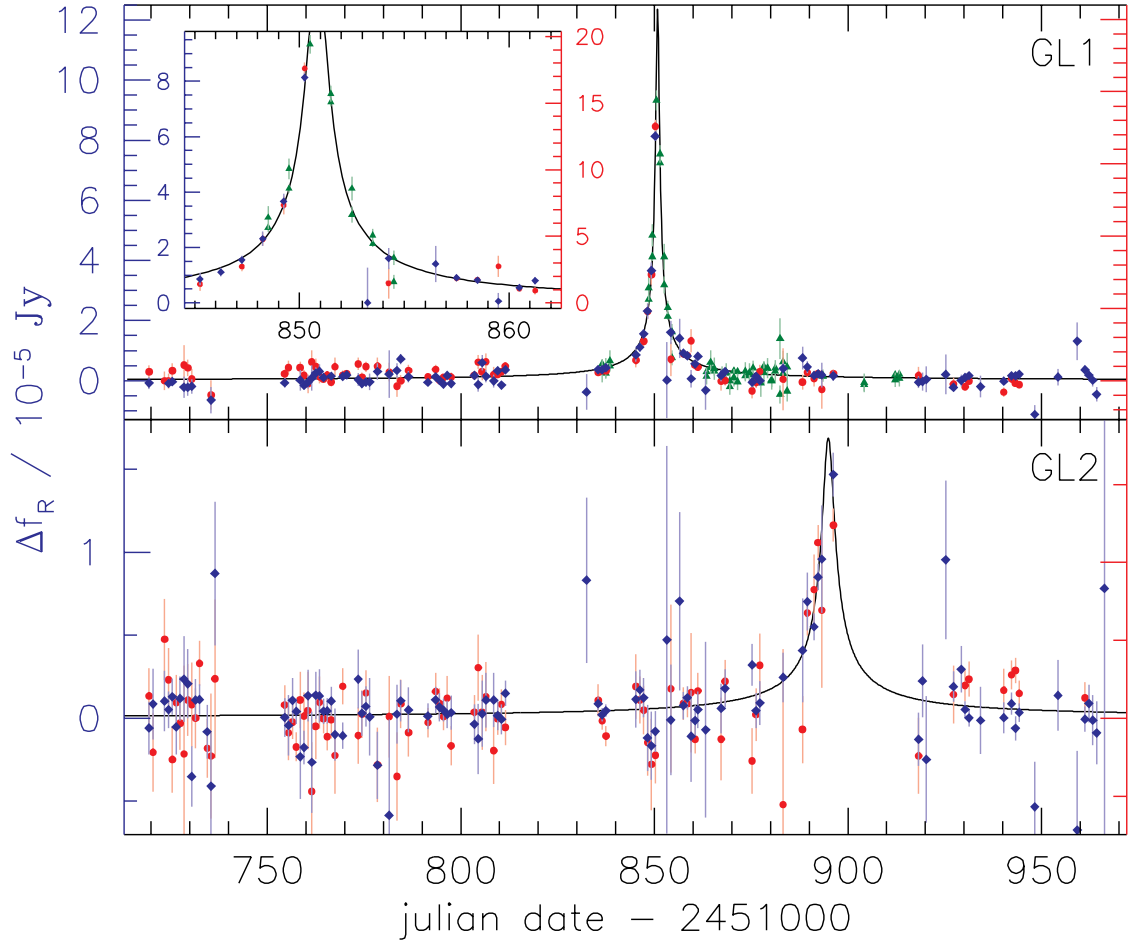
Figure 6.1: Light curves of WeCAPP-GL1 and WeCAPP-GL2. The *I*-band light curve (*red symbols, right axis*) has been scaled to the *R*-band light curve (*blue symbols, left axis*). The scaling factors were derived from the lensing fit (*black curve*) and correspond to a color $(R-I)$ of 1.05 for GL1 and 1.08 for GL2. In addition, we show the *r'* and *i'* data from the POINT-AGAPE PA-00-S3 event (*green symbols*) scaled to our data.

In order to obtain A_0, we evidently need to know the source flux F_0. We can get rough constraints by considering the colors of the light curves, which, due to our selection criteria, are achromatic. We obtain $(R-I)_{GL1} = 1.05$ and $(R-I)_{GL2} = 1.08$. For main-sequence stars, this converts[2] (Cassisi *et al.*, 1998) into absolute magnitudes of $M_I \approx 8$ mag. If the sources are giants, then the magnitudes are $M_I = -2.5$ mag with a minimum of -1.9 and a maximum of -3.7 (Bessell, 1979; Grillmair *et al.*, 1996). We now derive the lensing parameters as follows: $u_0 = F_{0,I}/F_{eff,I} \rightarrow t_E = t_{FWHM}/(u_0\sqrt{12}) \rightarrow M_{lens} = (v_t t_E)^2 c^2 D_{os}/[4GD_{ol}(D_{os} - D_{ol})]$, where t_E is the Einstein timescale, v_t is the transverse velocity between source and lens, and D_L and D_S are the angular distances to the lens and source, respectively.

To estimate plausible lens masses, the Einstein timescales t_E are calculated for fixed luminosities of

---

[2] Transformed on the observational plane by Maraston (1998)

possible source stars (see Table 6.4). Note that the errors in t_E reflect the accuracy of the determination of t_{FWHM} in the degenerate Gould fit only and do not account for the systematic uncertainties due to the unknown luminosities of the sources. If the source is a main-sequence star, we need very high magnifications, $A_0 \approx 10^5 - 10^6$. The corresponding lens masses (for $v_t = 210 \, \text{km s}^{-1}$, $D_{ol} = 768 \, \text{kpc}$, $D_{os} = 770 \, \text{kpc}$) are $M \approx 10^7 - 10^8 \, M_\odot$, an implausibly large value. If the source is a giant, the required magnifications are reduced to $A_{0,GL1} = 64$ and $A_{0,GL2} = 10$; the typical self-lensing masses become $M = 0.8 \, M_\odot$ and $M = 0.2 \, M_\odot$.

Assuming the source to be a red giant with $M_I = -2.5 \, \text{mag}$, we calculate the probability $p(M, t_E)$ that a microlensing event of an observed timescale t_E can be produced by a lens of the mass M. Following the calculations of (Jetzer & Massó, 1994, eq. (8)) and (Jetzer, 1994, eq. (11)), we get

$$p(M, t_E) \sim \xi(M) \int \rho_S(D_{os}) \int \rho_L(D_{ol}) f\left(\frac{R_E}{t_E}\right) \frac{R_E^3}{t_E^3} \, dD_{ol} \, dD_{os}$$

where $\xi(M)$ is the mass function (MF), $\rho_S(D_{os})$ is the sources' density, $\rho_L(D_{ol})$ is the lenses' density, $f(v_t)$ is the velocity distribution, and $R_E(D_{ol}, M, D_{os})$ is the Einstein radius.

Table 6.4: Parameters of the Microlensing Candidates

	GL1	with PA-00-S3[3]	GL2
α_{J2000}	$00^h 42^m 30\overset{s}{.}3$	$00^h 42^m 30\overset{s}{.}3$	$00^h 42^m 32\overset{s}{.}8$
δ_{J2000}	$+41°13'00\overset{''}{.}8$	$+41°13'00\overset{''}{.}8$	$+41°19'56\overset{''}{.}5$
t_0 (JD-2,451,000)	850.80 ± 0.13	850.84 ± 0.02	894.77 ± 0.21
t_{FWHM} (days)	1.38 ± 0.53	1.65 ± 0.10	5.41 ± 2.49
$F_{eff,R}$ (10^{-5} Jy)	13.4 ± 5.4	12.4 ± 0.6	1.7 ± 0.5
$F_{eff,I}$ (10^{-5} Jy)	28.0 ± 11.2	25.7 ± 1.5	3.6 ± 1.1
$(R-I)$[4]	1.05 ± 0.08	1.05 ± 0.08	1.08 ± 0.24
χ^2	1.23	1.22	1.02
$M_I = -1.9$ mag			
A_0	120	110	16
t_E (days)	47.4 ± 18.1	52.1 ± 3.2	23.9 ± 11.0
$M_I = -2.5$ mag			
A_0	69	64	10
t_E (days)	27.2 ± 10.4	30.0 ± 1.8	13.8 ± 6.3
$M_I = -3.7$ mag			
A_0	24	22	4
t_E (days)	9.0 ± 3.5	9.9 ± 0.6	4.6 ± 2.1
$M_I = 7.7$ mag			
A_0	8.2×10^5	7.6×10^5	1.1×10^5
t_E (10^5 days)	3.3 ± 1.3	3.6 ± 0.2	1.7 ± 0.8

The distribution of matter in the central part of M31 is based on the bulge model of Kent (1989b). The disk is modeled with a radial scale length of 6.4 kpc and an exponential shape and with a vertical scale length of 0.3 kpc and a sech^2 shape. The halo is modeled as an isothermal sphere with a core

radius of $r_c = 2\,\mathrm{kpc}$. The velocity distribution was calculated from a Maxwellian halo bulge and disk velocity distribution with an additional rotation for bulge and disk (Kerins *et al.*, 2001).

For the bulge lenses, we take the MF as derived for the galactic bulge, $\xi \sim M^{-1.33}$ (Zoccali *et al.*, 2000). For the disk population, we adopt a Gould MF $\xi \sim M^{-2.21}$ with a flattening $\xi \sim M^{-0.56}$ below $0.59\,M_\odot$ (Gould, 1996b). Both are cut at the lower end at the hydrogen-burning limit of $0.08\,M_\odot$. At the upper end, the bulge MF is cut at the main-sequence turnoff of $0.95\,M_\odot$ (C. Maraston 2003, private communication), and the disk MF is cut at $10\,M_\odot$. The MF for the potential MACHO population residing in the halo of M31 is of course unknown. We therefore calculate the probability distribution for halos consisting of one mass only, i.e., taking δ-function MFs centered on the lens mass $\xi = \delta(M - M_{\mathrm{lens}})/M_{\mathrm{lens}}$. Moreover, we assume that the whole dark halo of M31 consists of MACHOs. Lensing by Galactic halo objects has an order-of-magnitude smaller optical depth and is therefore neglected in our considerations.

The results are shown in Figure 6.2. For M31 halo lenses, the most probable masses are $0.08\,M_\odot$ for GL1 and $0.02\,M_\odot$ for GL2. In the case of self-lensing, the most probable masses are about a factor of 4 bigger. Taking the most likely halo lens masses, the ratio of the probabilities that the lenses are part of the dark halo or the stellar content $p_{\mathrm{halo}}/(p_{\mathrm{bulge}} + p_{\mathrm{disk}})$ is 1.6 for GL1 and 3.3 for GL2. We conclude therefore that it is likely that lenses residing in the halo of M31 caused the events in both cases.
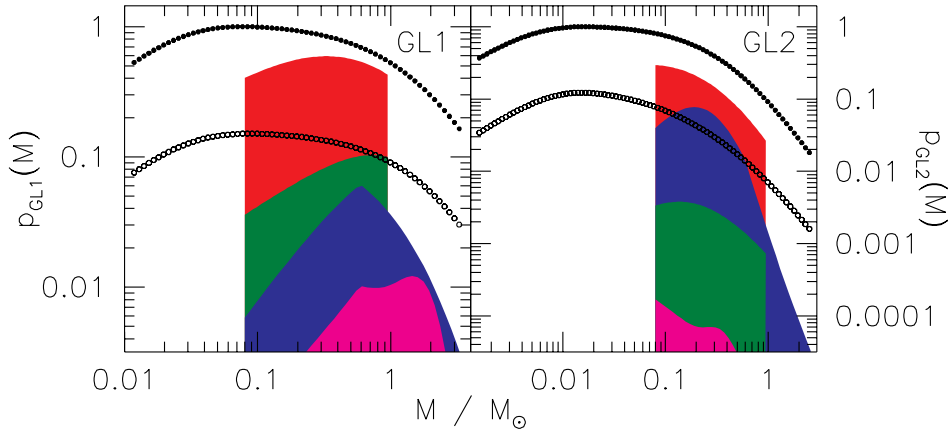
Figure 6.2: Mass probability for GL1 (left panel) and GL2 (right panel) for lens-source configurations: halo-bulge (*filled circles*), halo-disk (*open circles*), bulge-bulge (*red*), bulge-disk (*green*), disk-bulge (*blue*), disk-disk (*magenta*). The maximum of each curve is scaled to reflect the total probability of a respective lens-source event relative to the case of a halo-bulge lensing event with the most probable MACHO mass. For example in case of GL1 the probability for bulge-bulge lensing relative to halo-bulge lensing with $0.08\,M_\odot$ lenses becomes 0.6 (maximum of red curve). A halo consisting of $0.014\,M_\odot$ MACHOs would have the same probability as bulge-bulge lensing. Note that the shapes of the distributions for bulge and disk lenses are strongly affected by the mass function $\xi(M)$ used.

6.4.6   Discussion and outlook

We presented the first two high (S/N), short-timescale microlensing events from WeCAPP. GL1 is likely identical to PA-00-S3 found by POINT-AGAPE. Combining the data from AGAPE with ours

shows that the error bar of the derived Einstein timescale becomes smaller by a factor of 5 compared with the individual error bar. This demonstrates the importance of a good time sampling of the events. We derived the colors of the lensed stars, the amplification factors, and the likely lens masses for both bulge/disk self-lensing and halo lensing. We showed that red giants are the likely source objects, while main-sequence stars are highly implausible.

Self-lensing in the bulge can only be separated from halo lensing statistically. Halo lensing events show a spatial asymmetry because the optical depth for lensing events is higher for stars on the far side of M31 than for stars on the near side (Crotts, 1992) (J. Fliri et al. 2005, in preparation). In contrast, bulge self-lensing is symmetric.

The bulge self-lensing hypothesis yields lensing stars at or below the main-sequence turnoff of the M31 bulge. On the other hand, if the lensing events are caused by MACHOs, their masses are typically very low, most probable below $0.1 M_{\odot}$. Masses in the range of $0.5 - 1 M_{\odot}$ are more unlikely.

So far, we have analyzed one observing season and restricted the lensing search to short-time, high-amplification events in order to avoid confusion with variable stars. The whole WeCAPP data set will allow us to identify all variables and thus will enable us to search for lower amplitude and longer duration microlensing events.

Decreasing the amplitude threshold will increase the detected rate of events in two ways. As the event rate is proportional to the inverse of the minimum required magnification $A_{0,\mathrm{min}}$ in the pixellensing regime, we expect to detect more lensed giants. On the other hand, lowering the amplification threshold could also make it possible to detect highly amplified main-sequence stars (Gould, 1996b) that exceed the evolved stars in the bulge of M31 by a factor of more than a hundred. How many more lensing events will be detected depends on the mass function of the lenses, but we can expect at least a factor of a few (A. Riffeser et al. 2006, in preparation).

Finally, the effects of time sampling and of the noise properties of our sample on the detectability of lensing events have to be taken into account. The results of the modeling of these effects for events of different durations and amplitudes using Monte Carlo simulations will be presented in a future publication. With the full data set, we expect to increase the number of lensing events in order to detect the predicted asymmetry of MACHO lensing or to rule out a significant MACHO population in the halo of M31.

6.5 WeCAPP-GL1: no self-lensing event?

The analysis of WeCAPP-GL1 done in Riffeser *et al.* (2003) and reported in Sec. 6.4 was done with some simplifications that are overcome by now. One point regards the luminosity and mass properties of stars and is discussed in Sec. 6.9. The other one is the approximation of stars as point sources. The effect of finite source sizes is also demonstrated in Sec. 6.9. This section (Sec. 6.5) should provide a "back of envelope" estimate for the fact that GL1 can hardly be due to self-lensing.

We now analyse the gravitational lensing event WeCAPP-GL1, one of the brightest lensing events in M31 reported up to now. It is our goal to show that for this event the self-lensing hypothesis is very unlikely, although not completely excluded once the finiteness of source sizes (stellar radii are denoted by R_*) has been taken into account. The large flux excess can be used together with Eq. 2.18 to constrain the lensing configuration of the event (see Fig. 6.3). We transform Eq. 2.18 into

$$D_{\mathrm{ol}} = D_{\mathrm{os}} \left(\left(\frac{\Delta_{F,\mathrm{max}}}{4\sqrt{G}/c\sqrt{M}} \frac{R_*}{F_0} \right)^2 \frac{1}{D_{\mathrm{os}}} + 1 \right)^{-1} \quad , \tag{6.1}$$

where the unlensed source flux $F_0(D_{\mathrm{os}}, \mathrm{ext})$ depends on source distance and extinction toward the source.

Eq. 6.1 provides the maximum distance a lens can have to allow a lensing event with a flux-excess $\Delta_{F,\mathrm{max}}$ at maximum magnification. For a given source distance and a given source and lens population, the upper limit of that distance is set by the largest "F_0/R_*"-ratio for source stars and the largest lens mass possible.

The largest lens masses allowed for the M31 bulge and disk are $M_{0\mathrm{max}} = 1.01 M_\odot$ (bulge) and $M_{0\mathrm{max}} = 1.71 M_\odot$ (disk) [see Sec. 3.4 for details].

For the measured color of the WeCAPP-GL1 event ($R - I = 1.05\,\mathrm{mag}$) the largest flux-to-radius ratio for the bulge and disk populations are obtained for a bulge star with $\mathcal{M} = -0.74\,\mathrm{mag}$ and $R_* = 43.3 R_\odot$ and a disk star with $\mathcal{M} = -2.13\,\mathrm{mag}$ and $R_* = 33.9 R_\odot$.

The flux excess $\Delta_{F,\mathrm{max}}$ at maximum magnification can be obtained from the light curve of the event. The two most extreme ways to estimate that value are as follows

- one assumes that finite source effects do not play a role at all for that event, which therefore is perfectly described by the point-source approximation light curve (Eq. 2.2). The flux excess $\Delta_{F,\mathrm{max}}$ is then obtained from the point source light curve fit and equals

$$\Delta_{F,\mathrm{max}}^{\mathrm{WeCAPP-GL1}} = 12.4 \cdot 10^{-5}\,\mathrm{Jy} \quad . \tag{6.2}$$

  The assumption of a small source seems perfectly justified because one does not see any finite-source effects in the wings of the well sampled GL1 light curve (see Fig. 2.1).

- One takes the viewpoint that one does not know the flux at maximum magnification, and thus can not exclude that finite source effects decrease that maximum flux relative to the point-source approximation. In that case a robust lower limit for $\Delta_{F,\mathrm{max}}$ can be obtained from the highest data point of the light curve:

$$\Delta_{F,\mathrm{max}}^{\mathrm{WeCAPP-GL1}} = 9.0 \cdot 10^{-5}\,\mathrm{Jy} \quad . \tag{6.3}$$
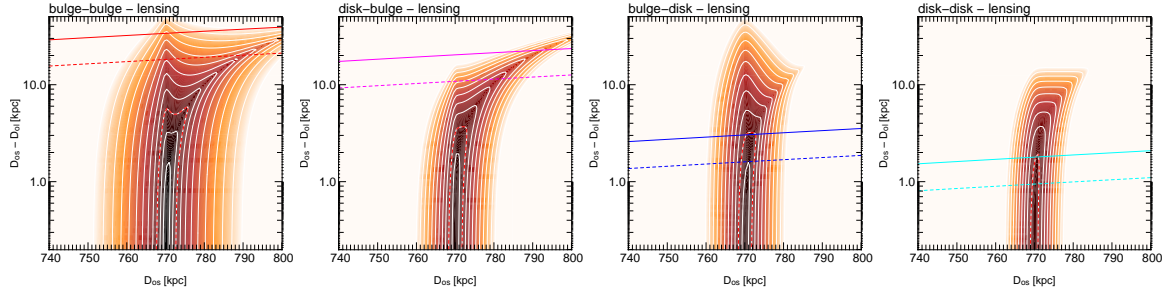
Figure 6.3: Minimum lens source distance for all possible self-lensing configurations of the WeCAPP-GL1 microlensing event using Eq. 6.1 and the source color $R-I = 1.05$ mag. The largest disk and bulge masses are $1.71 M_\odot$ and $1.01 M_\odot$ for the stellar populations assumed. *red:* bulge-bulge lensing, *magenta:* disk-bulge lensing. *blue:* bulge-disk lensing, *cyan:* disk-disk lensing. The *solid lines* are obtained if the maximum flux excess from a Paczynski light curve fit is used, Eq. 6.2, the *dashed line* takes the maximum flux excess observed as lower limit, Eq. 6.3. Contours show the product of the density of all source and lens stars as a function of the line-of-sight distance to GL1 and the lens-source separation, contour levels mark factor 10 steps where the *red dashed* contours mark $\rho^2 = 0.01 \, \mathrm{pc}^2$.
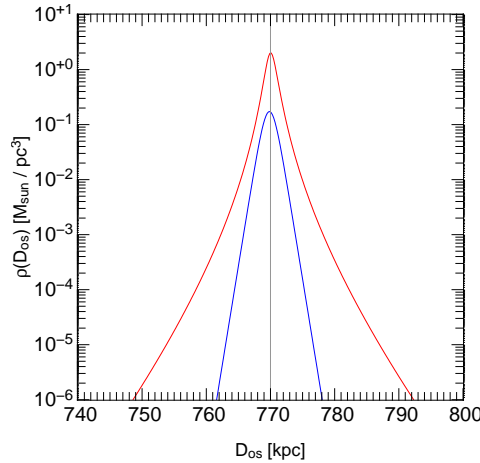
Figure 6.4: Density of bulge (*red*) and disk (*blue*) stars along the line-of-sight to GL1.

We now can insert the estimates for the excess brightness of the event at maximum, the largest source-flux-to-radius ratio and the largest self lensing mass possible and obtain the maximum lens distance as a function of the source distance. The results are shown in Fig.6.3.

For bulge sources at 770 kpc the separations are $D_{\mathrm{os}} - D_{\mathrm{ol}} = 10.8$ kpc for disk lenses with $M_0 = 1.71 M_\odot$ and $D_{\mathrm{os}} - D_{\mathrm{ol}} = 10.8$ kpc for bulge lenses with $M_0 = 1.01 M_\odot$ (see Fig 6.3 a,b). At those large distances from the center, the bulge density becomes very small, making bulge sources very unlikely. For a disk source at 770 kpc disk lenses with $M_0 = 1.71 M_\odot$ have to be separated by only 0.94 kpc. Bulge lenses with $M_0 = 1.01 M_\odot$ have to be separated from a source at 770 kpc by only 1.6 kpc.

For all configurations the densities are very small: In Fig. 6.4 we plot the density of the bulge and the disk at the position of GL1. It follows that the density of the bulge drops by a factor of 40 from 1 kpc to 4 kpc away from symmetry plane. In addition, according to our M31-model the bulge has nearly a

factor 2 more bright stars (< 1 mag) in the color range (of GL1) from $R-I 0.7$ mag to $R-I = 1.1$ mag than the disk (for the same mass density). Taking everything together it seems unlikely to produce the WeCAPP-GL1 event with self-lensing. The precise implication of the finite source sizes will be evaluated in Sec. 6.9.

6.6 Further WeCAPP candidates

We show all plausible microlensing event candidates found in WeCAPP data so far. We have analyzed the complete data set for 2000/2001, 2001/2002, and 2002/2003, and the main fraction (field F1) for the remaining seasons.

Since the data volume and the data quality varied within the 8 years of data collection[5], we slightly modified the detection criterias, which led to WeCAPP-GL1 and GL2, described in Sec. 6.4.4. We summarize our modifications in Tab. 6.5. Relative to Tab. 6.3 we softened the criteria for the reduced χ in R and I and allowed for all lightcurves with $\chi_R < 1.3$ or $\chi_I < 1.3$. We also decreased the amplitude criteria to a signal-to-noise of 6 to detect also fainter lensing events and extended the upper t_{FWHM}-limit to 200 days, since for the full (8 year) data set long-periodic variables can be ruled out. We alos allowed for shorter time scales $t_{\mathrm{FWHM}} = 0.5$ days.

Due to more sophisticated photometric methods (see Sec. 5) the light curves for GL1 and GL2 slightly differ from the published ones in (Riffeser *et al.*, 2003), but agree with them inside the error bars.

Criterion	Number
Analyzed light curves	4492250
Three successive 3 σ in *R* **or** *I*	1750041
$\chi_R < 1.3$ **or** $\chi_I < 1.3$	725572
$0.5\,\mathrm{d}d < t_{\mathrm{FWHM}} < 200\,\mathrm{d}$	563114
nearest light point inside t_{FWHM}	355125
Sampling: $\mathrm{side}_1 > 20\%$, $\mathrm{side}_2 > 5\%$	288040
$F_{\mathrm{eff}} > 6$ $\mathrm{median}_{\mathrm{error}}$ in *R* **and** *I*	1438
Candidates (inspected by eye)	13

Table 6.5: Selection criteria for the 8 year data

Figure 6.5 shows the Julian date distribution of all pixel light curves analyzed. The colored histograms show how the number of light curves fulfilling the criteria is reduced in the selection procedure. The total numbers correspond to those given in Tab. 6.5.

For GL 6, GL7, and GL12 the light curve fitting led to very high Δ_F and very small t_{FWHM}, with large relative errors. Therefore we used the highest data point in the lightcurve as minimum estimate for the excess flux Δ_F. According to this excess flux a maximum estimate for the FWHM time scale t_{FWHM} is derived by eye from the microlensing fits in Figs. 6.9, 6.10, and 6.12 .

Note that the χ reported here are not the same as those entering the selection process: This is the case because the candidatates were identified lensing pixel light curves where the χ can be smalller:

---

[5] We have analyzed the complete data set for 2000/2001, 2001/2002, and 2002/2003 for the whole field, and the remaining seasons for field F1.
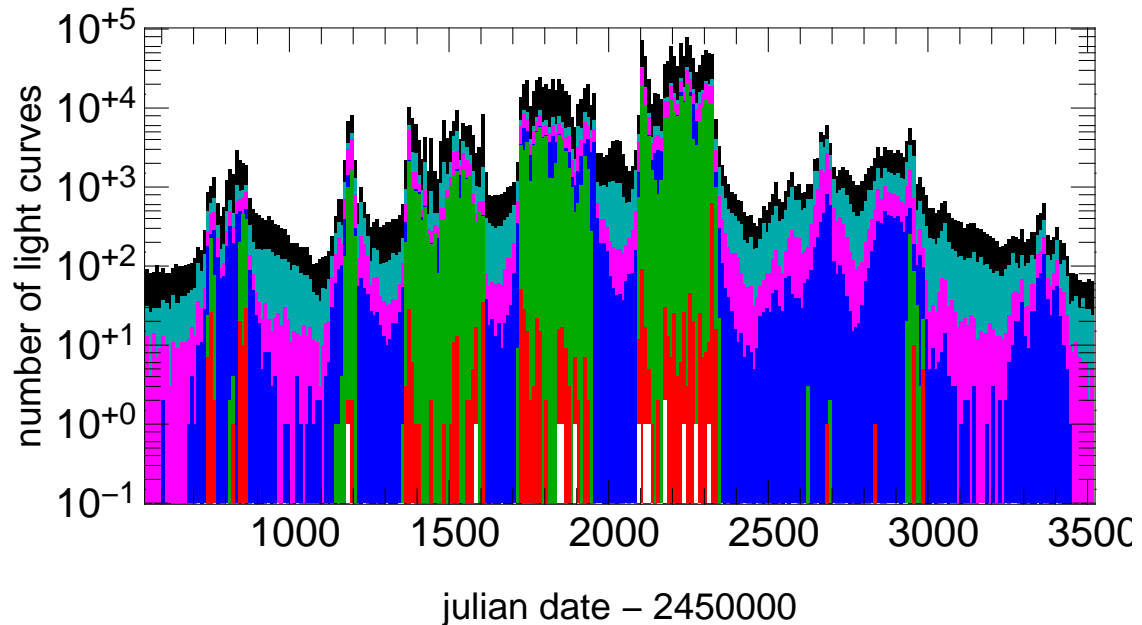
Figure 6.5: Histogram of the detection filters. *black:* analyzed lightcurves, *cyan:* 3 σ-limit, *magenta:* χ-limit, *blue:* timescale constraint, *green:* nearest light point constraint, *red:* flux excess constraint, *white:* selection by eye. See Table 6.5 for details.

Refitting the position and measuring the PSF flux of the lensing event at the correct position leads to slightly different χ-values.

All event candidates found in the WeCAPP data confirm our theoretical expectations, that mainly short time scale events can be identified in present experiments and that large flux excess events tend to have very short time scales.

The following figures show light curves of the 13 WeCAPP candidate events identified to date. To underline the candidate nature we also show the corresponding parts in the difference frames for times close to the light curve maximum below. These image rule out artefacts like hot pixels or cosmics as origin for the events; they also in some cases (GL2, GL8, GL9, GL11, GL12, GL13) show positions of nearby variables. This explains the low quality of the fit and the high χ in the I band for the candidates GL9 and GL11.

Note that still some more event candidates are possible, since some data of the fields F2, F3 and F4 are available for the years 1997-1999 and 2003-2005.

	α	δ	t_0	t_{FWHM}	Δ_{FR}	χ_R	Δ_{FI}	χ_I	$R-I$	χ
	[2000]	[2000]	[JD-2450000]	[d]	$[10^{-5}\,\text{Jy}]$		$[10^{-5}\,\text{Jy}]$		[mag]	
1	$00^h42^m30.28^s$	$41°13'01.1''$	1850.82	1.625 ±0.391	10.2 ±2.6	1.27	19.1 ±4.9	1.74	0.94	1.51
2	$00^h42^m33.08^s$	$41°19'58.2''$	1894.91	2.202 ±2.705	2.9 ±3.2	1.19	7.5 ±8.3	1.27	1.28	1.23
3	$00^h42^m57.26^s$	$41°12'27.5''$	1585.53	2.347 ±0.303	2.06 ±0.11	1.20	5.66 ±0.36	1.37	1.35	1.28
4	$00^h42^m54.77^s$	$41°14'36.7''$	2178.98	2.069 ±0.183	3.07 ±0.15	1.26	4.03 ±0.25	1.86	0.55	1.55
5	$00^h43^m02.36^s$	$41°18'28.8''$	2178.15	5.316 ±0.662	1.30 ±0.08	1.13	2.00 ±0.21	1.86	0.72	1.52
6	$00^h43^m25.97^s$	$41°12'57.4''$	1186.30	< 4	> 0.95	1.09	> 2.4	1.24	∼ 1.35	1.15
7	$00^h42^m57.75^s$	$41°08'12.4''$	2095.97	< 2	> 15	1.95	> 14	1.75	∼ 0.16	1.87
8	$00^h42^m49.16^s$	$41°14'54.8''$	2317.24	0.528 ±0.100	14.3 ±2.4	1.31	24.6 ±4.2	1.77	0.84	1.52
9	$00^h42^m40.28^s$	$41°15'23.5''$	2128.81	6.876 ±0.598	1.85 ±0.11	1.32	6.36 ±0.55	2.06	1.60	1.71
10	$00^h42^m55.31^s$	$41°18'50.6''$	1847.43	1.501 ±0.278	1.90 ±0.24	1.02	2.91 ±0.49	1.42	0.72	1.23
11	$00^h42^m52.95^s$	$41°18'07.1''$	2271.87	0.692 ±1.046	4.7 ±6.0	1.27	10.5 ±13.5	2.63	1.14	2.03
12	$00^h42^m50.30^s$	$41°18'40.2''$	2111.47	< 0.7	> 6.3	1.15	> 11	1.45	∼ 0.92	1.30
13	$00^h42^m44.75^s$	$41°12'54.7''$	2233.72	9.274 ±1.283	1.44 ±0.16	1.14	2.41 ±0.31	1.39	0.81	1.26

Table 6.6: WeCAPP microlensing candidates in M31: positions (α and δ) and other parameters (time of event, full-width-half-maximum time, flux excess in R, goodness of fit in R, flux excess in I, goodness of fit in I, color, goodness of fit).
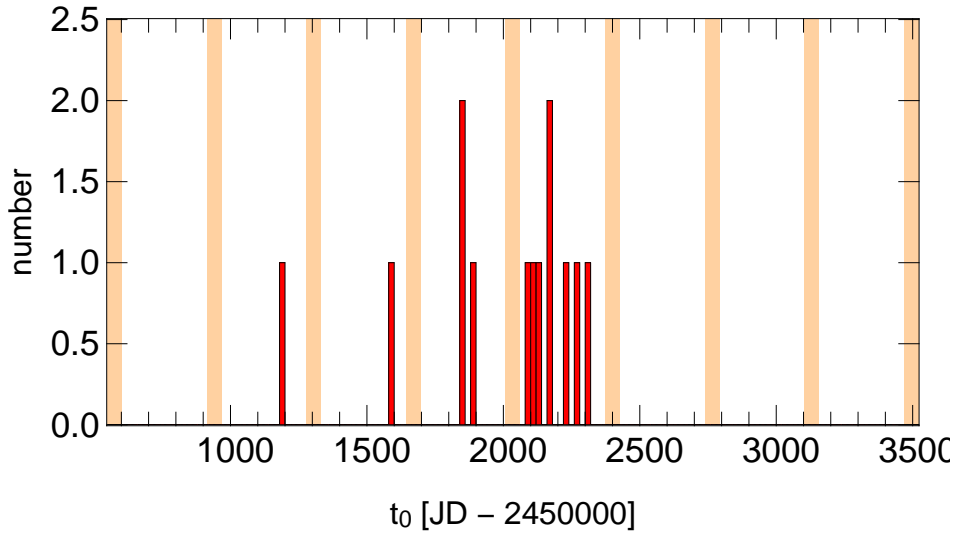
Figure 6.6: Histogram of the event time t_0. Areas marked in *yellow* show the 54 days (from 10th April to 1st June during which M31 cannot be observed.
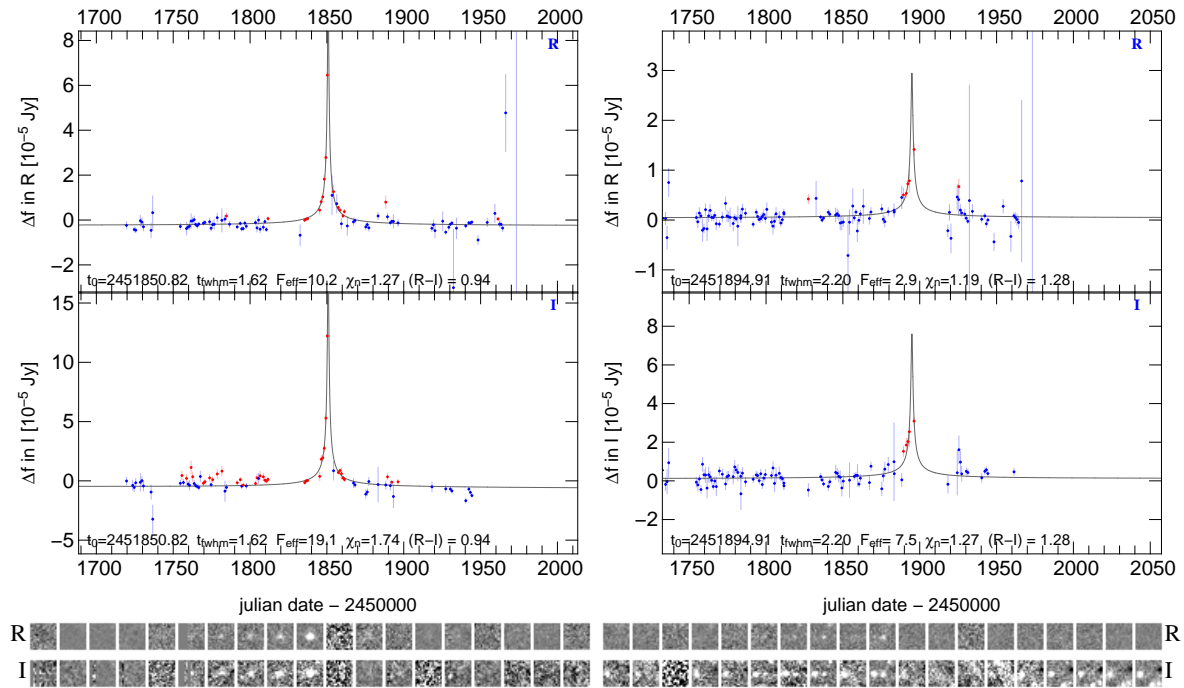
Figure 6.7: WeCAPP microlensing candidate light curves: GL1, GL2 with corresponding parts in the difference frames in R and I. red dots are light points which deviate more than 3σ from the constant level.
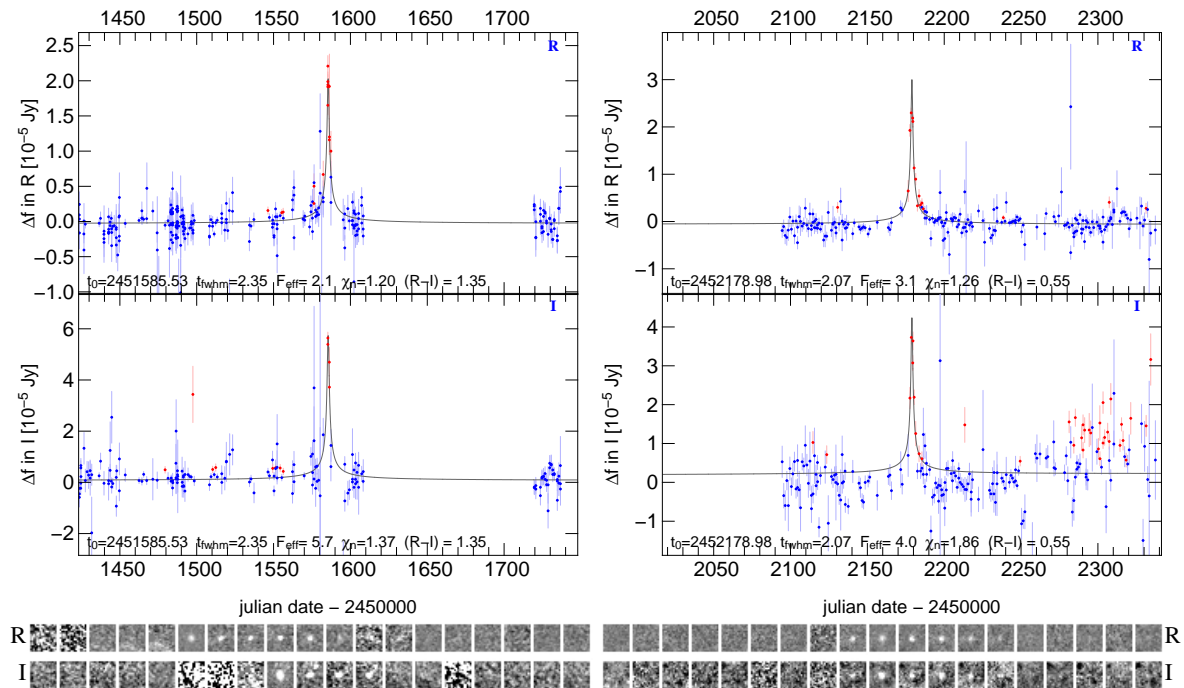
Figure 6.8: WeCAPP microlensing candidate light curves: GL3, GL4 with corresponding parts in the difference frames in R and I band.
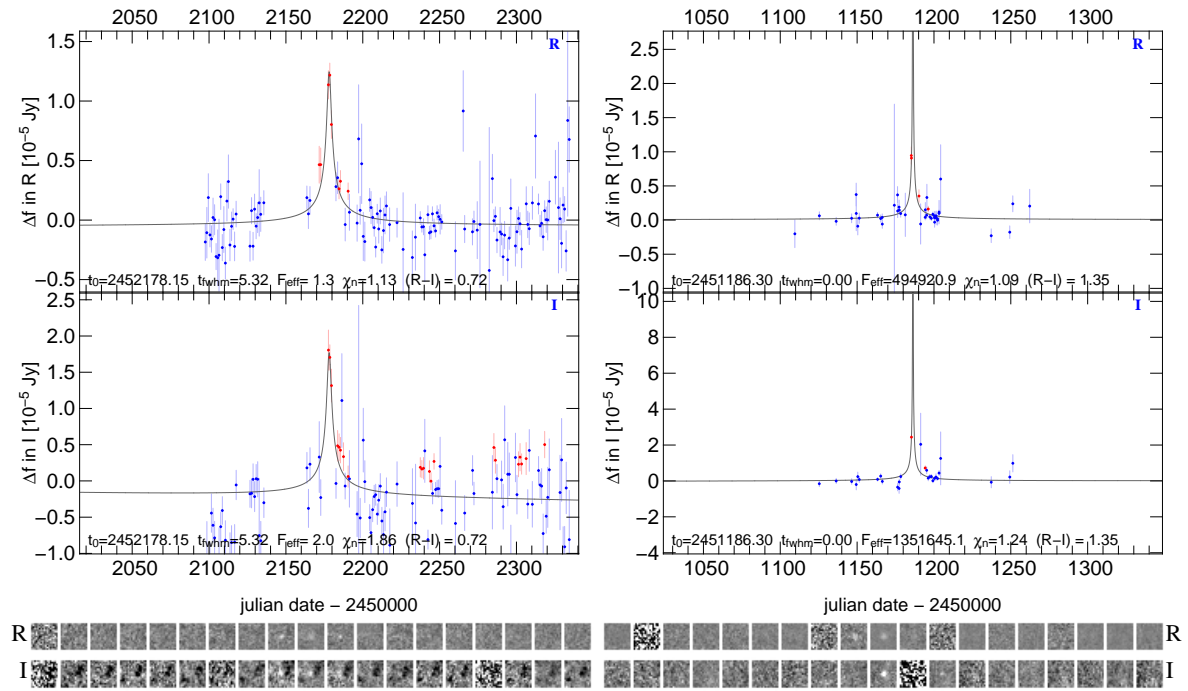
Figure 6.9: WeCAPP microlensing candidate light curves: GL5, GL6 with corresponding parts in the difference frames in R and I band.
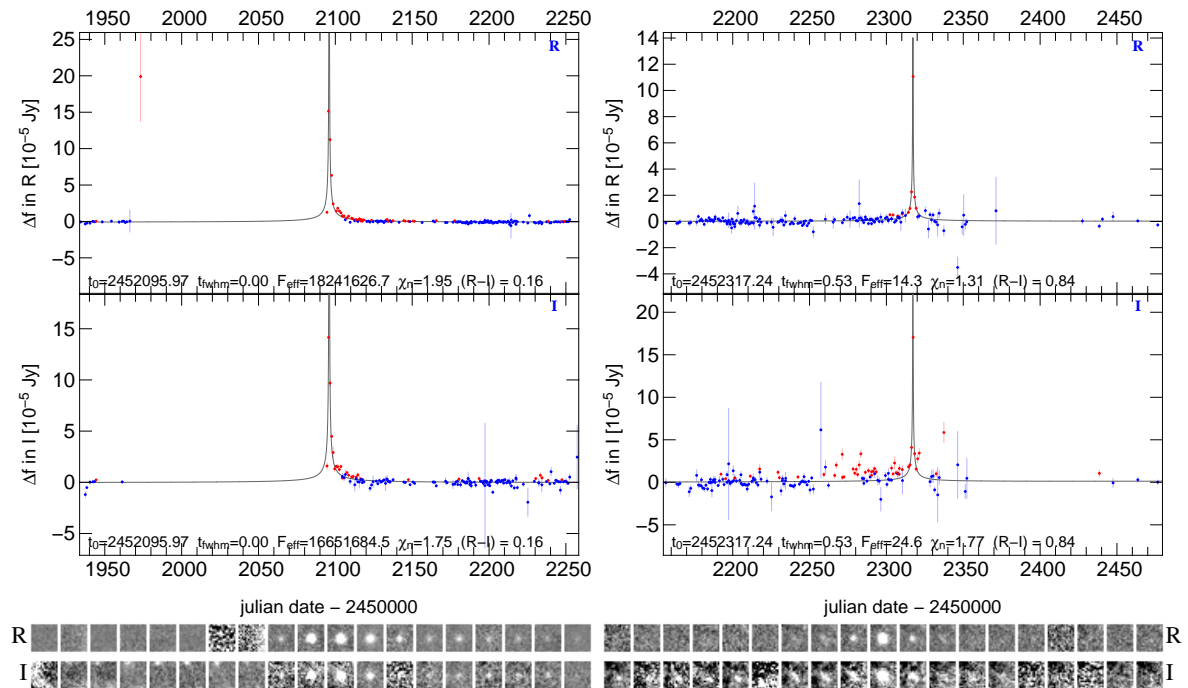
Figure 6.10: WeCAPP microlensing candidate light curves: GL7, GL8 with corresponding parts in the difference frames in R and I band.
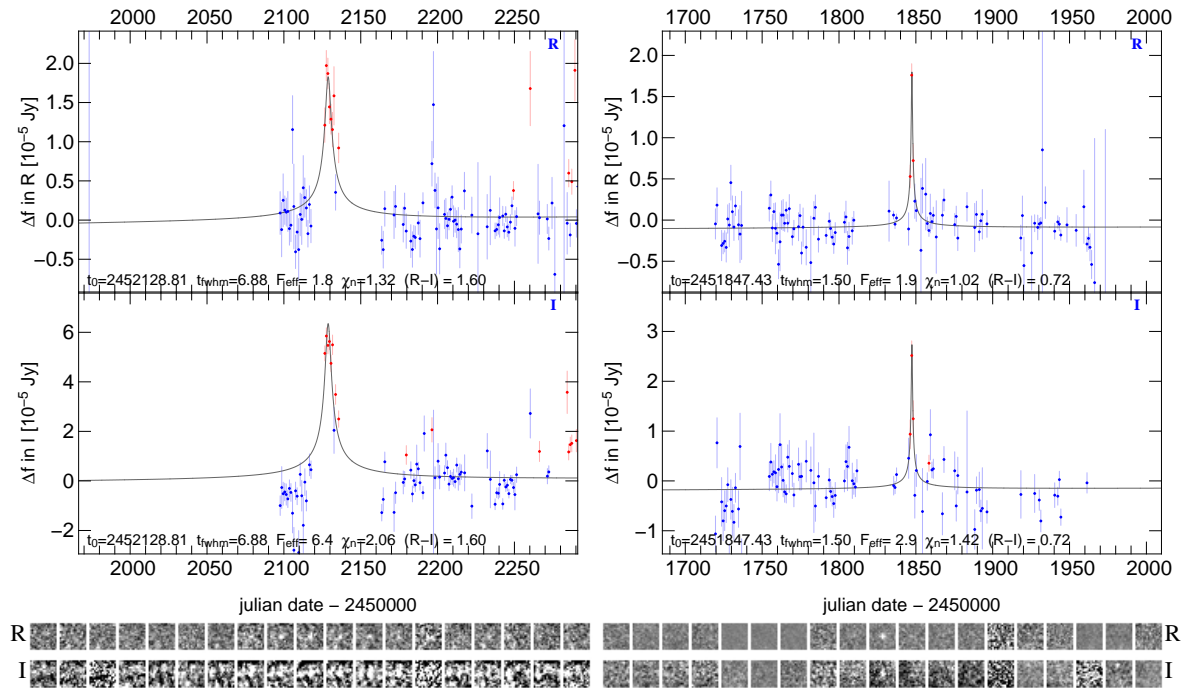
Figure 6.11: WeCAPP microlensing candidate light curves: GL9, GL10 with corresponding parts in the difference frames in R and I band.
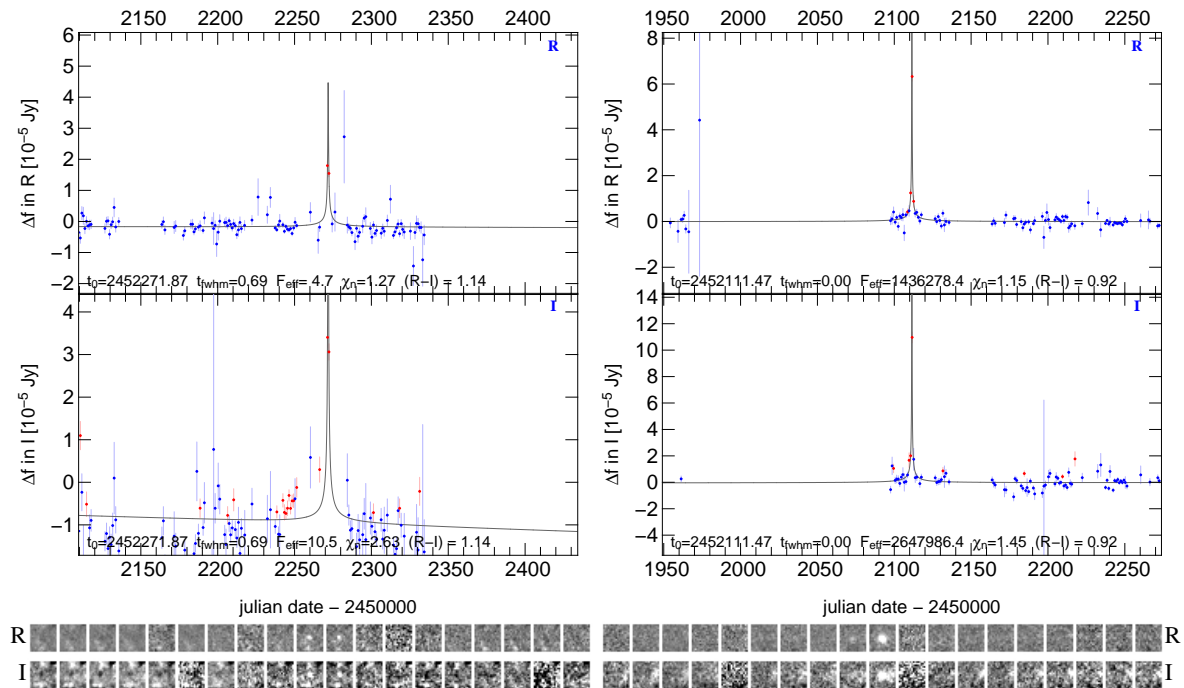
Figure 6.12: WeCAPP microlensing candidate light curves: GL11, GL12 with corresponding parts in the difference frames in R and I band.
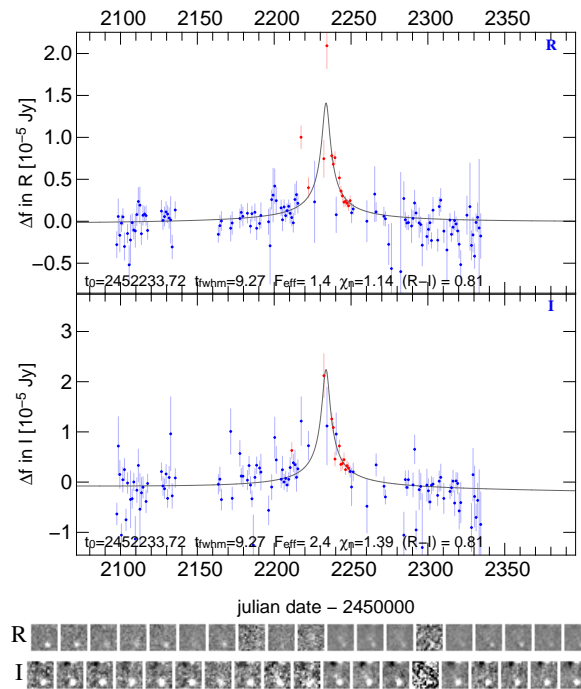
Figure 6.13: WeCAPP microlensing candidate light curves: GL13 with corresponding parts in the difference frames in R and I band.

6.7   Overview over all microlensing candidates in M31

Here we shortly summarize all known micro-lensing events, which we analyze in the following sections. We assign multiple detections to one group only and end up with 36 independent micro-lensing candidates for M31 in Table 6.7.

project	events	recent citation
WeCAPP	13	Riffeser *et al.* (2003)
AGAPE	1	Ansari *et al.* (1999)
POINT-AGAPE	6	Calchi Novati *et al.* (2005); Paulin-Henriksson *et al.* (2002)
	4	Belokurov *et al.* (2005)[6]
MEGA	11	de Jong *et al.* (2006)
NMS	1	Joshi *et al.* (2005)
total	36	

Table 6.7: Microlensing candidates in M31 (We do not count multiple identifications)
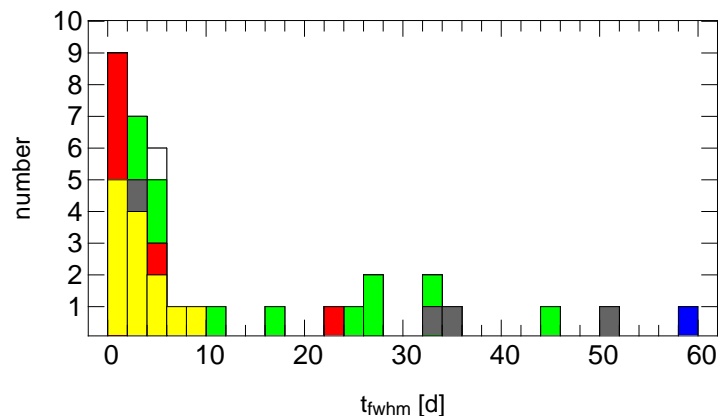
Figure 6.14: t_{FWHM} distributiom of all microlensing candidates in M31 reported up to now. Short events seem to be frequent. Between 10 and 20 days there is a gap which seems to separate short from long lensing event candidates. The WeCAPP events are plotted in *yellow*, POINT-AGAPE in *red*, Belokurov-AGAPE in *gray*, MEGA in *green*, AGAPE Z1 in *white*, NMS in *blue*. Note that part of the differences in the time scale distributions could be due to the detection efficiency. The WeCAPP time scale distribution however looks very much like the predicted one (see Fig. 2.20).

The WECAPP and POINT-AGAPE (Fig. 6.14, *yellow* and *red*) have short time scales. MEGA events (*green*) have an almost flat time scale distribution. The detection efficiency could suppress the long time scale events for WECAPP and POINT-AGAPE. But more plausible is that a large fraction of the long time scale "events" are intrinsic variable sources.

Figure 6.15 shows the positions of all microlensing event candidates in a $1° \times 1.2°$ degree field from Palomar Observatory Sky Survey (POSS-I).

---

[6] One of the 4 Belokurov *et al.* (2005) events not published by other teams is classified as nova in the de Jong *et al.* (2006). The three remainng candidates have very low signal-to-noise, and are hardly to judge.
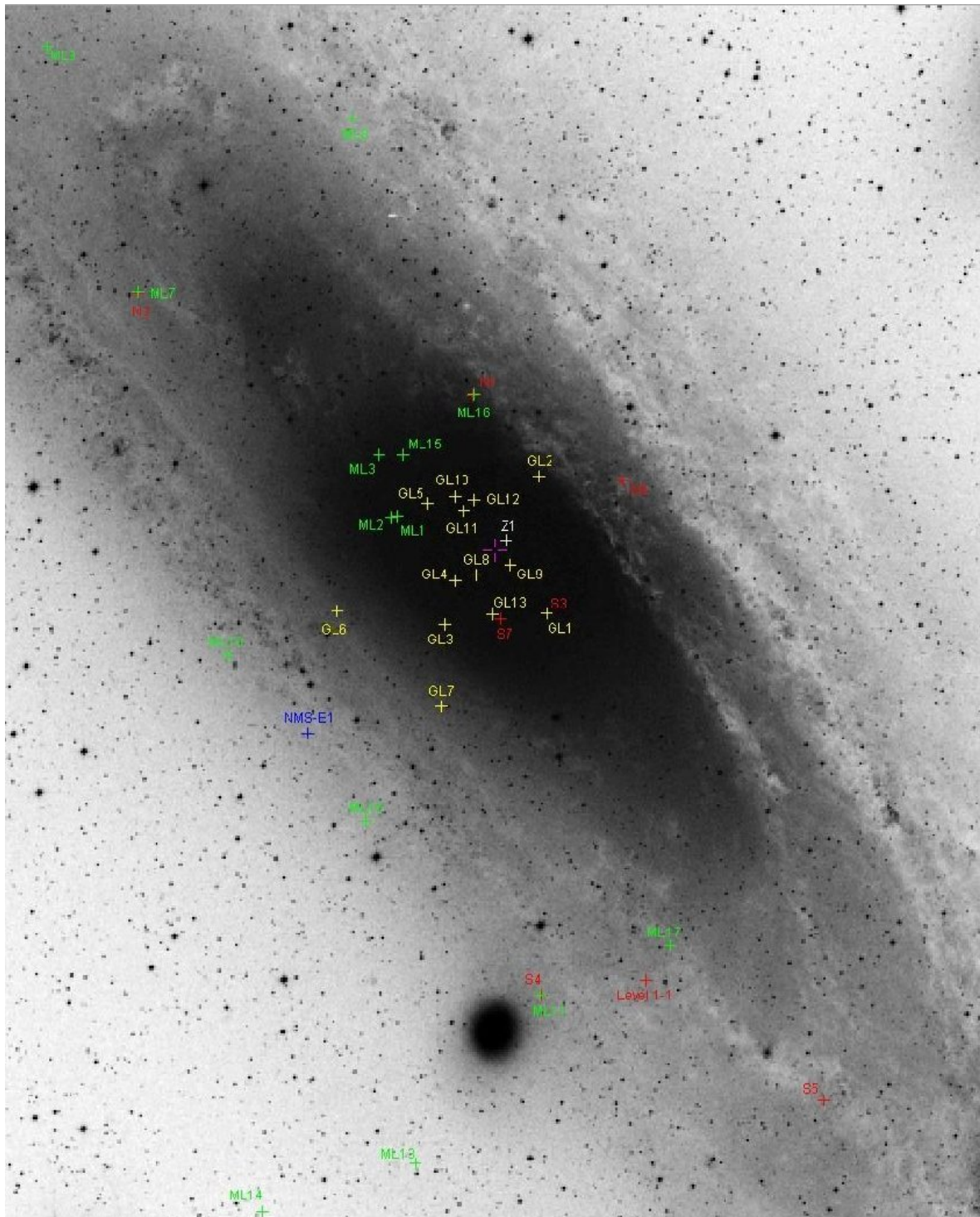
Figure 6.15: Microlensing candidates in M31. Wide field image from Palomar Observatory Sky Survey (POSS-I). The *magenta cross* marks the center of M31. The WeCAPP events are plotted in *yellow*, POINT-AGAPE and Belokurov-events in *red*, MEGA in *green*, AGAPE Z1 in *white*, NMS in *blue*.

6.8   The flux-excess - time scale distribution at the location of event candidates

In this chapter we use the formalism derived in Sec.2.7.1 show contours of the event rate per t_{FWHM} time scale and flux excess, per year and square arcminute, with finite source effects taken into account. The panels show the distribution for those events only that have no finite source signatures in their light-curves (Eq. 2.63 with Eq. 2.66).

The black areas indicate the event parameter space which is not available to source stars once their real sizes are taken into account: as finite source effects mainly occur at large amplifications, large Δ_F and small t_{FWHM} values are suppressed.

We evaluate the Δ_F-t_{FWHM} distribution for the candidate positions reported in Tab. 6.1 and Tab. 6.6. This can act as a first guess if microlensing is in principle possible at this position with the measured parameter. As an example for self-lensing we in all cases show results for bulge-bulge and disk-disk lensing. We allowed only source stars with $(R-I)$-colors in the intervall of $0.5\,$mag to $1.5\,$mag. This will be improved in a later stage, where we will derive the corresponding distribution for the source stars given by the color-measurement of each lensing event and its error.

For lensing events residing in the dark areas the possibility for a missdetection is high. If a missdetection can be ruled out such lensing events set strong constraints to the possible models for M31. Therefore paricularly interesting are the candidates WeCAPP-01, WeCAPP-07, WeCAPP-08 and WeCAPP-12.

As an example for self-lensing we in all cases show results for bulge-bulge and disk-disk lensing. We allowed only source stars with $(R-I)$ colors in the range of $0.5\,$mag to $1.5\,$mag.
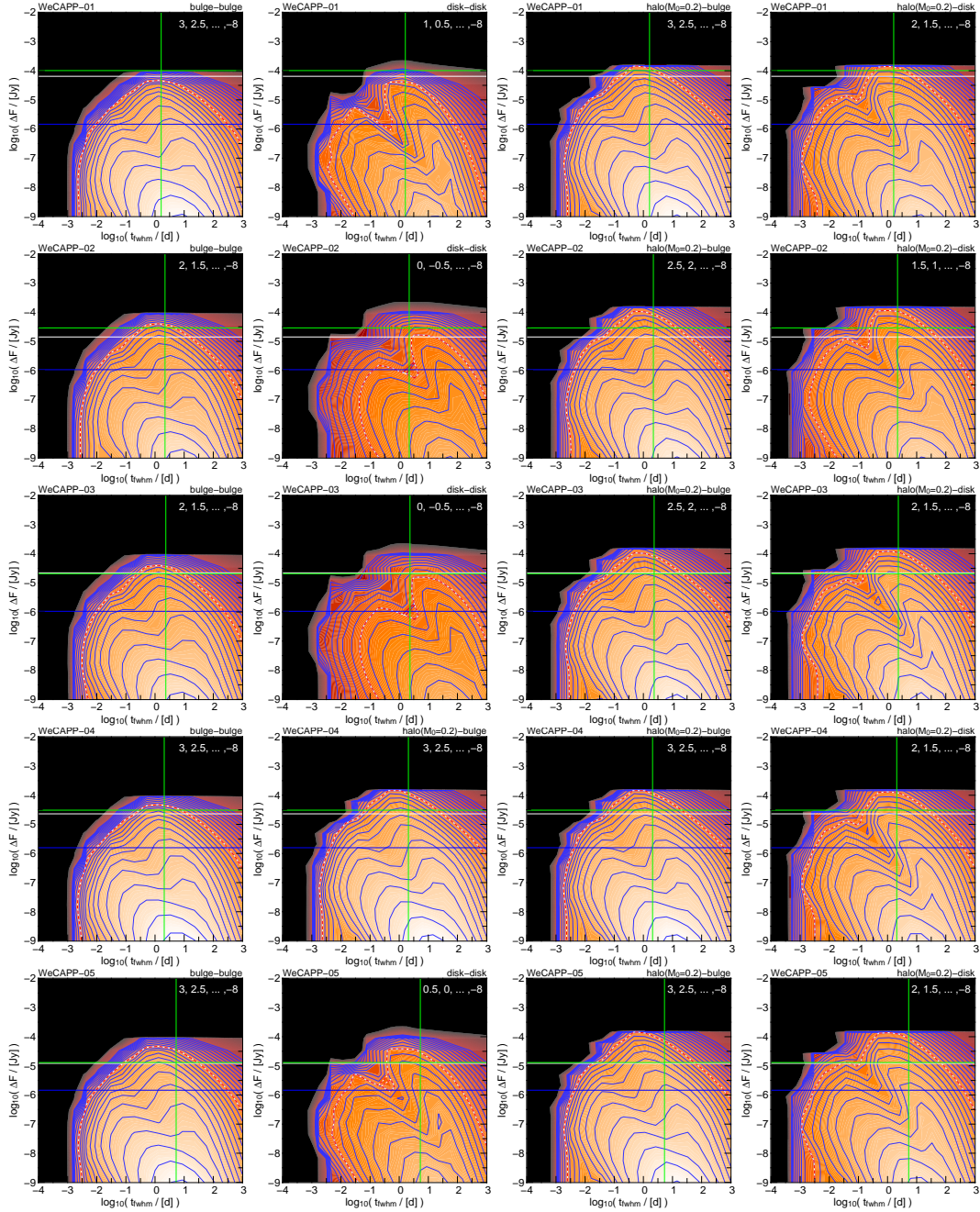
Figure 6.16: Flux excess and time scale distribution of events with colors between 0.5 mag and 1.5 mag, that can occur at the location of the WeCAPP candidates GL1, GL2, GL3, GL4, GL5. The two observables (flux excess and event time scale) are marked in *green*. We show an estimate for the noise level obtained for our M31 model in *blue*. The lower limit for the flux excess is shown as *white line*.
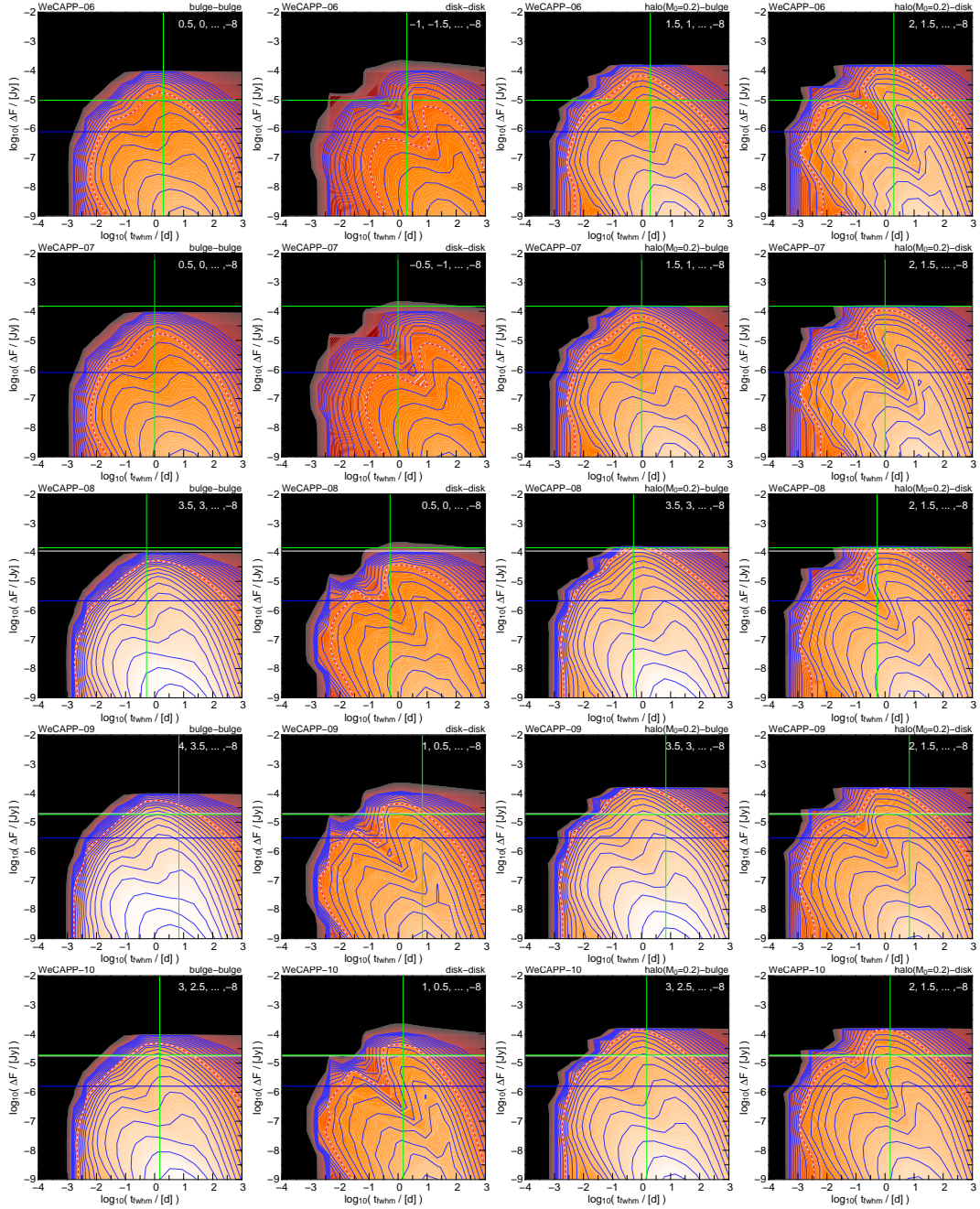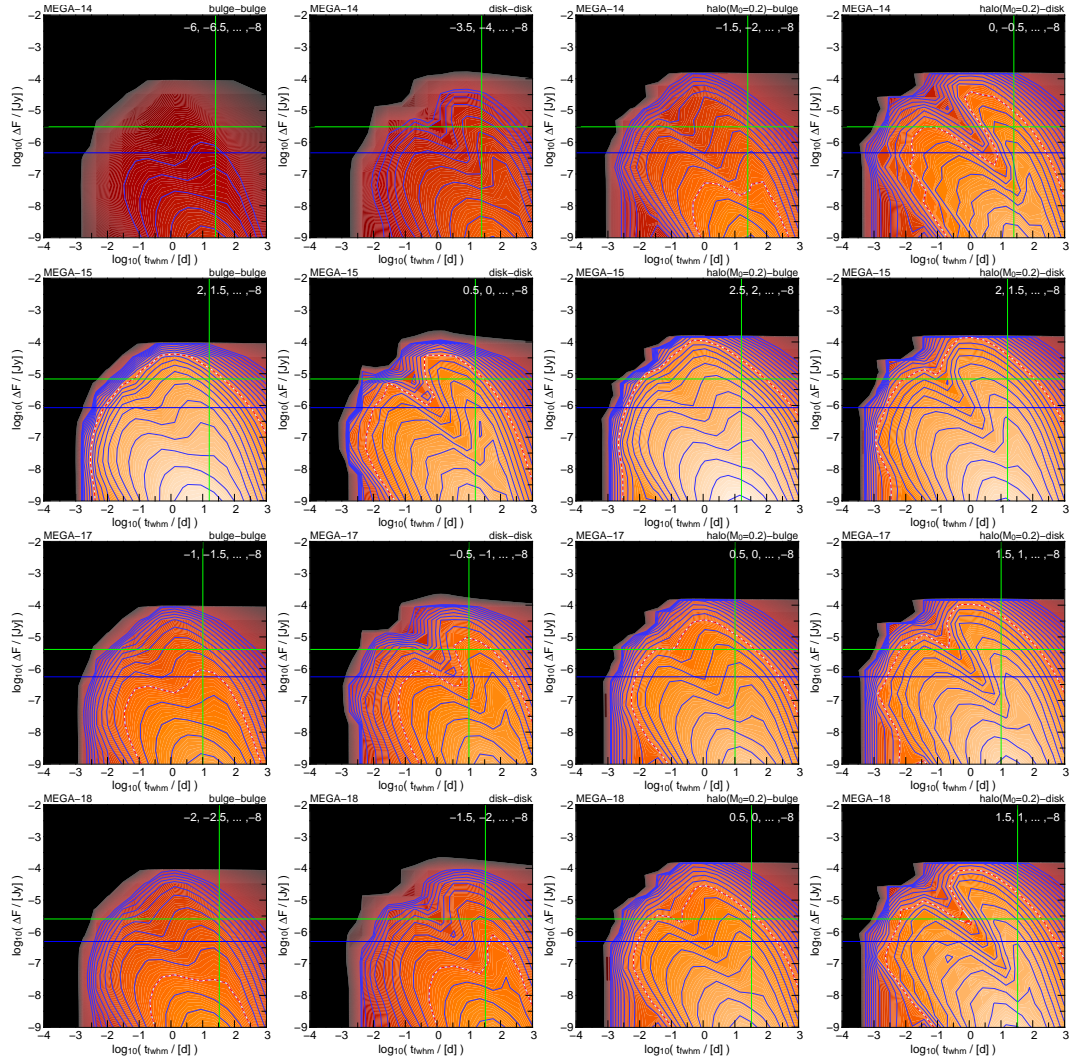
Figure 6.17: Flux excess and time scale distribution of events with colors between 0.5 mag and 1.5 mag, that can occur at the location of the WeCAPP candidates GL6, GL7, GL8, GL9, GL10. The two observables (flux excess and event time scale) are marked in *green*. We show an estimate for the noise level obtained for our M31 model in *blue*. The lower limit for the flux excess is shown as *white line*.
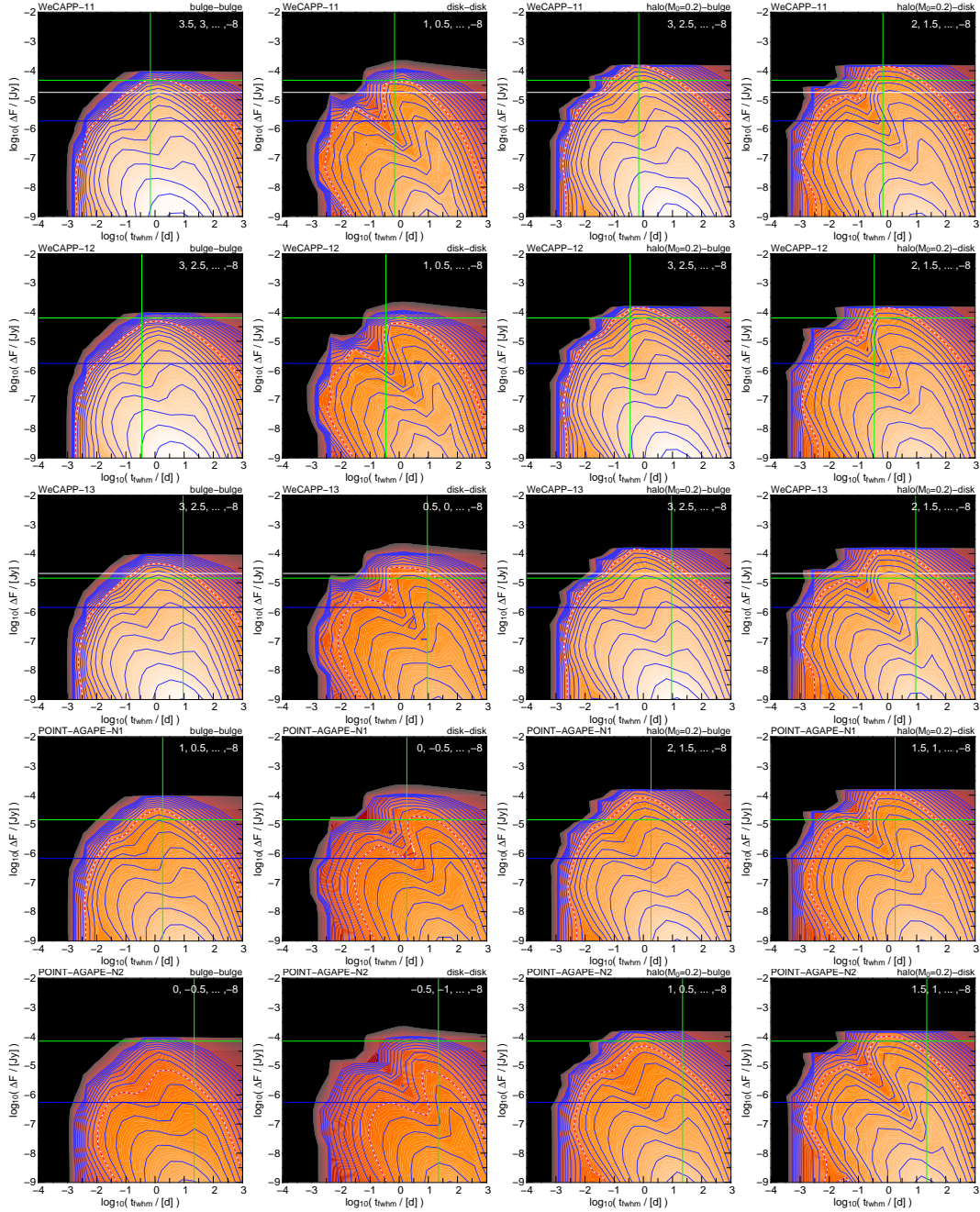
Figure 6.18: Flux excess and time scale distribution of events with colors between 0.5 mag and
1.5 mag, that can occur at the location of the WeCAPP candidates GL11, GL12, GL13 and the POINT-
AGAPE candidates N1, N2. The two observables (flux excess and event time scale) are marked in
green. We show an estimate for the noise level obtained for our M31 model in *blue*. The lower limit
for the flux excess is shown as *white line*.
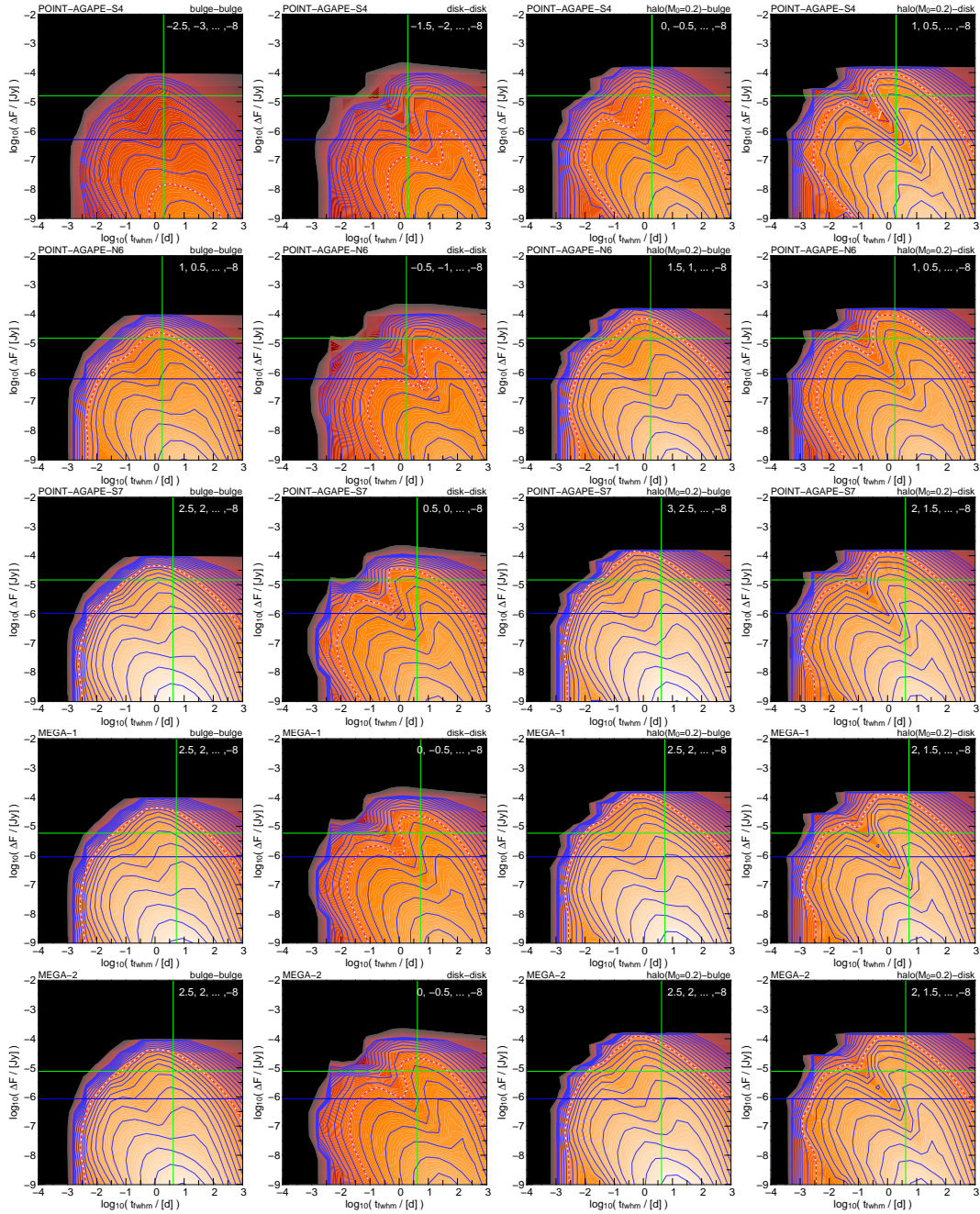
Figure 6.19: Flux excess and time scale distribution of events with colors between 0.5 mag and 1.5 mag, that can occur at the location of the POINT-AGAPE candidates S4, N6, S7 and MEGA candidates 1 and 2. The two observables (flux excess and event time scale) are marked in *green*. We show an estimate for the noise level obtained for our M31 model in *blue*.
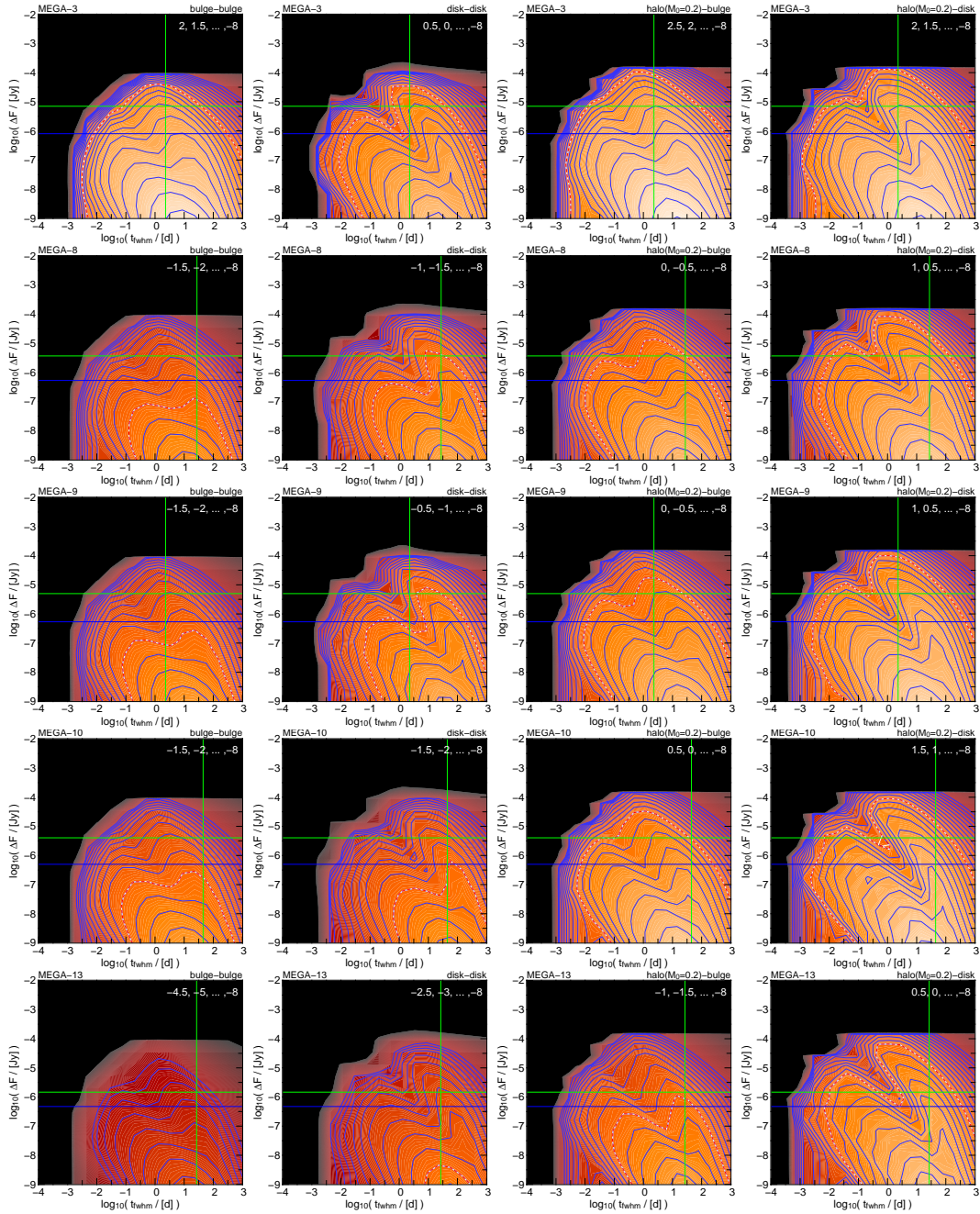
Figure 6.20: Flux excess and time scale distribution of events with colors between 0.5 mag and 1.5 mag, that can occur at the location of the MEGA candidates 3, 8, 9, 10, 13. The two observables (flux excess and event time scale) are marked in *green*. We show an estimate for the noise level obtained for our M31 model in *blue*.

Figure 6.21: Flux excess and time scale distribution of events with colors between 0.5 mag and 1.5 mag, that can occur at the location of the MEGA candidates 14, 15, 17, 18. The two observables (flux excess and event time scale) are marked in *green*. We show an estimate for the noise level obtained for our M31 model in *blue*.

6.9 Mass probability distributions

The mass probability distributions are not depending on the observation strategy and on noise or detection thresholds (efficiencies) but only on the parameters of detected lensing candidates. Therefore shows if the pair of observables, t_{FWHM} and Δ_F, are plausible for a lensing event, given its color.

In Sec. 2.9 we derived the lens mass probability distribution from the observables and errors obtained from light curve fits. The probability function for the lens mass derived in Sec. 2.7 (Riffeser *et al.*, 2006). Using teh symbols defined in Sec. 2.7 we can write for events without and with finite source signatures:

- Events with $u_0 > u_0^*$, i.e. those for which the finite source sizes are irrelevant (see Eqs. 2.65 and 2.66)

$$\frac{d^7\Gamma_{s,l}}{dx\,dy\,dt_{FWHM}\,d\Delta_F\,dM\,d.\mathscr{M}\,d\mathscr{C}} = \frac{2}{t_{FWHM}^3}\,p_{cmd_s}(\mathscr{M},\mathscr{C})\,\xi_l(M)\int\limits_0^\infty n_s(x,y,D_{os})\cdot$$
$$\cdot\frac{\Psi}{F_0}\int\limits_0^{D_{ol}^*(\Delta_F,D_{os})}\rho_l(x,y,D_{ol})\,R_E^{\,3}\,p_{v_t}\!\left(\frac{R_E\Upsilon}{t_{FWHM}},v_0\right)dD_{ol}\,dD_{os} \tag{6.4}$$

with $\Upsilon[A_0(F_0,\Delta_F)]$ and $\Psi[A_0(F_0,\Delta_F)]$.

- For events were the finite source sizes are relevant, i.e. events with $u_0 < u_0^*$, we use Eq. 2.66

$$\frac{d^7\Gamma_{s,l}}{dx\,dy\,dt_{FWHM}\,d\Delta_F\,dM\,d.\mathscr{M}\,d\mathscr{C}} = \frac{2}{t_{FWHM}^3}\,p_{cmd_s}(\mathscr{M},\mathscr{C})\,\xi(M)\int\limits_0^\infty n_s(x,y,D_{os})\cdot$$
$$\cdot\rho_l(x,y,D_{ol}^*)\Omega^*R_E^{\,3}\int\limits_0^{u_0^*(R_*,D_{ol}^*,D_{os})}p_{v_t}\!\left(\frac{R_E}{t_{FWHM}}\Upsilon^*\right)\Upsilon^{*2}\,du_0\,dD_{os}\,, \tag{6.5}$$

where $R_*(\mathscr{M},\mathscr{C})$, $D_{ol}^*(\Delta_F,D_{os},F_0,M,R_*)$, $\Omega^*(\Delta_F,D_{os},F_0,M,R_*)$, $\Upsilon^*(u_0,R_*,D_{ol}^*,D_{os},M)$ depend on the variables on the left side.

Integrating these two equations over $\mathscr{M}$ and inserting x^{meas} and y^{meas} (assuming no error) allows to combine measurements (probability distributions) of the observables t_{FWHM}, Δ_F, $\mathscr{C}$ with M31 models to obtain the probability function for the lens mass causing the event¿

$$\hat{p}_{l,s}(M) \sim \int\int\int\int\frac{d^6\Gamma_{l,s}(x^{meas},y^{meas},M,t_{FWHM},\Delta_F,\mathscr{C})}{dM\,dx\,dy\,dt_{FWHM}\,d\Delta_F\,d\mathscr{C}}\,p_{meas}(t_{FWHM})\,p_{meas}(\Delta_F)\,p_{meas}(\mathscr{C})\,dt_{FWHM}\,d\Delta_F\,d\mathscr{C}\,. \tag{6.6}$$

The M31 model used to evaluate these equations is described in detail in Sec. 3. We apply this formalism to most of the previously identified lensing events toward M31.

Note that in Sec. 6.4 (Riffeser *et al.*, 2003) we had already analyzed WeCAPP-GL1 and GL2 (see figure 6.2), in a slightly simplified treatment:

i) We approximated the color-magnitude-relation $p_{cmd_s}(\mathscr{M},\mathscr{C})$ of bulge and disk stars in M31 with observations of M32 to derive a brightness estimate for the lensed post main sequence star and convert the observed full width half maximum time of the event to its Einstein-time scale.
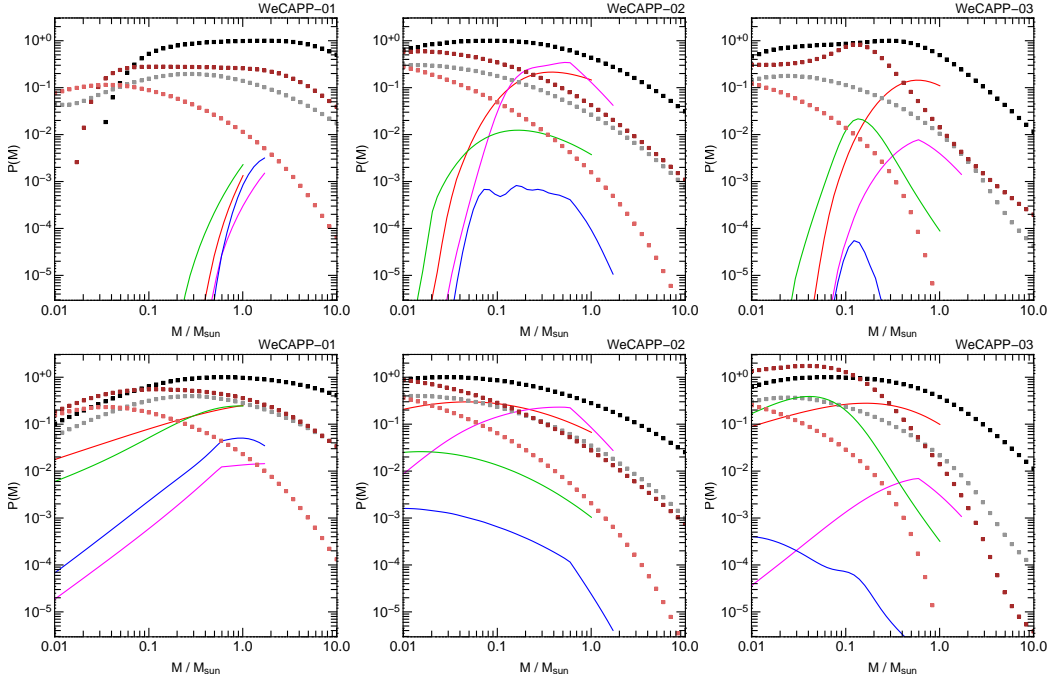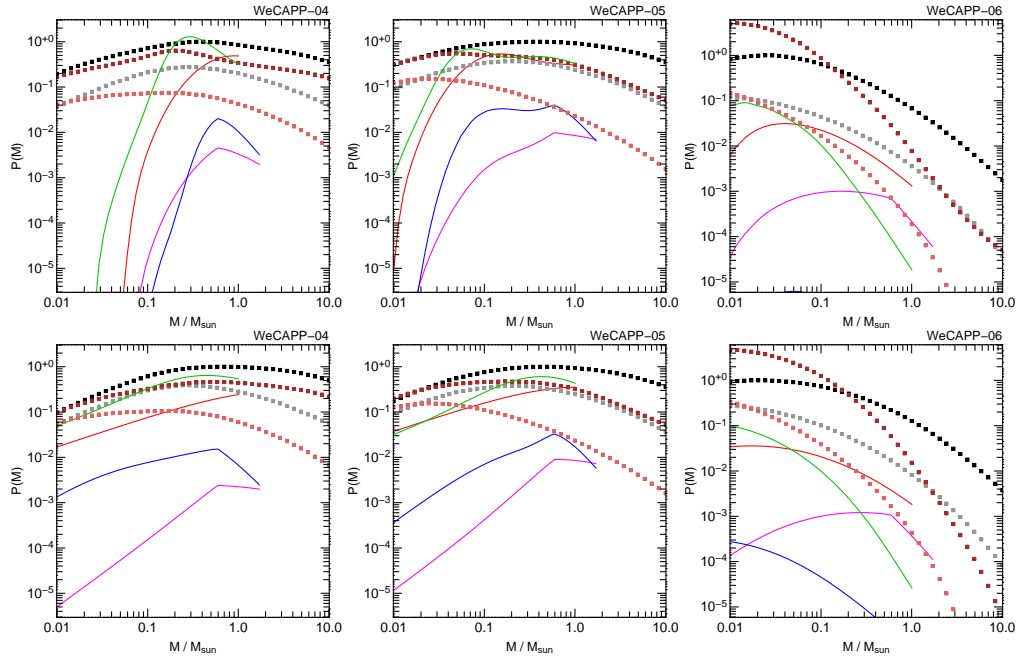
Figure 6.22: Most probable lens masses $p(M)$ for the event candidates WECAPP-GL1, WECAPP-GL2, WECAPP-GL3. *upper panels*: using stellar sizes. *lower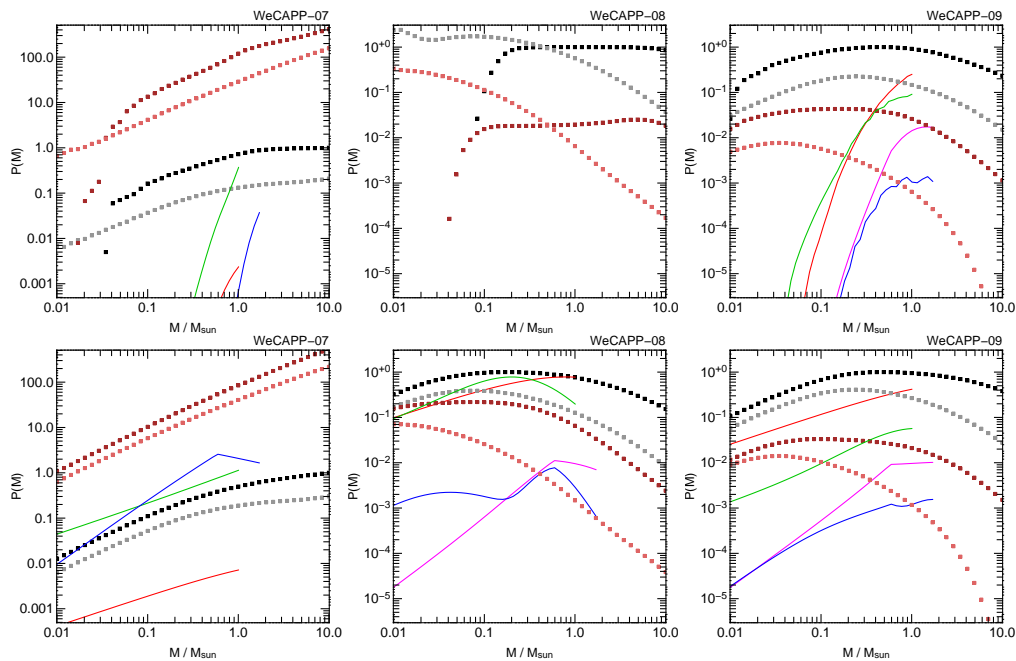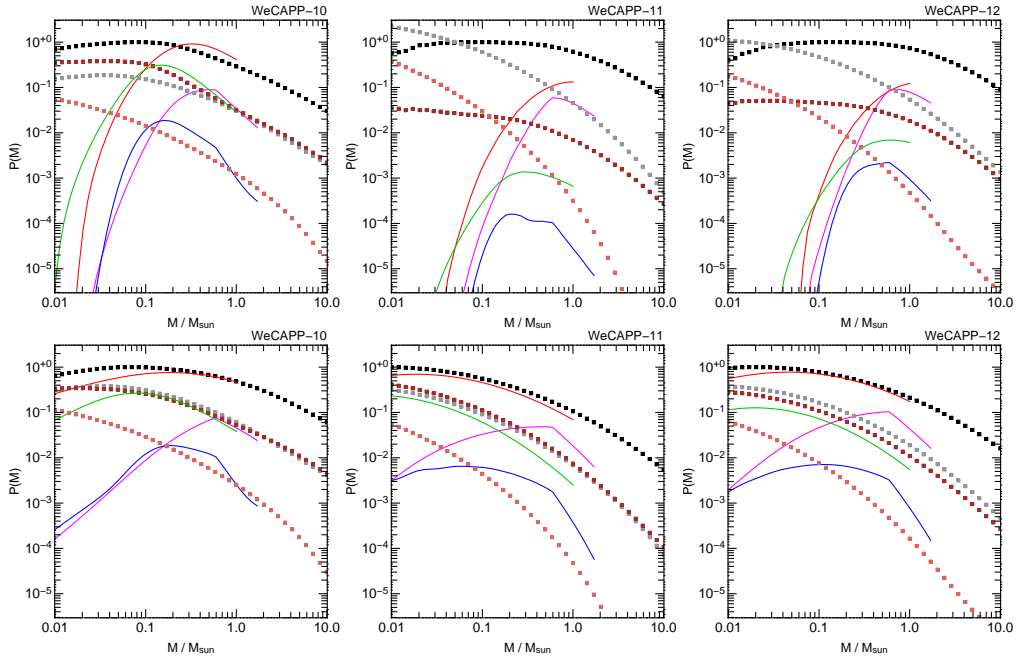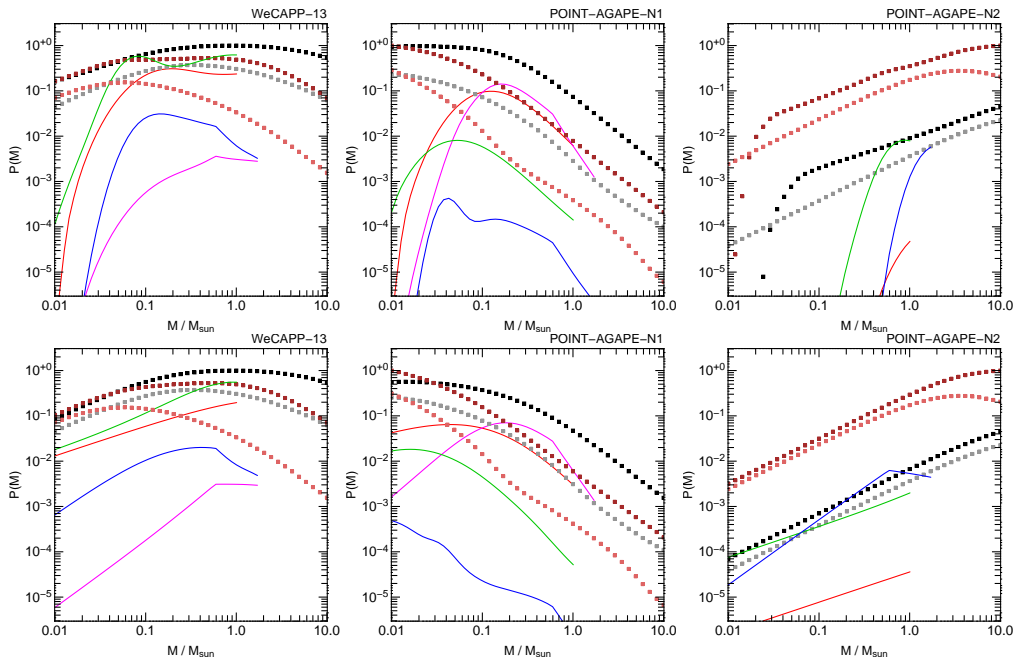 panels*: assuming stars to be point-like. The colors used translate into halo-bulge lensing (*black*), bulge-bulge lensing (*red*), halo-disk lensing (*brown*), bulge-disk lensing (*green*), disk-bulge lensing (*magenta*), disk-disk lensing (*blue*). Galactic halo-bulge lensing (*gray*), MWhalo-disk lensing (*light brown*). The maximum of each curve is scaled to reflect the total probability of a respective lens-source event relative to the case of a halo-bulge lensing event with the most probable Macho mass. The distribution was obtained by convolving 3 Gaussian distributions for t_{FWHM}, Δ_F and $(R-I)$, and using Eq. 6.6. All calculations assume an 100% Macho halo. For simplicity we assumed the errors for the color $(R-I)$ to be the same for all WeCAPP lensing events and to equal $0.1\,\mathrm{mag}$.

ii) We assumed that both disk and bulge stars are confined to a mass interval $0.08 M_\odot$ to $0.95 M_\odot$.

iii) Source stars were treated as point sources.

For the analysis in this chapter we use the M31-model described in Sec. 3 (Riffeser *et al.*, 2006), which includes a bulge and disk luminosity function of 12 Gyr and 2 yrs with $Z = 2Z_\odot$ and $Z = Z_\odot$ metalicity and Zoccali *et al.* (2000) IMF ($\xi \sim M^{-1.33}$) (isochrones are from Girardi *et al.* (2002), details are in Sec. 3). The lower and upper mass limits for the bulge are $0.01 M_\odot$ and $1.01 M_\odot$ and for the disk $0.01 M_\odot$ and $1.71 M_\odot$. We take for each star the radius derived from Girardi *et al.* (2002).
For this M31 model selected M31 lensing events (summarized in Table 6.1 and 6.6) we calculate the lens mass probability functions with equation 6.6 and show them in Figs. 6.22, 6.23, 6.24, 6.25, 6.26, 6.27, 6.28, 6.29, and 6.30. Note that we did not analyze the "NMS"-event and "Belokurov"-events, because it is very plausible that these are variables.
Comparing mass estimates with and without accounting for the finite source size the self lensing probability is dramatically reduced relative to halo lensing. This decrease is mostly due to the fact,
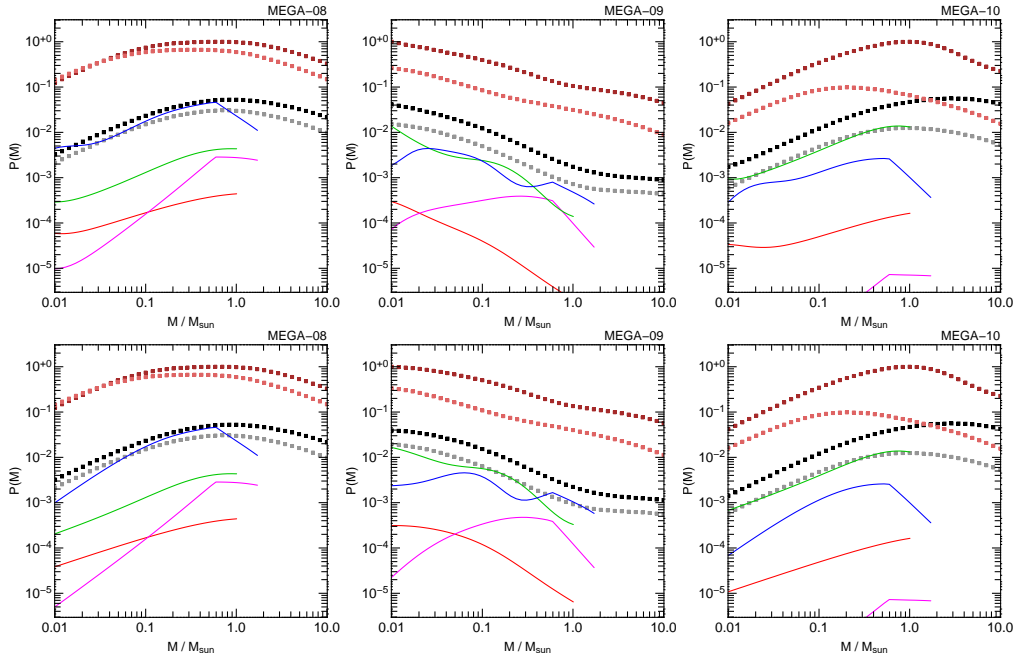
Figure 6.23: Most probable lens masses $p(M)$ for the event candidates WECAPP-GL4, WECAPP-GL5, WECAPP-GL6. *upper panels*: using stellar sizes. *lower panels*: assuming stars to be point-like.
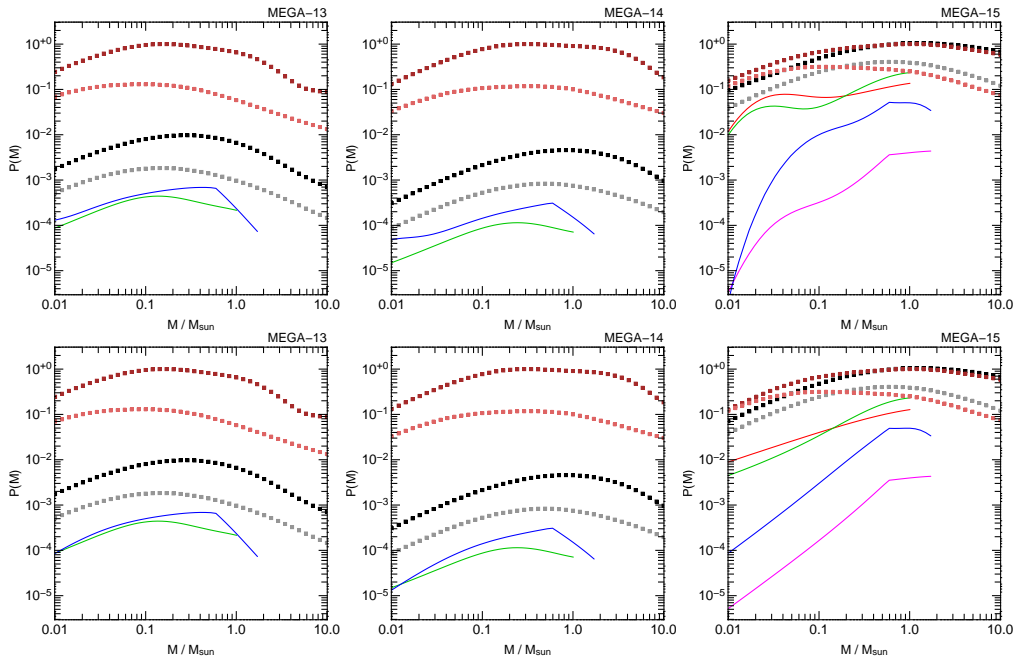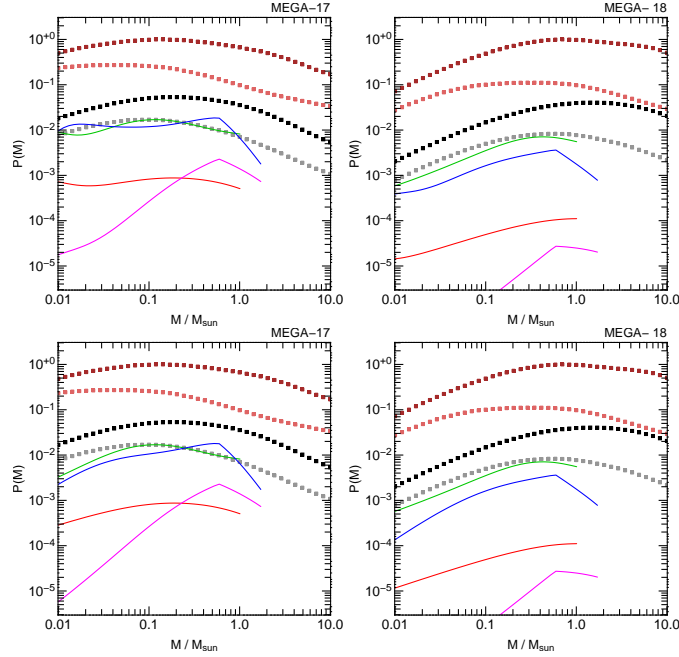

Figure 6.24: Most probable lens masses $p(M)$ for the event candidates WECAPP-GL7, WECAPP-GL8, WECAPP-GL9. *upper panels*: using stellar sizes. *lower panels*: assuming stars to be point-like.

Figure 6.25: Most probable lens masses $p(M)$ for the event candidates WECAPP-GL10, WECAPP-GL11, WECAPP-GL12. *upper panels*: using stellar sizes. *lower panels*: assuming stars to be point-like.

Figure 6.26: Most probable lens masses $p(M)$ for the event candidates WECAPP-GL13, POINT-AGAPE-N1, POINT-AGAPE-N2. *upper panels*: using stellar sizes. *lower panels*: assuming stars to be point-like.
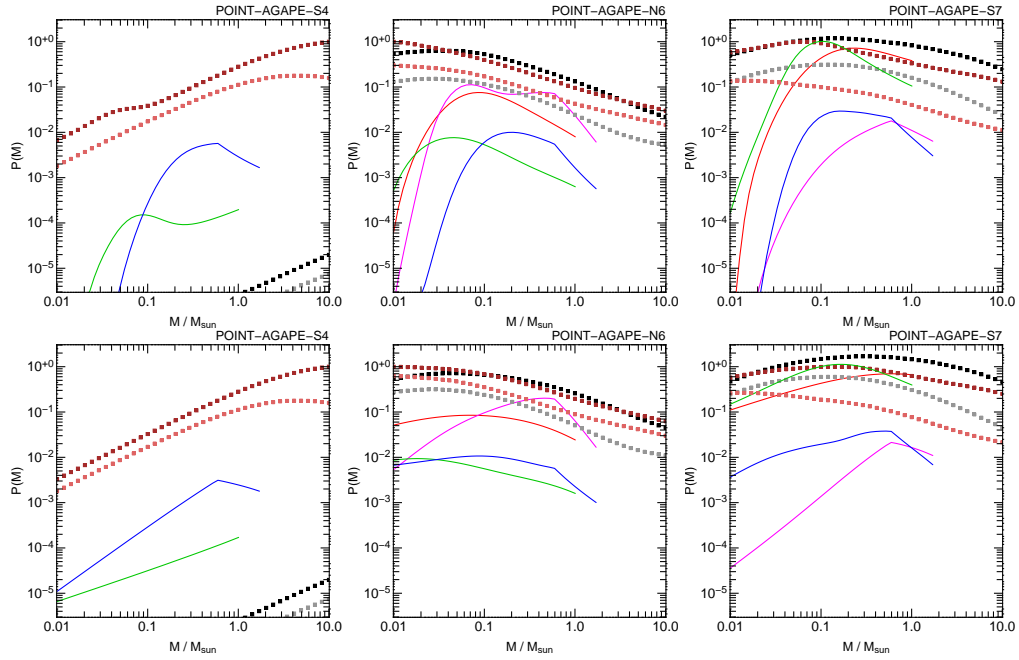
Figure 6.27: Most probable lens masses $p(M)$ for the event candidates POINT-AGAPE-S4, POINT-AGAPE-N6, POINT-AGAPE-S7. *upper panels*: using stellar sizes. *lower panels*: assuming stars to be point-like.
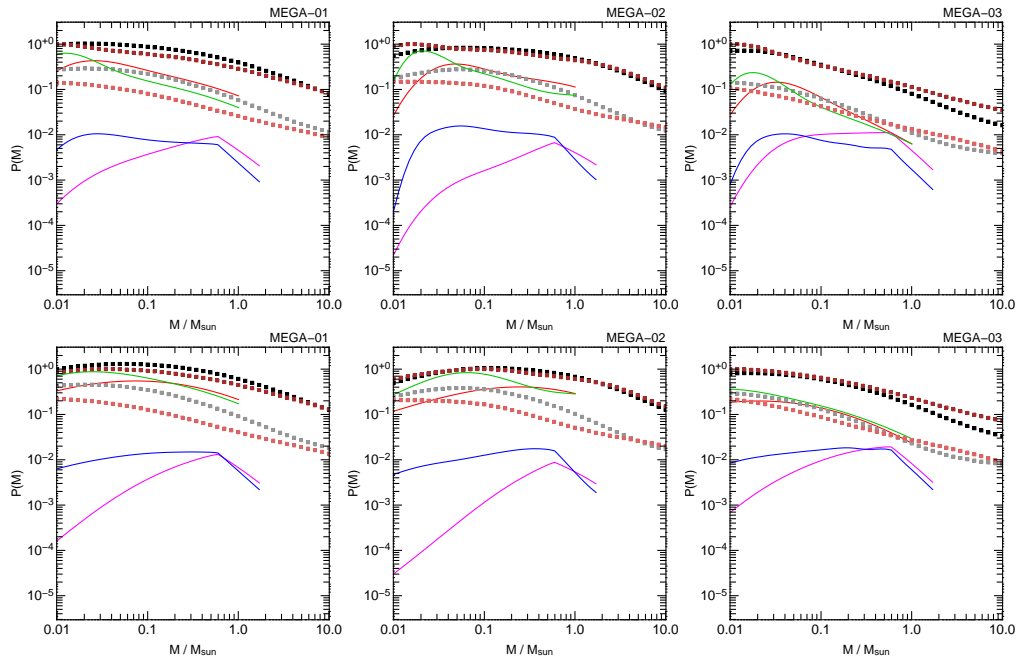
Figure 6.28: Most probable lens masses $p(M)$ for the event candidates MEGA-1, MEGA-2, MEGA-3. *upper panels*: using stellar sizes. *lower panels*: assuming stars to be point-like.

Figure 6.29: Most probable lens masses $p(M)$ for the event candidates MEGA-8, MEGA-9, MEGA-10. *upper panels*: using stellar sizes. *lower panels*: assuming stars to be point-like.

Figure 6.30: Most probable lens masses $p(M)$ for the event candidates MEGA-13, MEGA-14, MEGA-15. *upper panels*: using stellar sizes. *lower panels*: assuming stars to be point-like.

Figure 6.31: Most probable lens masses $p(M)$ for the event candidates MEGA-17, MEGA-18. *upper panels*: using stellar sizes. *lower panels*: assuming stars to be point-like.

that very bright events can hardly be caused by self lensing if finite source sizes are taken into account: For point sources, the magnification can become infinitely large if the source passes the line of sight to the lens. For extended sources the magnification rises earlier, when the source approaches the lens, but it saturates once the source comes closer to the lens sightline than its projected source radius. This leads to an increase in event times scale and a decrease in flux excess at maximum magnification (see Eqs. 2.13 and 2.16 in Sec. 2.3.1). The source radius projected onto the lens plane is the larger, the closer the lens-source pair. Therefore self lensing events are more strongly supressed in magnification and flux excess at the light curve maximum than halo lensing events.

All lensing events have time scales typical for lensed PMS stars as can easily seen comparing with Fig. 2.13.

Studying Fig. 6.22 to 6.30 yields the surprising result that all candidates analysed here are more likely to be caused by a 100% Macho halo with $0.2M_\odot$ than self-lensing.

Ignoring the halo-distributions in five cases (WeCAPP-6, Mega-1, Mega-2, Mega-3, Mega-9) brown dwarfs in the bulge with masses $\approx 0.02M_\odot$ which are lensing disk stars lead to the largest self-lensing contribution (e.g. Fig. 6.28, *green* curve). For all other candidates brown dwarf can nearly ruled out as lenses in the bulge or in the disk, because finite-source effects strongly suppress these low mass ranges.

WeCAPP-GL01 = POINT-AGAPE-S3

GL01 is located in the Δ_F-t_{FWHM} plane (see Fig. 6.16) in the unplausible area for self-lensing. For our M31-model only M31-Machos with masses above $0.2 M_\odot$ or Galactic Machos can cause an event with such a large magnification.

This can also be seen in Fig. 6.22. Without accounting for finite source sizes, the probability for self-lensing is only by a factor of 4 smaller than halo-lensing (lower panel). If we take into account the finite source size, self-lensing becomes very inplausible. Therefore an event as bright as WeCAPP-GL1 can hardly be caused by self lensing. (see Sec. 6.5).

The most probable Macho masses are between 0.2 and $6 M_\odot$ for halo-bulge lensing (Fig. 6.22, *black* points). Macho masses below $0.03 M_\odot$ can only cause the event if they are in the Galactic (MW) halo.

WeCAPP-GL02

Lensing event GL02 in this actual analysis can be interpreted as a lensed bulge source. The highest probability has a halo lens of $0.1 M_\odot$.

A disk lens would most likely have a mass of $0.5 M_\odot$ and a bulge lens a mass of $0.3 M_\odot$. Again finite-source effects suppress the probability for the low mass, $< 0.04 M_\odot$, self-lensing range.

WeCAPP-GL03

GL03 is most likely a halo lens with $0.1 - 0.5 M_\odot$ (for a 100% Macho halo). A bulge star with $0.1 M_\odot$ lensing a disk star or with $0.5 M_\odot$ lensing a bulge star is most likely for this candidate. for bulge sources is consistent with this candidate. A disk lens can be ruled out. Again finite-source effects suppress the probability for the low mass self-lensing below $0.06 M_\odot$.

WeCAPP-GL04

For GL04 lensing of a disk star by a bulge star is as likely as halo-bulge lensing. The most likely bulge and halo lens masses are about $0.3 M_\odot$ in both cases.

WeCAPP-GL05

Also for GL05 self-lensing is very likely. Bulge-disk lensing is most plausible with a $0.06 M_\odot$ mass star, while bulge-bulge lensing would have a slightly higher mass.

WeCAPP-GL06

For GL06 a halo lens with $0.01 M_\odot$ which lenses a disk star is the most likely configuration. A halo lens of $0.02 M_\odot$ is more probable for bulge sources. Self-lensing is very unlikely.

WeCAPP-GL07

This lensing candidate is quite doubtful, because of its blue color, high χ and the poor sampling in the rising light-curve. Therefore a very short burst, e.g. of a nova, could be an alternative interpretation. The most probable mass ranges also indicate that this is not a "normal" microlensing event.

The position of this event in the Δ_F-t_{FWHM} plane (see Fig. 6.16) is already in the unplausible area for self-lensing. Also the mass probability shows that this candidate event cannot be caused by star lenses in the bulge or disk. Halo-disk lensing would have a high probability for very high masses larger than $10M_\odot$.

WeCAPP-GL08

Fig. 6.17 shows that the brightness of GL08 is to large to be caused by self-lensing.

Ignoring finite source sizes would lead to quite wrong mass estimates for this event. Taking this candidate for real and accounting for finite-source effects can totally ruled out a self-lensing geometry. The mass ranges for halo Machos are quite uncertain: M31 -Machos above $0.2M_\odot$ are plausible, even as Galactic halo Machos below $0.4M_\odot$.

WeCAPP-GL09

Bulge stars as sources are a factor of 5 more likely to be lensed than disk stars. For a halo lens we can constrain the mass range to 0.1 - $2M_\odot$ The probability for a bulge lens ($1.0M_\odot$) is only a factor of 4 smaller, whereas a disk lens ($1.0M_\odot$) is a factor of 10 less likely.

WeCAPP-GL10

For GL10 bulge-bulge or halo-bulge lensing are highly favored with a lensing mass of $0.3M_\odot$ for the bulge or slightly smaller for the halo. After accounting for the stellar sizes a bulge-lens mass below $0.1M_\odot$ becomes very unlikely. Disk sources are a factor of 3 less likely.

WeCAPP-GL11

Using finite-source formalism drastically changes the distributions: Halo - bulge lensing is plausible for lenses with masses below $1M_\odot$, bulge - bulge lensing for masses around $1M_\odot$. A very low mass lens ($< 0.01M_\odot$) in the Galactic halo has the highest probability. Disk sources are at least a factor of 10 less likely.

WeCAPP-GL12

This lens is also located near the unplausible area for self-lensing analyzing the Δ_F-t_{FWHM} plane (see Fig. 6.16) Therfore self-lensing is a factor of 10 less likely than halo-lensing. If we would not account for the stellar sizes bulge-bulge lensing would be very likely! For bulge sources either M31 halo objectslenses above $0.1M_\odot$ or Galctic halo objects below $0.1M_\odot$ are possible lenses.

WeCAPP-GL13

Bulge-disk-lensing with $0.05 - 1M_\odot$ lenses has the highest self-lensing probability. For halo-bulge-lensing Machos with masses larger than $0.1M_\odot$ are likely.

POINT-AGAPE-N1 = MEGA-16

This lensing event was described by (Auriere *et al.*, 2001; Paulin-Henriksson *et al.*, 2003; de Jong *et al.*, 2004). Our analysis supports a halo lens smaller than $0.7M_\odot$ for a bulge source or smaller $0.2M_\odot$ for a disk source. A disk source with a mass around $0.2M_\odot$ has the highest self-lensing probability. This is slightly below the mass estimate derived by Auriere *et al.* (2001). Bulge-bulge lensing would most likely have a lens mass around $0.1M_\odot$ which is a factor of 5 lower than in Auriere *et al.* (2001). In Sec. 6.9.2 we showed that these differences are only partly due to the slightly different M31-model we use.

POINT-AGAPE-N2 = MEGA-7

This event is presented in (An *et al.*, 2004b; de Jong *et al.*, 2004). It is most likely a halo object lensing a disk star. Bulge stars as a source can be ruled out. This is consistent with the position of N2, far outside the bulge.

POINT-AGAPE-S4 = MEGA-11

The POINT-AGAPE event S4 (Paulin-Henriksson *et al.*, 2002, 2003) is situated close to the line of sight to M32. Since we do not account for this system, our mass estimates are not very accurate. Also for this lens a halo lens is very plausible. Disk-disk-lensing peaks at $0.5M_\odot$. The bulge does'nt play a role for this event.

POINT-AGAPE-N6

POINT-AGAPE N6 was presented by Calchi Novati *et al.* (2005). Despite the double peak in the light-curve we relate this candidate to a small mass halo object. As the bulge is situated behind the disk on the line-of-sight, disk-bulge lensing is only a faktor 10 lower than the highest halo lens scenario.

POINT-AGAPE-S7

POINT-AGAPE S7 was also published by Calchi Novati *et al.* (2005). Our analysis favours halo-bulge, halo-disk, bulge-disk or bulge-bulge lensing with masses below $0.5M_\odot$.

MEGA-1, MEGA-2, and MEGA-3

All three candidates show a quite similiar mass distributions: They can be interpreted as bulge or halo lenses in front of disk sources in the far side of the disk. The most probable masses are consistent with brown dwarfs below $0.1M_\odot$ peaking around $0.02M_\odot$.

MEGA-8

MEGA-8 is a microlensing event candidate with a quite long time scale $t_{\mathrm{FWHM}} > 20\,\mathrm{d}$. For this candidate halo (M31 or Galactic)-disk configurations have the highest probability. Disk-disk lensing is by factor of 20 below.

MEGA-9

For MEGA-9 M31 halo-disk lensing is a factor of 3 more probable than Galactic halo-disk lensing, whereas self-lensing is by a factor of 20 less likely.

MEGA-10

Also MEGA-10 is a microlensing event candidate with a quite long time scale, $t_{\mathrm{FWHM}} > 20\,\mathrm{d}$. Here M31 halo-disk lensing is a factor of 10 more likely than Galactic halo-disk lensing. Self-lensing is very unlikely.

MEGA-13 and MEGA-14

MEGA-13 and MEGA-14 have also quite long time scales $t_{\mathrm{FWHM}} > 20\,\mathrm{d}$ Therefore for both halo lensing is by factor of 1000 more likely than self-lensing. The lens masses are in the range of 0.1 to $2M_\odot$. The low densities in the Δ_F-t_{FWHM} plane (see Fig. 6.18) show that these events are extremely unlikely to happen at these locations at all. de Jong *et al.* (2004) makes a potential stellar stream responsible for the events. Other (Calchi Novati, priv. comm.) question the nature of these two events.

MEGA-15

For this long time scale candidate with $t_{\mathrm{FWHM}} \approx 16\,\mathrm{d}$ halo lenses are plausible above $0.02M_\odot$. Bulge-disk lensing with $1M_\odot$ lenses is by a factor of 4 below.

MEGA-17 and MEGA-18

MEGA-17 and MEGA-18 have also quite long time scales: MEGA-17 around $t_{\mathrm{FWHM}} \approx 10\,\mathrm{d}$, MEGA-18 longer than $t_{\mathrm{FWHM}} > 20\,\mathrm{d}$. For MEGA-17 a halo-disk lensing event with a lens mass around $0.2M_\odot$ is by a factor of 3 more likely than all other configurations. For MEGA-18 halo-disk lensing with a lens mass around $0.7M_\odot$ is by a factor of 10 more likely than the rest.

6.9.1 A younger disk population

We now discuss how the choice of the lumiosity-function or color-magnitude relation changes our results. Especially for the disk of M31 the age and metallicity of the polpulation are not clear.
In Fig. 6.32 we show the difference (compared to Fig. 6.16) for the mass probability distribution using a younger disk population with 1 Gyr age (see Fig. 6.33). The probability distributions can strongly change for a younger disk population, because younger stars are brighter and therefore larger flux excesses can be achieved. This underlines the importance of accurate models for M31. Recent deep measuremnts of M31 (Ferguson & Johnson, 2001; Davidge *et al.*, 2005; Sarajedini & Jablonka, 2005; Brown *et al.*, 2003) will improve the understanding of the M31 populations.
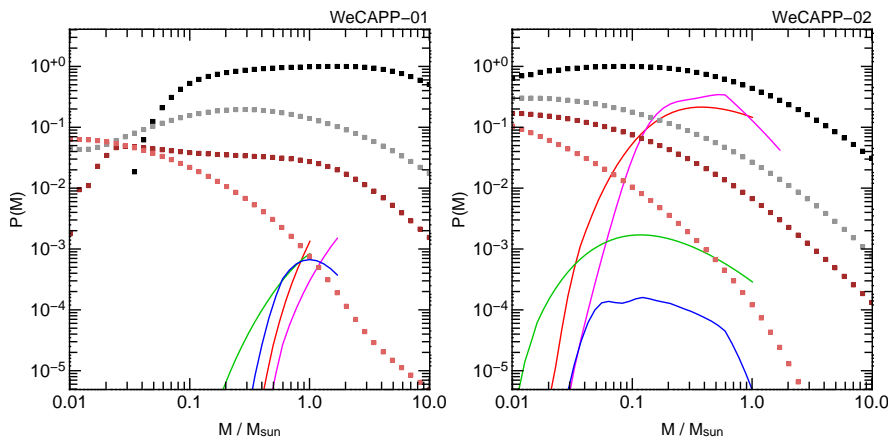
Figure 6.32: Most probable mass $p(M)$ for a 1 Gyr disk population for the measured lensing events WeCAPP-GL1 and WeCAPP-GL2 (Riffeser *et al.*, 2003): halo-bulge lensing (black), bulge-bulge lensing (red), halo-disk lensing (brown), bulge-disk lensing (green), disk-bulge lensing (blue), disk-disk lensing (magenta).
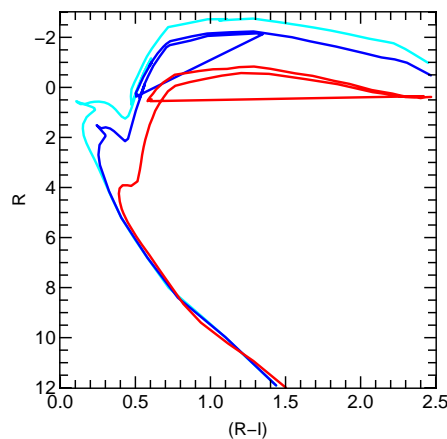
Figure 6.33: Color-magnitude (CM) relation for a 12 Gyr bulge with a metallicity $Z = 2Z_\odot$, a 2 Gyr disk with $Z = Z_\odot$ (*blue*) and a 1 Gyr disk with $Z = Z_\odot$ (*blue*) according to Girardi *et al.* (2002).

6.9.2 Previous mass estimates

In this section we compare our results to mass probability estimates derived from other groups.
In many publications the exact procedure to obtain the mass estimates are not described in a detail that allows to verify the calculations. Either the model is not well described or the authors just claim that they got $p(M)$ from Monte-Carlo-simulations.

Only Auriere *et al.* (2001) show at least the mass probability functions they obtain from POINT-AGAPE-N1. In Fig. 6.34 we compare our result to the original plots (transformed to a linear scale from their Fig. 3). To be able to compare our formalism with theirs we also used their models (based on Kerins *et al.* (2001), with a halo core radius of $r_c = 5$ kpc instead of our value of $r_c = 2$ kpc). Their probability for disk-bulge lensing peaks at $0.1 M_\odot$, for bulge-bulge lensing at $0.03 M_\odot$ (before a relative proper motion cut that can be made if finite source signatures are not present in the light curve). Using a logarithmic prior[7] for the Macho mass they got a peak in the mass distribution of $0.03 M_\odot$. We have calculated the mass probability distribution for the PA-N1 event using the analytical form of Eq. 2.80 on the one hand, and using our own Monte-Carlo simulation on the other hand. Our distributions obtained with Monte-Carlo are perfect agreement with our theoretical distributions.
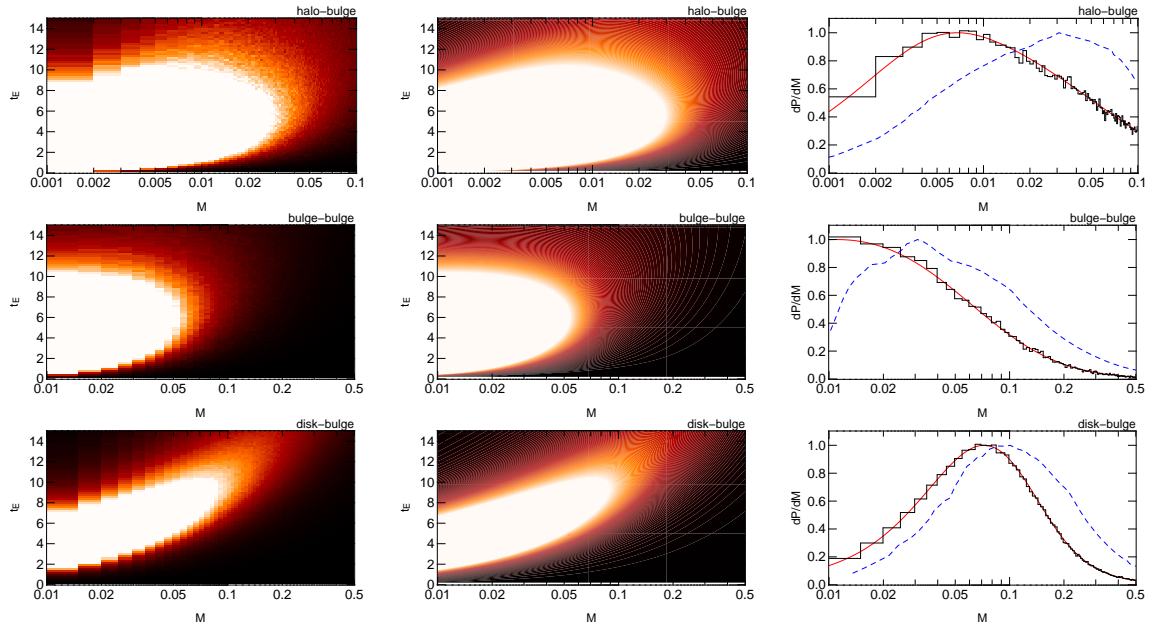
Figure 6.34: Comparison of different derivations of $d^2\Gamma(M, t_E)/(dM\,dt_E)$. We evaluated the distribution at the projected position of the event PA-N1. From top to bottom: halo-bulge lensing, bulge-bulge lensing, and disk-bulge lensing. *Left panel*: Monte-Carlo simulations. *Middle panel*: analytical calculation according to Eq. 2.80. In the *right panel* we present a cut trough the two-dimensional distribution at the measured value $t_E = 10.4$ d for PA-N1. The *black line* shows the resulting values for the Monte-Carlo simulation, the *red line* shows the analytical expression, both are in perfect agreement. The result of Auriere *et al.* (2001) for POINT-AGAPE-N1 is shown as *blue dashed line*. We cannot explain the discrepancies since not enough details are given on their model.

---

[7] The logarithmic prior can be written as $\xi(M) = \frac{\delta(M - M_{lens})}{M_{lens}}$ (Kerins *et al.*, 2001).

6.10   Summary and conclusions

We used the theory of Chap. 2 together with the M31-model of Chap. 3 to obtain the mass-probability functions (Sec. 2.9) for 29 lensing events identified toward M31 by WeCAPP, POINT-AGAPE and MEGA.

For the analysis of the halo-lensing we assumed the Machos to have all the same mass. One obtains that the probability for halo lensing is generally larger for small Macho masses, and peaks – very roughly – around 0.2 solar masses, i.e. not far from the brown dwarf regime. Closer inspection of Figs. 6.22 to 6.31 demonstrates: The Macho mass fraction in the halo has to be at least 30% for Macho masses of 0.2 solar masses, in order to keep the halo-lensing scenario for 23 events as or more likely than self-lensing. For Macho masses much larger or much smaller than these 0.2 solar masses the Macho mass fraction has to be even higher. Only for 5 lensing events (WeCAPP-GL04, GL05, GL10, MEGA-2) self-lensing is nearly as likely as halo-lensing assuming a 100% Macho fraction.

As finite source effects are accounted for, the high magnification events among those which contribute to the event rate are preferentially decreased. This effect is larger for self-lensing than for halo-lensing, because the source stars are much closer and projected sources sizes are much larger for self-lensing than for halo-lensing (see (Riffeser *et al.*, 2006)). We showed these differences for all 29 lensing events. If finite source effects are taken into account, halo-lensing of 0.2-solar mass lenses is at least 3 times more likely than self-lensing for 23 of the 29 events discussed here, if a full Macho halo is assumed.

We conclude that most likely halo masses are of order ~ 0.2 solar masses, and that the halo fraction has to be 30% to make for nearly all events halo-lensing as likely as self-lensing.

6.11   Outlook

Micro lensing in M31 provides 5 observables[8] (6 if we account also for the color). Since the theory devoloped in Sec. 2 fully describes the problem and provides a 4-dim distribution of the 4 observables, the final step for analysing microlensing events is to compare theoretical models with the measured lensing events. Note that events should be equally distributed in time (the $5^t h$ observable). The deviations from this uniform "date of the event"-distribution has to be shown to be caused by the selection function of the survey.

Since the efficiency plays an important role in detecting microlensing events, we will derive the 5 dim efficiency in the near future [9]. This allows to control if the events were very unlikly in a certain time interval. If the efficiency is equally distributed, it can be contracted to a mean efficiency over time, reducing the problem to a 4-dimensional distributions (used in theories).

For different experiments the efficiency has to be calculated separately, since different detection algorithms are used.

Using simple treshold models as described in Sec. 2.8.3 allready provide a rough estimate for the efficiency. More realistic models can only be achieved by Monte-Carlo simulations. There are different possibilities.

- One can use the expected photon noise level (depending on x and y) and the real sampling of the measurements.

---

[8] $t_{\mathrm{FWHM}}, \Delta_F, x, y, t_0$

[9] Note that the efficiency is depending on time

- This can be improved by using the real noise, which is provided by the error frames used by the WeCAPP experiment.

- Another improvement is to use the difference frames and derive the efficiency by simulating point sources, which have a microlensing light curve. The detection algorithms can then be apllied to these artificial events.

- The optimum would be to place the artifical ligth curves in the raw images, and applying the whole reduction pipeline to the images. This last method is very time consuming and should only bring marginal improvements compared to the step before.

Chapter 7

Summary and outlook of the thesis

Since the beginning of the seventies[1] we know that a large fraction of mass in galaxies is "dark". Although we by now can measure the amount and spatial distribution of dark matter in galaxies and on larger scales quite precisely, we still do not know what dark matter is made of . There are several candidates for dark matter-"particles", but the strategy to prove their existence depends on the particles nature. It is of great importance to find out if dark matter is smoothly distributed (e.g. WIMPs) or if it is in compact form (e.g. primordial black holes). In 1986 gravitational lensing was proposed to detect compact matter in galaxy halos in the mass range of $10^{-7}M_\odot$ to $10^5M_\odot$ by measuring the time dependent magnification of background stars. In 1992 two groups successfully identified the first microlensing events in the direction to the LMC galaxy.

Our gravitational microlensing survey
The Wendelstein Calar Alto Pixel lensing Project (WeCAPP) started in 1997 with the goal to constrain the fraction of massive compact halo objects (Machos) along the line of sight to the 10 times more distant M31 galaxy. The motivation was to test other lines of sight through our Galaxy (MW), and to investigate with M31 a target which - through its inclination - could make a discrimination between halo- and self lensing events more promising. In addition, M31 offers a much larger spatial density of stars that can be lensed than the SMC/LMC. This advantage implies that stars can not be resolved anymore individually, and that the flux-excess of a lensed star has to exceed the photon noise of the line of sight projected neighboring stars to be identified as an event.
WeCAPP imaged the central 4 kpc of M31 in 683 (part-time) nights in the R- and I filters. In 99 of the nights we observed from Wendelstein and Calar Alto, in 350 nights only from Wendelstein and in the remaining 234 only from Calar Alto observatory. The huge observing effort (carried out by myself, PhD-student Jürgen Fliri, and two night assistants at the Wendelstein allowed a 61% and 69% coverage of the M31-visibility period in the two best seasons of 2000/2001 and 2001/2002. It is a lucky coincidence that weather is correlated such, that observing conditions are hardly ever bad at both observatories at the same time. The reduced WeCAPP data were searched for microlensing events. The variable content was investigated in another PhD-project (Fliri *et al.*, 2006).

Optimal data reduction pipeline
The light curves of variable objects are obtained by subtracting the flux within the PSF at the position

---

[1] e.g. Ostriker & Peebles (1973); Roberts & Rots (1973)

of the variable object from the PSF-flux of a reference image at the same position. The small difference PSF-flux thus is obtained by subtracting two "big numbers", and therefore, systematic errors have to be as small as possible to allow solid PSF-difference flux-estimates.

We had to develop an optimal image reduction pipeline for WeCAPP including all steps from observation to the extraction of the light curves.

We applied our new algorithms for the geometrical, photometric and optical image alignment. We could show that the detection of variable sources is possible, that systematic errors are negligible and that photometric errors are as small as the lower limit set by the Poisson noise of the photons in science and calibration images. Very important for the error estimates in the final light curves is the exact error propagation through all reduction steps. We showed that one can not obtain reliable results from a crude error estimate starting from the reduced science images, and that microlensing candidates obtained in that way would not be trustable. Our reduction pipeline finally is already applied in the context of other scientific questions (e.g. planet search with the transient method).

We reduced and photometrically calibrated M31 images taken in 683 nights (corresponding to 100 GB of raw data) with our reduction pipeline. Altogether we - and the pipeline - had to deal with ten thousands of science frames and with thousands of calibration frames.

Theory

Theoretical predictions available from other authors at the beginning of WeCAPP predicted a large number Macho-lensing and self-lensing events. These numbers could not be achieved by the WeCAPP, which led us to doubt some of these predictions. We therefore rederived the theory for microlensing in M31 from scratch avoiding unjustified approximations and ending with exact predictions for the observables (flux excess, time scale, color and location of events) in the pixel lensing regime for a given M31- and MW-model. This straightforward relation between model and observables was not provided by any previous work before. Furthermore we demonstrated that accounting for finite source sizes is essential for the correct interpretation of bright lensing events. We further show in (Riffeser *et al.*, 2006) that our formalism is also applicable to the present nearby micro lensing surveys toward LMC, SMC and Galactic bulge and could improve the analysis of these surveys.

We predicted the number of lensing events per year that can be observed with the experimental setup of WeCAPP: We expect 4 "bright" self-lensing events per year with a time scale larger than 2 d (more details see Table 2.2) and a comparable rate for halo-lensing (assuming a 25%- Macho-halo). Our event-number expectation values do only use the signal-to-noise ratio of events expected for the given M31-model, but do not account for the sampling frequency of the survey. (The corresponding efficiency is not evaluated for WeCAPP in detail yet)

These numbers are small (with respect to previous estimates) but fit very well to the number of events we observe taking into account that self-lensing provides a lower limit for the observations. Our low predictions are also confirmed meanwhile by the results of Calchi Novati *et al.* (2005).

Microlensing candidates analysis

WeCAPP collected data from 1997 to 2005. The time sampling was particularly good in the two seasons from 2000 to 2002. The detection of two events with a signal-to-noise ratio larger than 10 at peak flux and a time scale larger than 1 day in the WeCAPP 2000/2001 data is in good agreement with our model predictions.

We analyzed all data from 2000-2002 and a major fraction of data from the remaining years (1997-2005) and end up with 13 microlensing event candidates: 1 in 1998/1999, 1 in 1999/2000, 3 in

2000/2001 and 8 during our best-sampled season 2000/2001. Noticeable is that our micro lensing candidates have timescale below 10 days, whereas other surveys toward M31 came up with a large fraction of long time scale candidates. The time scale distribution observed by WeCAPP is also supported by our model predicting very few long time scale events.

To analyze the WeCAPP, POINT-AGAPE, and MEGA lensing event candidates we obtained the event rate density as a function of time scale and flux excess at all those positions where promising candidates have been reported up to now. With these distributions one can immediately see "problematic" candidates, i.e. those which have an unlikely long time scale given their brightness. In deed, some of the MEGA candidates spotted in that way, have been withdrawn meanwhile.

The flux excess - time scale diagrams also identify four particularly interesting WeCAPP-candidates: they are too bright to be caused by self-lensing for the M31-model we investigated. For these four events the Macho lensing hypothesis is much more likely than self-lensing. We showed for GL1 how some self-lensing scenarios can be ruled out with "back of the envelope estimates" once the finiteness of stellar sources is taken into account.

Most interesting are the lens masses causing the lensing events. Although exact confidence limits on lens masses and Macho fraction require detection efficiencies for each survey to be known, one can use the mass probability distributions for each event to characterize the event (e.g. relative probability for bulge-bulge and bulge-disk self-lensing) and the likely mass range for the lens. We analyzed all 30 event candidates of the WeCAPP, POINT-AGAPE and MEGA surveys obtained up to now. For all microlensing candidates halo lensing (e.g $0.2 M_\odot$) is more likely than self-lensing (assuming a 100% Macho halo component). On the other hand, if we would have a 100% Macho halo, we would predict 4 times as many halo events as star-star lensing events. This would only be compatible with our total number of events, if our efficiency was much lower than expected.

Outlook

- We will obtain the missing accurate event detection efficiency maps with Monte-Carlo simulations in the immediate future and constrain the Macho fraction quantitatively

- We used and will further use the formalism derived in the theory work of (Riffeser *et al.*, 2006) to design new lensing surveys and to estimate the observable lensing rates: we propose a satellite campaign with the HST ACS camera. It would allow to identify more than 100 self-lensing events during a short 30 day observation period and up to 50 Macho events for a 100% Macho fraction with $0.1 M_\odot$ objects. It is ideally suited to measure the faint end mass function of the bulge population.

- The technical upgrades at the Wendelstein-observatory in the near future will also yield many more events: The new "AMiGo" multichannel camera (Gössl, private communication) will increase the photon collecting efficiency by a factor 9. A new 2.0 m telescope to be built on Wendelstein will improve this by another factor of 7. The improved spatial resolution of Wendelstein-2m data will further increase the signal-to-noise of lensing events. Taking the technical advances and our imaging reduction pipeline together, we for the first time have the realistic chance to place much stronger constraints on Macho fraction and masses than those obtained up to now.

Bibliography

Afonso, C., Alard, C., Albert, J., Amadon, A., Andersen, J., Ansari, R., Aubourg, É., Bareyre, P., Bauer, F., Beaulieu, J., Bouquet, A., et al. 1999: *Observation of microlensing towards the galactic spiral arms. EROS II. 2 year survey*, A&A, 351, 87, cited on p. 7, 160

Afonso, C., Albert, J. N., Alard, C., Andersen, J., Ansari, R., Aubourg, É., Bareyre, P., Bauer, F., Beaulieu, J. P., Blanc, G., Bouquet, A., et al. 2003a: *Bulge microlensing optical depth from EROS 2 observations*, A&A, 404, 145, cited on p. 155

Afonso, C., Albert, J. N., Andersen, J., Ansari, R., Aubourg, É., Bareyre, P., Beaulieu, J. P., Blanc, G., Charlot, X., Couchot, F., Coutures, C., et al. 2003b: *Limits on Galactic dark matter with 5 years of EROS SMC data*, A&A, 400, 951, cited on p. 5, 7

Alard, C. 1999: *Analysis of the OGLE microlensing candidates using the image subtraction method*, A&A, 343, 10, cited on p. 7, 23, 160

Alard, C. 2001: *Unbiased reconstruction of the mass function using microlensing survey data*, MN-RAS, 320, 341, cited on p. 10, 17

Alard, C. & Guibert, J. 1997: *The DUO single lens candidates. I. The 1994 campaign.*, A&A, 326, 1, cited on p. 7, 16

Alard, C., Guibert, J., Bienayme, O., Valls-Gabaud, D., Robin, A. C., Terzan, A., & Bertin, E. 1995: *The DUO programme : first results of a microlensing investigation of the Galactic Disk and Bulge conducted with the ESO Schmidt telescope.*, The Messenger, 80, 31, cited on p. 7

Alard, C. & Lupton, R. H. 1998: *A Method for Optimal Image Subtraction*, ApJ, 503, 325+, cited on p. 11, 85, 90, 97, 98, 99, 137, 139, 154, 161

Albrow, M. D., Pollard, K. R., Beaulieu, J.-P., Caldwell, J. A. R., Menzies, J., Vermaak, P., Depoy, D. L., Gaudi, B. S., Gould, A., Pogge, R. W., Dominik, M., et al. 2000: *Variable Star Research by the PLANET Collaboration*, in ASP Conf. Ser. 203: IAU Colloq. 176: The Impact of Large-Scale Surveys on Pulsating Star Research, 25–30, cited on p. 7

Alcock, C., Akerloff, C. W., Allsman, R. A., Axelrod, T. S., Bennett, D. P., Chan, S., Cook, C. H., Freeman, K. C., Griest, K., Marshall, S. L., Park, H. S., et al. 1993: *Possible Gravitational Microlensing of a Star in the Large Magellanic Cloud*, Nat, 365, 621, cited on p. 7

Alcock, C., Allsman, R. A., Alves, D., Axelrod, T. S., Becker, A. C., Bennett, D. P., Cook, K. H., Drake, A. J., Freeman, K. C., Griest, K., Lehner, M. J., et al. 1999: *Difference Image Analysis of Galactic Microlensing. II. Microlensing Events*, ApJS, 124, 171, cited on p. 98

Alcock, C., Allsman, R. A., Alves, D., Axelrod, T. S., Becker, A. C., Bennett, D. P., Cook, K. H., Freeman, K. C., Griest, K., Guern, J., Lehner, M. J., et al. 1997: *The MACHO Project Large Magellanic Cloud Microlensing Results from the First Two Years and the Nature of the Galactic Dark Halo*, ApJ, 486, 697+, cited on p. 7, 16

Alcock, C., Allsman, R. A., Alves, D. R., Axelrod, T. S., Becker, A. C., Bennett, D. P., Cook, K. H., Dalal, N., Drake, A. J., Freeman, K. C., Geha, M., et al. 2000a: *The MACHO Project: Microlensing Results from 5.7 Years of Large Magellanic Cloud Observations*, ApJ, 542, 281, cited on p. 5, 7, 160

Alcock, C., Allsman, R. A., Alves, D. R., Axelrod, T. S., Becker, A. C., Bennett, D. P., Cook, K. H., Dalal, N., Drake, A. J., Freeman, K. C., Geha, M., et al. 2001a: *The MACHO Project Hubble Space Telescope Follow-Up: Preliminary Results on the Location of the Large Magellanic Cloud Microlensing Source Stars*, ApJ, 552, 582, cited on p. 9, 16

Alcock, C., Allsman, R. A., Alves, D. R., Axelrod, T. S., Becker, A. C., Bennett, D. P., Cook, K. H., Drake, A. J., Freeman, K. C., Geha, M., Griest, K., et al. 2000b: *The MACHO Project: Microlensing Optical Depth toward the Galactic Bulge from Difference Image Analysis*, ApJ, 541, 734, cited on p. 7, 160

Alcock, C., Allsman, R. A., Alves, D. R., Axelrod, T. S., Becker, A. C., Bennett, D. P., Cook, K. H., Drake, A. J., Freeman, K. C., Geha, M., Griest, K., et al. 2001b: *The MACHO Project: Microlensing Detection Efficiency*, ApJS, 136, 439, cited on p. 59, 155

Alcock, C., Allsman, R. A., Axelrod, T. S., Bennett, D. P., Cook, K. H., Evans, N. W., Freeman, K. C., Griest, K., Jijina, J., Lehner, M., Marshall, S. L., et al. 1995: *Theory of Exploring the Dark Halo with Microlensing. I. Power-Law Models*, ApJ, 449, 28, cited on p. 10, 16, 40

Aldering, G., Akerlof, C. W., Amanullah, R., Astier, P., Barrelet, E., Bebek, C., Bergstrom, L., Bercovitz, J., Bernstein, G. M., Bester, M., Bonissent, A., et al. 2002: *Overview of the Super-Nova/Acceleration Probe (SNAP)*, in Future Research Direction and Visions for Astronomy. Edited by Dressler, Alan M. Proceedings of the SPIE, Volume 4835, pp. 146-157 (2002)., 146–157, cited on p. 3

An, J. H., Evans, N. W., Hewett, P., Baillon, P., Calchi Novati, S., Carr, B. J., Crézé, M., Giraud-Héraud, Y., Gould, A., Jetzer, P., Kaplan, J., et al. 2004a: *The POINT-AGAPE Survey - I. The variable stars in M31*, MNRAS, 351, 1071, cited on p. 60

An, J. H., Evans, N. W., Kerins, E., Baillon, P., Calchi Novati, S., Carr, B. J., Crézé, M., Giraud-Héraud, Y., Gould, A., Hewett, P., Jetzer, P., et al. 2004b: *The Anomaly in the Candidate Microlensing Event PA-99-N2*, ApJ, 601, 845, cited on p. 194

Ansari, R., Aurière, M., Baillon, P., Bouquet, A., Coupinot, G., Coutures, C., Ghesquière, C., Giraud-Héraud, Y., Gillieron, D., Gondolo, P., Hecquet, J., et al. 2004: *Variable stars towards the bulge of M 31: The AGAPE catalogue*, A&A, 421, 509, cited on p. 60

Ansari, R., Aurière, M., Baillon, P., Bouquet, A., Coupinot, G., Coutures, C., Ghesquière, C., Giraud-Héraud, Y., Gondolo, P., Hecquet, J., Kaplan, J., et al. 1999: *AgapeZ1: a large amplification*

microlensing event or an odd variable star towards the inner bulge of M31, A&A, 344, L49, cited on p. 9, 16, 156, 158, 159, 160, 176

Ansari, R., Auriere, M., Baillon, P., Bouquet, A., Coupinot, G., Coutures, C., Ghesquiere, C., Giraud-Heraud, Y., Gondolo, P., Hecquet, J., Kaplan, J., et al. 1997: *AGAPE: a search for dark matter towards M 31 by microlensing effects on unresolved stars.*, A&A, 324, 843, cited on p. 9, 16, 156

Ansari, R., Cavalier, F., Moniez, M., Aubourg, E., Bareyre, P., Brehin, S., Gros, M., Lachieze-Rey, M., Laurent, B., Lesquoy, E., Magneville, C., et al. 1996: *Observational limits on the contribution of sub-stellar and stellar objects to the galactic halo.*, A&A, 314, 94, cited on p. 7

Arras, P. & Wasserman, I. 1999: *Canaries in a coal mine: using globular clusters to place limits on massive black holes in the Galactic halo*, MNRAS, 306, 257, cited on p. 4

Aubourg, E., Bareyre, P., Brehin, S., Gros, M., Lachieze-Rey, M., Laurent, B., Lesquoy, E., Magneville, C., Milsztajn, A., Moscoso, L., Queinnec, F., et al. 1993: *Evidence for Gravitational Microlensing by Dark Objects in the Galactic Halo*, Nat, 365, 623+, cited on p. 7, 16

Auriere, M., Baillon, P., Bouquet, A., Carr, B. J., Crézé, M., Evans, N. W., Giraud-Héraud, Y., Gould, A., Hewett, P. C., Kaplan, J., Kerins, E., et al. 2001: *A Short-Timescale Candidate Microlensing Event in the POINT-AGAPE Pixel Lensing Survey of M31*, ApJ, 553, L137, cited on p. 11, 71, 156, 158, 160, 194, 197

Bacon, D. J., Refregier, A. R., & Ellis, R. S. 2000: *Detection of weak gravitational lensing by large-scale structure*, MNRAS, 318, 625, cited on p. 6

Bahcall, J. N., Soneira, R. M., & Schmidt, M. 1983: *The galactic spheroid*, ApJ, 265, 730, cited on p. 80

Bahcall, N. A., Cen, R., Davé, R., Ostriker, J. P., & Yu, Q. 2000: *The Mass-to-Light Function: Antibias and Ω_m*, ApJ, 541, 1, cited on p. 2

Baillon, P., Bouquet, A., Giraud-Héraud, Y., & Kaplan, J. 1993: *Detection of Brown Dwarfs by the Microlensing of Unresolved Stars*, A&A, 277, 1+, cited on p. 8, 160

Baltz, E. A., Lauer, T. R., Zurek, D. R., Gondolo, P., Shara, M. M., Silk, J., & Zepf, S. E. 2004: *Microlensing Candidates in M87 and the Virgo Cluster with the Hubble Space Telescope*, ApJ, 610, 691, cited on p. 9, 16

Baltz, E. A. & Silk, J. 2000: *Event Rate and Einstein Time Evaluation in Pixel Microlensing*, ApJ, 530, 578, cited on p. 10, 17, 18, 20, 23, 35, 39, 43, 45, 48, 55

Belokurov, V., An, J., Evans, N. W., Hewett, P., Baillon, P., Novati, S. C., Carr, B. J., Crézé, M., Giraud-Héraud, Y., Gould, A., Jetzer, P., et al. 2005: *The POINT-AGAPE survey - II. An unrestricted search for microlensing events towards M31*, MNRAS, 357, 17, cited on p. 11, 158, 159, 176

Bennett, C. L., Halpern, M., Hinshaw, G., Jarosik, N., Kogut, A., Limon, M., Meyer, S. S., Page, L., Spergel, D. N., Tucker, G. S., Wollack, E., et al. 2003: *First-Year Wilkinson Microwave Anisotropy Probe (WMAP) Observations: Preliminary Maps and Basic Results*, ApJS, 148, 1, cited on p. 1, 2

Bessell, M. S. 1979: *UBVRI photometry. II - The Cousins VRI system, its temperature and absolute flux calibration, and relevance for two-dimensional photometry*, PASP, 91, 589, cited on p. 163

Bessell, M. S. 1995: *UBVRI Systems: Resolving Different Versions*, PASP, 107, 672, cited on p. 150

Binney, J. & Merrifield, M. 1998, Galactic Astronomy (Princeton: Princeton Univ. Press), cited on p. 78

Binney, J. & Tremaine, S. 1987, Galactic Dynamics (Princeton, Princeton Univ. Press), cited on p. 25, 84

Blanchard, A., Sadat, R., Bartlett, J. G., & Le Dour, M. 2000: *A new local temperature distribution function for X-ray clusters: cosmological applications*, A&A, 362, 809, cited on p. 2

Böhringer, H. 2002: *Galaxy Clusters as Probes for Matter in the Universe*, Space Science Reviews, 100, 49, cited on p. 2, 5

Bond, I. A., Abe, F., Dodd, R. J., Hearnshaw, J. B., Honda, M., Jugaku, J., Kilmartin, P. M., Marles, A., Masuda, K., Matsubara, Y., Muraki, Y., et al. 2001: *Real-time difference imaging analysis of MOA Galactic bulge observations during 2000*, MNRAS, 327, 868, cited on p. 7, 98

Borgani, S., Rosati, P., Tozzi, P., & Norman, C. 1999: *Cosmological Constraints from the ROSAT Deep Cluster Survey*, ApJ, 517, 40, cited on p. 2

Bozza, V., Calchi Novati, S., Capaccioli, M., Capozziello, S., Cardone, V., Covone, G., de Paolis, F., de Ritis, R., Ingrosso, G., Iovane, G., Lambiase, G., et al. 2000: *SLOTT-AGAPE project.*, Mem. Soc. Astron. Italiana, 71, 1113, cited on p. 9, 16

Braun, R. 1991: *The distribution and kinematics of neutral gas in M31*, ApJ, 372, 54, cited on p. 79

Brinks, E. & Burton, W. B. 1984: *A high resolution hydrogen line survey of Messier 31. II - The warped flaring hydrogen layer*, A&A, 141, 195, cited on p. 79

Brown, T. M., Ferguson, H. C., Smith, E., Kimble, R. A., Sweigart, A. V., Renzini, A., Rich, R. M., & VandenBerg, D. A. 2003: *Evidence of a Significant Intermediate-Age Population in the M31 Halo from Main-Sequence Photometry*, ApJ, 592, L17, cited on p. 196

Buil, C. 1991, CCD astronomy. Construction and use of an astronomical CCD camera (Richmond: Willmann-Bell), 253+, cited on p. 97, 107

Burles, S., Nollett, K. M., & Turner, M. S. 2001: *Big Bang Nucleosynthesis Predictions for Precision Cosmology*, ApJ, 552, L1, cited on p. 3

Calchi Novati, S., Iovane, G., Marino, A. A., Aurière, M., Baillon, P., Bouquet, A., Bozza, V., Capaccioli, M., Capozziello, S., Cardone, V., Covone, G., et al. 2002: *Microlensing search towards M 31*, A&A, 381, 848, cited on p. 156

Calchi Novati, S., Jetzer, P., Scarpetta, G., Giraud-Héraud, Y., Kaplan, J., Paulin-Henriksson, S., & Gould, A. 2003: *Microlensing towards M 31 with MDM data*, A&A, 405, 851, cited on p. 11, 16, 156, 160

Calchi Novati, S., Paulin-Henriksson, S., An, J., Baillon, P., Belokurov, V., Carr, B. J., Crézé, M., Evans, N. W., Giraud-Héraud, Y., Gould, A., Hewett, P., et al. 2005: *POINT-AGAPE pixel lensing survey of M 31. Evidence for a MACHO contribution to galactic halos*, A&A, 443, 911, cited on p. 11, 16, 155, 156, 158, 159, 176, 194, 202

Carlberg, R. G., Morris, S. L., Yee, H. K. C., & Ellingson, E. 1997a: *Redshift Evolution of Galaxy Cluster Densities*, ApJ, 479, L19+, cited on p. 2

Carlberg, R. G., Yee, H. K. C., & Ellingson, E. 1997b: *The Average Mass and Light Profiles of Galaxy Clusters*, ApJ, 478, 462, cited on p. 2

Cassisi, S., Castellani, V., degl'Innocenti, S., & Weiss, A. 1998: *An updated theoretical scenario for globular cluster stars*, A&AS, 129, 267, cited on p. 163

Cen, R. & Ostriker, J. P. 1999: *Where Are the Baryons?*, ApJ, 514, 1, cited on p. 5

Chabrier, G. 2003: *Galactic Stellar and Substellar Initial Mass Function*, PASP, 115, 763, cited on p. 80

Ciardullo, R., Tamblyn, P., & Phillips, A. C. 1990: *A search for novae in M 31 globular clusters*, PASP, 102, 1113, cited on p. 137

Cole, S., Norberg, P., Baugh, C. M., Frenk, C. S., Bland-Hawthorn, J., Bridges, T., Cannon, R., Colless, M., Collins, C., Couch, W., Cross, N., et al. 2001: *The 2dF galaxy redshift survey: near-infrared galaxy luminosity functions*, MNRAS, 326, 255, cited on p. 5

Collins, C. A., Guzzo, L., Böhringer, H., Schuecker, P., Chincarini, G., Cruddace, R., De Grandi, S., MacGillivray, H. T., Neumann, D. M., Schindler, S., Shaver, P., et al. 2000: *The ROSAT-ESO Flux-Limited X-ray (REFLEX) galaxy cluster survey - II. The spatial correlation function*, MNRAS, 319, 939, cited on p. 2

Croft, R. A. C., Dalton, G. B., Efstathiou, G., Sutherland, W. J., & Maddox, S. J. 1997: *The richness dependence of galaxy cluster correlations: results from a redshift survey of rich APM clusters*, MNRAS, 291, 305, cited on p. 2

Crotts, A. P. S. 1992: *M31 - A unique laboratory for gravitational microlensing*, ApJ, 399, L43, cited on p. 8, 61, 160, 166

Crotts, A. P. S., de Jong, J. T. A., Uglesich, R. R., Baltz, E. A., Kuijken, K. H., Sackett, P. D., Boyle, R. P., Sutherland, W. J., Cseresnjes, P., Corbally, C. J., Gyuk, G., et al. 2003: *Results from Two Surveys Indicating Massive Lensing Objects in The Halo of M31*, American Astronomical Society Meeting Abstracts, 203, , cited on p. 156

Crotts, A. P. S. & Tomaney, A. B. 1996: *Results from a Survey of Gravitational Microlensing toward M31*, ApJ, 473, L87, cited on p. 9, 16, 156, 160

Crotts, A. P. S., Uglesich, R., Gyuk, G., & Tomaney, A. B. 1999a: *MEGA: Mapping Halo and Bulge Microlensing in M31*, in ASP Conf. Ser. 182: Galaxy Dynamics - A Rutgers Symposium, 409+, cited on p. 9, 98

Crotts, A. P. S., Uglesich, R., Gyuk, G., & Tomaney, A. B. 1999b: *MEGA: Mapping Halo and Bulge Microlensing in M31*, in: ASP Conf. Ser. 182, 409+, cited on p. 9

Davé, R., Cen, R., Ostriker, J. P., Bryan, G. L., Hernquist, L., Katz, N., Weinberg, D. H., Norman, M. L., & O'Shea, B. 2001: *Baryons in the Warm-Hot Intergalactic Medium*, ApJ, 552, 473, cited on p. 5

Davidge, T. J., Olsen, K. A. G., Blum, R., Stephens, A. W., & Rigaut, F. 2005: *Deep ALTAIR+NIRI Imaging of the Disk and Bulge of M31*, AJ, 129, 201, cited on p. 196

de Bernardis, P., Ade, P. A. R., Bock, J. J., Bond, J. R., Borrill, J., Boscaleri, A., Coble, K., Contaldi, C. R., Crill, B. P., De Troia, G., Farese, P., et al. 2002: *Multiple Peaks in the Angular Power Spectrum of the Cosmic Microwave Background: Significance and Consequences for Cosmology*, ApJ, 564, 559, cited on p. 2

de Bernardis, P., Ade, P. A. R., Bock, J. J., Bond, J. R., Borrill, J., Boscaleri, A., Coble, K., Crill, B. P., De Gasperis, G., Farese, P. C., Ferreira, P. G., et al. 2000: *A flat Universe from high-resolution maps of the cosmic microwave background radiation*, Nat, 404, 955, cited on p. 2

de Jong, J. T. A., Kuijken, K., Crotts, A. P. S., Sackett, P. D., Sutherland, W. J., Uglesich, R. R., Baltz, E. A., Cseresnjes, P., Gyuk, G., Widrow, L. M., & The MEGA collaboration. 2004: *First microlensing candidates from the MEGA survey of M 31*, A&A, 417, 461, cited on p. 11, 16, 60, 72, 156, 158, 194, 195

de Jong, J. T. A., Widrow, L. M., Cseresnjes, P., Kuijken, K., Crotts, A. P. S., Bergier, A., Baltz, E. A., Gyuk, G., Sackett, P. D., Uglesich, R. R., & Sutherland, W. J. 2006: *MACHOs in M 31? Absence of evidence but not evidence of absence*, A&A, 446, 855, cited on p. 11, 60, 155, 156, 158, 159, 176

De Marchi, G., Sirianni, R., Gilliland, R., Bohlin, R., Pavlovsky, C., Jee, M., Mack, J., van der Marel, R., & Boffi, F. 2004: *Detector Quantum Efficiency and Photometric Zero Points of the ACS*, STScI - Instrument Science Report, ACS 2004-08, cited on p. 63

de Rujula, A., Jetzer, P., & Masso, E. 1991: *Dark mass moments*, MNRAS, 250, 348, cited on p. 16, 31, 48, 69

de Rujula, A., Jetzer, P., & Masso, E. 1992: *On the Nature of the Dark Halo of Our Galaxy*, A&A, 254, 99, cited on p. 4

Della Ceca, R., Scaramella, R., Gioia, I. M., Rosati, P., Fiore, F., & Squires, G. 2000: *BeppoSAX observations of two high redshift clusters of galaxies: RXJ 0152.7-1357 and MS 2053.7-0449*, A&A, 353, 498, cited on p. 2

Dominik, M. 1998: *Estimating physical quantities for an observed galactic microlensing event*, A&A, 330, 963, cited on p. 16, 69

Donahue, M., Voit, G. M., Gioia, I., Lupino, G., Hughes, J. P., & Stocke, J. T. 1998: *A Very Hot, High-Redshift Cluster of Galaxies: More Trouble for Omega 0=1*, ApJ, 502, 550, cited on p. 2

Dong, S., DePoy, D. L., Gaudi, B. S., Gould, A., Han, C., Park, B.-G., Pogge, R. W., Udalski, A., Szewczyk, O., Kubiak, M., Szymański, M. K., et al. 2006: *Planetary Detection Efficiency of the Magnification 3000 Microlensing Event OGLE-2004-BLG-343*, ApJ, 642, 842, cited on p. 43

Drory, N., Feulner, G., Bender, R., Botzler, C. S., Hopp, U., Maraston, C., Mendes de Oliveira, C., & Snigula, J. 2001: *The Munich Near-Infrared Cluster Survey - I. Field selection, object extraction and photometry*, MNRAS, 325, 550, cited on p. 153

Eke, V. R., Cole, S., Frenk, C. S., & Patrick Henry, J. 1998: *Measuring Omega_0 using cluster evolution*, MNRAS, 298, 1145, cited on p. 2

Evans, N. W. & Kerins, E. 2000: *Is the Large Magellanic Cloud a Large Microlensing Cloud?*, ApJ, 529, 917, cited on p. 7, 160

Fabian, A. C., Crawford, C. S., Ettori, S., & Sanders, J. S. 2001: *Chandra detection of the intracluster medium around 3C 294 at z=1.786*, MNRAS, 322, L11, cited on p. 2

Ferguson, A. M. N. & Johnson, R. A. 2001: *Constraints on Galaxy Formation from Stars in the Far Outer Disk of M31*, ApJ, 559, L13, cited on p. 196

Feulner, G., Bender, R., Drory, N., Hopp, U., Snigula, J., & Hill, G. J. 2003: *The Munich Near-Infrared Cluster Survey - V. The evolution of the rest-frame K- and J-band galaxy luminosity functions to z~0.7*, MNRAS, 342, 605, cited on p. 153

Fischer, P., McKay, T. A., Sheldon, E., Connolly, A., Stebbins, A., Frieman, J. A., Jain, B., Joffre, M., Johnston, D., Bernstein, G., Annis, J., et al. 2000: *Weak Lensing with Sloan Digital Sky Survey Commissioning Data: The Galaxy-Mass Correlation Function to 1 H^{-1} Mpc*, AJ, 120, 1198, cited on p. 6

Fliri, J., Riffeser, A., Seitz, S., & Bender, R. 2006: *The Wendelstein Calar Alto Pixellensing Project (WeCAPP): the M 31 variable star catalogue*, A&A, 445, 423, cited on p. 9, 60, 90, 153, 201

Freedman, W. L. & Madore, B. F. 1990: *An empirical test for the metallicity sensitivity of the Cepheid period-luminosity relation*, ApJ, 365, 186, cited on p. 8

Freedman, W. L., Madore, B. F., Gibson, B. K., Ferrarese, L., Kelson, D. D., Sakai, S., Mould, J. R., Kennicutt, R. C., Ford, H. C., Graham, J. A., Huchra, J. P., et al. 2001: *Final Results from the Hubble Space Telescope Key Project to Measure the Hubble Constant*, ApJ, 553, 47, cited on p. 1

Fruchter, A. & Hook, R. N. 1997: *Novel image reconstruction method applied to deep Hubble space telescope images*, Proceedings of SPIE, 3164, 120, cited on p. 125

Fukugita, M., Hogan, C. J., & Peebles, P. J. E. 1998: *The Cosmic Baryon Budget*, ApJ, 503, 518, cited on p. 5

Fukugita, M. & Peebles, P. J. E. 2004: *The Cosmic Energy Inventory*, ApJ, 616, 643, cited on p. 5

Gössl, C. A. & Riffeser, A. 2002: *Image reduction pipeline for the detection of variable sources in highly crowded fields*, A&A, 381, 1095, cited on p. 12, 97, 161

Geiss, J. & Gloeckler, G. 1998: *Abundances of Deuterium and Helium-3 in the Protosolar Cloud*, Space Science Reviews, 84, 239, cited on p. 3

Girardi, L., Bertelli, G., Bressan, A., Chiosi, C., Groenewegen, M. A. T., Marigo, P., Salasnich, B., & Weiss, A. 2002: *Theoretical isochrones in several photometric systems. I. Johnson-Cousins-Glass, HST/WFPC2, HST/NICMOS, Washington, and ESO Imaging Survey filter sets*, A&A, 391, 195, cited on p. 77, 78, 79, 81, 186, 196

Gondolo, P. 1999: *Optical Depth Evaluation in Pixel Microlensing*, ApJ, 510, L29, cited on p. 10, 17, 19

Gössl, C. A., Snigula, J., & Hopp, U. 2006: *Using delta Cep stars to study northern dwarf irregular galaxies of the Local Group* ., Mem. Soc. Astron. Italiana, 77, 299, cited on p. 153

Gould, A. 1994a: *MACHO velocities from satellite-based parallaxes*, ApJ, 421, L75, cited on p. 25

Gould, A. 1994b: *Proper motions of MACHOs*, ApJ, 421, L71, cited on p. 19, 20, 25, 71

Gould, A. 1995: *Search for Intracluster MACHOs by Pixel Lensing of M87*, ApJ, 455, 44, cited on p. 20

Gould, A. 1996a: *Microlensing and the Stellar Mass Function*, PASP, 108, 465, cited on p. 48

Gould, A. 1996b: *Theory of Pixel Lensing*, ApJ, 470, 201+, cited on p. 8, 10, 16, 17, 21, 58, 161, 162, 165, 166

Gould, A. 2001a: *Applications of Microlensing to Stellar Astrophysics*, PASP, 113, 903, cited on p. 6

Gould, A. 2001b: *Theory of Microlensing*, in ASP Conf. Ser. 239: Microlensing 2000: A New Era of Microlensing Astrophysics, 3–+, cited on p. 6

Gould, A. 2003: *The New Era of Precision Microlensing*, in ASP Conf. Ser. 289: The Proceedings of the IAU 8th Asian-Pacific Regional Meeting, Volume I, 453–560, cited on p. 7

Gould, A., Bahcall, J. N., & Flynn, C. 1997: *M Dwarfs from Hubble Space Telescope Star Counts. III. The Groth Strip*, ApJ, 482, 913, cited on p. 78, 79, 80

Gould, A. & Welch, D. L. 1996: *MACHO Proper Motions from Optical/Infrared Photometry*, ApJ, 464, 212+, cited on p. 86

Gouliermis, D., Brandner, W., & Henning, T. 2005: *The Initial Mass Function toward the Low-Mass End in the Large Magellanic Cloud with Hubble Space Telescope WFPC2 Observations*, ApJ, 623, 846, cited on p. 63

Grego, L., Carlstrom, J. E., Reese, E. D., Holder, G. P., Holzapfel, W. L., Joy, M. K., Mohr, J. J., & Patel, S. 2001: *Galaxy Cluster Gas Mass Fractions from Sunyaev-Zeldovich Effect Measurements: Constraints on Ω_M*, ApJ, 552, 2, cited on p. 2

Greisen, E. W., Wells, D. C., & Harten, R. H. 1981: *The FITS Tape Formats - Flexible Image Transport Systems*, Proceedings of SPIE, 264, 298+, cited on p. 99

Griest, K. 1991: *Galactic microlensing as a method of detecting massive compact halo objects*, ApJ, 366, 412, cited on p. 9, 16, 18, 37, 41

Grillmair, C. J., Lauer, T. R., Worthey, G., Faber, S. M., Freedman, W. L., Madore, B. F., Ajhar, E. A., Baum, W. A., Holtzman, J. A., Lynds, C. R., O'Neil, E. J., et al. 1996: *Hubble Space Telescope Observations of M32: The Color-Magnitude Diagram*, AJ, 112, 1975+, cited on p. 90, 163

Grosbol, P., Harten, R. H., Greisen, E. W., & Wells, D. C. 1988: *Generalized extensions and blocking factors for FITS*, A&AS, 73, 359, cited on p. 99

Gyuk, G. & Crotts, A. 2000: *Optical Depth from Realistic Microlensing Models of M31*, ApJ, 535, 621, cited on p. 35, 37, 71, 80

Halverson, N. W., Leitch, E. M., Pryke, C., Kovac, J., Carlstrom, J. E., Holzapfel, W. L., Dragovan, M., Cartwright, J. K., Mason, B. S., Padin, S., Pearson, T. J., et al. 2002: *Degree Angular Scale Interferometer First Results: A Measurement of the Cosmic Microwave Background Angular Power Spectrum*, ApJ, 568, 38, cited on p. 2

Han, C. 1996: *Pixel Lensing Experiment toward the M31 Bulge*, ApJ, 472, 108+, cited on p. 10, 17, 37, 56, 58, 72, 77

Han, C. & Gould, A. 1996a: *Galactic versus Extragalactic Pixel Lensing Events toward M31*, ApJ, 473, 230+, cited on p. 10, 17, 39, 41, 56, 58, 79, 80, 83, 86

Han, C. & Gould, A. 1996b: *Statistical Determination of the MACHO Mass Spectrum*, ApJ, 467, 540, cited on p. 10, 16, 48

Han, C. & Park, S. 2001: *Colour change measurements of gravitational microlensing events by using the difference image analysis method*, MNRAS, 320, 41, cited on p. 86

Han, C., Park, S., & Jeong, J. 2000: *Chromaticity of gravitational microlensing events*, MNRAS, 316, 97, cited on p. 48, 86

Harten, R. H., Grosbol, P., Greisen, E. W., & Wells, D. C. 1988: *The FITS tables extension*, A&AS, 73, 365, cited on p. 99

Heger, A., Fryer, C. L., Woosley, S. E., Langer, N., & Hartmann, D. H. 2003: *How Massive Single Stars End Their Life*, ApJ, 591, 288, cited on p. 5

Heidt, J., Appenzeller, I., Gabasch, A., Jäger, K., Seitz, S., Bender, R., Böhm, A., Snigula, J., Fricke, K. J., Hopp, U., Kümmel, M., et al. 2003: *The FORS Deep Field: Field selection, photometric observations and photometric catalog*, A&A, 398, 49, cited on p. 153

Henry, J. P. 2000: *Measuring Cosmological Parameters from the Evolution of Cluster X-Ray Temperatures*, ApJ, 534, 565, cited on p. 2

Hook, R. N. & Fruchter, A. S. 1997: *Variable-Pixel Linear Combination*, in ASP Conf. Ser. 125: Astronomical Data Analysis Software and Systems VI, Vol. 6, 147+, cited on p. 125

Izotov, Y. I. & Thuan, T. X. 2004: *Systematic Effects and a New Determination of the Primordial Abundance of ^{4}He and dY/dZ from Observations of Blue Compact Galaxies*, ApJ, 602, 200, cited on p. 3

Jablonka, P., Bridges, T. J., Sarajedini, A., Meylan, G., Maeder, A., & Meynet, G. 1999: *No Increase of the Red Giant Branch Tip Luminosity toward the Center of M31*, ApJ, 518, 627, cited on p. 162

Jacoby, G. H. 1990: *CCDs in astronomy; Proceedings of the Conference, Tucson, AZ, Sept. 6-8, 1989*, in ASP Conf. Ser. 8: CCDs in astronomy, cited on p. 97

Jetzer, P. 1994: *On the mass of the dark compact objects in the Galactic disk*, ApJ, 432, L43, cited on p. 48, 69, 164

Jetzer, P. 2002: *Clouds and Diffuse Baryonic Dark Matter*, Space Science Reviews, 100, 117, cited on p. 5

Jetzer, P. & Massó, E. 1994: *On the mass of the dark compact halo objects*, Physics Letters B, 323, 347, cited on p. 10, 16, 48, 69, 164

Joshi, Y. C., Pandey, A. K., Narasimha, D., & Sagar, R. 2001: *Search for Microlensing Events Towards M31 Galaxy*, Bull. Astron. Soc. India, 29, 531, cited on p. 9, 16

Joshi, Y. C., Pandey, A. K., Narasimha, D., & Sagar, R. 2005: *First microlensing candidate towards M 31 from the Nainital Microlensing Survey*, A&A, 433, 787, cited on p. 11, 158, 176

Kabana, S. & Minkowski, P. 2002: *Dark quark 'stars': do they matter for Ω_{matter}?*, Space Science Reviews, 100, 175, cited on p. 4

Kaiser, N. & Squires, G. 1993: *Mapping the dark matter with weak gravitational lensing*, ApJ, 404, 441, cited on p. 6

Kajita, T. 2002: *Neutrino mass and oscillations*, Space Science Reviews, 100, 221, cited on p. 4

Kent, S. M. 1989a: *A comparison of optical and H I rotation curves in M 31*, PASP, 101, 489, cited on p. 79

Kent, S. M. 1989b: *An improved bulge model for M31*, AJ, 97, 1614, cited on p. 75, 76, 78, 79, 164

Kerins, E. 2001: *Pixel Lensing Towards Andromeda: the POINT-AGAPE Survey*, in Identification of Dark Matter, 269–+, cited on p. 9

Kerins, E., Carr, B. J., Evans, N. W., Hewett, P., Lastennet, E., Le Du, Y., Melchior, A.-L., Smartt, S. J., & Valls-Gabaud, D. 2001: *Theory of pixel lensing towards M31 - I. The density contribution and mass of MACHOs*, MNRAS, 323, 13, cited on p. 75, 78, 79, 83, 165, 197

Kim, T.-S., Cristiani, S., & D'Odorico, S. 2001: *The Lyalpha forest at $1.5 < z < 4$*, A&A, 373, 757, cited on p. 5

Kirkman, D., Tytler, D., Suzuki, N., O'Meara, J. M., & Lubin, D. 2003: *The Cosmological Baryon Density from the Deuterium-to-Hydrogen Ratio in QSO Absorption Systems: D/H toward Q1243+3047*, ApJS, 149, 1, cited on p. 3

Krist, J. 2003: *ACS WFC & HRC field-dependent PSF variations due to optical and charge diffusion effects*, STScI - Instrument Science Report, ACS 2003-06, cited on p. 63

Landolt, A. U. 1992: *UBVRI photometric standard stars in the magnitude range 11.5-16.0 around the celestial equator*, AJ, 104, 340, cited on p. 150

Lasserre, T., Afonso, C., Albert, J. N., Andersen, J., Ansari, R., Aubourg, E., Bareyre, P., Bauer, F., Beaulieu, J. P., Blanc, G., Bouquet, A., et al. 2000: *Not enough stellar mass Machos in the Galactic halo*, A&A, 355, L39, cited on p. 7, 160

Lawrie, D. G. 1983: *Velocity dispersion of planetary nebulae in the nuclear bulge of M31*, ApJ, 273, 562, cited on p. 83

Lee, A. T., Ade, P., Balbi, A., Bock, J., Borrill, J., Boscaleri, A., de Bernardis, P., Ferreira, P. G., Hanany, S., Hristov, V. V., Jaffe, A. H., et al. 2001: *A High Spatial Resolution Analysis of the MAXIMA-1 Cosmic Microwave Background Anisotropy Data*, ApJ, 561, L1, cited on p. 2

Lejeune, T., Cuisinier, F., & Buser, R. 1998: *A standard stellar library for evolutionary synthesis. II. The M dwarf extension*, A&AS, 130, 65, cited on p. 90

Loinard, L., Allen, R. J., & Lequeux, J. 1995: *An unbiased survey for CO emission in the inner disk of the Andromeda galaxy.*, A&A, 301, 68, cited on p. 79

Méndez, R. H., Riffeser, A., Kudritzki, R.-P., Matthias, M., Freeman, K. C., Arnaboldi, M., Capaccioli, M., & Gerhard, O. E. 2001: *Detection, Photometry, and Slitless Radial Velocities of 535 Planetary Nebulae in the Flattened Elliptical Galaxy NGC 4697*, ApJ, 563, 135, cited on p. 153

Mackay, C. D. 1986: *Charge-coupled devices in astronomy*, ARA&A, 24, 255, cited on p. 97, 107

Magnier, E. A., Lewin, W. H. G., van Paradijs, J., Hasinger, G., Jain, A., Pietsch, W., & Truemper, J. 1992: *BV RI CCD photometry of 361,281 objects in the field of M 31*, A&AS, 96, 379, cited on p. 162

Mao, S. & Paczyński, B. 1996: *Mass Determination with Gravitational Microlensing*, ApJ, 473, 57, cited on p. 48

Maraston, C. 1998: *Evolutionary synthesis of stellar populations: a modular tool*, MNRAS, 300, 872, cited on p. 163

Marigo, P. & Girardi, L. 2001: *Coupling emitted light and chemical yields from stars: A basic constraint to population synthesis models of galaxies*, A&A, 377, 132, cited on p. 81

McLean, I. S. 1997, Electronic imaging in astronomy: detectors and instrumentation (John Wiley & Sons), 127+, cited on p. 97, 106

Milsztajn, A. 2002: *The Galactic Halo from Microlensing*, Space Science Reviews, 100, 103, cited on p. 6

Mochejska, B. J., Kaluzny, J., Stanek, K. Z., Sasselov, D. D., & Szentgyorgyi, A. H. 2001: *DIRECT Distances to Nearby Galaxies Using Detached Eclipsing Binaries and Cepheids. VII. Additional Variables in the Field M33A Discovered with Image Subtraction*, AJ, 121, 2032, cited on p. 98

Modjaz, M. & Li, W. D. 1999: *Nova in M31*, IAUC, 7218, 2+, cited on p. 90, 92

Moehler, S., Koester, D., Zoccali, M., Ferraro, F. R., Heber, U., Napiwotzki, R., & Renzini, A. 2004a: *Spectral types and masses of white dwarfs in globular clusters*, A&A, 420, 515, cited on p. 153

Moehler, S., Sweigart, A. V., Landsman, W. B., Hammer, N. J., & Dreizler, S. 2004b: *Spectroscopic analyses of the blue hook stars in NGC 2808: A more stringent test of the late hot flasher scenario*, A&A, 415, 313, cited on p. 153

Moffat, A. F. J. 1969: *A Theoretical Investigation of Focal Stellar Images in the Photographic Emulsion and Application to Photographic Photometry*, A&A, 3, 455+, cited on p. 144, 146

Moro, D. & Munari, U. 2000: *The Asiago Database on Photometric Systems (ADPS). I. Census parameters for 167 photometric systems*, A&AS, 147, 361, cited on p. 77

Moscardini, L., Matarrese, S., De Grandi, S., & Lucchin, F. 2000: *The correlation function of X-ray galaxy clusters in the ROSAT All-Sky Survey 1 Bright Sample*, MNRAS, 314, 647, cited on p. 2

Mushotzky, R. F. & Scharf, C. A. 1997: *The Luminosity-Temperature Relation at z=0.4 for Clusters of Galaxies*, ApJ, 482, L13+, cited on p. 2

Mutchler, M. & Fruchter, A. 1997: *Drizzling dithered WFPC2 images*, in American Astronomical Society Meeting, Vol. 191, 4107+, cited on p. 125

Netterfield, C. B., Ade, P. A. R., Bock, J. J., Bond, J. R., Borrill, J., Boscaleri, A., Coble, K., Contaldi, C. R., Crill, B. P., de Bernardis, P., Farese, P., et al. 2002: *A Measurement by BOOMERANG of Multiple Peaks in the Angular Power Spectrum of the Cosmic Microwave Background*, ApJ, 571, 604, cited on p. 2

Oppenheimer, B. R., Hambly, N. C., Digby, A. P., Hodgkin, S. T., & Saumon, D. 2001: *Direct Detection of Galactic Halo Dark Matter*, Science, 292, 698, cited on p. 4

Ostriker, J. P. & Peebles, P. J. E. 1973: *A Numerical Study of the Stability of Flattened Galaxies: or, can Cold Galaxies Survive?*, ApJ, 186, 467, cited on p. 201

Paczyński, B. 1986: *Gravitational microlensing by the galactic halo*, ApJ, 304, 1, cited on p. 6, 9, 16, 18, 26, 35, 155

Paczyński, B. 1987: *Giant Luminous Arcs Discovered in Two Clusters of Galaxies*, Nat, 325, 572, cited on p. 6

Paczyński, B., Stanek, K. Z., Udalski, A., Szymanski, M., Kaluzny, J., Kubiak, M., Mateo, M., & Krzeminski, W. 1994: *Are the OGLE microlenses in the galactic bar?*, ApJ, 435, L113, cited on p. 7

Palanque-Delabrouille, N., Afonso, C., Albert, J. N., Andersen, J., Ansari, R., Aubourg, E., Bareyre, P., Bauer, F., Beaulieu, J. P., Bouquet, A., Char, S., et al. 1998: *Microlensing towards the Small Magellanic Cloud EROS 2 first year survey*, A&A, 332, 1, cited on p. 7

Paulin-Henriksson, S., Baillon, P., Bouquet, A., Carr, B. J., Crézé, M., Evans, N. W., Giraud-Héraud, Y., Gould, A., Hewett, P., Kaplan, J., Kerins, E., et al. 2002: *A Candidate M31/M32 Intergalactic Microlensing Event*, ApJ, 576, L121, cited on p. 11, 156, 158, 160, 176, 194

Paulin-Henriksson, S., Baillon, P., Bouquet, A., Carr, B. J., Crézé, M., Evans, N. W., Giraud-Héraud, Y., Gould, A., Hewett, P., Kaplan, J., Kerins, E., et al. 2003: *The POINT-AGAPE survey: 4 high signal-to-noise microlensing candidates detected towards M 31*, A&A, 405, 15, cited on p. 11, 16, 156, 158, 159, 160, 162, 194

Paulin-Henriksson, S. & Calchi Novati, S. 2004: *The POINT-AGAPE microlensing survey: First constraints on Machos towards M31*, arXiv:astro-ph/0408204., cited on p. 156

Penton, S. V., Shull, J. M., & Stocke, J. T. 2000: *The Local Lyα Forest. II. Distribution of H I Absorbers,Doppler Widths, and Baryon Content*, ApJ, 544, 150, cited on p. 5

Perlmutter, S., Aldering, G., Goldhaber, G., Knop, R. A., Nugent, P., Castro, P. G., Deustua, S., Fabbro, S., Goobar, A., Groom, D. E., Hook, I. M., et al. 1999: *Measurements of Omega and Lambda from 42 High-Redshift Supernovae*, ApJ, 517, 565, cited on p. 3

Phillips, A. C. & Davis, L. E. 1995: *Registering, PSF-Matching and Intensity-Matching Images in IRAF*, in ASP Conf. Ser. 77: Astronomical Data Analysis Software and Systems IV, Vol. 4, 297+, cited on p. 98

Pietsch, W., Fliri, J., Freyberg, M. J., Greiner, J., Haberl, F., Riffeser, A., & Sala, G. 2005: *Optical novae: the major class of supersoft X-ray sources in M 31*, A&A, 442, 879, cited on p. 153

Ponz, J. D., Thompson, R. W., & Munoz, J. R. 1994: *The FITS image extension*, A&AS, 105, 53, cited on p. 99

Pratt, M., Marshall, S., Alcock, C., Alves, D., Cook, K., Purdue, P., Allsman, R., Axelrod, T., Freeman, K., Peterson, B., Rodgers, A., et al. 1995: *The MACHO Project: Exotic Microlensing from GMAN*, Bulletin of the American Astronomical Society, 27, 1351, cited on p. 7

Puzia, T. H., Kissler-Patig, M., Thomas, D., Maraston, C., Saglia, R. P., Bender, R., Richtler, T., Goudfrooij, P., & Hempel, M. 2004: *VLT spectroscopy of globular cluster systems. I. The photometric and spectroscopic data set*, A&A, 415, 123, cited on p. 153

Raffelt, G. 2002: *Axions*, Space Science Reviews, 100, 153, cited on p. 4

Ratnatunga, K. U., Griffiths, R. E., Casertano, S., Neuschaefer, L. W., & Wyckoff, E. W. 1994: *Calibration of HST wide field camera for quantitative analysis of faint galaxy images*, AJ, 108, 2362, cited on p. 112

Reeves, H. 2002: *Baryonic Matter and Dark Energy*, Space Science Reviews, 100, 311, cited on p. 4

Rhie, S., Becker, A., Bennett, D., Calitz, J., Cook, K., Fragile, P., Johnson, B., Gurovich, S., Han, C., Hoffman, M., Laws, C., et al. 2000: *Microlensing Planet Search Project*, in IAU Symposium, cited on p. 7

Rhoads, J. E. 2000: *Cosmic-Ray Rejection by Linear Filtering of Single Images*, PASP, 112, 703, cited on p. 119

Riess, A. G., Filippenko, A. V., Challis, P., Clocchiatti, A., Diercks, A., Garnavich, P. M., Gilliland, R. L., Hogan, C. J., Jha, S., Kirshner, R. P., Leibundgut, B., et al. 1998: *Observational Evidence from Supernovae for an Accelerating Universe and a Cosmological Constant*, AJ, 116, 1009, cited on p. 3

Riffeser, A., Fliri, J., Bender, R., Seitz, S., & Gössl, C. A. 2003: *The Wendelstein Calar Alto Pixellensing Project (WeCAPP): First MACHO Candidates*, ApJ, 599, L17, cited on p. 11, 13, 16, 156, 160, 167, 169, 176, 185, 196

Riffeser, A., Fliri, J., Gössl, C. A., Bender, R., Hopp, U., Bärnbantner, O., Ries, C., Barwig, H., Seitz, S., & Mitsch, W. 2001: *WeCAPP - Wendelstein Calar Alto pixellensing project I. Tracing dark and bright matter in M 31*, A&A, 379, 362, cited on p. 9, 12, 16, 57, 59, 85, 119, 150, 151, 153, 160

Riffeser, A., Fliri, J., Seitz, S., & Bender, R. 2006: *Microlensing toward Crowded Fields: Theory and Applications to M31*, ApJS, 163, 225, cited on p. 12, 15, 155, 156, 185, 186, 198, 202, 203

Roberts, M. S. & Rots, A. H. 1973: *Comparison of Rotation Curves of Different Galaxy Types*, A&A, 26, 483, cited on p. 1, 201

Rosati, P., della Ceca, R., Burg, R., Norman, C., & Giacconi, R. 1995: *A first determination of the surface density of galaxy clusters at very low x-ray fluxes*, ApJ, 445, L11, cited on p. 2

Roulet, E. & Mollerach, S. 1997: *Microlensing*, Physics Reports, 279, 67, cited on p. 6, 39

Rubin, V. C., Burstein, D., Ford, W. K., & Thonnard, N. 1985: *Rotation velocities of 16 SA galaxies and a comparison of Sa, Sb, and SC rotation properties*, ApJ, 289, 81, cited on p. 2

Rubin, V. C., Thonnard, N., & Ford, W. K. 1978: *Extended rotation curves of high-luminosity spiral galaxies. IV - Systematic dynamical properties, SA through SC*, ApJ, 225, L107, cited on p. 1

Salzberg, S., Chandar, R., Ford, H., Murthy, S. K., & White, R. 1995: *Decision trees for automated identification of cosmic-ray hits in Hubble Space Telescope images*, PASP, 107, 279, cited on p. 119

Sarajedini, A. & Jablonka, P. 2005: *The Metallicity Distribution Function of Field Stars in M31's Bulge*, AJ, 130, 1627, cited on p. 196

Savage, B. D., Tripp, T. M., & Lu, L. 1998: *The intervening and associated O VI absorption-line systems in the ultraviolet spectrum of H1821+643*, AJ, 115, 436, cited on p. 5

Schindler, S. 1999: *Distant clusters of galaxies: X-ray properties and their relations*, A&A, 349, 435, cited on p. 2

Schlegel, D. J., Finkbeiner, D. P., & Davis, M. 1998: *Maps of Dust Infrared Emission for Use in Estimation of Reddening and Cosmic Microwave Background Radiation Foregrounds*, ApJ, 500, 525, cited on p. 77, 78

Scholz, A. & Eislöffel, J. 2004a: *Rotation and accretion of very low mass objects in the σ Ori cluster*, A&A, 419, 249, cited on p. 153

Scholz, A. & Eislöffel, J. 2004b: *Rotation periods for very low mass stars in the Pleiades*, A&A, 421, 259, cited on p. 153

Schuecker, P., Böhringer, H., Guzzo, L., Collins, C. A., Neumann, D. M., Schindler, S., Voges, W., De Grandi, S., Chincarini, G., Cruddace, R., Müller, V., et al. 2001: *The ROSAT-ESO Flux-Limited X-Ray (REFLEX) galaxy cluster survey. III. The power spectrum*, A&A, 368, 86, cited on p. 2

Silk, J. 1968: *Cosmic Black-Body Radiation and Galaxy Formation*, ApJ, 151, 459, cited on p. 2

Snigula, J., Gössl, C., & Hopp, U. 2006: *Toward a census of variable stars in northern local group dwarf irregular galaxies .*, Mem. Soc. Astron. Italiana, 77, 344, cited on p. 153

Snigula, J., Gössl, C., Hopp, U., & Barwig, H. 2004: *Variable star monitoring in local group dwarf irregular galaxies*, in ASP Conf. Ser. 310: IAU Colloq. 193: Variable Stars in the Local Group, 70–+, cited on p. 153

Spergel, D. N., Verde, L., Peiris, H. V., Komatsu, E., Nolta, M. R., Bennett, C. L., Halpern, M., Hinshaw, G., Jarosik, N., Kogut, A., Limon, M., et al. 2003: *First-Year Wilkinson Microwave Anisotropy Probe (WMAP) Observations: Determination of Cosmological Parameters*, ApJS, 148, 175, cited on p. 2

Stanek, K. Z. & Garnavich, P. M. 1998: *Distance to M31 with the Hubble Space Telescope and HIPPARCOS Red Clump Stars*, ApJ, 503, L131+, cited on p. 75

Stephens, A. W., Frogel, J. A., DePoy, D. L., Freedman, W., Gallart, C., Jablonka, P., Renzini, A., Rich, R. M., & Davies, R. 2003: *The Stellar Content of the Bulge of M31*, AJ, 125, 2473, cited on p. 78

Surma, P. 1993: *Shutter-free flatfielding for CCD detectors*, A&A, 278, 654, cited on p. 103

Susperregi, M. 2001: *Breaking the Degeneracy of Cosmological Parameters in Galaxy Redshift Surveys*, ApJ, 546, 85, cited on p. 2

Tegmark, M., Strauss, M. A., Blanton, M. R., Abazajian, K., Dodelson, S., Sandvik, H., Wang, X., Weinberg, D. H., Zehavi, I., Bahcall, N. A., Hoyle, F., et al. 2004: *Cosmological parameters from SDSS and WMAP*, Phys. Rev. D, 69, 103501, cited on p. 2

Teodorescu, A. M., Méndez, R. H., Saglia, R. P., Riffeser, A., Kudritzki, R.-P., Gerhard, O. E., & Kleyna, J. 2005: *Planetary Nebulae and Stellar Kinematics in the Flattened Elliptical Galaxy NGC 1344*, ApJ, 635, 290, cited on p. 153

Tisserand, P. 2005: *Preliminary results on galactic dark matter from the complete EROS2 microlensing survey*, in SF2A-2005: Semaine de l'Astrophysique Francaise, 569–+, cited on p. 155

Tomaney, A. B. & Crotts, A. P. S. 1996: *Expanding the Realm of Microlensing Surveys with Difference Image Photometry*, AJ, 112, 2872+, cited on p. 9, 61, 86, 98, 137, 139, 156

Tripp, T. M. & Savage, B. D. 2000: *O VI and Multicomponent H I Absorption Associated with a Galaxy Group in the Direction of PG 0953+415: Physical Conditions and Baryonic Content*, ApJ, 542, 42, cited on p. 5

Tripp, T. M., Savage, B. D., & Jenkins, E. B. 2000: *Intervening O VI Quasar Absorption Systems at Low Redshift: A Significant Baryon Reservoir*, ApJ, 534, L1, cited on p. 5

Tyson, N. D. & Gal, R. R. 1993: *An exposure guide for taking twilight flatfields with large format CCDs*, AJ, 105, 1206, cited on p. 108

Udalski, A., Szymanski, M., Kaluzny, J., Kubiak, M., Krzeminski, W., Mateo, M., Preston, G. W., & Paczyński, B. 1993: *The optical gravitational lensing experiment. Discovery of the first candidate microlensing event in the direction of the Galactic Bulge*, Acta Astronomica, 43, 289, cited on p. 7

Udalski, A., Szymanski, M., Kaluzny, J., Kubiak, M., & Mateo, M. 1992: *The Optical Gravitational Lensing Experiment*, Acta Astronomica, 42, 253, cited on p. 160

Udalski, A., Zebrun, K., Szymanski, M., Kubiak, M., Pietrzynski, G., Soszynski, I., & Wozniak, P. 2000: *The Optical Gravitational Lensing Experiment. Catalog of Microlensing Events in the Galactic Bulge*, Acta Astronomica, 50, 1, cited on p. 7, 16

Uglesich, R., Crotts, A. P. S., Tomaney, A. B., & Gyuk, G. 1998: *Results from the Columbia/VATT Microlensing Survey of M31*, Bulletin of the American Astronomical Society, 30, 890, cited on p. 9, 156

Uglesich, R., Crotts, A. P. S., Tomaney, A. B., & Gyuk, G. 1999: *The Columbia/VATT Microlensing Survey of M31: Preliminary results from 5 seasons of observations*, Bulletin of the American Astronomical Society, 31, 983, cited on p. 9, 156

Uglesich, R. R., Crotts, A. P. S., & Tomaney, A. B. 1997: *Continuing Observations from the Columbia-VATT Microlensing Survey of M31*, Bulletin of the American Astronomical Society, 29, 837, cited on p. 9, 156

Valls-Gabaud, D. 1994: *Chromatic, spectroscopic and polarisation effects in microlensing events from stellar sources*, in: Large scale structure in the universe, 326+, cited on p. 86

Valls-Gabaud, D. 1995: *Chromatic, spectroscopic and polarisation effects in microlensing events from stellar sources*, in Large Scale Structure in the Universe, 326, cited on p. 48

Van Waerbeke, L., Mellier, Y., Erben, T., Cuillandre, J. C., Bernardeau, F., Maoli, R., Bertin, E., Mc Cracken, H. J., Le Fèvre, O., Fort, B., Dantel-Fort, M., et al. 2000: *Detection of correlated galaxy ellipticities from CFHT data: first evidence for gravitational lensing by large-scale structures*, A&A, 358, 30, cited on p. 6

Viana, P. T. P. & Liddle, A. R. 1999: *Galaxy clusters at 0.3¡z¡0.4 and the value of Omega$_0$*, MNRAS, 303, 535, cited on p. 2

Walker, A. R. 1990: *Precision UBVRI CCD photometry*, in ASP Conf. Ser. 8: CCDs in astronomy, 319–325, cited on p. 150

Walterbos, R. A. M. & Kennicutt, R. C. 1987: *Multi-color photographic surface photometry of the Andromeda galaxy*, A&AS, 69, 311, cited on p. 8, 77, 78

Wells, D. C., Greisen, E. W., & Harten, R. H. 1981: *FITS - a Flexible Image Transport System*, A&AS, 44, 363+, cited on p. 99

Wetterich, C. 1988: *Cosmology and the fate of dilatation symmetry*, Nuclear Physics B, 302, 668, cited on p. 3

Widrow, L. M., Perrett, K. M., & Suyu, S. H. 2003: *Disk-Bulge-Halo Models for the Andromeda Galaxy*, ApJ, 588, 311, cited on p. 79

Williams, B. F. 2002: *Clues about the star formation history of the M31 disc from WFPC2 photometry*, MNRAS, 331, 293, cited on p. 81

Willick, J. A. & Strauss, M. A. 1998: *Maximum Likelihood Comparison of Tully-Fisher and Redshift Data. II. Results from an Expanded Sample*, ApJ, 507, 64, cited on p. 2

Wilson, G., Kaiser, N., & Luppino, G. A. 2001: *Mass and Light in the Universe*, ApJ, 556, 601, cited on p. 6

Windhorst, R. A., Franklin, B. E., & Neuschaefer, L. W. 1994: *Removing cosmic-ray hits from multi-orbit HST Wide Field Camera images*, PASP, 106, 798, cited on p. 119

Witt, H. J. 1995: *The Effect of the Stellar Size on Microlensing at the Baade Window*, ApJ, 449, 42+, cited on p. 48, 86

Wozniak, P. & Paczyński, B. 1997: *Microlensing of Blended Stellar Images*, ApJ, 487, 55+, cited on p. 10, 17

Wozniak, P. R. 2000: *The Optical Gravitational Lensing Experiment (OGLE-II). Difference Image Analysis of the Bulge Data.*, in American Astronomical Society Meeting, Vol. 197, 6702+, cited on p. 98

Zaritsky, D. & Lin, D. N. C. 1997: *Evidence for an Intervening Stellar Population Toward the Large Magellanic Cloud*, AJ, 114, 2545, cited on p. 7

Zoccali, M., Cassisi, S., Frogel, J. A., Gould, A., Ortolani, S., Renzini, A., Rich, R. M., & Stephens, A. W. 2000: *The Initial Mass Function of the Galactic Bulge down to $\sim 0.15 M_\odot$*, ApJ, 530, 418, cited on p. 77, 80, 165, 186

Zwicky, F. 1933: *Die Rotverschiebung von extragalaktischen Nebeln*, Helvetica Physica Acta, 6, 110, cited on p. 2

Zwicky, F. 1937: *On the Masses of Nebulae and of Clusters of Nebulae*, ApJ, 86, 217, cited on p. 6

Acknowledgments / Danksagung

Curriculum Vitae

Name:	Arno Riffeser
Born:	April the 24th, 1973, Bozen, Italy
Marital Status:	Single
Citizenship:	Italian
Home:	Forstenrieder Allee 208, 81476 Munich, Germany

Education	1979 – 1987	Elementary School Student in Eppan
	1987 – 1992	High-School Student, Realgymnasium, Bozen
	1992	Abitur, Realgymnasium, Bozen
	1992 – 1997	Diploma Student, Physics, LMU Munich
	1997 – 1998	Diploma Thesis, Physics, LMU Munich
	1999 – 2005	Ph.D. Student, Universitäts-Sternwarte, LMU Munich